

Lattice QCD at the physical point: pion-pion scattering and structure of the nucleon.

Thibault Métivet

► **To cite this version:**

Thibault Métivet. Lattice QCD at the physical point: pion-pion scattering and structure of the nucleon.. Nuclear Experiment [nucl-ex]. Université Paris Sud, 2015. English. <tel-01243018>

HAL Id: tel-01243018

<https://hal.archives-ouvertes.fr/tel-01243018>

Submitted on 14 Dec 2015

HAL is a multi-disciplinary open access archive for the deposit and dissemination of scientific research documents, whether they are published or not. The documents may come from teaching and research institutions in France or abroad, or from public or private research centers.

L'archive ouverte pluridisciplinaire **HAL**, est destinée au dépôt et à la diffusion de documents scientifiques de niveau recherche, publiés ou non, émanant des établissements d'enseignement et de recherche français ou étrangers, des laboratoires publics ou privés.

UNIVERSITÉ PARIS-SUD

ECOLE DOCTORALE PARTICULES, NOYAUX ET COSMOS
SERVICE DE PHYSIQUE NUCLÉAIRE, IRFU, CEA SACLAY

DISCIPLINE : PHYSIQUE

THÈSE DE DOCTORAT

Soutenue le 29 septembre 2015 par

Thibaut METIVET

Lattice QCD at the physical point: pion-pion scattering and structure of the nucleon

Directeur de thèse :	M. Pierre GUICHON	Chercheur CEA (SPhN, IRFU, CEA Saclay)
Co-directeur de thèse :	M. Laurent LELLOUCH	Directeur de recherche CNRS (CPT Marseille)
Composition du jury :		
Président du jury :	M. Jaume CARBONELL	Directeur de recherche CNRS (IPN Orsay)
Rapporteurs :	M. Benoit BLOSSIER	Chargé de recherche CNRS (LPT Orsay)
	M. Christian HOELBLING	Senior Physicist (Wuppertal Universität)
Examineurs :	M. Samuel WALLON	Maître de conférences (UPMC Paris)

*Un coup de dés
jamais
Quand bien même lancé dans
des circonstances éternelles ...*

Contents

Aknowledgements	6
1. Introduction	7
2. QCD on the lattice	13
2.1. QCD basics	13
2.1.1. Quarks, gluons and chromodynamics	13
2.1.2. Quantization	15
2.1.3. Renormalization, asymptotic freedom and confinement	17
2.1.4. Chiral symmetry	18
2.2. QCD on the lattice	19
2.2.1. QCD lattice action	19
2.2.2. Symanzik improvement program	22
2.2.3. Gauge-link smearing	24
2.3. Computing vacuum expectation values	25
2.3.1. Path integrals on the lattice	25
2.3.2. Hybrid Monte-Carlo method	26
2.4. Hadron spectrum and scale setting	29
2.4.1. Gauge configuration ensembles	29
2.4.2. Hadron spectrum	31
2.4.3. Scale setting	33
3. $\pi\pi$ scattering: the ρ resonance	37
3.1. Introduction	37
3.2. $\pi\pi$ scattering in finite volume	37
3.2.1. Lüscher's method	37
3.2.2. Symmetry considerations	39
3.2.3. Finite volume formula	40
3.3. Methodology	41
3.3.1. Extraction of the energies: the generalized eigenvalue method	41
3.3.2. Kinematics and interpolating operators	43
3.3.3. Parametrization of the resonance	44
3.3.4. Pion mass dependence of the resonance	45
3.4. Lattice calculation details	47
3.4.1. Ensembles	47
3.4.2. Contractions and stochastic propagators	48

3.5. Results	51
3.5.1. GEVP energies	51
3.5.2. Results for the “GEVP” ensembles	56
3.5.3. Global fit and systematic error analysis	56
3.5.4. Resonance parameters	63
3.5.5. Conclusion	65
4. Nucleon form factors	68
4.1. Form factors	68
4.1.1. Electromagnetic form factors	68
4.1.2. Axial form factors	72
4.2. Methodology	74
4.2.1. Lattice currents, renormalization and Ward identities	74
4.2.2. Spectral decomposition	78
4.2.3. Form factor extraction	82
4.2.4. Excited states	83
4.3. Lattice calculation details	85
4.3.1. Ensembles, kinematics and parameters	85
4.3.2. Contractions and smearing	86
4.4. Results	90
4.4.1. Form factors	90
4.4.2. Electric charge radius	102
4.4.3. Magnetic moment	106
4.4.4. Axial charge	107
4.5. Conclusion	108
5. Conclusion and outlooks	109
Appendices	112
Appendix A. Statistics	112
Appendix B. Two-point functions	114
Appendix C. Lüscher equation	118
C.1. Some useful results	118
C.2. Quantization Condition	124
C.3. Angular momentum cut-off	129
Appendix D. Lüscher equation and symmetries	131
D.1. Introduction	131
D.2. Kinematics	131
D.3. Symmetry considerations	133
D.3.1. Symmetries and group theory	133
D.3.2. Symmetries and interpolating operators	136

Contents	5
----------	---

D.4. Finite-size formulae	138
-------------------------------------	-----

Appendix E. Variable projection method	142
---	------------

Remerciements

Je tiens tout d’abord à remercier chaleureusement Pierre GUICHON, pour son soutien, sa volonté de transmettre et sa disponibilité. Sa culture scientifique, ainsi que son approche passionnée de la physique ont été la meilleure porte d’entrée que je puisse avoir dans le monde de la recherche. J’exprime aussi toute ma reconnaissance à Laurent LELLOUCH, pour ses conseils toujours avisés, sa rigueur et son exigence, sans lesquels ce travail ne serait pas ce qu’il est.

Je remercie aussi Benoit BLOSSIER, Christian HOELBLING et Samuel WALLON, pour avoir accepté de rapporter et d’examiner ce travail, ainsi que pour leurs commentaires et questions pertinents qui ont contribué à l’aboutissement de cette thèse. J’exprime aussi toute ma gratitude à Jaume CARBONELL, pour avoir accepté de présider mon jury, et pour toutes nos discussions toujours enrichissantes.

Je tiens aussi à remercier amicalement Nicole D’HOSE, David LHUILLIER, Alain LETOURNEAU et Thomas MATERNA pour tous ces déjeuners sympathiques qui ne manquaient jamais de panache.

J’assure de toute ma gratitude Valérie POYETON, Danielle CORET et Isabelle RICHARD pour leur aide inestimable tout au long de mes récurrentes traversées des eaux administrativement troubles du CEA.

Je tiens aussi à exprimer toute mon amitié à Valérian SIBILLE, pour nos débats houleux et passionnés mais toujours agréables et Thibault MAIN DE BOISSIERE pour nos délires dignes de Carroll. Je remercie aussi Nicolas GERARD-CASTAING et Aurélie BONHOMME pour tous ces repas animés et sympathiques.

Je remercie très chaleureusement mes amis basketteurs, Vincent REVERET, Cédric BACOUR et Pierre LAURENT, avec une pensée toute particulière pour Jean-Baptiste LADANT et Pierre SEPULCHRE, pour les “Mamane” d’après jeu, les inoubliables trajets dans les bouchons parisiens (malheureusement trop rarement en Audi) et les pauses café toujours plaisantes et divertissantes. Les *playgrounds* de Grenoble vous attendent !

J’adresse aussi un immense merci à mon ami Maxime PEQUIGNOT, pour son soutien permanent, sa bonne humeur inébranlable, même face aux caprices d’un théoricien, et sa présence toujours opportune.

Enfin, je tiens à remercier très affectueusement mes amis, en particulier Simon BOUZY, pour nos bouffées d’air du week-end, et ma famille, qui m’ont supporté toutes ces années, et auprès desquels j’ai eu la chance de grandir et de m’épanouir.

1. Introduction

Quantum Chromodynamics (QCD) is the theory of strong interaction between quarks and gluons. The essential features of QCD are, on the one hand, the existence of spin 1/2 quarks coming in color triplets and spin 1 gluons coming in color octets and, on the other hand, the existence of a coupling of equal strength between the quarks and gluons and between gluons themselves. Moreover QCD has the property of asymptotic freedom which means that the coupling decreases logarithmically with the relative momentum of the interacting particles.

Quarks were first introduced in 1964 [1–3] to explain the rich spectroscopy of mesons and baryons in terms of quark-antiquark or three-quark bound states. The first evidence for quarks came in 1968 from the SLAC deep inelastic electron-proton experiments which could be interpreted as scattering on quasi-free point-like objects. This was confirmed by the later observation of the jets produced in e^+e^- annihilation.

The 3 color degrees of freedom were introduced to reconcile spin 1/2 Fermi statistics with the existence of the Δ^{++} which is made of three u quarks and therefore would have a symmetric wave function if one takes only space, spin and flavour into account. Moreover in e^+e^- annihilation, the ratio

$$R = \frac{\sigma(e^+e^- \rightarrow \text{hadrons})}{\sigma(e^+e^- \rightarrow \mu^+\mu^-)}$$

is predicted by QED and the quark-parton model to be equal to $N_c \sum_f Q_f^2$ where Q_f is the electric charge of the flavour f and the sum runs over all active flavours at the given energy. Fig. 1.1 shows a collection of experimental results where the charm and bottom threshold are clearly visible. The inter-threshold plateaus are only compatible with $N_c = 3$.

The proof for existence of the gluon as well as its coupling to the quarks was provided by the 3-jet events interpreted as $e^+e^- \rightarrow q\bar{q}g$ observed in 1979 at PETRA. A more recent example of such a 3-jet event is shown in Fig. 1.2.

An important point is that the angular distribution of one jet with respect to the other is sensitive to the spin of the gluon. As shown on Fig. 1.3 the data clearly favours the spin 1 case. Further studies, analogous to this one, have also excluded the spin 2 case. While the 3-jet events reveal the existence of the quark gluon coupling, the genuine non-abelian character of QCD implies that there also exists a 3- and 4-gluon coupling. The 3-gluon coupling has been observed in the 4-jet events at LEP with a strength compatible with the quark gluon coupling but the 4-gluon coupling is more elusive because it can appear only in the 5-jet events. A more detailed discussion of the phenomenological tests of QCD can be found in [4].

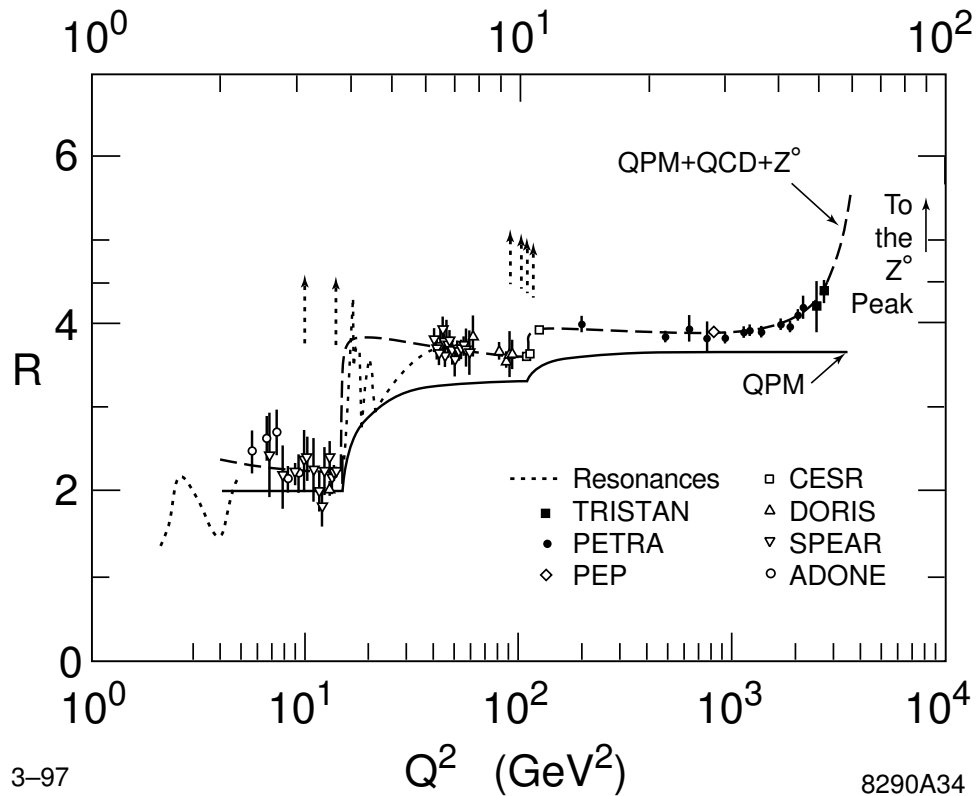


Figure 1.1.: The ratio R as a function of CM energy. The expectation for $N_c = 3$ is the continuous line.

The most spectacular prediction of QCD is that its coupling decreases with the energy scale at which it is measured. Many experiments have been performed to test this important property and Fig. 1.4 shows that it is actually satisfied in a wide energy range.

Since the coupling gets smaller when the energy scale increases, it is possible to use perturbation theory to make detailed predictions. In particular, one can predict how the quark distributions in the nucleon evolve when the resolution of the probe improves. The results are shown in Fig. 1.5 for the structure function F_2 which is a combination of quark distributions. The evolution is very well fitted by the QCD perturbative evolution in a huge energy range.

In the above rapid presentation of tests of QCD there was no reference to the fact that neither the quarks nor the gluons have ever been observed. The reason is that the tests are performed at such high energies that the elementary reaction is not affected by confinement, another fundamental property of QCD. The idea behind this is that the amplitude factorises into a part which involves the microscopic constituents, the quarks and the gluons, and another one which describes how those microscopic constituents are bound into the observed hadrons. This second factor is completely non-perturbative and

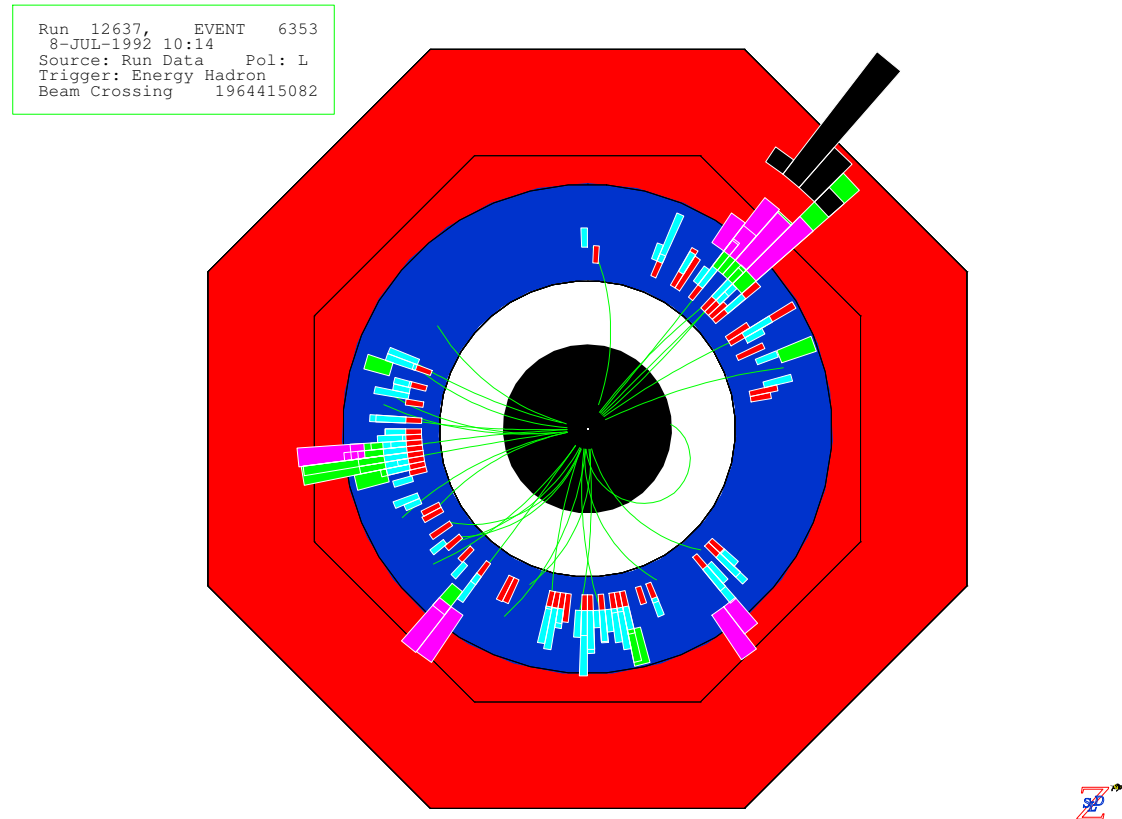


Figure 1.2.: 3-jet event in the SLD SLAC detector

is either fitted to the experimental data or computed using non-perturbative approaches.

In this context, symmetries play a crucial role since their consequences do not rely on an explicit solution of the non-perturbative problem. Beside the usual space-time symmetries, QCD satisfies an approximate $SU(N_f) \times SU(N_f)$ chiral symmetry due to the small masses of the first N_f flavours of quarks. In practice, if $N_f = 2$, one assumes that the *up* and *down* quarks are light while $N_f = 3$ requires that the *strange* quark is also light, a more questionable approximation. Chiral symmetry is spontaneously broken to $SU(N_f)$ by the QCD vacuum which, according to Goldstone's theorem, leads to the existence of $N_f^2 - 1$ light pseudo-scalars. For $N_f = 2$ these are the pions, which mass (~ 140 MeV), small compared to a typical hadronic mass (~ 1 GeV), sets the scale to rate the zero mass approximation. The consequences of chiral symmetry come in the form of low-energy theorems which can be derived in the framework of chiral perturbation theory. This amounts to considering that the low-energy effective theory for QCD has the light pions as degrees of freedom interacting with point-like heavy particles in a chiral symmetric fashion [5]. The method is useful only when the pion mass and momenta considered are small, but it has nonetheless provided many quantitative tests of QCD

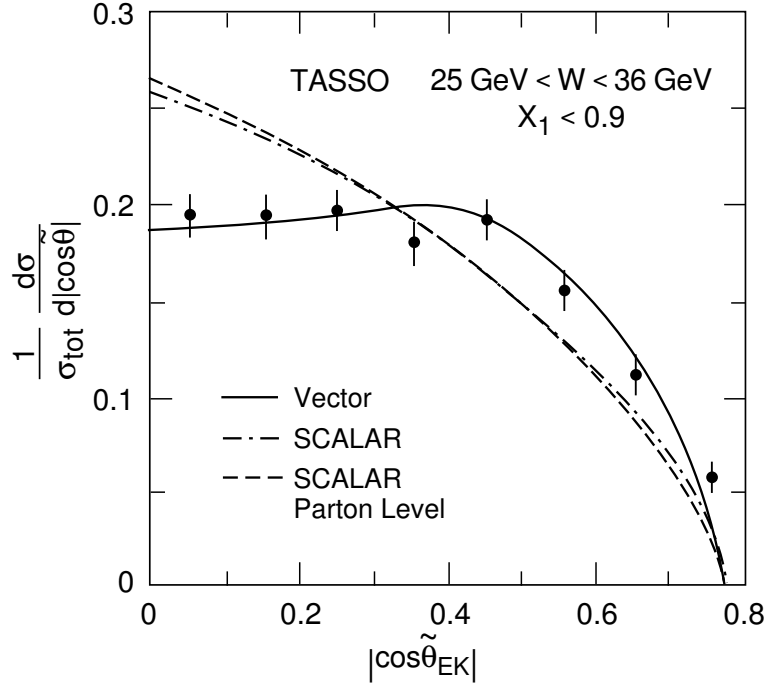
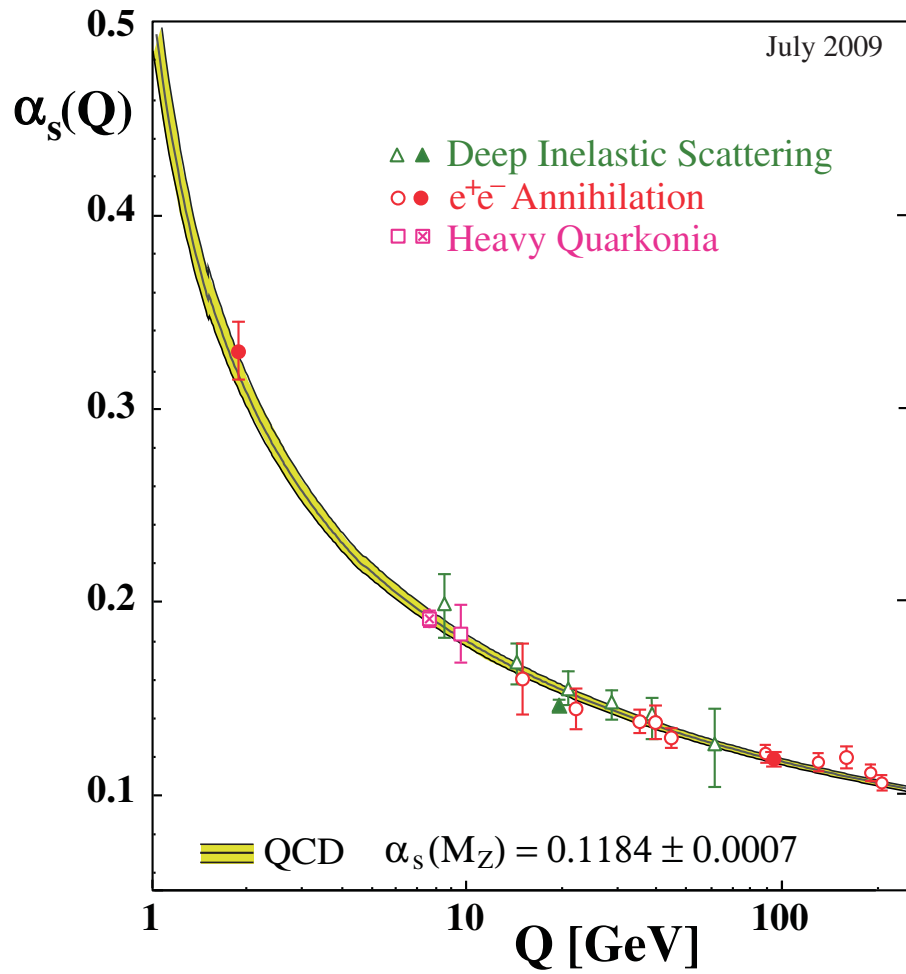


Figure 1.3.: Angular distribution of 3-jet events compared to the prediction for a spin 0 or spin 1 gluon.

in the non-perturbative domain [6].

For a full access to the non-perturbative regime of QCD, one has to rely on the numerical simulations of QCD on the lattice and this is the framework of this thesis. The lattice allows a gauge invariant regularization of the theory with the ultraviolet cut-off given by the lattice spacing and the infrared one given by the lattice size. One then has a well formulated many body problem for which one can use Monte-Carlo methods to compute the relevant Green functions and then the observables. This aspect will be presented in Chapter 2, along with a brief general review of QCD as a quantum field theory. In Chapter 3, we present Lüscher's finite-volume framework to study scattering states on the lattice, as well as its application to the case of $\pi\pi$ scattering in the ρ resonant channel. We also give our results for a full calculation of the corresponding phase-shifts, using several gauge configuration ensembles including one at the physical pion mass. The ρ resonance parameters are computed using a global analysis procedure with control on the systematic errors. In Chapter 4, we undertake a full study of the nucleon electroweak form factors, with a detailed analysis of the electric radius and axial charge. Our calculation goes down to the physical pion mass with fine control of excited-state contaminations.

Figure 1.4.: QCD coupling constant as a function of the energy scale Q .

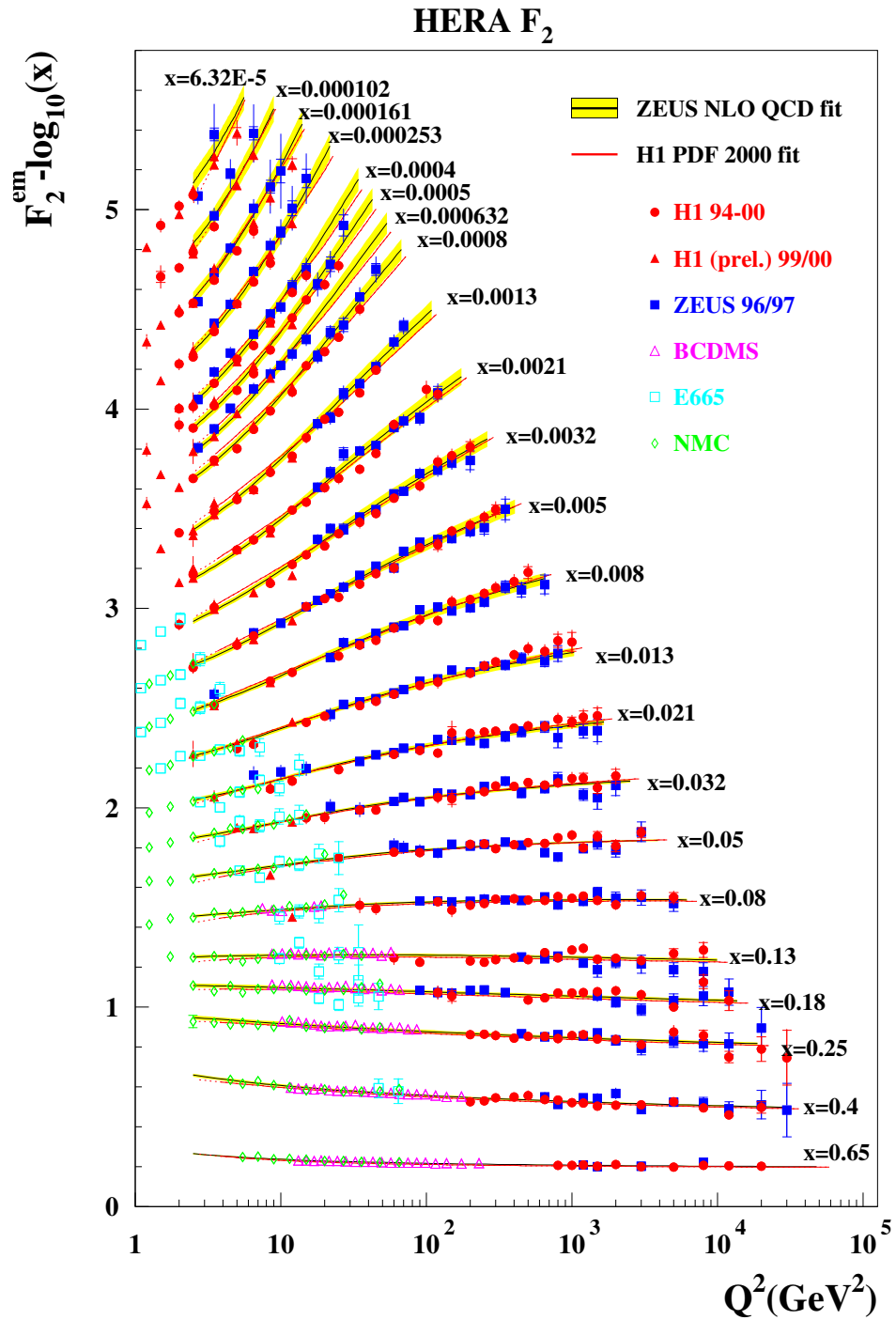


Figure 1.5.: The structure function plotted with respect to Q^2 for several values of x_{Bjorken} .

2. QCD on the lattice

2.1. QCD basics

2.1.1. Quarks, gluons and chromodynamics

The quarks are spin- $\frac{1}{2}$ massive fermions, coming with six different flavours and 3 different *color* charges. We restrict ourselves to the 3 lightest flavours, called *up*, *down* and *strange*. Each quark is described by a Dirac 4-spinor field

$$q_{(f)}(x)_\alpha, \quad (f) = u, d, s, \quad \alpha = 1, \dots, 4, \quad a = 1, \dots, 3 \quad (2.1)$$

where α is the spinor index and a the color one. We shall subsequently denote spinor indices with Greek letters, and color indices with Latin letters, and hide irrelevant indices when they are not required.

In the absence of interactions, $q_{(f)}(x)_\alpha$ is solution of the free Dirac equation

$$(i\gamma \cdot \partial - m) q = 0 \quad (2.2)$$

where $\gamma \cdot \partial \equiv \gamma^\mu \partial_\mu$ with γ^μ , $\mu = 1, \dots, 4$ the Dirac matrices satisfying $\{\gamma^\mu, \gamma^\nu\} = 2g^{\mu\nu}$, and where spinor matrix multiplications are implied. Eq. (2.2) corresponds to the Euler-Lagrange equation of the Lagrangian density

$$\mathcal{L}_{\text{Dirac}} = \bar{q} (i\gamma \cdot \partial - m) q$$

where we have introduced $\bar{q} \equiv q^\dagger \gamma^0$.

Note that Eq. (2.2) is unchanged if one performs a global SU(3) color gauge transformation

$$q(x)_a \rightarrow \sum_b \mathbf{g}_{ab} q(x)_b \equiv \mathbf{g} q(x)$$

with $\mathbf{g} \in \text{SU}(3)$.

Quantum Chromodynamics is built on the assumption that Eq. (2.2) should also remain invariant under a *local* SU(3) gauge transformation

$$q(x) \rightarrow \mathbf{g}(x) q(x) \quad (2.3)$$

which amounts to the assumption that physics is independent of the local color frame. To turn Eq. (2.2) into a locally gauge-invariant form, we need to generalize the derivative to

$$D_\mu q(x) \equiv \lim_{\epsilon \rightarrow 0} \frac{1}{\epsilon} [U(x, x + \epsilon \hat{\mu}) q(x + \epsilon \hat{\mu}) - q(x)] \quad (2.4)$$

where the *gauge link* $U(x, y)$ is a phase going to 1 at zero separation. For small ϵ , $U(x, x + \epsilon n)$ can be expanded as

$$U(x, x + \epsilon n) = 1 + i\epsilon n^\mu A_\mu(x) + O(\epsilon^2)$$

where $A_\mu(x)$ – the so-called gauge fields, are hermitian color matrices which act as *connections* between infinitesimally separated points.

If we now require that under local gauge transformations,

$$U(x, y) \rightarrow \mathbf{g}(x)U(x, y)\mathbf{g}(y)^{-1} \quad (2.5)$$

or equivalently

$$A_\mu(x) \rightarrow \mathbf{g}(x) (A_\mu(x) + i\partial_\mu) \mathbf{g}(x)^{-1} \quad (2.6)$$

then the derivative

$$D_\mu \equiv \partial_\mu - iA_\mu$$

transforms as q , and the modified Dirac equation

$$(i\gamma \cdot D - m)q = 0 \quad (2.7)$$

is invariant under local gauge transformations.

Introducing $\{T_k, k = 1, \dots, 8\}$ a basis of generators of $\mathfrak{su}(3)$, the Lie algebra of $SU(3)$, which satisfies

$$[T_i, T_j] = if_{ijk}T_k$$

where f_{ijk} is the antisymmetric structure constant, we can expand $A_\mu(x)$ like any hermitian matrix as

$$A_\mu = \sum_{k=1}^8 A_{\mu k} T_k$$

The 8 real $A_{\mu k}$ fields are then the gluon fields.

To find the complete Lagrangian of QCD, we need to build the gauge-invariant terms controlling the dynamics of A_μ . We introduce the field strength tensor

$$F^{\mu\nu} = \sum_{k=1}^8 F_k^{\mu\nu} T_k \equiv \partial^\mu A^\nu - \partial^\nu A^\mu - i[A^\mu, A^\nu] \quad (2.8)$$

Under the gauge transformation (2.6),

$$F^{\mu\nu} \rightarrow \mathbf{g}F^{\mu\nu}\mathbf{g}^{-1}$$

and we can build the Yang-Mills Lagrangian density of QCD from $\text{Tr}[F^{\mu\nu}F_{\mu\nu}]$. We get finally

$$\mathcal{L}_{\text{QCD}} = -\frac{1}{2g^2} \text{Tr}[F^{\mu\nu}F_{\mu\nu}] + \bar{q}(i\gamma \cdot D - m)q \quad (2.9)$$

where g is the coupling constant of QCD.

Expanding the trace, and defining $\Pi_{\mu k}$ and $\Pi(q)$ the conjugate momenta of $A^{\mu k}$ and q respectively

$$\Pi_{\mu k} = \frac{\partial \mathcal{L}}{\partial \partial_0 A^{\mu k}} = -\frac{1}{g^2} F_{\mu 0 k} \quad (2.10)$$

$$\Pi(q) = \frac{\partial \mathcal{L}}{\partial \partial_0 q} = iq^\dagger \quad (2.11)$$

we obtain after some algebra the Hamiltonian

$$H_{\text{QCD}} = \int d\mathbf{x} \left(\frac{g^2}{2} \mathbf{\Pi}_k \cdot \mathbf{\Pi}_k + \frac{1}{2g^2} \mathbf{B}_k \cdot \mathbf{B}_k + \bar{q}(-i\boldsymbol{\gamma} \cdot \nabla + m)q - \bar{q}\boldsymbol{\gamma} \cdot \mathbf{A}q - A_k^0 G_k \right) \quad (2.12)$$

where $B_k^1 = F_k^{23}$, $B_k^2 = F_k^{31}$, $B_k^3 = F_k^{12}$ and

$$G_k \equiv \nabla \cdot \mathbf{\Pi}_k - f_{kij} \mathbf{\Pi}_i \cdot \mathbf{A}_j - q^\dagger T_k q$$

is the Gauss operator.

An important property of the Gauss operator is that it generates the gauge transformations 2.3 and 2.6, in the sense that if we write

$$\mathbf{g}(x) = e^{i\omega(x)_k T_k}$$

with $\omega(x)$ going to 0 as $|\mathbf{x}| \rightarrow \infty$, then (see [7] for a more comprehensive proof)

$$\begin{aligned} e^{i \int d\mathbf{x} \omega_k G_k} q e^{-i \int d\mathbf{x} \omega_k G_k} &= \mathbf{g} q \\ e^{i \int d\mathbf{x} \omega_k G_k} \mathbf{A} e^{-i \int d\mathbf{x} \omega_k G_k} &= \mathbf{g}(x) (\mathbf{A} + i\nabla) \mathbf{g}(x)^{-1} \end{aligned}$$

This Gauss operator shall play an important role in the definition of the physical states of the quantized theory.

2.1.2. Quantization

The canonical prescription to quantize a field theory is to promote the canonical variables to operators, denoted with a $\hat{}$, and impose commutation relations. However, the situation of gauge theories is made trickier as the symmetries impose relations between variables, which are therefore no longer independent.

In QCD, the problem involves the definition of the gluon conjugate momentum $\hat{\Pi}_\mu$, as the antisymmetry of $F_{\mu\nu}$ gives

$$\hat{\Pi}_0(\mathbf{x}, t) = 0, \quad \forall t$$

If we impose the canonical equal-time commutation relations

$$\left[\hat{\Pi}_{\mu k}(\mathbf{x}, t), \hat{A}_{\nu l}(\mathbf{y}, t) \right] = -i\delta_{kl} g_{\mu\nu} \delta^3(\mathbf{x} - \mathbf{y}) \quad (2.13)$$

then Eq. (2.12) gives

$$\left[\hat{H}_{\text{QCD}}, \hat{\Pi}_{0k}(\mathbf{x}, t) \right] = -i\hat{G}_k(\mathbf{x}, t)$$

which gives the Gauss law

$$\hat{G}_k(\mathbf{x}, t) = 0, \quad \forall t \quad (2.14)$$

Note that

$$\left[\hat{H}_{\text{QCD}}, \hat{G}_k(\mathbf{x}, t) \right] = 0$$

so that it is sufficient to have $\hat{\Pi}_0 = 0$ and $\hat{G}_k = 0$ at $t = 0$ to ensure that these will be satisfied for all t .

As mentioned above, \hat{G}_k generates gauge transformations, so the conditions $\hat{\Pi}_0 = 0$ and $\hat{G}_k = 0$ at $t = 0$ impose that possible physical states must be independent of \hat{A}_0 and gauge invariant.

The basic objects to build such gauge invariant physical states are the Wilson line and the Wilson loop. The Wilson line corresponds to the generalization of the gauge link $U(x, y)$ for x and y far apart

$$U_{\mathcal{C}}(x, y) \equiv \mathcal{P} \exp \left[i \int_{\mathcal{C}} dx^\mu A_\mu(x) \right] \quad (2.15)$$

where \mathcal{C} is a curve going from x to y , and \mathcal{P} is the path-ordering operator, which imposes that in the exponential of (2.15), defined as a series expansion, the matrices are always ordered such that they “go forward” along \mathcal{C} . The Wilson line is not gauge invariant *per se*, but becomes so when quarks are attached to its ends.

The Wilson loop is the trace of the Wilson line along a closed curve:

$$L_{\mathcal{C}} \equiv \text{Tr} [U_{\mathcal{C}}(x, x)] \quad (2.16)$$

It is the basic building block of “pure gauge” gauge invariant quantities.

Constructing all the gauge invariant states is however unworkable, which makes canonical quantization unsuitable for practical calculations. Instead, we use the Feynman path integral formalism.

If we consider \hat{O} a canonically quantized operator, with the time-dependence

$$\hat{O}(\mathbf{x}, t) \equiv e^{-Ht} \hat{O}(\mathbf{x}, 0) e^{Ht} \quad (2.17)$$

then one can show by dividing the $[0, t]$ time interval into small steps and inserting complete sets of states at each step that the vacuum expectation value $\langle \Omega | \hat{O} | \Omega \rangle$ is equal to the expectation value

$$\langle O \rangle \equiv \frac{1}{\mathcal{Z}} \int \text{D}A_\mu \text{D}q \text{D}\bar{q} O[A_\mu, q, \bar{q}] e^{-S_E[A_\mu, q, \bar{q}]} \quad (2.18)$$

of the operator O seen as a functional of A_μ , q and \bar{q} , where \mathcal{Z} is the partition function

$$\mathcal{Z} = \int \text{D}A_\mu \text{D}q \text{D}\bar{q} e^{-S_E[A_\mu, q, \bar{q}]} \quad (2.19)$$

$S_E[A_\mu, q, \bar{q}]$ the Euclidean action

$$\begin{aligned} S_E[A_\mu, q, \bar{q}] &= \int dx \frac{1}{4g^2} F_{\mu\nu}^k(x) F_{\mu\nu}^k(x) + \int dx \bar{q}(x) (\gamma^0 D_0 + i\gamma^i D_i + m) q(x) \\ &\equiv S_G[A] + S_F[A, q, \bar{q}] \end{aligned} \quad (2.20)$$

and where the integral runs over all functions A_μ , and Grassmann number valued functions q, \bar{q} .

2.1.3. Renormalization, asymptotic freedom and confinement

The functional integral formulation Eq. (2.18) has no proper meaning in this form, as the functional measures are not well defined. This can be overcome by discretizing space-time – the lattice QCD approach, which we describe comprehensively in Sec. 2.2, thereby introducing a finite lattice spacing a , which we shall eventually take to 0. This approach naturally introduces a regularization of the theory, in the sense that it imposes a momentum cut-off at $\frac{\pi}{a}$, and makes momentum integrals finite. Eq. (2.18) is then defined as the limit as $a \rightarrow 0$ of its discrete counterpart.

Consider now some operator $O(a, g(a))$ written in terms of the bare fields appearing in the action (2.20). To get its vacuum expectation value using our functional integral formalism, we must compute (2.18) at non-zero a (i.e. finite momentum cut-off) and then take the continuum limit $a \rightarrow 0$. Following Wilson's approach [8], we must then define a renormalized action and a renormalized operator in order to obtain a smooth limit as $a \rightarrow 0$. These renormalized quantities are defined to smoothly incorporate and account for contributions coming from momenta higher than $\frac{\pi}{a}$. The renormalized action has the same form as the original one, but with rescaled fields, and parameters which now depend on a . Assuming that O does not mix with other operators in the presence of radiative corrections, the renormalized operator O_R is related to the bare one by a multiplicative constant, called the *renormalization constant*, and should be independent of a :

$$O_R \equiv Z(a, g) O(a, g)$$

Z is a dimensionless quantity, so that a new scale μ must be introduced in the definition of O_R to compensate for the dimension of a and form the dimensionless $a\mu$ quantity. μ has therefore the dimension of an energy, and is called the *renormalization scale* as it is in practice the scale at which we shall specify renormalization conditions to properly define the integral. This artificially introduces a dependence of O_R on the renormalization scale μ , i.e.

$$O_R = O_R(\mu, g(\mu))$$

However, if the theory is to give robust predictions, any physical observable involving $O_R(\mu, g(\mu))$ must be independent of the scale μ at which we imposed the conditions to completely define the Lagrangian. This independence can be expressed through the so-called Callan-Symanzik equation [9] [10]:

$$\mu \frac{d}{d\mu} \langle \mathcal{O} [O_R(\mu, g(\mu))] \rangle = \left(\mu \frac{\partial}{\partial \mu} + \beta(g) \frac{\partial}{\partial g} \right) \langle \mathcal{O} [O_R(\mu, g(\mu))] \rangle = 0 \quad (2.21)$$

where \mathcal{O} is the observable, and we have introduced the β function

$$\beta(g) \equiv \mu \frac{dg}{d\mu} \quad (2.22)$$

which encodes all the dependence of the coupling g on the energy scale.

The *running* of $g(\mu)$ depends on the sign of the β function, which was first computed perturbatively (i.e. near $g = 0$) in [11] and [12] with the result

$$\beta(g) = -\frac{g^3}{16\pi^2} \left(11 - \frac{2}{3}N_f \right) + O(g^5) \quad (2.23)$$

where N_f is the number of quark flavours considered. Introducing the usual strong coupling

$$\alpha_s \equiv \frac{g^2}{4\pi}$$

we can integrate Eq. (2.22) using Eq. (2.23) to obtain the running (at leading order)

$$\alpha_s(\mu^2) = \frac{\alpha_s(\mu_0^2)}{1 + \frac{\alpha_s(\mu_0^2)}{2\pi} \left(11 - \frac{2}{3}N_f \right) \ln \left(\frac{\mu^2}{\mu_0^2} \right)} \quad (2.24)$$

In practice, $N_f = 6$, so that

$$\alpha_s(\mu^2) \xrightarrow{\mu \rightarrow \infty} 0 \quad (2.25)$$

This result is the well-known *asymptotic freedom* property of QCD.

Note that to obtain this property, we have assumed that there existed an energy scale for which g was small enough to use perturbation theory. However, this result has also been confirmed non-perturbatively using lattice QCD calculations of the string tension, i.e. the “long-distance” force between static quarks. The first calculation for QCD was done in [13], and showed that the evolution of the string tension as a function of the coupling follows the perturbative prediction.

This pioneering calculation of the string tension also highlighted that the latter is non-zero, which is directly related to the *confinement* property of QCD. This property implies that coloured particles (such as the quarks) cannot be observed and always clump into colorless structures called hadrons.

2.1.4. Chiral symmetry

In the massless-quark limit, the action of QCD appearing in Eq. (2.20) is invariant under global $SU(N_f) \times SU(N_f) \times U(1)$ transformations [6], where N_f is the number of flavours considered and the rotations act in flavour space. This is called the *chiral* symmetry property of QCD, as the $SU(N_f)_R \times SU(N_f)_L$ transformations act on the right- and left-handed fermion fields

$$q_R \equiv \frac{\mathbf{1} + \gamma_5}{2} q \quad \text{and} \quad q_L \equiv \frac{\mathbf{1} - \gamma_5}{2} q$$

respectively. We consider more specifically the case $N_f = 3$, with 2 light *up* and *down* quarks and 1 heavier *strange* quark.

The absence of parity doubling in the observed hadron spectrum and the eight rather “light” π , K and η pseudoscalar mesons suggest that the axial $SU(3)_{R-L}$ symmetry is spontaneously broken, i.e.

$$SU(3)_R \times SU(3)_L \rightarrow SU(3)_{R+L}$$

The 8 generators of $SU(3)_{R-L}$ do not leave the QCD vacuum invariant and lead to the existence of 8 massless Goldstone bosons. These are the π^\pm , π^0 , K^\pm , K^0 , \bar{K}^0 and η mesons already mentioned. They are not exactly massless as the quark masses are not zero, so that the spontaneously broken symmetry is only approximate even at the Lagrangian level.

The up and down quarks however have small masses, so that the use of the spontaneous breaking of the $SU(2)_R \times SU(2)_L$ subgroup down to $SU(2)_{R+L}$ can be expected to give accurate predictions. This can be done using chiral effective Lagrangians as proposed by Weinberg [14,15], and led to the development of the so-called *chiral perturbation theory*. We refer the reader to [16,17] and [18,19] for more a comprehensive presentation of the chiral effective field theory and some of its applications.

2.2. QCD on the lattice

As mentioned above, to give a proper meaning to the functional integral 2.18, we define it as the continuum limit of an integral in a discrete Euclidean space-time and finite volume, and introduce the 4-dimensional lattice

$$\Lambda = \{x \equiv an = a(\mathbf{n}, n_0) \mid \mathbf{n}_i = [0..L], n_0 \in [0..T]\} \quad (2.26)$$

where a is the lattice spacing, aL is the lattice volume, and aT the lattice time extent. Note that we shall for convenience use the integer 4-vector n to label lattice sites.

We must now define a discrete action on this lattice which reproduces the continuum action (2.20) as $a \rightarrow 0$.

2.2.1. QCD lattice action

The fermion spinor fields are now Grassmann variables defined at each lattice site $q(n)$, $\bar{q}(n)$, and the continuum partial derivative operator is replaced by the symmetric difference

$$\frac{1}{2} (\partial_\mu + \partial_\mu^*) q(n) \equiv \frac{1}{2a} [q(n + \hat{\mu}) - q(n - \hat{\mu})] \quad (2.27)$$

where $\hat{\mu}$ is the vector with components $\hat{\mu}_\nu = \delta_{\mu\nu}$ and where we have defined the forward and backward lattice derivatives

$$\partial_\mu q(n) = \frac{1}{a} [q(n + \hat{\mu}) - q(n)] \quad (2.28)$$

$$\partial_\mu^* q(n) = \frac{1}{a} [q(n) - q(n - \hat{\mu})] \quad (2.29)$$

Note that the Grassmann fermion variables still have implied spinor and color indices, and also come in several flavours. Summation over the flavours shall be understood when applicable in the following.

On the lattice, the integral over dx turns to the sum $a^4 \sum_n$, and the free lattice Dirac action then writes

$$S_{\text{Dirac}}[q, \bar{q}] = a^4 \sum_n \bar{q}(n) \left[\frac{1}{2} \sum_{\mu} \gamma_{\mu}^E (\partial_{\mu} + \partial_{\mu}^*) + m \right] q(n) \quad (2.30)$$

where we have introduced the Euclidean γ matrices

$$\gamma_0^E \equiv \gamma_0, \quad \gamma_i^E \equiv i\gamma_i$$

which satisfy the relations

$$\begin{aligned} \gamma_{\mu}^E &= \gamma^{E\mu} = \gamma^{E\mu\dagger} \\ \{\gamma_{\mu}^E, \gamma_{\nu}^E\} &= 2\delta_{\mu\nu}\mathbf{1} \end{aligned}$$

They naturally lead to the definition of

$$\gamma_5^E \equiv \gamma_1^E \gamma_2^E \gamma_3^E \gamma_0^E \quad (2.31)$$

After Fourier transform, the free Dirac action gives the lattice free quark propagator in momentum space

$$D_{\text{Dirac,free}}^{-1}(p) = \frac{m\mathbf{1} - \frac{i}{a} \sum_{\mu} \gamma_{\mu} \sin(p_{\mu}a)}{m^2 + \frac{1}{a^2} \sum_{\mu} \sin^2(p_{\mu}a)} \quad (2.32)$$

which has the correct naive continuum limit. However, the $\sin^2(p_{\mu}a)$ in the denominator of Eq. (2.32) gives rise to additional unwanted poles, called the *doublers*. This phenomenon is a direct consequence of the discretization of first order derivatives with central differences, and to overcome this issue, Wilson proposed [20] to add an extra term proportional to $a \partial_{\mu}^* \partial_{\mu}$, which leads to the Wilson fermion action

$$S_{\text{Wilson}}[q, \bar{q}] = S_{\text{Dirac}}[q, \bar{q}] - \frac{a^5}{2} \sum_{n,\mu} \bar{q}(n) \partial_{\mu}^* \partial_{\mu} q(n) \quad (2.33)$$

and the momentum space free quark propagator

$$D_{\text{free}}^{-1}(p) = \frac{\left[m + \frac{1}{a} \sum_{\mu} (1 - \cos(p_{\mu}a)) \right] \mathbf{1} - \frac{i}{a} \sum_{\mu} \gamma_{\mu} \sin(p_{\mu}a)}{\left[m + \frac{1}{a} \sum_{\mu} (1 - \cos(p_{\mu}a)) \right]^2 + \frac{1}{a^2} \sum_{\mu} \sin^2(p_{\mu}a)} \quad (2.34)$$

The Wilson term solves the doubler problem, but explicitly breaks chiral symmetry. The quark masses must then undergo an *additive* renormalization proportional to $\frac{1}{a}$, which comes from the mixing between the axial vector and scalar operators (see [21])

for additional details). The bare quark mass must then be carefully tuned to its *critical value*, where it cancels the additive renormalization, so that one obtains a finite renormalized continuum mass, and recovers the axial Ward identities.

Note that the general properties of fermionic actions on a lattice are constrained by the Nielsen-Ninomiya theorem [22–24]. Other lattice actions (such as the *overlap* or *domain-wall* fermion actions, c.f. the review [25]) can then solve the doubler problem while respecting a lattice form of chiral symmetry (the Ginsparg-Wilson equation) but this comes at the expense of ultra-locality and requires an order of magnitude more computing power.

As before, we also impose local gauge invariance of our lattice Lagrangian, and, following Eq. (2.4), we introduce the lattice covariant derivative

$$\nabla_\mu q(n) = \frac{1}{a} [U_\mu(n)q(n + \hat{\mu}) - q(n)] \quad (2.35)$$

$$\nabla_\mu^* q(n) = \frac{1}{a} [q(n) - U_\mu(n - \hat{\mu})^\dagger q(n - \hat{\mu})] \quad (2.36)$$

where the gauge link

$$U_\mu(n) \equiv U(an, an + a\hat{\mu}) \quad (2.37)$$

is a SU(3) matrix attached to the link between sites n and $n + \hat{\mu}$.

To build the Lagrangian controlling the dynamics of gauge links, we consider the *plaquette*, which is the simplest Wilson loop (2.16):

$$P_{\mu\nu}(n) \equiv U_\mu(n)U_\nu(n + \hat{\mu})U_\mu(n + \hat{\nu})^\dagger U_\nu(n)^\dagger \quad (2.38)$$

and define the Wilson gauge action [26]:

$$S_{\text{Wilson,G}}[U_\mu] = \frac{2}{g^2} \sum_{n,\mu<\nu} \text{Re Tr} [\mathbf{1} - P_{\mu\nu}(n)] \quad (2.39)$$

which reproduces the continuum gauge action as $a \rightarrow 0$.

Using covariant derivatives in Eq. (2.33) to couple the quarks to the gluons, we obtain the lattice QCD action

$$\begin{aligned} S_{\text{Wilson}}[q, \bar{q}, U_\mu] &= \frac{\beta}{3} \sum_{n,\mu<\nu} \text{Re Tr} [\mathbf{1} - P_{\mu\nu}(n)] + a^4 \sum_f \sum_n \bar{q}(n) \mathfrak{D}_W q(n) \\ &\equiv S_{\text{Wilson,G}}[U_\mu] + S_{\text{Wilson,F}}[q, \bar{q}, U_\mu] \end{aligned} \quad (2.40)$$

where \mathfrak{D}_W is the Wilson operator:

$$\mathfrak{D}_W \equiv D_W + m = \frac{1}{2} \sum_\mu [\gamma_\mu^E (\nabla_\mu + \nabla_\mu^*) - a \nabla_\mu^* \nabla_\mu] + m$$

i.e.

$$\mathfrak{D}_W(n, m) = \left(m + \frac{4}{a}\right) \mathbf{1} - \frac{1}{2a} \sum_\mu \left[(\mathbf{1} - \gamma_\mu^E) U_\mu(n) \delta_{n+\hat{\mu},m} + (\mathbf{1} + \gamma_\mu^E) U_\mu(n - \hat{\mu})^\dagger \delta_{n-\hat{\mu},m} \right] \quad (2.41)$$

and we have traditionally defined

$$\beta \equiv \frac{6}{g^2}$$

To fully define the discrete theory, we need to specify boundary conditions for the lattice variables. We choose periodic boundary conditions for the gauge field, as this preserves discrete translation invariance of the lattice. The fermion fields are given periodic boundary conditions in the spatial directions and anti-periodic ones in the temporal direction, as suggested in [27], to ensure proper reconstruction of a positive and self-adjoint Hamiltonian operator from the lattice formulation.

2.2.2. Symanzik improvement program

The lattice gauge and fermion actions built above are discretized versions of their continuum counterparts. As such, they give rise to discretization effects, which go like powers of the lattice spacing a . More specifically, using the expansion of gauge links into gauge fields

$$U_\mu(n) = \mathbf{1} + iaA_\mu(an) + O(a^2)$$

and the definition of the Wilson term, one can show that the discretization effects for the Wilson action are of $O(a^2)$ for the gauge part and of $O(a)$ for the fermion part, i.e.

$$S_{\text{Wilson,G}}[U_\mu] = S_G[A] + O(a^2) \quad (2.42)$$

$$S_{\text{Wilson,F}}[q, \bar{q}, U_\mu] = S_F[q, \bar{q}A] + O(a) \quad (2.43)$$

Practical calculations are performed at finite a , and taking the continuum limit with the raw Wilson action often proves to be a costly task as one needs to go to very small lattice spacings in order to control the extrapolation.

However, the discretization errors can be reduced by adding to the Wilson action irrelevant terms which vanish in the continuum and compensate the leading finite a effects. A way to systematically cancel discretization effects in lattice theories was proposed by Symanzik [28, 29] and is known as the *Symanzik improvement program*.

The idea is to consider the lattice action as an effective action S_{lat} which matches the continuum one as $a \rightarrow 0$, i.e.

$$S_{\text{lat}} = S^{(0)} + \int dx \left(a\mathcal{L}^{(1)}(x) + a^2\mathcal{L}^{(2)}(x) + \dots \right)$$

where S_0 is the usual continuum QCD action 2.20, and where $\mathcal{L}^{(k)}$, $k \geq 1$ are Lagrangian densities built from the continuum quantities q , \bar{q} and A_μ . These “finite a ” Lagrangians have the same symmetries as S_0 , and dimensional analysis shows that $\mathcal{L}^{(k)}$ has dimension $[\text{Length}]^{-(k+4)}$.

We also consider lattice operators as effective operators, and write similarly for an arbitrary operator O :

$$O_{\text{lat}} = O^{(0)} + aO^{(1)} + \dots$$

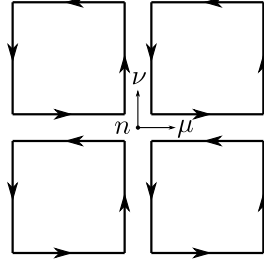


Figure 2.1.: Representation of the clover term in the $\hat{\mu} - \hat{\nu}$ plane at site n . The square loops are plaquettes.

Symanzik's prescription to reduce discretization effects is then to modify the lattice action and operator with irrelevant lattice Lagrangians or operators so as to cancel finite a terms. More formally, we define an improved action and operator as

$$S_{\text{lat,improved}} = S_{\text{lat}} + a^4 \sum_n \sum_i c_i^{(1)} L_i^{(1)}(x) + \dots \quad (2.44)$$

$$O_{\text{lat,improved}} = O_{\text{lat}} + \sum_i d_i^{(1)} O_i^{(1)} + \dots \quad (2.45)$$

where the $L_i^{(k)}$, $O_i^{(k)}$ are independent lattice operators chosen to cancel the corresponding finite a contributions in S_{lat} and O_{lat} .

This method can be used to perform $O(a)$ improvement of the lattice Wilson fermion action and $O(a^2)$ improvement of the Wilson gauge action.

The cancellation of $O(a)$ corrections in the fermion action involves one new dimension-5 operator¹, often referred to as the *Sheikholeslami-Wohlert* [30] or *clover* term. The improved fermion action then writes

$$S_{\text{Wilson,F,imp}} = S_{\text{Wilson,F}} - i c_{\text{SW}} a^5 \sum_{n,\mu<\nu} \bar{q}(n) \frac{\sigma_{\mu\nu}}{2} \frac{Q_{\mu\nu}(n) - Q_{\mu\nu}(n)^\dagger}{8} q(n) \quad (2.46)$$

where $\sigma_{\mu\nu} = \frac{i}{2} [\gamma_\mu^E, \gamma_\nu^E]$ and $Q_{\mu\nu}(n)$ is the sum of plaquettes $P_{\mu\nu}(n)$ in the $\hat{\mu} - \hat{\nu}$ plane represented in Fig. 2.1, whose appearance lead to the name. Complete improvement of the action requires the non-perturbative calculation of the Sheikholeslami-Wohlert coefficient c_{SW} which depends on the coupling g (see for instance [31]). However, one often restricts the improvement to on-shell quantities at tree-level, which corresponds to

$$c_{\text{SW}} = 1$$

¹One can actually build 5 such operators, but 2 of them are already present in the Wilson action, so that including them in the improvement only amounts to a redefinition of the bare parameters m and g , and the remaining 3 are related by the Dirac equation.

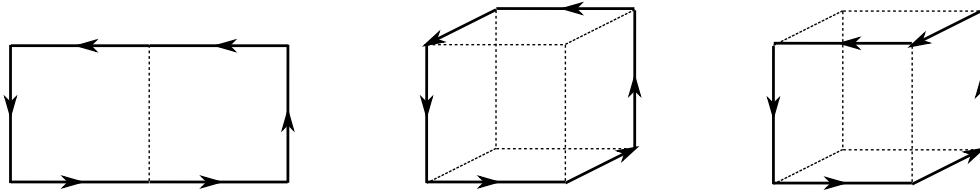


Figure 2.2.: Rectangle loops used in the Lüscher-Weisz improved gauge action.

The $O(a^2)$ improvement of the gauge action involves the “rectangular” Wilson loops shown in Fig. 2.2 and is derived in [32]. It gives the improved gauge action

$$S_{\text{Wilson,G,imp}} = c_0 S_{\text{Wilson,G}} + c_1 \frac{\beta}{3} \sum_{n,\text{rect } R} \text{Re Tr} [\mathbf{1} - R(n)] \quad (2.47)$$

where the rectangles R are of the three kinds shown in Fig. 2.2, and the coefficients for tree-level improvement of on-shell quantities are

$$c_0 = \frac{5}{3} \quad \text{and} \quad c_1 = -\frac{1}{12}$$

2.2.3. Gauge-link smearing

The study of hadronic correlation functions physically involves the long-range behaviour of QCD, but violent UV fluctuations can hinder our calculations, and give rise to strong discretization effects. As mentioned above, the Symanzik improvement program provides a well-defined approach to control these finite a contaminations, but the determination of the improvement coefficients is difficult, and the iteration of the procedure to higher orders in a turns out to be unworkable. Therefore, we use the low order tree-level improvement described in Sec. 2.2.2, and combine it with a *smearing* of the gauge links coupled to the fermions². The smearing consists in some kind of averaging of the links over some neighbourhood, and helps smoothing strong local fluctuations of the gauge configuration. This is equivalent to a redefinition of the coupling between quarks and gluons with a different discretization of the action.

Several smearing procedures have been devised, the most popular being studied in [33]. These are covariant procedures, which do not require fixing the gauge, but need projection of the resulting averaged *fat* link onto the gauge group $SU(3)$ as it is not stable under matrix addition. The smearing methods can be iterated, but keeping in mind that every iteration increases the averaging range and hence affects longer-range behaviours.

We use two steps of HEX smearing in the fermion Wilson clover-improved action. This procedure combines the exponential (EXP) smearing [34] with the hypercubic (HYP)

²The gauge part of the action has indeed naturally $O(a^2)$ discretization errors, and we are interested in hadronic observables, mainly sensitive to the quarks-gluons coupling.

approach [35] to build fat links, which we denote $V_\mu(n)$. The explicit procedure can be found in [36].

The action then reads

$$S_{\text{imp,2HEX}} = S_{\text{Wilson,G,imp}}[U_\mu] + S_{\text{Wilson,F,imp}}[V_\mu, q, \bar{q}]$$

2.3. Computing vacuum expectation values

2.3.1. Path integrals on the lattice

The lattice discretization of QCD was introduced to give proper meaning to the Feynman path integral introduced in Sec. 2.1.2. In this approach, we define the expectation value of any operator O as the continuum limit of the lattice functional integral

$$\langle O \rangle_{\text{lat}} = \frac{1}{\mathcal{Z}} \int DU_\mu Dq D\bar{q} O[U_\mu, q, \bar{q}] e^{-S[U_\mu, q, \bar{q}]} \quad (2.48)$$

where $S = S_{\text{imp,2HEX}}$, and

$$\mathcal{Z} = \int DU_\mu Dq D\bar{q} e^{-S[U_\mu, q, \bar{q}]} \quad (2.49)$$

The functional measures are now well-defined as

$$\begin{aligned} DU_\mu &\equiv \prod_n \prod_\mu dU_\mu(n) \\ Dq &\equiv \prod_n \prod_{f,\alpha,a} dq_{(f)}(n)_a^\alpha \\ D\bar{q} &\equiv \prod_n \prod_{f,\alpha,a} d\bar{q}_{(f)}(n)_a^\alpha \end{aligned} \quad (2.50)$$

where we have explicitly recalled all the indices for definiteness. $dq_{(f)}(n)_a^\alpha$ and $d\bar{q}_{(f)}(n)_a^\alpha$ are the usual integration measures for Grassmann numbers, and $dU_\mu(n)$ is the SU(3) Haar measure [37]. We shall from now on drop the ‘lat’ subscript where it is not explicitly needed, and assume that vacuum expectation values refer to the ones computed on the lattice.

As we can see from Eqs. (2.40) and (2.46), the fermion action is quadratic in the quark fields, so that integration over q and \bar{q} can be performed explicitly using Wick’s theorem [38], which gives in this case

$$\langle O \rangle = \frac{1}{\mathcal{Z}} \int DU_\mu \langle O \rangle_{\text{F}} \det(\mathfrak{D}) e^{-S_{\text{G}}[U_\mu]} \quad (2.51)$$

where $\mathfrak{D} = \mathfrak{D}_{W,\text{imp}}[V_\mu]$ is the clover-improved Wilson fermion operator with smeared gauge links, $S_{\text{G}} = S_{\text{Wilson,G,imp}}$, and $\langle O \rangle_{\text{F}}$ denotes the Wick contractions obtained by associating all q, \bar{q} pairs in O into quark propagators \mathfrak{D}^{-1} . $\langle O \rangle_{\text{F}}$ is in general a sum of products of propagators, with appropriate permutation coefficients.

Note that a product over the quark flavours is implied in the determinant expression $\det(\mathfrak{D})$. We are interested in the “2 + 1” flavours case – that is 2 light mass-degenerate flavours (the up and down quarks) and 1 heavier flavour (the strange quark). The fermion determinant then reads explicitly

$$\det(\mathfrak{D}) = |\det(\mathfrak{D}_{u/d})|^2 \det(\mathfrak{D}_s)$$

To perform integration over the gauge group, one then notices that

$$dP(U) \equiv \frac{1}{Z} \det(\mathfrak{D}) e^{-S_G} DU_\mu \quad (2.52)$$

can be interpreted as a probability measure, as long as the determinant is positive. As mentioned in [39], the relatively heavy physical mass of the strange quark supports the assumption that $\det(\mathfrak{D}_s)$ remains positive in the regions which mostly contributes to the integral, so that $\det(\mathfrak{D}) > 0$ and (2.52) is a well-defined probability measure. In a regularization that respects chiral symmetry, $\det(\mathfrak{D})$ is always positive. However for Wilson fermions, which require an additive mass renormalization, $\det(\mathfrak{D})$ for a single flavour may be negative at finite lattice spacing on a given configuration. This is less often the case for large quark mass and smearing further reduces the probability of it happening.

This therefore allows us to use Monte-Carlo methods to estimate the integral (2.51) over gauge fields. These methods are indeed very efficient for high-dimensional integrals and allow the use of *importance sampling*, which consists in sampling the space of gauge configurations $U = \{U_\mu(n)\}$ according to the weight dP . Eq. (2.51) can then be evaluated as the sum

$$\langle O \rangle = \frac{1}{N} \sum_{i=1}^N \langle O \rangle_F [U^{(i)}] + O\left(\frac{1}{\sqrt{N}}\right) \quad (2.53)$$

where $\{U^{(i)}, i = 1, \dots, N\}$ is a set of N independent random gauge configurations distributed according to the density dP .

2.3.2. Hybrid Monte-Carlo method

The *hybrid Monte-Carlo* (HMC) algorithm was introduced in [40] to generate independent gauge configurations following the distribution law dP . The major challenge in drawing these configurations lies in the non-locality of the fermion determinant. Efficient sampling of the configuration space thus requires global updates in the generation of new candidates from existing ones. One then has to deal with the violent fluctuations of the Boltzmann weight e^{-S_G} , which prohibits random draws. The HMC algorithm provides a solution through the combined use of Markov chain Monte-Carlo and Molecular Dynamics evolution.

Markov chains

A Markov chain is a random process which generates a sequence of “states” (gauge configurations $U^{(1)}, U^{(2)}, \dots, U^{(N)}$ in our case) distributed with some probability P . Any

state $U^{(i)}$ in the chain depends on $U^{(i-1)}$ only, and the process is characterized by the transition probability $T(U \rightarrow U')$ to get U' starting from U .

To obtain a correct and stable equilibrium probability distribution of the U 's, we request that P is a fixed point of the update process, i.e.

$$\sum_U P(U) T(U \rightarrow U') = P(U') \quad (2.54)$$

and that the process is *ergodic*, for which the condition

$$T(U \rightarrow U') > 0, \quad \forall U, U' \quad (2.55)$$

is sufficient.

Note that, although not strictly required, the *detailed balance* condition is often used to impose that the probability P is a fixed point of the algorithm. This strong sufficient condition, which can be stated as

$$P(U) T(U \rightarrow U') = P(U') T(U' \rightarrow U) \quad (2.56)$$

requests *reversibility* of the Markov process, and implies 2.54.

In the HMC algorithm, the transition probability is then given by a molecular dynamics symplectic evolution followed by an accept-reject step.

Molecular dynamics

Molecular dynamics evolution provides an efficient way to find a new and reasonable candidate to incorporate in our Markov chain from the current gauge configuration. The idea, to circumvent the large fluctuations of the action when updating many gauge links to draw the new configuration, is to use some kind of Hamiltonian evolution in the configuration space.

Using the *pseudo-fermion* representation introduced in [41], the fermion determinant appearing in the probability P 2.52 can be written as

$$\det(\mathfrak{D}) = \text{constant} \times \int D\phi e^{-S_{\text{pf,u/d}}[U,\phi] - S_{\text{pf,s}}[U,\phi]}$$

where the pseudo-fermions $\phi(n)$ are complex (not Grassmann) variables with color and Dirac indices coming in several flavours, and the integration measure is

$$D\phi = \prod_{n,f,\alpha,a} d\text{Re } \phi_f(n)_\alpha d\text{Im } \phi_f(n)_\alpha$$

More details about the pseudo-fermion actions can be found in [39]. We only state that they assume the general form

$$S_{\text{pf}} = \phi^\dagger \Delta^{-1} \phi$$

with Δ a positive definite matrix related to the fermion operator \mathfrak{D} .

We also introduce an $\mathfrak{su}(3)$ -valued field

$$\pi_\mu(n) = \sum_{k=1}^8 \pi_{\mu k}(n) T_k$$

distributed with a Gaussian law

$$e^{-\frac{1}{2}(\pi, \pi)} \quad \text{with} \quad (\pi, \pi) = \sum_{n, \mu, k} \pi_{\mu k}(n) \pi_{\mu k}(n)$$

and notice that the vacuum expectation value 2.51 can be rewritten

$$\langle O \rangle = \frac{1}{\mathcal{Z} \mathcal{Z}_\pi} \int \mathcal{D}U_\mu \mathcal{D}\pi_\mu \mathcal{D}\phi \langle O \rangle_{\text{F}} e^{-S_{\text{G}}[U_\mu] - S_{\text{pf}}[U, \phi] - \frac{1}{2}(\pi, \pi)}$$

with $\mathcal{Z}_\pi = \int \mathcal{D}\pi_\mu e^{-\frac{1}{2}(\pi, \pi)}$.

The latter integral can be regarded as representing a microcanonical system, whose evolution in a fictitious time τ is controlled by the Hamiltonian

$$H[\pi, U] = \frac{1}{2}(\pi, \pi) + S_{\text{G}} + S_{\text{pf}}$$

This classical Hamiltonian evolution only involves the U and π conjugate fields; the pseudofermion field plays a spectator role at this point and shall be accounted for later in the accept-reject step.

The equations of motion

$$\frac{d\pi_\mu}{d\tau} = -F_\mu \tag{2.57}$$

$$\frac{dU_\mu}{d\tau} = \pi_\mu U_\mu \tag{2.58}$$

with the force

$$F_\mu \equiv \frac{\partial S[U]}{\partial U_\mu} \tag{2.59}$$

can be numerically integrated, taking some configuration (π, U) to the next (π', U') one.

Evolution with Sections 2.3.2 and 2.3.2 formally follows trajectories of constant energy, and therefore satisfies the detailed balance condition (2.56) (see again [39] or [42] for additional details).

Acceptance-rejection

In practice, the equations of motion are integrated numerically using a symplectic integrator, such as the leapfrog scheme³, in order to preserve reversibility of the trajectory. The numerical integration errors can then break the Markov chain requirements, so that

³in our work, we use the Omelyan integrator [43], which performs about twice as well as the leapfrog integrator [44].

we add an accept-reject correction step at the end of our molecular dynamics evolution. The gauge configuration U' obtained after integration of Hamilton's equation from the configuration (π, U) at $\tau = 0$ to some time τ is accepted with probability

$$P_{\text{accept}}(\pi', U') = \min \left\{ 1, e^{-(H[\pi', U'] - H[\pi, U])} \right\} \quad (2.60)$$

If rejected, U' is set to U .

The integration steps are usually tuned so as to obtain acceptance rates of about 75%, and the Markov time τ is empirically adjusted to reduce autocorrelation of the configurations sequence while preserving stability of the algorithm.

To summarize, the HMC Metropolis step to generate the new configuration U' from the current one U is given by:

1. Generate random momentum π and pseudo-fermion ϕ fields with probability density $e^{-\frac{1}{2}(\pi, \pi) - S_{\text{pf}}[U, \phi]}$
2. Numerically integrate the molecular dynamics equations from $\tau = 0$ to some time τ to obtain the new candidate U' (and the momentum π')
3. Accept U' as the new state if some random number $r \in [0, 1)$ is smaller than $P_{\text{accept}}(\pi', U')$. Otherwise, set U' to U .

The most challenging part in the algorithm is the Hamiltonian evolution, and more precisely the computation of the force (2.59). The meaning of derivation with respect to a group element can be found in [42], and proper accounting of the gauge smearing introduced in Sec. 2.2.3 can be found in [36].

The bulk of the computation lies in the inversion of fermion operator systems of the form $\mathfrak{D}\psi = \eta$ required to get the fermion force. This system is usually solved with preconditioned Krylov subspace methods (see [39] and [45] for additional details).

2.4. Hadron spectrum and scale setting

2.4.1. Gauge configuration ensembles

In our work, we use gauge configuration ensembles generated with the HMC algorithm in the Budapest-Marseille-Wuppertal collaboration setup. Thorough review of the practical implementation of the simulation as well as the complete set of configuration parameters are given in [36] (c.f. Table 1). These ensembles are simulated with “2+1” flavours (i.e. isospin-degenerate up and down quarks and a heavier strange quark) using the Wilson action with tree-level “clover” improvement of the fermion action, tree-level “Lüscher-Weisz” improvement of the gauge action, and 2 steps of HEX smearing, as presented in Sections 2.2.2 and 2.2.3. The volumes are as large as $L^3 \times T \sim 6^3 \times 8 \text{ fm}^4$. 5 different coupling values are used to allow accurate continuum extrapolation, and the pion masses range from about 675 MeV down to 120 MeV.

β	am_{ud}^{bare}	am_s^{bare}	volume	# conf.	am_π	$m_\pi L$
3.31	-0.07000	-0.0400	$16^3 \times 32$	164	0.3517(13)	5.63
	-0.08500	-0.0400	$16^3 \times 32$	1238	0.2519(07)	4.03
	-0.09300	-0.0400	$16^3 \times 48$	935	0.1802(13)	2.88
	-0.09530	-0.0400	$16^3 \times 48$	974	0.1577(10)	2.52
	-0.09300	-0.0400	$24^3 \times 48$	429	0.1769(06)	4.25
	-0.09530	-0.0400	$24^3 \times 48$	245	0.1500(14)	3.60
	-0.09300	-0.0400	$32^3 \times 48$	455	0.1769(05)	5.66
	-0.09756	-0.0400	$32^3 \times 48$	221	0.1202(11)	3.85
	-0.09530	-0.0400	$32^3 \times 48$	419	0.1498(06)	4.81
	-0.09900	-0.0400	$48^3 \times 48$	569	0.0887(06)	4.26
	-0.09933	-0.0400	$48^3 \times 48$	656	0.0804(13)	3.86
	-0.09756	-0.0400	$24^3 \times 64$	253	0.1110(12)	2.66
	-0.09000	-0.0440	$24^3 \times 64$	209	0.2015(08)	4.84
	-0.09300	-0.0440	$32^3 \times 64$	205	0.1716(06)	5.49
-0.09530	-0.0440	$32^3 \times 64$	235	0.1450(06)	4.66	
-0.09756	-0.0440	$32^3 \times 64$	203	0.1087(09)	4.66	
3.5	-0.02500	-0.0023	$16^3 \times 32$	133	0.2920(16)	4.67
	-0.02500	-0.0060	$16^3 \times 32$	1461	0.2890(05)	4.62
	-0.03100	-0.0060	$24^3 \times 48$	297	0.2535(04)	6.08
	-0.04900	-0.0060	$32^3 \times 64$	108	0.1206(07)	3.86
	-0.05294	-0.0060	$64^3 \times 64$	364	0.0609(04)	3.92
-0.05150	-0.0120	$48^3 \times 64$	1200	0.0841(04)	4.01	
3.61	-0.02000	0.0045	$32^3 \times 48$	207	0.1986(04)	6.36
	-0.02800	0.0045	$32^3 \times 48$	387	0.1479(03)	4.73
	-0.03000	0.0045	$32^3 \times 48$	194	0.1325(05)	4.24
	-0.03300	0.0045	$48^3 \times 48$	210	0.1026(04)	4.92
	-0.03121	0.0045	$48^3 \times 48$	218	0.1207(03)	5.79
	-0.03440	0.0045	$48^3 \times 48$	188	0.0864(04)	4.15
	-0.02000	-0.0042	$32^3 \times 48$	171	0.1962(04)	6.28
	-0.03000	-0.0042	$32^3 \times 48$	142	0.1285(06)	4.11
-0.0365	-0.003	$64^3 \times 72$	360	0.0459(03)	2.94	
3.7	-0.01500	0.0500	$32^3 \times 64$	313	0.1707(03)	5.46
	-0.02080	0.0010	$32^3 \times 64$	229	0.1253(04)	4.01
	-0.02080	0.0000	$32^3 \times 64$	206	0.1241(04)	3.97
	-0.02540	0.0000	$48^3 \times 64$	118	0.0806(03)	3.87
	-0.02700	0.0000	$64^3 \times 64$	207	0.0602(02)	3.86
	-0.02080	-0.0050	$32^3 \times 64$	207	0.1245(04)	3.98
-0.02540	-0.0050	$48^3 \times 64$	264	0.0807(02)	3.87	
3.8	-0.01400	0.0030	$32^3 \times 64$	510	0.1238(03)	3.96
	-0.01900	0.0030	$48^3 \times 64$	206	0.0832(03)	3.99
	-0.01400	0.0000	$32^3 \times 64$	424	0.1226(03)	3.92
-0.01900	0.0000	$48^3 \times 64$	176	0.0819(04)	3.93	

Table 2.1.: Overview of our $N_f = 2+1$ ensembles. We give the ensembles characteristics, the number of configurations used for the analysis, the pion mass in lattice units am_π and the corresponding $m_\pi L$ value.

2.4.2. Hadron spectrum

One of the most simple quantities to compute on the lattice is the mass of hadronic particles. This can be obtained through analysis of the time-dependence of plain two-point correlation functions.

We consider some fermion functional $O_h(n) = O_h[q(n)]$, chosen with the quantum numbers of the hadron h that we want to study. We define the corresponding zero-momentum functional as

$$O_h(\mathbf{p} = \mathbf{0}, t) \equiv \tilde{O}_h(t) = \sum_{\mathbf{n}} O_h(\mathbf{n}, t)$$

As mentioned in Sec. 2.1.2, one can show that the expectation value $\langle \tilde{O}_h(t) \bar{O}_h(0) \rangle$ is, in the limit $T \rightarrow \infty$, equal to the time-ordered vacuum expectation value of the corresponding operators

$$\langle \tilde{O}_h(t) \bar{O}_h(0) \rangle = \langle \Omega | \mathcal{T} \left\{ \hat{\tilde{O}}_h(t) \hat{O}_h^\dagger(0) \right\} | \Omega \rangle \quad (2.61)$$

where \mathcal{T} is the time-ordering operator. For $t > 0$,

$$\begin{aligned} \mathcal{T} \left\{ \hat{\tilde{O}}_h(t) \hat{O}_h^\dagger(0) \right\} &= \hat{\tilde{O}}_h(t) \hat{O}_h^\dagger(0) \\ &= e^{-Ht} \hat{\tilde{O}}_h(0) e^{Ht} \hat{O}_h^\dagger(0) \end{aligned} \quad (2.62)$$

Assuming eigenvectors of the QCD Hamiltonian span the physical Hilbert space, we can write a closure relation

$$\mathbf{1} = \sum_{\text{states } k} \frac{|k\rangle \langle k|}{2E_k} \quad (2.63)$$

and insert it in the left-hand side of Eq. (2.61) to obtain the spectral representation of the expectation value:

$$\langle \tilde{O}_h(t) \bar{O}_h(0) \rangle = \sum_k \frac{\langle \Omega | \tilde{O}_h(0) | k \rangle \langle k | O_h^\dagger(0) | \Omega \rangle}{2E_k} e^{-tE_k} \quad (2.64)$$

where we have dropped the operator superscript $\hat{}$ and explicitly recalled the lattice spacing a .

Note that all states k with non-vanishing overlap with O_h (i.e. such that $\langle k | O_h^\dagger(0) | \Omega \rangle \neq 0$) contribute to the sum 2.64, but only the lowest energy state (the ground state) survives at large t , because of the exponentially-suppressed time-dependence. This also shows that many different interpolating operators can be used to extract the spectrum of some given hadron, as one only requests selective overlap of the operator with the particle of interest. The interpolating operators for some of the light hadrons used in this thesis are listed in Table 2.2. These hadrons are stable under strong interaction.

They involve the spatially extended *smear*d quark fields q^S defined as:

$$q^S(\mathbf{n}, t) \equiv \sum_{\mathbf{n}'} \mathcal{S}(\mathbf{n}' - \mathbf{n}) q(\mathbf{n}', t) \quad (2.65)$$

h	I	J	O_h
π	1	0	$\bar{q}_d^S \gamma_5^E q_u^S$
K	$\frac{1}{2}$	0	$\bar{q}_s^S \gamma_5^E q_u^S$
N	$\frac{1}{2}$	$\frac{1}{2}$	$\epsilon_{abc} q_u^S \alpha_a (q_u^{ST} C \gamma_5^E q_d^S)$
Σ	1	$\frac{1}{2}$	$\epsilon_{abc} q_u^S \alpha_a (q_s^{ST} C \gamma_5^E q_u^S)$
Ξ	$\frac{1}{2}$	$\frac{1}{2}$	$\epsilon_{abc} q_s^S \alpha_a (q_u^{ST} C \gamma_5^E q_s^S)$
Ω	0	$\frac{3}{2}$	$\epsilon_{abc} q_s^S \alpha_a (q_s^{ST} C \gamma_5^E q_s^S)$

Table 2.2.: Examples of light-hadron interpolating operators used in this work. I is the total isospin and J the total spin. The subscript of the quark field q denotes its flavour and the superscript S indicates that these are smeared quarks (2.65). $C = \gamma_2^E \gamma_0^E$ is the charge conjugation matrix. Summation over color indices a, b, c is implied. Note that we work in the isospin limit, in which hadronic isospin multiplets become degenerate.

where \mathcal{S} is the quark smearing function. In this work, we choose to evaluate correlation functions in the fixed Coulomb gauge, so that \mathcal{S} need not be gauge invariant. To obtain good overlap of the operators built out of smeared quarks with the hadron ground state, we take \mathcal{S} Gaussian with a radius of about 0.3 fm.

In practice, $\langle \tilde{O}_h(t) \bar{O}_h(0) \rangle$ is evaluated using Wick's theorem as

$$\langle \tilde{O}_h(t) \bar{O}_h(0) \rangle = \frac{1}{N} \sum_{i=1}^N \langle \tilde{O}_h(t) \bar{O}_h(0) \rangle_{\text{F}} [U^{(i)}] \quad (2.66)$$

where $\{U^{(i)}, i = 1, \dots, N\}$ are the gauge configurations generated with the HMC algorithm fixed to the Coulomb gauge⁴, and $\langle \tilde{O}_h(t) \bar{O}_h(0) \rangle_{\text{F}}$ are the 2pt-function Wick contractions, which depend on the quark propagators

$$D_{(f)}^{-1}(m, n)_\alpha$$

for a given gauge configuration. Coulomb-gauge configurations are obtained through the minimization of the functional

$$F[U] = - \sum_n \sum_{\mu \neq 0} \text{Re Tr} [U_\mu(n)] \quad (2.67)$$

See [46] and references therein for additional details.

⁴Note that the HMC procedure is processed without gauge fixing. Coulomb-gauge fixing is only done afterwards, when computing hadronic observables.

To reduce statistical errors in the evaluation of Eq. (2.66), we actually use the translation-invariance property of the 2-pt correlator to compute it at different time-slices, i.e.

$$\langle \tilde{O}_h(t) \bar{O}_h(0) \rangle = \frac{1}{N_{t_i}} \langle \tilde{O}_h(t + t_i) \bar{O}_h(\mathbf{0}, t_i) \rangle \quad (2.68)$$

where the number of sources N_{t_i} ranges from $\frac{T}{4}$ up to T , depending on the ensemble.

To extract the hadron mass m_h , we then build the effective mass, which is given by

$$m_{h \text{ eff}}(t) \equiv \ln \left[\frac{\langle \tilde{O}_h(t) \bar{O}_h(0) \rangle}{\langle \tilde{O}_h(t+1) \bar{O}_h(0) \rangle} \right] \quad (2.69)$$

if h is a baryon, or which is solution of the equation

$$\frac{\cosh \left[m_{h \text{ eff}} \left(t - \frac{T}{2} \right) \right]}{\cosh \left[m_{h \text{ eff}} \left(t + 1 - \frac{T}{2} \right) \right]} = \frac{\langle \tilde{O}_h(t) \bar{O}_h(0) \rangle}{\langle \tilde{O}_h(t+1) \bar{O}_h(0) \rangle} \quad (2.70)$$

if h is a meson, the latter expression accounting for the backward contribution coming from the boundary conditions (see Appendix B for additional details).

For t large, $m_{h \text{ eff}}(t)$ exhibits a plateau whose value provides us with the ground state mass of the hadron, in units of a . We then fit this plateau with a constant in some given time range by minimizing a standard correlated χ^2 . The covariance matrix required in the χ^2 function is estimated through a bootstrap resampling analysis [47] (see Appendix A for a short presentation) with 2000 samples. Fig. 2.3 shows a plot of the nucleon effective mass $m_{N \text{ eff}}$ versus t with the fitted plateau for an ensemble with $L = 48$, $T = 48$, $\beta = 3.31$, $m_{\text{ud}} = -0.09933$ and $m_s = -0.04$, which corresponds to the physical pion mass.

2.4.3. Scale setting

As mentioned above, physical energies extracted from lattice QCD calculations are dimensionless numbers expressed in units of the lattice spacing a . As mentioned in Sec. 2.1.3, a is not an external parameter of the theory, but is related to the coupling β through renormalization. Hence we need to get its value – and set the physical *scale* of our simulation – by imposing some relation between a lattice-computed quantity and its experimental value.

In our work, we follow [48] and [49] and use the Ω baryon mass, as it is expected to be weakly sensitive to the light quarks mass. More precisely, we interpolate the Ω plateaus to the physical mass point, characterized by the physical values of the ratios $\frac{m_\pi}{M_\Omega}$ and

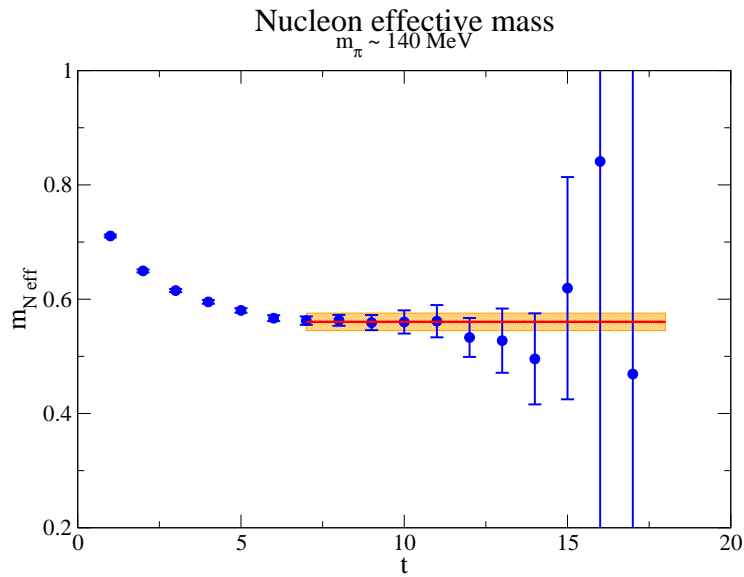


Figure 2.3.: Example of a nucleon effective mass, along with the fitted plateau for an ensemble at the physical pion mass. The χ^2 per degrees of freedom obtained at the minimum is 0.99 and the orange band gives the 95% confidence interval computed with the bootstrap method. The mass central value is $aM_N = 0.560$.

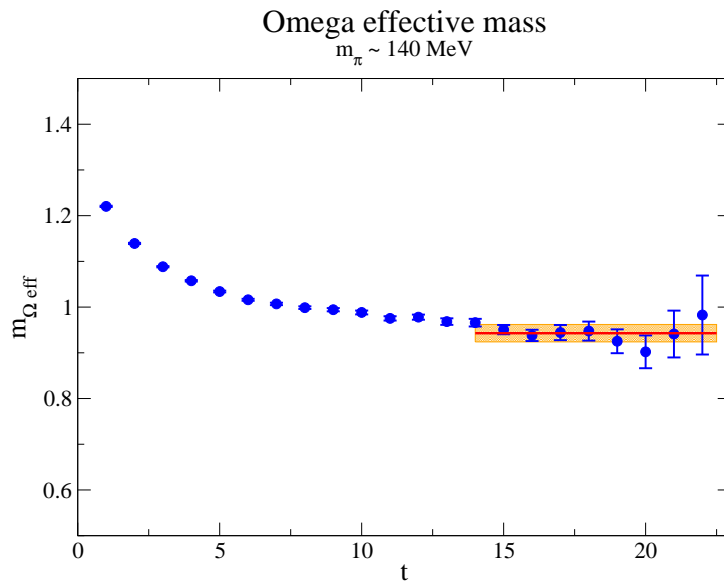


Figure 2.4.: Example of Ω effective mass for an ensemble at the physical pion mass. The χ^2 per degrees of freedom obtained at the minimum is 1.06 and the orange band gives the 95% confidence interval computed with the bootstrap method. The mass central value is $aM_\Omega = 0.943$.

β	a (fm)	a^{-1} (GeV)
3.31	0.1138(4)	1.735(6)
3.5	0.0891(6)	2.217(16)
3.61	0.0771(5)	2.562(16)
3.7	0.0631(6)	3.129(28)
3.8	0.0532(6)	3.706(42)

Table 2.3.: Typical values of the lattice spacing a for each β . The errors are only statistical.

$\frac{m_K}{M_\Omega}$. For this purpose, we use the functional form

$$aM_\Omega(\beta, am_\pi, aM_{s\bar{s}}) = a(\beta) M_\Omega^{\text{phy}} \left\{ 1 + c_s \left[\left(\frac{aM_{s\bar{s}}}{aM_\Omega} \right)^2 - \left(\frac{M_{s\bar{s}}^{\text{phy}}}{M_\Omega^{\text{phy}}} \right)^2 \right] + c_{\text{ud}} \left[\left(\frac{am_\pi}{aM_\Omega} \right)^2 - \left(\frac{m_\pi^{\text{phy}}}{M_\Omega^{\text{phy}}} \right)^2 \right] \right\} \quad (2.71)$$

where $M_{s\bar{s}}^2 = M_K^2 - \frac{m_\pi^2}{2}$, and fix the scales for our 5 values of β simultaneously. Note that the fit coefficients c_s and c_{ud} are taken β -independent, as suggested by our data.

We show an example of Ω effective mass plateau in Fig. 2.4 obtained for the aforementioned physical pion mass ensemble.

Indicative results for the lattice spacings are given in Table 2.3. In practice, the scale setting analysis is performed in a combined statistical and systematic errors analysis with the quantity of interest.

Using the values of Table 2.3, we can compute the lattice nucleon masses for our ensembles. These “raw” results are shown in Fig. 2.5 with statistical errors only. We can then parametrize the nucleon plateaus obtained from our lattice calculations as [48]:

$$M_N(m_\pi, m_K, a) = M + c_a a^2 + c_\pi^{(2)} m_\pi^2 + c_\pi^{(3)} m_\pi^3 + c_{s\bar{s}}^{(2)} M_{s\bar{s}}^2 \quad (2.72)$$

where M , c_a , $c_\pi^{(1,2)}$ and $c_{s\bar{s}}$ are free parameters, and fit this functional form to our data. We then use this parametrization to extrapolate our results to the continuum and to interpolate to the physical values of m_π and $M_{s\bar{s}}$. Considering only simulations with $m_\pi \leq 400$ MeV, this gives us the results shown in Fig. 2.6, and the physical point value

$$M_N = 943 \pm 11 \text{ MeV} \quad (2.73)$$

in excellent agreement with experimental data.

Note that no systematic error estimation was undertaken in this analysis, which is shown here only for illustrative purposes.

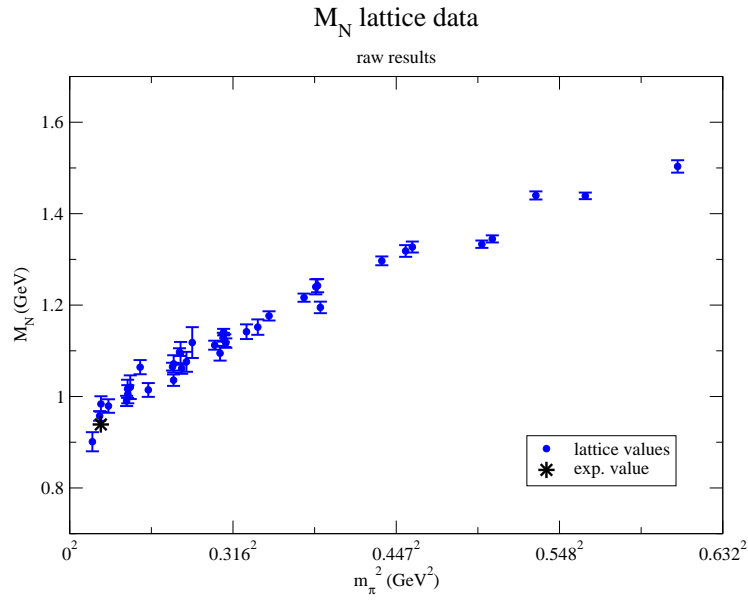


Figure 2.5.: Nucleon mass in physical units for our lattice ensembles plotted with respect to m_π^2 . The green dot shows the experimental nucleon mass.

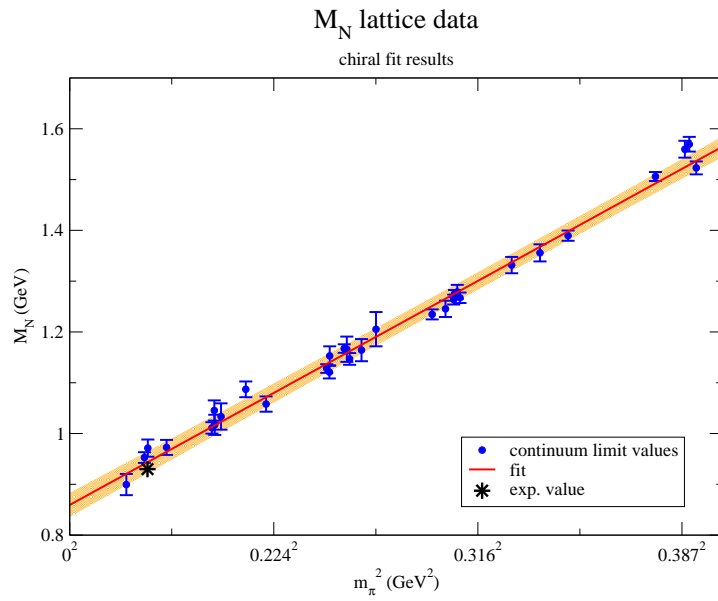


Figure 2.6.: Nucleon masses of our ensembles obtained with the parametrization 2.72 plotted versus m_π^2 after subtraction of the fitted m_π^3 term. The red line shows the fit, along with the 95% confidence interval bands in orange.

3. $\pi\pi$ scattering: the ρ resonance

3.1. Introduction

Most lattice QCD calculations performed today – including those of the stable hadron spectrum – include dynamical sea quarks effects, and thereby take into account one of the most striking features of quantum field theories – and therefore of QCD: the possibility for myriad of particles to spontaneously flit in and out of existence. In particular, the creation and annihilation of quark-antiquark pairs from the vacuum directly opens the way to the decay of hadrons which are unstable under the strong interaction, also known as resonances.

The ρ meson is an emblematic example of such a resonant hadron state, which decays nearly exclusively into two pions. It is therefore an ideal case to study this very important aspect of the strong interaction on the lattice. The first lattice studies of the ρ decay were made in quenched QCD [50, 51], where no actual decay occurs. There has been for the past few years several calculations of the ρ decay width [52–59], some of them with quark masses light enough to allow infinite-volume decay of the ρ . However, none could really see the decay, as the ρ was still stable in the finite-volume because of the quantization of momenta.

We propose to perform a fully controlled calculation of the ρ width at low and even physical pion mass, which allows us to actually observe the decay of the ρ on the lattice. We use Lüscher’s method to extract infinite-volume quantities from the finite-volume $\pi\pi$ spectrum, computed with a multi-channel variational analysis.

3.2. $\pi\pi$ scattering in finite volume

At first glance, the study of scattering states on the lattice could seem strongly limited by the need to define asymptotic ‘in’ and ‘out’ states in a finite volume, as these states contain particles which are so far apart they do not interact. However, M. Lüscher developed a finite size method [60, 61] which allows us to extract physical infinite-volume scattering quantities through the volume effects in the two-particle spectrum. We use this method to study $\pi\pi$ scattering in the ρ channel.

3.2.1. Lüscher’s method

When particles are put in a finite-volume box with periodic boundary conditions - as is done when computing QCD quantities on the lattice, one naturally expects the energies of the system to be quantized. The interaction modifies the free particle energy levels, and the information about these level shifts can be related to scattering observables.

The finiteness of the space-time volume we consider for our studies results in errors in the evaluation of physical quantities. When the system we consider consists of at most one hadron, the finite-volume effects decrease exponentially with the size L of the space-time box (cf. [62]). Physically, these finite-volume effects are generated by the vacuum polarization phenomenon: a stable point-like particle – as described by quantum field theories – is surrounded by a cloud of virtual particles. Intuitively, each particle species generate a cloud which size is of order of its Compton wavelength $\lambda = h/mc$, so that the system is affected by the finite-volume effects as soon as $L \cong \lambda_0$ the Compton length of the lightest particle in the theory, i.e. when the cloud starts to be squeezed by the box¹.

However, when two or more hadrons are present, the finite-volume errors are no longer exponentially suppressed as one extends the size of the space-time box. In fact, *real* scattering processes must now to be taken into account. The interactions between the hadrons – through the exchange of massive particles – enter the game, with an effect which is expected to be proportional to L^{-3} , the probability for particles to meet. Since these power-law finite-volume effects are closely linked to scattering processes between external hadron states, it seems natural that they can be related to infinite-volume – physical – scattering quantities. The Lüscher equation [63] – and its generalization for particles in moving frames, also called the Rummukainen-Gottlieb equation [64] – describes this phenomenon and relates the two-particle eigenstate energies to the infinite volume scattering phase-shifts.

We consider two pions of equal masses m_π with total momentum \mathbf{P} in a cubic box of size L with periodic boundary conditions, and we assume the center-of-mass energy E^* to sit below the 4-pion inelastic threshold. We denote by $2q^*$ the magnitude of the relative momentum so that $E^{*2} = (2q^*)^2 + (2m_\pi)^2$. In the case of non-degenerate hadrons, the results are easily generalized with standard modifications to the kinematic relations. The generalized Lüscher equation can then be written as the formal quantization condition

$$\det \left(1 - i \frac{ML^{FV}}{2} \right) \Big|_{l_1, l_2 \leq l_{max}} = 0 \quad (3.1)$$

with a possible angular momentum cut-off l_{max} in the partial wave basis and

$$M_{l_1, m_1; l_2, m_2} = \delta_{l_1, l_2} \delta_{m_1, m_2} \frac{16\pi E^*}{q^*} \frac{e^{2i\delta_{l_1}} - 1}{2i} \quad (3.2)$$

$$L_{l_1, m_1; l_2, m_2}^{FV} = -\frac{q^*}{8\pi E^*} (\delta_{l_1, l_2} \delta_{m_1, m_2} + i \mathfrak{L}_{l_1, m_1; l_2, m_2}^{FV}) \quad (3.3)$$

$$\mathfrak{L}_{l_1, m_1; l_2, m_2}^{FV} = \frac{(4\pi)^2}{q^* \gamma L^3} \sum_{l, m} \frac{1}{q^{*l}} \left(\frac{2\pi}{L} \right)^{l-2} \mathcal{Z}_{lm}^P(1; \tilde{q}^{*2}) \int d\Omega^* Y_{l_1, m_1}^* Y_{l, m}^* Y_{l_2, m_2} \quad (3.4)$$

and where γ is the Lorentz factor $\gamma = E/\sqrt{E^2 - \mathbf{P}^2}$ and $\mathcal{Z}_{lm}^P(s; a^2)$ is the generalized

¹Actually, the single hadron state is a bound state of quarks. These quarks are confined so that their wave functions go to zero exponentially. Hence the quarks self-interactions “around the world” because of periodic boundary conditions can be neglected and the main contribution to the single hadron state finite-volume errors comes from the virtual pion cloud squeezing.

zeta function, defined as the meromorphic analytic continuation of the series

$$\sum_{\mathbf{n} \in \mathbb{Z}^3} \frac{1}{(r_{\mathbf{n}}^2 - a^2)^s} r_{\mathbf{n}}^l Y_{lm}(\hat{r}_{\mathbf{n}})$$

in the whole complex plane, with

$$r_{\mathbf{n}}^2 = \frac{1}{\gamma^2} \left(\mathbf{n}_{\parallel} - \left(\frac{L}{2\pi} \right) \frac{\mathbf{P}}{2} \right)^2 + \mathbf{n}_{\perp}^2$$

\mathbf{n}_{\parallel} and \mathbf{n}_{\perp} being the components of \mathbf{n} respectively parallel and perpendicular to \mathbf{P} . We have defined $q^* = (2\pi/L) \tilde{q}^*$ and $Y_{lm}(\hat{r})$ are the spherical harmonics of the direction \hat{r} .

A comprehensive proof of the generalized Lüscher equation based on [65] can be found in Appendix C.

3.2.2. Symmetry considerations

On the lattice, Lorentz invariance is broken, and rotation symmetry is replaced by the *cubic* group symmetry O_h . However, this still provides us with simplifications of the quantization condition Eq. (3.1) thanks to the symmetry transformation properties of the spherical harmonics – and therefore of $\mathcal{Z}_{lm}^P(1; a^2)$. For computing time reasons, we will restrict our lattice calculations to the case $\mathbf{P} = 0$ – the center-of-mass (COM) frame, which we consider in this section. We shall therefore drop the $*$ superscripts for the remainder of this chapter, and assume that kinematical quantities are in the COM frame. A more detailed analysis of the use of symmetries to simplify the quantization condition in other frames can be found in Appendix D.

In the COM frame, we have

$$\mathcal{Z}_{lm}^{\text{COM}}(s; a^2) = \sum_{\mathbf{n} \in \mathbb{Z}^3} \frac{1}{(\mathbf{n}^2 - a^2)^s} n^l Y_{lm}(\hat{\mathbf{n}}) \quad (3.5)$$

and therefore

$$\mathcal{Z}_{lm}^{\text{COM}} = \sum_{\mathbf{n} \in \mathbb{Z}^3} \frac{1}{(\mathbf{n}^2 - a^2)^s} n^l Y_{lm}(R\hat{\mathbf{n}}) \quad \forall R \in O_h \quad (3.6)$$

Choosing R to be the inversion, we can show that the even and odd l sectors decouple while the rotations in O_h give us the simplifications

$$\begin{aligned} \mathcal{Z}_{lm}^{\text{COM}} &= 0 \quad \text{if } m \not\equiv 0 \pmod{4} \\ \mathcal{Z}_{20}^{\text{COM}} &= 0 \end{aligned} \quad (3.7)$$

As a consequence of the symmetry, the determinant in Eq. (3.1) involves either the $l = 0, 2, 4, \dots$ or the $l = 1, 3, 5, \dots$ phase shifts. Since the ρ resonance takes place in the $l = 1$ partial wave, we need to cut the equation at $l < 3$ to obtain a practical equation for the relevant phase shift δ_1 .

The typical contribution of a partial wave to the scattering state goes like $j_l(q^*r)$ with r the range of the interaction which is of the order of 0.5 fm. Using the value of the momentum at the ρ resonance for a physical pion one finds

$$\frac{j_3(q^*r)}{j_1(q^*r)} \simeq 0.03$$

which is reasonably small and justifies our neglect of the partial waves other than $l = 1$. On the lattice the COM-frame operators transform in representations of O_h and we shall work in the T_1^- irreducible representation because it is the only one which appears in the decomposition of the $l = 1$ representation of the rotation group.

We shall also, for the sake of readability, drop the $*$ superscript for COM-frame quantities in the remainder of this chapter, as we only work in the COM frame.

3.2.3. Finite volume formula

The T_1^- irreducible representation is 3-dimensional, so that we can choose the vectors $\{|m = -1\rangle, |m = 0\rangle, |m = +1\rangle\}$ as basis vectors, and after some algebra, the determinant in Eq. (3.1) simplifies to

$$\begin{aligned} & \det \left(1 - \frac{4\pi E^*}{q^*} (e^{2i\delta_1} - 1) L_{1,m_1;1,m_2}^{FV} \right) \Big|_{l_1, l_2 \leq 2} \\ &= \left(1 + \frac{e^{2i\delta_1} - 1}{2} (1 + i \mathfrak{L}_{1,0;1,0}^{FV}) \right)^3 \\ &= 0 \end{aligned} \quad (3.8)$$

which provides us with the finite-volume formula we use to extract the phase-shifts from the eigenstate energies:

$$\cot \delta_1(q) = \frac{1}{\tilde{q}\pi^{3/2}} \mathcal{Z}_{00}^{COM}(1; \tilde{q}^2) \quad (3.9)$$

recalling that \tilde{q} is the lattice reduced momentum

$$\tilde{q} = \frac{L}{2\pi} \sqrt{\frac{E^2}{4} - m_\pi^2}$$

. We numerically evaluate $\mathcal{Z}_{00}^{COM}(1; \tilde{q}^2)$ using the integral representation of [66]:

$$\begin{aligned} \mathcal{Z}_{00}^{COM}(1; \tilde{q}^2) &= -\pi + \frac{1}{\sqrt{4\pi}} \sum_{\mathbf{n} \in \mathbb{Z}^3} \frac{e^{-(\mathbf{n}-\tilde{q})^2}}{\mathbf{n} - \tilde{q}^2} + \frac{\pi}{2} \int_0^1 \frac{dt}{t^{3/2}} (e^{t\tilde{q}^2} - 1) \\ &\quad + \frac{\pi}{2} \sum_{\mathbf{n} \neq \mathbf{0}} \int_0^1 \frac{dt}{t^{3/2}} e^{t\tilde{q}^2 - \frac{\pi^2 \mathbf{n}}{t}} \end{aligned} \quad (3.10)$$

Lüscher's formula Eq. (3.9) is strictly valid as long as one stays below the 4π inelastic threshold, which is not the case of the ρ resonance for small pion masses. However,

the 4π channel can be neglected up to 1 GeV [67], the reason being that the very small $\rho \rightarrow 4\pi$ partial width implies a small coupling in this channel. We can therefore safely carry out the phase-shifts analysis with Lüscher’s formula at low – and even physical – pion masses.

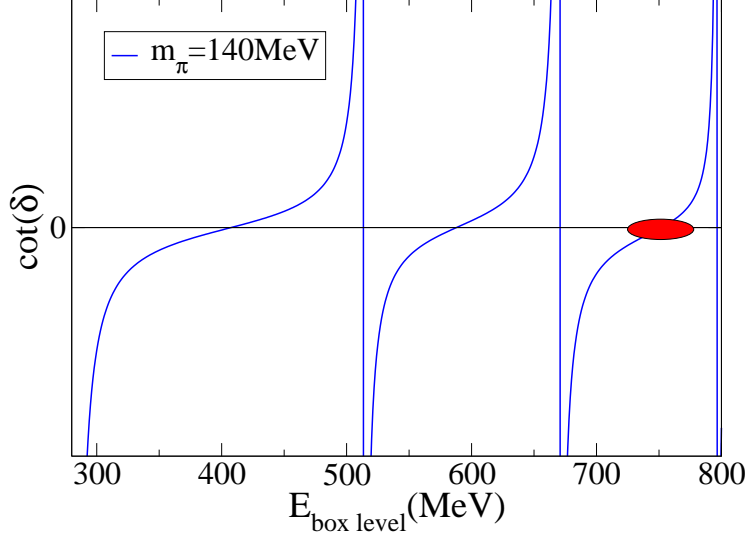


Figure 3.1.: Plot of $\cot \delta(E)$ computed with Lüscher’s formula for $m_\pi = 140$ MeV, $L = 48$ and $a \sim 0.114$ fm. The red spot shows the physical ρ resonance region. The singularities of $\cot \delta(E)$ correspond to non-interacting 2π states. The lowest energy considered is the minimal energy of two back-to-back pions with $J = 1$ in the box: $E_{min} = 2 \sqrt{(2\pi/L)^2 + m_\pi^2}$.

Fig. 3.1 shows a plot of $\cot \delta_1$ with respect to E computed from Lüscher’s formula Eq. (3.9) at a pion mass close to the physical value. It highlights the expected singularities of $\cot \delta_1$ associated with the non-interacting 2π states. The filled blob shows the expected position of the resonance and energy levels in this region are obviously *excited* 2π states. For such a configuration we will have to extract excited states energy from our lattice calculations.

3.3. Methodology

3.3.1. Extraction of the energies: the generalized eigenvalue method

As mentioned above, we can obtain the $\pi\pi$ scattering phase-shifts in the $I = J = 1$ channel at the “box” discrete energies with Lüscher’s equation, and thereby probe the ρ meson resonance. For that purpose, we need to extract one or several spectrum energies from our lattice simulations, sometimes even focusing on excited states. As in usual

lattice calculations, the energy spectrum is retrieved from the asymptotic time behaviour of euclidean correlators, but since we are interested not only in the lowest level, we use the variational method of [68] – also known as the generalized eigenvalue method. This consists in using a cross correlator matrix $C_{ij}(t)$ instead of the usual single correlator:

$$C_{ij}(t) = \langle \mathcal{O}_i(t) \bar{\mathcal{O}}_j(0) \rangle \quad (3.11)$$

with $\{\mathcal{O}_i\}$ a set of N independent appropriate interpolators with good overlap with the ρ or $\pi\pi$ eigenstates.

$C_{ij}(t)$ has the usual spectral decomposition

$$C_{ij}(t) = \sum_n \langle 0 | \mathcal{O}_i(0) | n \rangle \langle n | \mathcal{O}_j^\dagger(0) | 0 \rangle e^{-E_n t} \quad (3.12)$$

which can be written in matrix form

$$C(t) = VD(t)V^\dagger \quad (3.13)$$

with $V_{in} = \langle 0 | \mathcal{O}_i(0) | n \rangle$ and $D(t) = \text{diag}(e^{-E_n t})$.

Now, the main idea behind the variational method is that, at large time, one can neglect the contributions coming from high-energy states because of the exponential suppression. In that case V and D are finite matrices and one has:

$$C(t)C^{-1}(t_0) = VD(t)V^\dagger(VD(t_0)V^\dagger)^{-1} = VD(t-t_0)V^{-1} \quad (3.14)$$

so that the eigenvalues of $C(t)C^{-1}(t_0)$ – solutions of the generalized eigenvalue problem $C(t)u = \lambda(t, t_0)C(t_0)u$ – provide the requested energies through:

$$\lambda_n(t, t_0) = e^{-E_n(t-t_0)} \quad (3.15)$$

In practice, we diagonalize $C(t)C^{-1}(t_0)$ for each t and fixed t_0 to obtain the generalized eigenvalues and then extract the energies from the plateaus of the effective mass

$$m_{\text{eff}} = \frac{\log \lambda_n(t, t_0)}{t_0 - t} \quad (3.16)$$

at large t . Thanks to this method, we can obtain the N lowest eigenstates energies.

Moreover, it has been shown in [69] that if we consider the situation $t_0 \geq t/2$, then the contamination of E_n as given by Eq. (3.15) by higher excited states is of order $O(e^{-(E_{N+1}-E_n)t})$ and low energy states are “protected” from excited states contamination by the GEV states above them.

Note that in practice, computation times limit the number of independent interpolators that we can use, but it is often interesting to use at least one more interpolator than the number of energies that we want to extract.

3.3.2. Kinematics and interpolating operators

Following [70] and [56], we choose to focus on the ρ^0 , which is a p-wave ($J = 1$) $\pi\pi$ scattering resonance with $I = 1$, $I_3 = 0$. As such, in the COM frame, the 2 pions must have opposite non-zero momenta. In our variational method, we use up to 5 independent interpolators with the quantum numbers of the ρ . In order to ensure good overlap with the ρ , we include a 2-quark operator, with zero momentum

$$\mathcal{O}_{\rho i}(t) = \frac{1}{2} \sum_{\mathbf{x}} \bar{u}(\mathbf{x}) \gamma_i u(\mathbf{x}) - \bar{d}(\mathbf{x}) \gamma_i d(\mathbf{x}) \quad (3.17)$$

with γ_i ($i = 1, 2, 3$) a Dirac matrix, and i is the polarization of the ρ .

The other independent operators are built from non-local $I = 1$, $I_3 = 0$ combinations of charged π interpolators with different lattice momenta:

$$\mathcal{O}_{\pi\pi}(t, \mathbf{p}) = \pi^+(\mathbf{p})\pi^-(-\mathbf{p}) - \pi^-(\mathbf{p})\pi^+(-\mathbf{p}) \quad (3.18)$$

with $\mathbf{p} = \frac{2\pi}{L} \mathbf{n}$ and

$$\pi^\pm(\mathbf{p}) = \sum_{\mathbf{x}} \bar{q}(\mathbf{x}) \gamma_5 q'(\mathbf{x}) e^{i\mathbf{p}\cdot\mathbf{x}}, \quad q, q' = u \text{ or } d$$

Note that the COM frame $I = 1$ combination is odd under parity transformation so that it can only couple to odd l states². Henceforth, it can be used to compute phase-shifts in the ρ channel without interference from the $l = 0$ phase-shift.³ As already noted, the $l \geq 3$ contribution can be neglected.

In practice, knowing that the ρ resonance can be rather accurately described by the effective Lagrangian:

$$\mathcal{L}_{\text{eff}} = g_{\rho\pi\pi} \epsilon_{abc} \rho_\mu^a \pi^b \partial^\mu \pi^c \quad (3.19)$$

we see that in order to have the best possible overlap between the $\mathcal{O}_{\pi\pi}(\mathbf{p})$ and $\mathcal{O}_{\rho i}$ operators, we need to choose \mathbf{p} such that $\mathbf{p} - (-\mathbf{p}) = 2\mathbf{p}$ is not orthogonal to the polarization i of the ρ . The chosen momenta are given in Table 3.1.

We then compute the cross-correlators

$$C_i(t) = \begin{pmatrix} \langle \mathcal{O}_{\rho i}(t) \overline{\mathcal{O}_{\rho i}(0)} \rangle & \langle \mathcal{O}_{\rho i}(t) \overline{\mathcal{O}_{\pi\pi i}^{(1)}(0)} \rangle & \cdots & \langle \mathcal{O}_{\rho i}(t) \overline{\mathcal{O}_{\pi\pi i}^{(N-1)}(0)} \rangle \\ \langle \mathcal{O}_{\pi\pi i}^{(1)}(t) \overline{\mathcal{O}_{\rho i}(0)} \rangle & \langle \mathcal{O}_{\pi\pi i}^{(1)}(t) \overline{\mathcal{O}_{\pi\pi i}^{(1)}(0)} \rangle & \cdots & \langle \mathcal{O}_{\pi\pi i}^{(1)}(t) \overline{\mathcal{O}_{\pi\pi i}^{(N-1)}(0)} \rangle \\ \vdots & \vdots & \ddots & \vdots \\ \langle \mathcal{O}_{\pi\pi i}^{(N-1)}(t) \overline{\mathcal{O}_{\rho i}(0)} \rangle & \langle \mathcal{O}_{\pi\pi i}^{(N-1)}(t) \overline{\mathcal{O}_{\pi\pi i}^{(1)}(0)} \rangle & \cdots & \langle \mathcal{O}_{\pi\pi i}^{(N-1)}(t) \overline{\mathcal{O}_{\pi\pi i}^{(N-1)}(0)} \rangle \end{pmatrix} \quad (3.20)$$

for $i = 1, 2, 3$, where $\mathcal{O}_{\pi\pi i}^{(k)} \equiv \mathcal{O}_{\pi\pi}(t, \mathbf{p}_i^{(k)})$ and average on the polarizations i to get the final cross-correlation matrix that we use in the variational method.

²Recalling that a system of 2 pseudoscalars has parity $(-1)^l$.

³In moving frames, this is no more true, and the interpolators need to be projected onto irreducible representations the corresponding groups belonging to $D^{(1)}$.

	$\mathbf{p}^{(1)}$	$\mathbf{p}^{(2)}$	$\mathbf{p}^{(3)}$	$\mathbf{p}^{(4)}$
$i = 1$	(1, 0, 0)	(1, 1, 0)	(1, 1, 1)	(2, 0, 0)
$i = 2$	(0, 1, 0)	(0, 1, 1)	(1, 1, 1)	(0, 2, 0)
$i = 3$	(0, 0, 1)	(1, 0, 1)	(1, 1, 1)	(0, 0, 2)

Table 3.1.: Table of the COM frame momenta used in the 4-quark operators $\mathcal{O}_{\pi\pi i}$ to build the cross-correlator matrix for each polarization of the 2-quark operator $\mathcal{O}_{\rho i}$.

3.3.3. Parametrization of the resonance

Lüscher's formula Eq. (3.9) provides us with some values of the p-wave phase-shift at the energies extracted with the variational method. To interpret these phase-shifts, and obtain a good description of the ρ resonance, we need to use an analytic parametrization of the energy dependence of δ_1 . Hence, we assume that in this channel, $\pi\pi$ scattering is dominated by the narrow ρ resonance, and following [67] and [61], we describe it with an Effective Range formula, which is known to parametrize experimental data rather well:

$$\cot \delta = \frac{E}{\Gamma_\rho} \left(\frac{q_\rho}{q} \right)^3 \frac{M_\rho^2 - E^2}{M_\rho^2} \quad (3.21)$$

with $q_\rho = \sqrt{M_\rho^2/4 - m_\pi^2}$.

Due to the phase space factor the width has a strong kinematical dependence on the pion mass. Therefore it is convenient to define an effective coupling constant $g_{\rho\pi\pi}$ through the point-like interaction

$$\mathcal{L}_{\text{eff}} = g_{\rho\pi\pi} \epsilon_{abc} \rho_\mu^a \pi^b \partial^\mu \pi^c \quad (3.22)$$

which gives at tree level

$$\Gamma_\rho = \frac{g_{\rho\pi\pi}^2}{6\pi} \frac{q_\rho^3}{M_\rho^2} \quad (3.23)$$

The effective coupling is expected to have a mild dependence on the pion mass and therefore is a more convenient parametrisation than the width itself.

Inserted into Lüscher's formula, this leads to:

$$M_\rho^2 = E^2 + g_{\rho\pi\pi}^2 \frac{4\sqrt{\pi}}{3} \frac{\tilde{q}^2 \mathcal{Z}_{00}(1; \tilde{q}^2)}{EL^3} \quad (3.24)$$

where M_ρ and $g_{\rho\pi\pi}$ are the unknowns that we want to determine from measurements of at least two E 's, and we recall $q = \sqrt{E^2/4 - m_\pi^2} = \frac{2\pi}{L} \tilde{q}$. Since we always have at least two energy levels from the variational method, this formula can be used either directly in a system of equations involving two levels, or in a fit with all the levels. For the latter, we actually compute and fit $\sin^2 \delta(E)$ using the equivalent formula:

$$\sin^2 \delta(E) = \left(1 + \frac{\mathcal{Z}_{00}^2(1; q^2)}{\tilde{q}^2 \pi^3} \right)^{-1} = \left(1 + \left[\frac{6\pi}{g_{\rho\pi\pi}^2} \frac{E}{q^3} (M_\rho^2 - E^2) \right]^2 \right)^{-1} \quad (3.25)$$

Results for the fits of the phase-shifts with Eq. (3.25) for the suitable ensembles are shown in Sec. 3.5.1

3.3.4. Pion mass dependence of the resonance

At physical pion mass, experimental data inserted in Eq. (3.23) give for the $\rho\pi\pi$ coupling

$$g_{\rho\pi\pi} \simeq 6 \quad (3.26)$$

We shall use a simple low order Pade parametrization to model the mild pion mass dependence of the coupling.

The variation of the mass – or pole position – of the resonance with m_π is more problematic. As for any hadron the pion mass dependence is not negligible and its evaluation is beyond chiral perturbation theory because the pions emitted in the decay are not soft. Moreover there may be threshold effects at the point $M_\rho(m_\pi)$ which, *a priori*, could induce a non-polynomial behaviour.

To investigate this problem, we use the model of [71] in which we have retained the contributions which dominate the result in our domain. The ρ mass is the solution of the equation

$$M_\rho^2 = (\alpha_0 + \alpha_2 m_\pi^2)^2 + \Sigma_{\pi\omega} + \Sigma_{\pi\pi}(M_\rho) \quad (3.27)$$

where the self-energies corresponding respectively to $\pi\omega$ and $\pi\pi$ intermediate states are given by

$$\Sigma_{\pi\pi} = -\frac{f_{\rho\pi\pi}^2}{6\pi^2} \mathcal{P} \int_0^\infty \frac{k^4 u_{\pi\pi}^2(k) dk}{\omega(k) (\omega^2(k) - M_\rho^2/4)} \quad (3.28)$$

$$\Sigma_{\pi\omega} = -\frac{f_{\rho\pi\omega}^2}{3\pi^2 f_\pi^2} \int_0^\infty \frac{k^4 u_{\pi\omega}^2(k) dk}{\omega^2(k)} \quad (3.29)$$

with $\omega(k) = \sqrt{k^2 + m_\pi^2}$. When $m_\pi < M_\rho/2$ the mass is complex in infinite volume and Eq. (3.27) refers to the real part. The form factors used to regulate the integrals are chosen as

$$u_{\pi\omega}(k) = u(k), \quad u_{\pi\pi}(k) = \frac{u(k)}{u\left(\sqrt{\mu_\rho^2/4 - \mu_\pi^2}\right)}, \quad u(k) = \frac{\Lambda^4}{(k^2 + \Lambda^2)^2} \quad (3.30)$$

with $\mu_\pi = 0.14$ GeV, $\mu_\rho = 0.78$ GeV, $\Lambda = 0.63$ GeV and the couplings are $f_{\rho\pi\pi} = 6.028$, $f_{\rho\pi\omega} = 0.74 \sqrt{\mu_\rho}$, $f_\pi = 0.0924$ GeV. The parameters α_0, α_2 have been adjusted on lattice data with large pion masses leading to $\alpha_0 = 0.83$ GeV, $\alpha_2 = 0.494$ GeV⁻¹.

The dotted curve in Fig. 3.2 shows the solution of Eq. (3.27) when the ρ mass in the $\pi\pi$ self energy 3.28 is fixed at its physical value M_ρ^{phys} . One observes the expected kink at $m_\pi = M_\rho^{phys}/2$. However this is a direct consequence of keeping M_ρ constant in the self energy. If one solves Eq. (3.27) self consistently, one gets the full curve which exhibits a smooth behaviour compatible with a low order polynomial. Though based on a specific model, we think that our qualitative conclusion has a general character.

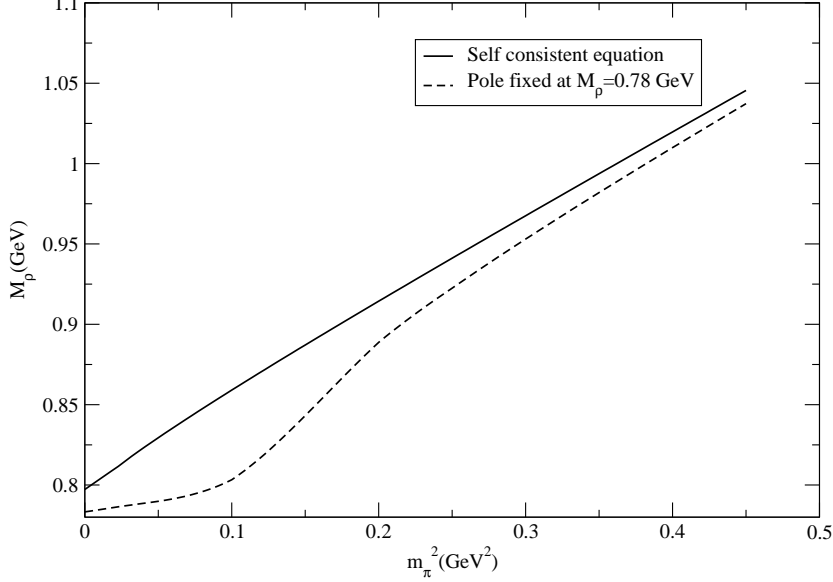


Figure 3.2.: M_ρ as a function of m_π^2 computed with Eq. (3.27). The plain line shows the fully self-consistent solution, while the dotted line corresponds to the solution of the equation with fixed pole mass in the self-energies.

We use the same model to anticipate the stability or instability of the ρ on the lattice. In fact, the stability of a level E is characterized by the lattice quantity

$$\tilde{q}^2 = \left(\frac{L}{2\pi}\right)^2 \left(\frac{E^2}{4} - m_\pi^2\right) \quad (3.31)$$

Applied with $E = M_\rho$, we can compute the values of $\tilde{q}_\rho^2 = \left(\frac{L}{2\pi}\right)^2 \left(\frac{M_\rho^2}{4} - m_\pi^2\right)$ for all our ensembles, shown in Fig. 3.3. These values can be used to tune our strategy, in particular to choose the number of operators (and therefore of available eigenstates energies) we use for each ensemble.

- If $\tilde{q}_\rho^2 < 0$, the rho is below the 2π threshold and is therefore stable on the lattice and in infinite volume. The variational method is not needed, and we can use only the $\mathcal{O}_{\rho i}$ interpolator.
- If $0 \leq \tilde{q}_\rho^2 < 1$, the rho is above the infinite volume threshold, but momentum quantization on the lattice prevents its decay because of the P-wave coupling. The lowest state on the lattice is a ρ -like state, but the strong coupling with the first $\pi\pi$ state strongly pushes toward the use of a 2-level cross-correlator for ensembles

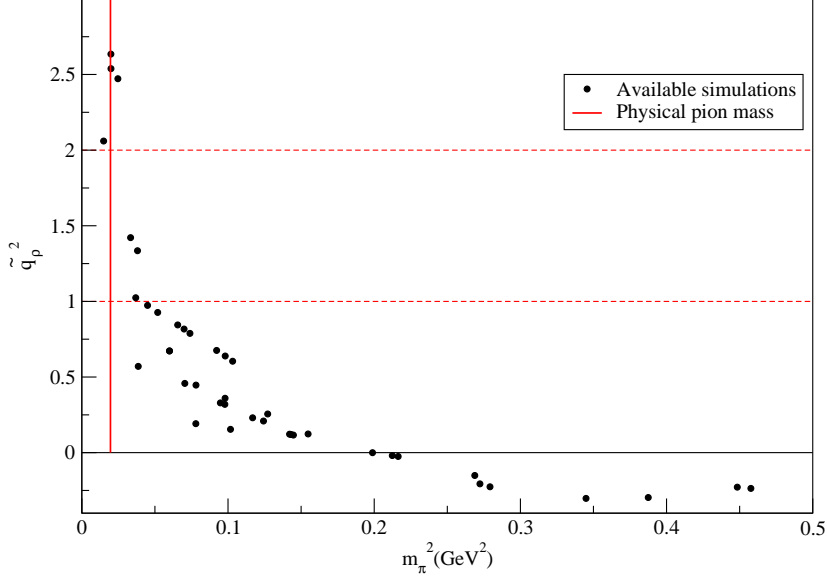


Figure 3.3.: Landscape of the \tilde{q}_ρ^2 values for our ensembles. Note that the figure shows the values of \tilde{q}_ρ^2 for all our ensembles, even if we have only used a subset of them for our analysis, in particular for the ensembles with $\tilde{q}_\rho^2 > 1$, for which only one has been used for computing time reasons.

with $\tilde{q}_\rho^2 \lesssim 1$. If $\tilde{q}_\rho^2 < 0.9$, we can safely neglect the ρ width (i.e. the interaction with $\pi\pi$ states), and use only a 2-quark operator.

- If $1 \leq \tilde{q}_\rho^2$, the rho is unstable even on the lattice, and has strong coupling with excited $\pi\pi$ states. We then need to use the GEV method with more than 2 operators.

3.4. Lattice calculation details

3.4.1. Ensembles

We use the ensembles presented in Sec. 2.4.1. The pion masses range from $m_\pi = 480$ MeV to 120 MeV, and the lattice spacings from 0.053 to 0.11 fm. Among these, 5 ensembles are analysed with the multi-channel GEV variational method mentioned above (we refer to these ensembles as the “GEVP” ones), while 29 others (referred to as the “single” ones) are analysed with a local 2-quark \mathcal{O}_ρ interpolator. The parameters relevant for the “GEVP” and “single” ensembles are given in Table 3.2 and Table 3.3 respectively.

β	am_{ud}^{bare}	am_s^{bare}	volume	# conf.	am_π	$m_\pi L$	\tilde{q}_ρ^2	N
3.31	-0.09300	-0.0400	$32^3 \times 48$	450	0.1771(05)	5.67	0.64	2
	-0.09756	-0.0400	$32^3 \times 48$	221	0.1202(11)	3.85	0.97	5
	-0.09933	-0.0400	$48^3 \times 48$	656	0.0804(13)	3.86	2.54	5
3.61	-0.03300	0.0045	$48^3 \times 48$	210	0.1026(4)	4.92	0.79	2
	-0.03440	0.0045	$48^3 \times 48$	188	0.0864(4)	4.15	0.93	5

Table 3.2.: Ensembles used to study $\pi\pi$ scattering in the ρ channel, with the GEV method (the “GEVP” set). We give the ensembles characteristics, the number of configurations used for the analysis, the pion mass in lattice units am_π , the \tilde{q}_ρ^2 computed with Eq. (3.27) and the size of the cross-correlator that we use (or equivalently the number of eigenstates energies extracted).

3.4.2. Contractions and stochastic propagators

To compute the correlation functions needed in the cross-correlator Eq. (3.20), we follow [53] and [72] and use U(1) time-diluted stochastic and stochastic generalized propagators. This is required since we want to fix the momenta of each initial and final pion independently, but cannot afford to compute the L^3 all-to-all propagators. Note that we work in the isospin limit $m_u = m_d$ so that quark-disconnected contractions cancel.

We introduce N_Q three-dimensional U(1) noises $\{\xi_j(\mathbf{x})\}$, $j = 1, \dots, N_Q$, distributed uniformly so that they have the property

$$\sum_{j=1}^{N_Q} \xi_j^*(\mathbf{x}) \xi_j(\mathbf{y}) \xrightarrow{N_Q \rightarrow \infty} \delta^{(3)}(\mathbf{x} - \mathbf{y}) \quad (3.32)$$

We then use these noises as sources in the inversion of the Wilson Dirac operator D_q ($q = u, d, s$), and obtain the stochastic quark propagators $Q_q(\mathbf{x}, t; \mathbf{p}, t_i, \xi_j)_{\alpha\beta}^{ab}$ defined as the solution of the equation

$$\sum_{\mathbf{x}, t, b, \beta} D_q(\mathbf{y}, t'; \mathbf{x}, t)_{\alpha\beta}^{ab} Q_q(\mathbf{x}, t; \mathbf{p}, t_i, \xi_j)_{\beta\gamma}^{bc} = e^{i\mathbf{p}\cdot\mathbf{y}} \xi_j(\mathbf{y}) \delta(t' - t_i) \delta^{ac} \delta_{\alpha\gamma} \quad (3.33)$$

where color indices are written with Latin letters, and spinor indices with Greek letters. These indices are only explicitly written when needed.

Eq. (3.32) then ensures that, when contracted and for large N_Q , the Q propagators reproduce all-to-all propagators

$$D_q^{-1}(\mathbf{x}, t; \mathbf{x}_i, t_i) = \sum_{j=1}^{N_Q} Q_q(\mathbf{x}, t; \mathbf{0}, t_i, \xi_j) \xi_j^*(\mathbf{x}_i) \quad (3.34)$$

For bilinears, it leads to

$$\sum_{j=1}^{N_Q} Q_q(\mathbf{x}, t; \mathbf{p}, t_i, \xi_j) \Gamma Q_q^\dagger(\mathbf{y}, t'; \mathbf{q}, t_i, \xi_j) = \sum_{\mathbf{z}} e^{i(\mathbf{p}-\mathbf{q})\cdot\mathbf{z}} D_q^{-1}(\mathbf{x}, t; \mathbf{z}, t_i) \Gamma D_q^{-1}(\mathbf{y}, t'; \mathbf{z}, t_i) \quad (3.35)$$

β	am_{ud}^{bare}	am_s^{bare}	volume	# conf.	am_π	$m_\pi L$	\tilde{q}_ρ^2
3.31	-0.07000	-0.0400	$16^3 \times 32$	164	0.3517(13)	5.63	-0.30
	-0.08500	-0.0400	$16^3 \times 32$	1238	0.2519(07)	4.03	0.00
	-0.09300	-0.0400	$16^3 \times 48$	935	0.1802(13)	2.88	0.15
	-0.09530	-0.0400	$16^3 \times 48$	974	0.1577(10)	2.52	0.19
	-0.09300	-0.0400	$24^3 \times 48$	429	0.1769(06)	4.25	0.36
	-0.09530	-0.0400	$24^3 \times 48$	245	0.1500(14)	3.60	0.46
	-0.09756	-0.0400	$24^3 \times 64$	253	0.1110(12)	2.66	0.57
	-0.09000	-0.0440	$24^3 \times 64$	209	0.2015(08)	4.84	0.26
3.5	-0.02500	-0.0023	$16^3 \times 32$	133	0.2920(16)	4.67	-0.24
	-0.02500	-0.0060	$16^3 \times 32$	1461	0.2890(05)	4.62	-0.23
	-0.03100	-0.0060	$24^3 \times 48$	297	0.2535(04)	6.08	-0.30
	-0.04900	-0.0060	$32^3 \times 64$	108	0.1206(07)	3.86	0.45
3.61	-0.02000	0.0045	$32^3 \times 48$	207	0.1986(04)	6.36	-0.23
	-0.02800	0.0045	$32^3 \times 48$	387	0.1479(03)	4.73	0.12
	-0.03000	0.0045	$32^3 \times 48$	194	0.1325(05)	4.24	0.21
	-0.03121	0.0045	$48^3 \times 48$	218	0.1207(03)	5.79	0.60
	-0.02000	-0.0042	$32^3 \times 48$	171	0.1962(04)	6.28	-0.21
	-0.03000	-0.0042	$32^3 \times 48$	142	0.1285(06)	4.11	0.23
3.7	-0.01500	0.0500	$32^3 \times 64$	313	0.1707(03)	5.46	-0.15
	-0.02080	0.0010	$32^3 \times 64$	229	0.1253(04)	4.01	0.12
	-0.02080	0.0000	$32^3 \times 64$	206	0.1241(04)	3.97	0.12
	-0.02540	0.0000	$48^3 \times 64$	118	0.0806(03)	3.87	0.67
	-0.02080	-0.0050	$32^3 \times 64$	207	0.1245(04)	3.98	0.12
	-0.02540	-0.0050	$48^3 \times 64$	264	0.0807(02)	3.87	0.67
3.8	-0.01400	0.0030	$32^3 \times 64$	510	0.1238(03)	3.96	-0.02
	-0.01900	0.0030	$48^3 \times 64$	206	0.0832(03)	3.99	0.32
	-0.01400	0.0000	$32^3 \times 64$	424	0.1226(03)	3.92	-0.02
	-0.01900	0.0000	$48^3 \times 64$	176	0.0819(04)	3.93	0.33

Table 3.3.: Ensembles used to study $\pi\pi$ scattering in the ρ channel, with the 2-quark interpolator only (the “single” set). We give the ensembles characteristics, the number of configurations used for the analysis, the pion mass in lattice units am_π and the \tilde{q}_ρ^2 computed with Eq. (3.27)

with Γ an arbitrary spin-color matrix. The last property shows that a straightforward replacement of point-source – “usual” – propagators by stochastic propagators leads to the required contractions for hadron 2-point correlators.

To compute 3-point and 4-point functions (for example the $\langle \mathcal{O}_{\pi\pi i}^{(1)}(t) \overline{\mathcal{O}}_{\rho i}(0) \rangle$ and $\langle \mathcal{O}_{\pi\pi i}^{(1)}(t) \mathcal{O}_{\pi\pi i}^{(1)}(0) \rangle$ correlators), we introduce a sequential stochastic quark propagator

$W_q(\mathbf{x}, t; \mathbf{k}, t_1; \mathbf{p}, t_i, \xi_j)_{\alpha\beta}^{ab}$ solution of the equation

$$\sum_{\mathbf{x}, t, b, \beta} D_q(\mathbf{y}, t'; \mathbf{x}, t)_{\alpha\beta}^{ab} W_q(\mathbf{x}, t; \mathbf{k}, t_1; \mathbf{p}, t_i, \xi_j)_{\beta\gamma}^{bc} = e^{i\mathbf{k}\cdot\mathbf{y}} \delta(t' - t_1) Q_q(\mathbf{y}, t_1; \mathbf{p}, t_i, \xi_j)_{\alpha\beta}^{ab} \quad (3.36)$$

and another set of N_Q three-dimensional $U(1)$ noises $\{\eta_j(\mathbf{x})\}$ with property (3.32).

We can then use the Q and W propagators to compute the contractions which appear in the cross-correlator, shown schematically in Fig. 3.4 and given in the general case by the following equations ⁴

$$\begin{aligned} G_{\rho_i \rightarrow \rho_i} &= \sum_{j=1}^{N_Q} \sum_{\mathbf{x}} e^{-i\mathbf{P}\cdot\mathbf{x}} \left\langle Q(\mathbf{x}, t; \mathbf{P}, t_i, \xi_j) \gamma_i \gamma_5 Q^\dagger(\mathbf{x}, t; \mathbf{0}, t_i, \xi_j) \gamma_5 \gamma_i \right\rangle, \\ G_{\rho_i \rightarrow \pi\pi}^{[1st]} &= - \sum_{j=1}^{N_Q} \sum_{\mathbf{x}} e^{-i\mathbf{p}\cdot\mathbf{x}} \left\langle W^\dagger(\mathbf{x}, t; \mathbf{q}, t; \mathbf{0}, t_i, \xi_j) Q(\mathbf{x}, t; \mathbf{p}, t_i, \xi_j) \gamma_5 \gamma_i \right\rangle, \\ G_{\rho_i \rightarrow \pi\pi}^{[2nd]} &= - \sum_{j=1}^{N_Q} \sum_{\mathbf{x}} e^{-i\mathbf{p}\cdot\mathbf{x}} \left\langle Q^\dagger(\mathbf{x}, t; \mathbf{p}, t_i, \xi_j) W(\mathbf{x}, t; \mathbf{q}, t; \mathbf{0}, t_i, \xi_j) \gamma_5 \gamma_i \right\rangle. \\ G_{\pi\pi \rightarrow \rho_i}^{[1st]} &= \sum_{j=1}^{N_Q} \sum_{\mathbf{x}} e^{-i\mathbf{P}\cdot\mathbf{x}} \left\langle Q(\mathbf{x}, t; \mathbf{0}, t_i, \xi_j) W^\dagger(\mathbf{x}, t; -\mathbf{p}, t; -\mathbf{q}, t_i, \xi_j) \gamma_5 \gamma_i \right\rangle, \\ G_{\pi\pi \rightarrow \rho_i}^{[2nd]} &= \sum_{j=1}^{N_Q} \sum_{\mathbf{x}} e^{-i\mathbf{P}\cdot\mathbf{x}} \left\langle W(\mathbf{x}, t; \mathbf{p}, t; \mathbf{q}, t_i, \xi_j) Q^\dagger(\mathbf{x}, t; \mathbf{0}, t_i, \xi_j) \gamma_5 \gamma_i \right\rangle, \\ G_{\pi\pi \rightarrow \pi\pi}^{[1st]} &= \sum_{j=1}^{N_Q} \sum_{\mathbf{x}, \mathbf{y}} e^{-i(\mathbf{p}\cdot\mathbf{x} + \mathbf{q}\cdot\mathbf{y})} \left\langle Q^\dagger(\mathbf{x}, t; \mathbf{0}, t_i, \xi_j) Q(\mathbf{x}, t; \mathbf{p}, t_i, \xi_j) \right\rangle \left\langle Q^\dagger(\mathbf{y}, t; \mathbf{0}, t_i, \eta_j) Q(\mathbf{y}, t; \mathbf{q}, t_i, \eta_j) \right\rangle, \\ G_{\pi\pi \rightarrow \pi\pi}^{[2nd]} &= \sum_{j=1}^{N_Q} \sum_{\mathbf{x}, \mathbf{y}} e^{-i(\mathbf{q}\cdot\mathbf{x} + \mathbf{p}\cdot\mathbf{y})} \left\langle Q^\dagger(\mathbf{x}, t; \mathbf{0}, t_i, \xi_j) Q(\mathbf{x}, t; \mathbf{p}, t_i, \xi_j) \right\rangle \left\langle Q^\dagger(\mathbf{y}, t; \mathbf{0}, t_i, \eta_j) Q(\mathbf{y}, t; \mathbf{q}, t_i, \eta_j) \right\rangle, \\ G_{\pi\pi \rightarrow \pi\pi}^{[3rd]} &= \sum_{j=1}^{N_Q} \sum_{\mathbf{x}} e^{-i\mathbf{p}\cdot\mathbf{x}} \left\langle W^\dagger(\mathbf{x}, t; -\mathbf{q}, t; -\mathbf{p}, t_i, \xi_j) W(\mathbf{x}, t; -\mathbf{q}, t; \mathbf{0}, t_i, \xi_j) \right\rangle, \\ G_{\pi\pi \rightarrow \pi\pi}^{[4th]} &= \sum_{j=1}^{N_Q} \sum_{\mathbf{x}} e^{-i\mathbf{p}\cdot\mathbf{x}} \left\langle W(\mathbf{x}, t; \mathbf{q}, t; \mathbf{p}, t_i, \xi_j) W^\dagger(\mathbf{x}, t; \mathbf{q}, t; \mathbf{0}, t_i, \xi_j) \right\rangle, \\ G_{\pi\pi \rightarrow \pi\pi}^{[5th]} &= \sum_{j=1}^{N_Q} \sum_{\mathbf{x}} e^{-i\mathbf{p}\cdot\mathbf{x}} \left\langle W(\mathbf{x}, t; \mathbf{p}, t; \mathbf{0}, t_i, \xi_j) W^\dagger(\mathbf{x}, t; \mathbf{q}, t; -\mathbf{q}, t_i, \xi_j) \right\rangle, \\ G_{\pi\pi \rightarrow \pi\pi}^{[6th]} &= \sum_{j=1}^{N_Q} \sum_{\mathbf{x}} e^{-i\mathbf{p}\cdot\mathbf{x}} \left\langle W^\dagger(\mathbf{x}, t; -\mathbf{p}, t; \mathbf{0}, t_i, \xi_j) W(\mathbf{x}, t; -\mathbf{q}, t; \mathbf{q}, t_i, \xi_j) \right\rangle. \end{aligned} \quad (3.37)$$

⁴Recall that we work in the isospin limit, so that $D_u(\mathbf{y}, t'; \mathbf{x}, t)_{\alpha\beta}^{ab} = D_d(\mathbf{y}, t'; \mathbf{x}, t)_{\alpha\beta}^{ab}$, and $Q_u = Q_d = Q$, $W_u = W_d = W$.

with \mathbf{P} the total momentum, \mathbf{p} and \mathbf{q} the respective momenta of the pions, and where the bracket $\langle \cdot \rangle$ denotes a trace on color and spinor indices. In our case – in the COM frame, $\mathbf{P} = \mathbf{0}$ and $\mathbf{q} = -\mathbf{p}$.

Most of the cost of the lattice computation comes from the sequential stochastic propagators W , as we require them with equal intermediate and final times t , for all t . This is because we chose to use time-diluted (three-dimensional) stochastic sources, which save us only of a factor L^3 out of the L^4 all-to-all inversions. However, using four-dimensional stochastic sources would have been more noisy, since it would have polluted the spectral time dependence (of the form $e^{-E(t-t_i)}$) with possible propagations on much smaller time extents.

In practice, and after some tests, we chose to use $N_Q = 10$ stochastic sources. This does not seem like much, but these sources are generated independently for each configuration, so that we have a few thousand noises after gauge average.

We also use time-translation invariance of the correlators to improve our signal on the cross-correlator by averaging it over multiple time-shifted sources: if $C(t, t_i)$ denotes the cross-correlator with initial time t_i made explicit, we actually compute

$$C(t) = \frac{1}{N_{t_i}} \sum_{t_i} C(t + t_i, t_i) \quad (3.38)$$

Although we may have correlation from one time-slice to the next, it appears that time-slices separated by a few steps decorrelate and do enhance the signal. We chose to use 4 time-slice sources evenly spread within the lattice time extent.

Note that the 2-point correlator $\langle \mathcal{O}_{\rho i}(t) \overline{\mathcal{O}_{\rho i}}(0) \rangle$ can also be computed with the usual point-source or gaussian-source propagators:

$$\langle \mathcal{O}_{\rho i}(t) \overline{\mathcal{O}_{\rho i}}(0) \rangle = - \sum_{\mathbf{x}} \left\langle \gamma_i \gamma_5 D^{-S\dagger}(\mathbf{x}, t; \mathbf{0}, t_i) \gamma_5 \gamma_i D^{-S}(\mathbf{x}, t; \mathbf{0}, t_i) \right\rangle \quad (3.39)$$

where S denotes the smearing (point or gauss) of the source. We use the latter expression to compute the ρ correlator for ensembles of the “single” set. Since it only requires one inversion per configuration, it is much less expensive than stochastic propagators method. Hence, we could again benefit from time-translation invariance and improve our statistics using up to T time-slice sources.

3.5. Results

3.5.1. GEVP energies

In Figs. 3.5–3.9, we show the effective mass as a function of time obtained either with the GEV method and Eq. (3.16) or with the 2-quark interpolator only, for the 5 ensembles of Table 3.2. We indicate the GEV reference times t_0 used for each figure in the captions.

The statistical errors are evaluated throughout this section with the bootstrap method presented in Appendix A with 2000 bootstrap samples and the robust statistical estimators mentioned in the same appendix. The need for robustness in this analysis is driven

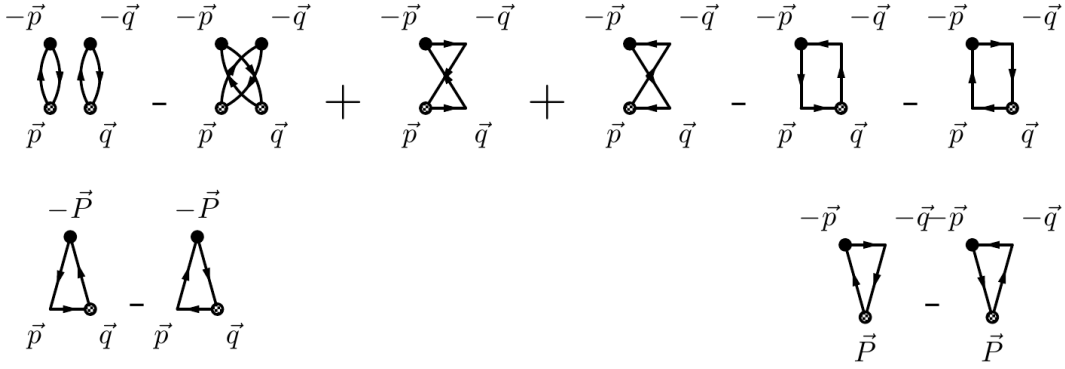


Figure 3.4.: The contractions of $\pi\pi \rightarrow \pi\pi$ (top), $\pi\pi \rightarrow \rho$ (bottom-left) and $\rho \rightarrow \pi\pi$ (bottom-right), the $\rho \rightarrow \rho$ being trivial. Time flows upward from 0 to t . Black dots represent an explicit summation whereas shaded dots represent a noise-noise contact. Between those dots we can have stochastic (one-line segments) or sequential stochastic (two-line segments) propagators. Reprinted from [57].

by the singular nature of Lüscher's equation Eq. (3.9), in which the zeta function shows poles for integer values of \tilde{q}^2 . These singularities favour the appearance of outliers in the bootstrap samples as the finite-volume calculation is carried out, and the usual mean and standard deviation estimators fail to give accurate representations of the distribution. For consistency, we use the robust estimators even for quantities not affected by the singularities of zeta.

The \tilde{q}_ρ^2 indicated are the ones obtained with Eq. (3.27); though model-dependent, they can be used to interpret the effective masses.

For the ensemble of Fig. 3.5, we have \tilde{q}_ρ^2 much smaller than 1, so that we expect a predominantly ρ -like lowest eigenstate. In fact, we can see that the 2-quark interpolator succeeds in providing us with the lowest eigenstate plateau, but at larger times than the GEV method does. Indeed, the latter disentangles the eigenstates and therefore removes the $\pi\pi^{(1)}$ -like state⁵ contamination, leading to an improved convergence to the plateaus. The GEV method also improves the signal for the lowest eigenstate, as it takes information coming from the whole cross-correlator.

In Fig. 3.9 and Fig. 3.8, the observations are similar, but as \tilde{q}_ρ^2 is closer to 1, we see that the 2-quark interpolator barely manages to give lowest eigenstate energy. Indeed, this eigenstate is now a strongly coupled $\rho - \pi\pi^{(1)}$ -like state with a relatively small overlap with the 2-quark operator.

The ensemble of Fig. 3.6 has $\tilde{q}_\rho^2 \approx 1$, and we can see that the 2-quark interpolator has no overlap with the lowest eigenstate given by the GEV method. The latter seems to be

⁵ $\pi\pi^{(k)}$ -like means state which main content consists of two pions with momenta $\mathbf{p}^{(k)}$ and $-\mathbf{p}^{(k)}$ (c.f. Table 3.1).

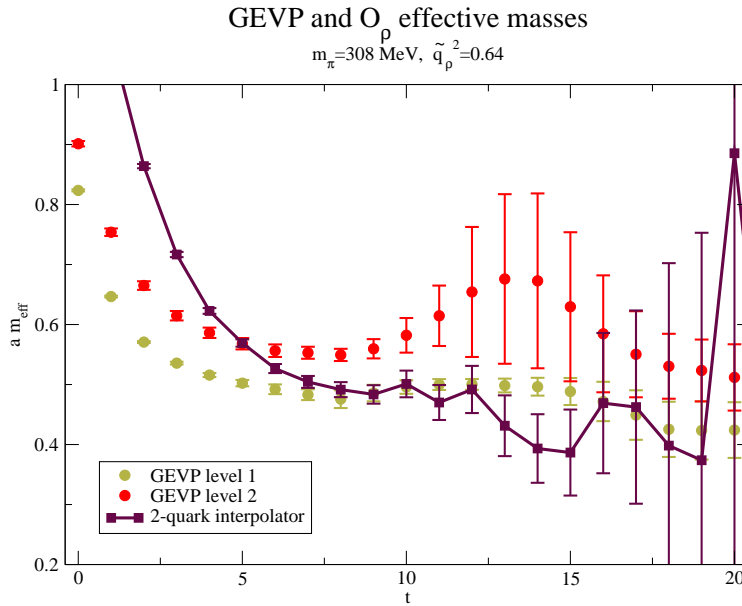


Figure 3.5.: GEVP and 2-quark interpolator effective masses for the ensemble $\beta = 3.31$, $am_{ud}^{\text{bare}} = -0.093$, $am_s^{\text{bare}} = -0.04$, $\Lambda = 32^3 \times 48$. The pion mass is provided for guidance, and does not take full error analysis into account. The GEVP reference time is $t_0 = 7$.

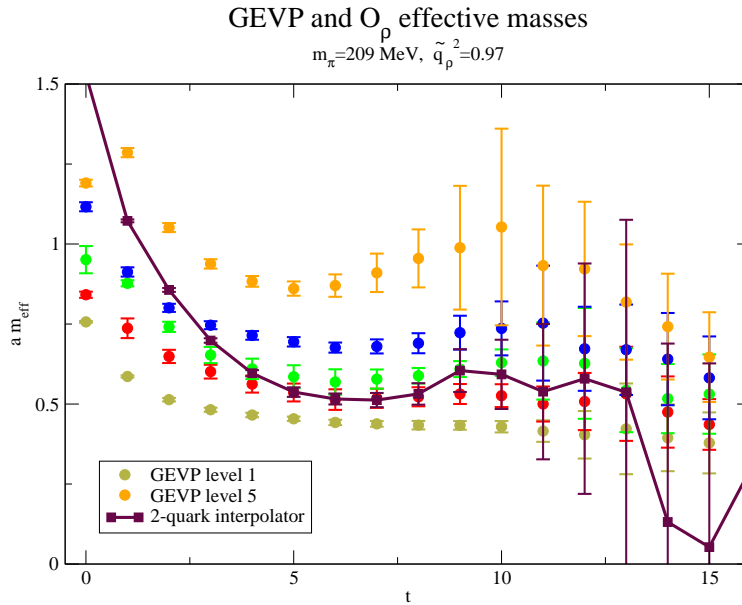


Figure 3.6.: GEVP and 2-quark interpolator effective masses for the ensemble $\beta = 3.31$, $am_{ud}^{\text{bare}} = -0.09756$, $am_s^{\text{bare}} = -0.04$, $\Lambda = 32^3 \times 48$. The pion mass is provided for guidance, and does not take full error analysis into account. The GEVP reference time is $t_0 = 7$.

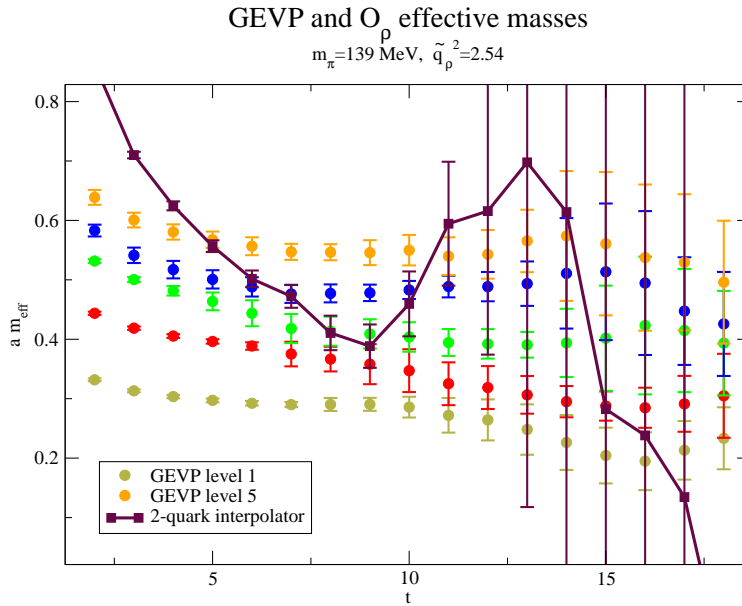


Figure 3.7.: GEV and 2-quark interpolator effective masses for the ensemble $\beta = 3.31$, $am_{ud}^{\text{bare}} = -0.09933$, $am_s^{\text{bare}} = -0.04$, $\Lambda = 48^3 \times 48$. The pion mass is provided for guidance, and does not take full error analysis into account. The GEV reference time is $t_0 = 8$.

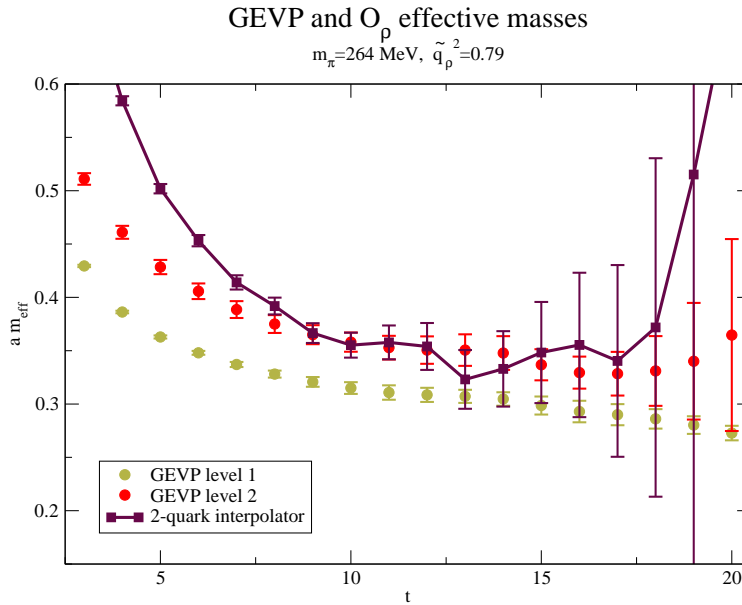


Figure 3.8.: GEV and 2-quark interpolator effective masses for the ensemble $\beta = 3.61$, $am_{ud}^{\text{bare}} = -0.033$, $am_s^{\text{bare}} = 0.0045$, $\Lambda = 48^3 \times 48$. The pion mass is provided for guidance, and does not take full error analysis into account. The GEV reference time is $t_0 = 10$.

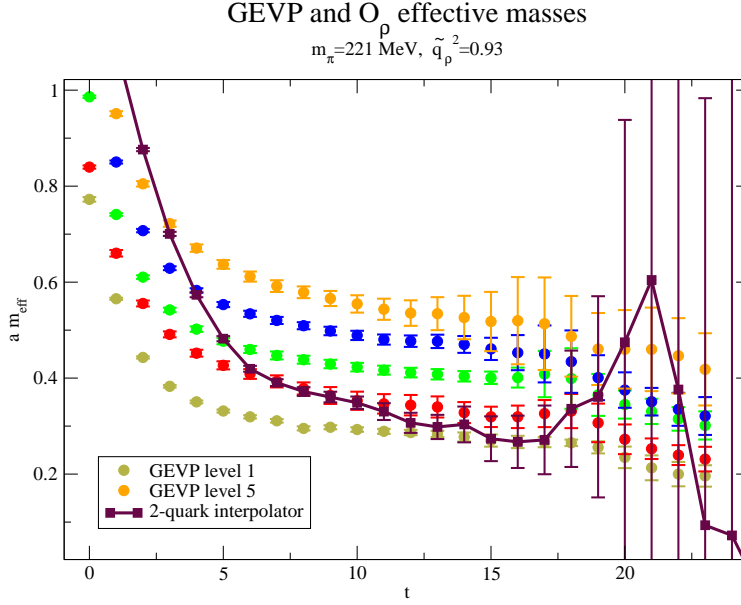


Figure 3.9.: GEV and 2-quark interpolator effective masses for the ensemble $\beta = 3.61$, $am_{ud}^{\text{bare}} = -0.0344$, $am_s^{\text{bare}} = 0.0045$, $\Lambda = 48^3 \times 48$. The pion mass is provided for guidance, and does not take full error analysis into account. The GEV reference time is $t_0 = 8$.

a $\pi\pi^{(1)}$ -like state, while the second and third states seem to be coupled $\rho - \pi\pi^{(2)}$ states.

Fig. 3.7 is the most spectacular, as we can observe the decay of the ρ on the lattice, for a physical pion mass. $\tilde{q}_\rho^2 > 1$ (and even > 2), so that the ρ is expected to be unstable even on the lattice, which is confirmed by the fact that the 2-quark interpolator fails to give a plateau. The lowest eigenstates are $\pi\pi$ -like states, and the third and fourth eigenstates are expected to hold most of the information on the ρ width.

The last two cases illustrate the fact that, as mentioned above, we can expect strong coupling between the ρ and excited $\pi\pi^{(k)}$ (i.e. with $k > 1$) states. The GEV method with more than 2 operators is then essential to extract the eigenstates sensitive to the $\rho\pi\pi$ coupling.

We use the GEV effective masses to extract the eigenstates energies required for the Lüscher analysis through a constant fit of the plateau between t_{min} and t_{max} . The fit ranges are adjusted on the GEV reference times t_0 (c.f. Eq. (3.16)) and are given in Table 3.4 for each ensemble. We can then vary t_0 to assess our control of the systematics. The full systematic errors analysis is spelled out in Sec. 3.5.3.

The results for the energy-level fits are given in Table 3.4, together with the χ^2/dof . They correspond to the particular reference times t_0 given in the captions of the figures. The plateau fits are fully correlated, and lead to satisfactory χ^2/dof .

We can now compute the values of the phase-shift δ_1 at these energies with Eq. (3.9).

Ensemble ($\beta, am_{ud}^{\text{bare}}, am_s^{\text{bare}}, L, T$)	t_0	t_{\min}	t_{\max}	$a E_n$	χ^2/dof
3.31, -.093, -.04, 32, 48	7	$t_0 + 1 = 8$	$t_0 + 1$	0.497(8) 0.555(12)	0.65 0.68
3.31, -.09756, -.04, 32, 48	7	$t_0 + 1 = 8$	$t_0 + 1$	0.435(12) 0.522(31) 0.601(21) 0.702(37) 0.951(89)	0.35 0.48 0.95 0.84 0.83
3.31, -.09933, -.04, 48, 48	8	$t_0 + 3 = 11$	$t_0 + 3$	0.277(20) 0.302(22) 0.389(12) 0.489(19) 0.542(21)	0.33 0.32 0.31 0.37 0.56
3.61, -.033, -.0045, 48, 48	10	$t_0 + 1 = 11$	$t_0 + 1$	0.309(5) 0.349(12)	0.27 0.15
3.61, -.0344, .0045, 48, 48	8	$t_0 + 2 = 10$	$t_0 + 2$	0.288(5) 0.337(22) 0.411(8) 0.479(11) 0.541(21)	1.28 0.53 0.87 0.75 0.54

Table 3.4.: Numerical results for the energy levels of the “GEVP” ensembles, with the corresponding χ^2/dof .

3.5.2. Results for the “GEVP” ensembles

We show the results for the phase-shifts of the ensembles with $N = 5$ in Figs. 3.10–3.12. They correspond to the pion masses 140, 209 and 222 GeV. Notwithstanding the large errors, one clearly observes the expected resonant behaviour of the phase shift. To our knowledge it is the first time that this behaviour is observed at the physical pion mass, for which the ρ is unstable even on the finite lattice.

To get the values of M_ρ and $g_{\rho\pi\pi}$ we either fit the phase-shifts as functions of the energy Eq. (3.25) when we have more than 2 energy levels available, or solve the system provided by Eq. (3.24) satisfied by the two energies. The fits are plotted along with the values of δ_1 in Figs. 3.10–3.12, and the results for the ρ resonance parameters from the “GEVP” ensembles are given in Table 3.5, and shown in Figs. 3.13–3.14.

These results confirm the weak dependence of $g_{\rho\pi\pi}$ on the pion mass, and appear compatible with experimental data.

3.5.3. Global fit and systematic error analysis

To enhance the statistical precision on the ρ resonance parameters and to estimate the systematics we combine the results coming from the multi-channel GEV Lüscher analysis

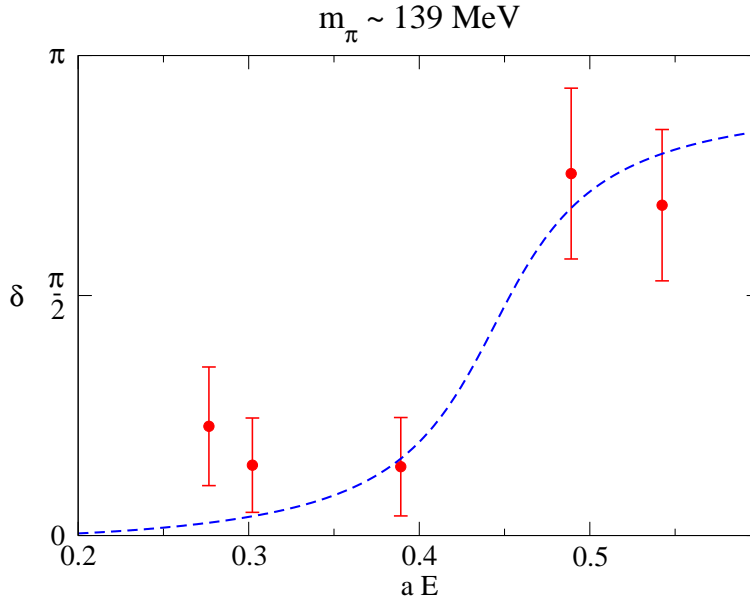


Figure 3.10.: δ_1 phase shift values obtained through a Lüscher analysis of the GEVP energies for the ensemble $\beta = 3.31$, $am_{ud}^{\text{bare}} = -0.09933$, $am_s^{\text{bare}} = -0.04$, $\Lambda = 48^3 \times 48$.

with the data coming from the “single” ensembles set. More precisely we want to get the values of M_ρ and $g_{\rho\pi\pi}$ at the physical point using data from both the “GEVP” and “single” ensembles. The latter are listed in Table 3.3. They all have $\tilde{q}_\rho^2 < 0.8$ so we expect that the lowest energy state is actually a ρ -like state with good overlap with the local 2-quark O_ρ interpolator. Therefore, for these ensembles, we only compute the correlators $\langle \mathcal{O}_\rho(t) \mathcal{O}_\rho(0) \rangle$ and extract the lowest eigenstate energy with a fit of the effective mass plateau. Fig. 3.15 shows an example of such a plateau.

This plateau corresponds to the finite volume energy E of a stable ρ meson in a box. It depends on the ensemble parameters, or equivalently on the pion mass m_π , the kaon mass m_K , the lattice spacing a and the lattice volume L . As discussed above, the lattice volume effect depends on the value of $\tilde{q} = \frac{L}{2\pi} \sqrt{\frac{E^2}{4} - m_\pi^2}$. If $0 \leq \tilde{q}^2 < 1$, the leading volume effects are of order $O(1/L^3)$, and are given by Eq. (3.24) where M_ρ corresponds to the infinite-volume mass of the ρ ⁶, while if $\tilde{q}^2 < 0$, they are exponentially suppressed at least as $e^{-m_\pi L}$, as shown in [62].

We combine these “single” ρ plateaus with the “GEVP” values of M_ρ and $g_{\rho\pi\pi}$ to fit simultaneously the physical ρ mass and the $\rho \rightarrow \pi\pi$ coupling. It is worth noting that while the “GEVP” plateaus may still have leading $O(1/L^3)$ volume effects, these have already been removed by Lüscher’s analysis from the “GEVP” M_ρ , which is by definition

⁶This ρ mass however still has dependencies on m_π , m_K , and a .

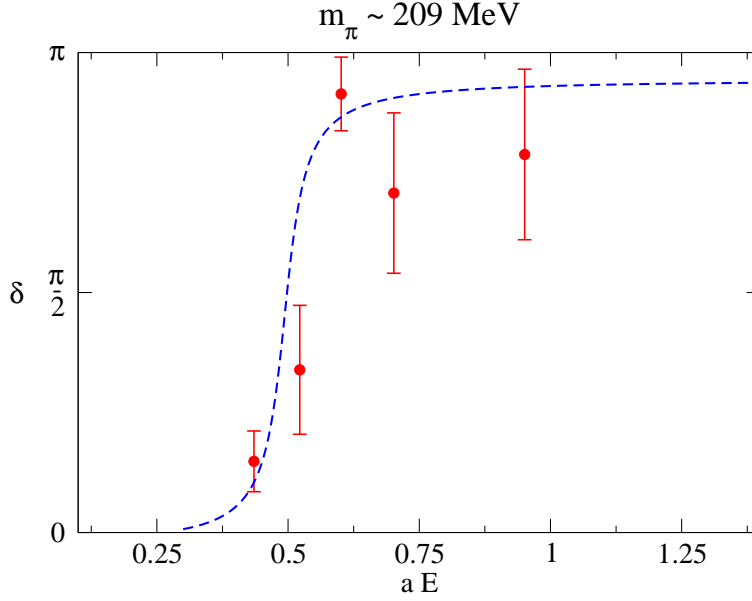


Figure 3.11.: δ_1 phase shift values obtained through a Lüscher analysis of the GEVP energies for the ensemble $\beta = 3.31$, $am_{ud}^{\text{bare}} = -0.09756$, $am_s^{\text{bare}} = -0.04$, $\Lambda = 32^3 \times 48$.

the mass of the ρ in infinite volume for given m_π , m_K and a :

$$M_\rho = M_\rho(m_\pi, m_K, a) \quad (3.40)$$

If $\tilde{q}^2 < 0$, we simply have

$$E = M_\rho(m_\pi, m_K, a) \quad (3.41)$$

i.e. the ρ plateau and mass are equal, since we neglect the exponentially suppressed finite-volume effects.

If $0 \leq \tilde{q}^2 < 1$, M_ρ and E are related through the finite-volume formula

$$M_\rho^2(m_\pi, m_K, a) = E^2 + \frac{4\sqrt{\pi}}{3} g_{\rho\pi\pi}^2 \frac{\tilde{q}^2 Z_{00}(1; \tilde{q}^2)}{L^3 E} \equiv \mathcal{L}(E, m_\pi, g, L) \quad (3.42)$$

where the quantities are now in physical units.

Available data for the global fit therefore consists in M_ρ^2 and $g_{\rho\pi\pi}$ for "GEVP" data, M_ρ^2 only for "single" data with $\tilde{q}^2 < 0$ and E^2 (Eq. (3.9)) for "single" data with $0 \leq \tilde{q}^2 < 1$. As seen in Sec. 3.3.4, the pion mass dependence of M_ρ^2 is well described by a low-order polynomial in m_π^2 . As for the coupling constant, the data only come from the 5 "GEVP" ensembles, and indirectly from the finite-volume effects in the "single" ρ plateaus. We neglect its dependences on m_K or a , and assume a possible dependence on m_π , parametrized by a low-order Padé function.

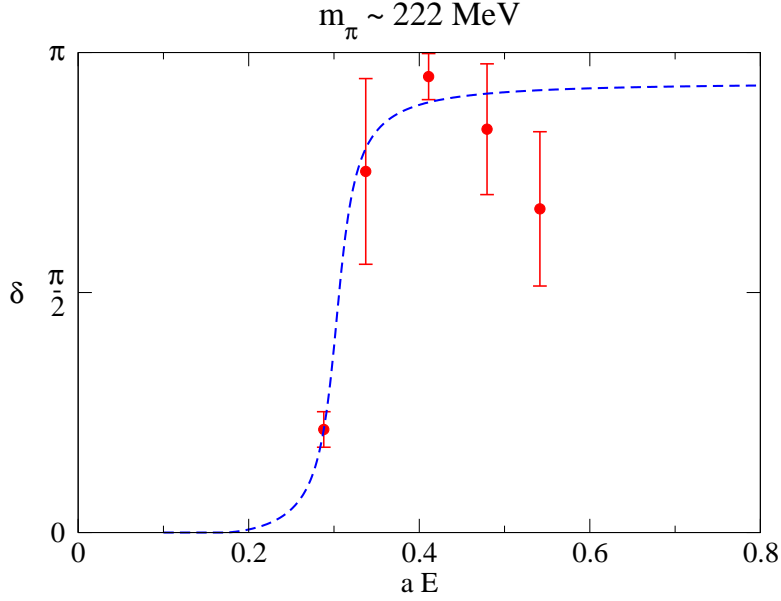


Figure 3.12.: δ_1 phase shift values obtained through a Lüscher analysis of the GEVP energies for the ensemble $\beta = 3.61$, $am_{ud}^{\text{bare}} = -0.0344$, $am_s^{\text{bare}} = 0.0045$, $\Lambda = 48^3 \times 48$.

Thus we model the dependencies as

$$M_\rho^2(m_\pi, m_K, a) = M^2 + \sum_{i=2}^{d_\pi} A_i m_\pi^i + \sum_{j=2}^{d_K} B_j m_K^j + \sum_{k=1}^{d_a} C_k a^{2k} \quad (3.43)$$

$$E = \mathcal{L}^{-1}(M_\rho^2(m_\pi, m_K, a), g, L) \quad (3.44)$$

$$g = g_0 \left[\frac{1 + (m_\pi^{\text{phy}}/\Lambda)^2}{1 + (m_\pi/\Lambda)^2} \right]^{d_g} \quad (3.45)$$

where M^2 , $\{A_i\}$, $\{B_j\}$, $\{C_k\}$, g_0 , and Λ are the fit parameters, denoted P , and d_π , d_K , d_a and d_g are integers defining the model. Note that the leading discretization errors are theoretically of order $\alpha_s(a)a$ and a^2 , the former coming from the fact that improvement of the action is only performed at tree-level. However, for the considered quantity, these errors are small, and the $O(\alpha_s(a)a)$ and $O(a^2)$ cannot be discriminated, so that we only include the $O(a^2)$ one.

We write

$$\begin{aligned} F_{\text{single}}(m_\pi, m_K, a, L; P) &\equiv E(m_\pi, m_K, a, L; P) \\ F_{\text{GEVP}}(m_\pi, m_K, a, L; P) &\equiv \{M_\rho^2(m_\pi, m_K, a; P), g(m_\pi; P)\} \end{aligned} \quad (3.46)$$

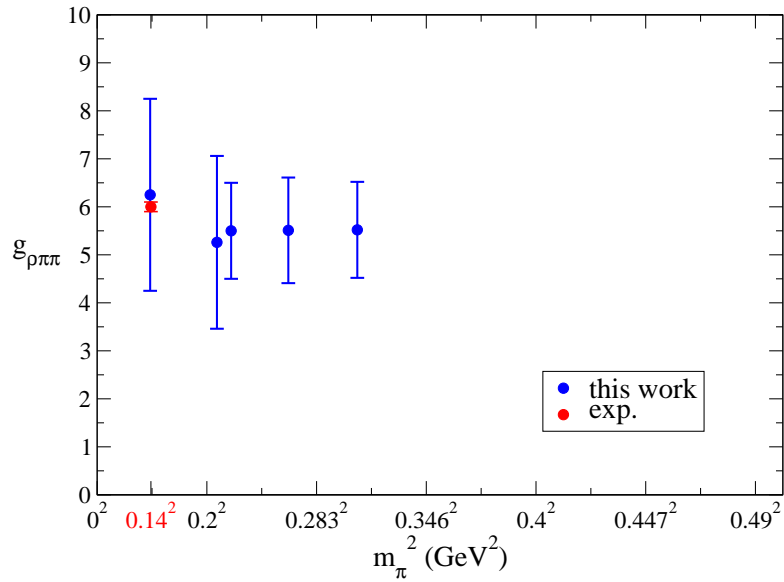


Figure 3.13.: Values of the $\rho\pi\pi$ coupling obtained for the GEVP ensembles plotted against m_π^2 .

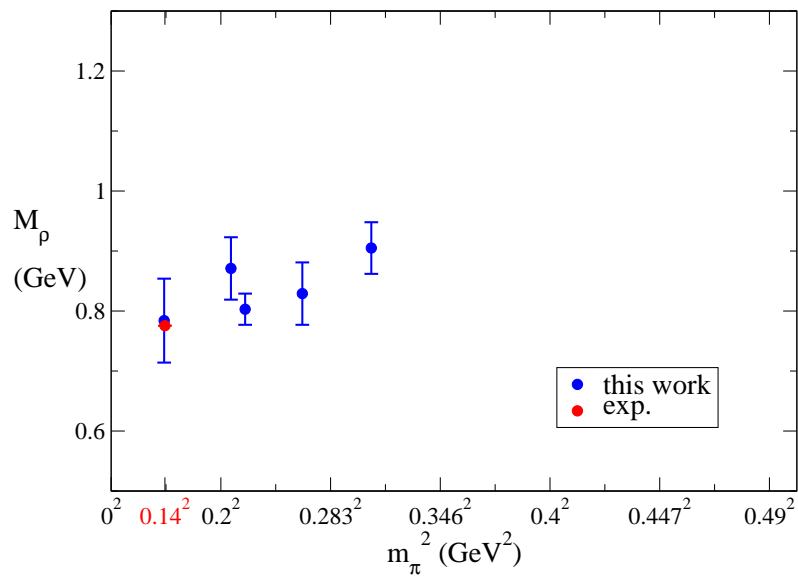


Figure 3.14.: Values of M_ρ obtained for the GEVP ensembles plotted against m_π^2 .

Ensemble ($\beta, am_{ud}^{\text{bare}}, am_s^{\text{bare}}, V, T$)	t_0	m_π (MeV)	aM_ρ	M_ρ (MeV)	$g_{\rho\pi\pi}$	Γ_ρ (MeV)
3.31, -.093, -.04, 32, 48	7	308	0.52(2)	905(43)	5.52(1.12)	71(36)
3.31, -.09756, -.04, 32, 48	7	209	0.50(3)	871(52)	5.26(1.81)	97(59)
3.31, -.09933, -.04, 48, 48	8	139	0.45(4)	784(70)	6.25(2.01)	164(101)
3.61, -.033, -.0045, 48, 48	10	264	0.32(2)	829(52)	5.51(119)	76(44)
3.61, -.0344, .0045, 48, 48	8	221	0.31(1)	803(26)	5.50(1.09)	90(44)

Table 3.5.: Resonance parameters results for the ‘‘GEVP’’ ensembles. We indicate the pion mass in physical units, the computed ρ mass M_ρ in lattice and physical, the $g_{\rho\pi\pi}$ coupling and the corresponding width Γ_ρ as given by Eq. (3.23) in physical units.

and the fit is performed through the minimization of the χ^2 function:

$$\begin{aligned} \chi^2(Y_{\text{GEVP}}, Y_{\text{single}}; X; P) &= (Y_{\text{single}} - F_{\text{single}}(X_{\text{single}}; P))^T C_{\text{single}}^{-1} (Y_{\text{single}} - F_{\text{single}}(X_{\text{single}}; P)) \\ &+ (Y_{\text{GEVP}} - F_{\text{GEVP}}(X_{\text{GEVP}}; P))^T C_{\text{GEVP}}^{-1} (Y_{\text{GEVP}} - F_{\text{GEVP}}(X_{\text{GEVP}}; P)) \end{aligned} \quad (3.47)$$

where $Y_{\text{GEVP}} \equiv \{M_\rho, g\}_{\text{GEVP}}$, $Y_{\text{single}} \equiv \{E\}_{\text{single}}$, $X \equiv \{m_\pi, m_K, a, L\}_{\text{GEVP+single}}$ and $C_{\text{GEVP}, \text{single}}$ are the respective correlation matrices, estimated with the bootstrap samples. Note that the different ensembles are uncorrelated with each other, so that only the quantities within one ensemble are correlated.

To estimate our systematic errors, we then vary the different sources of systematics in our analysis independently and measure the spread of the results. The varied parameters are

- Scale-setting plateaus time fit ranges ⁷
→ 2 ranges (aggressive or conservative, see Table 3.6)
- Scale setting m_π cut (in the chiral fit of M_Ω)
→ 2 cuts ($m_\pi \leq 380\text{MeV}$ or $m_\pi \leq 480\text{MeV}$)
- ‘‘Single’’ ensemble plateaus time fit ranges for m_π , m_K and M_ρ
→ 2 ranges for each plateau (2^3 variations)
- Single data \tilde{q}^2 cut (we restrict ourselves to $\tilde{q}^2 \leq 0.9$ to avoid ensembles where the central value of \tilde{q}^2 is less than 1, but where the error bar goes across 1, see Fig. 3.16)
→ 3 q^2 -cuts ($q^2 \leq 0.7$, $q^2 \leq 0.8$ or $q^2 \leq 0.9$)
- GEV analysis t_0
→ 2 t_0 , which give 2 GEV plateau fit ranges (see Table 3.7)

⁷Recall that the scale is set with the Ω mass as explained in Sec. 2.4.3. The procedure involves the fits of the pion, kaon and omega plateaus, which ranges are varied simultaneously.

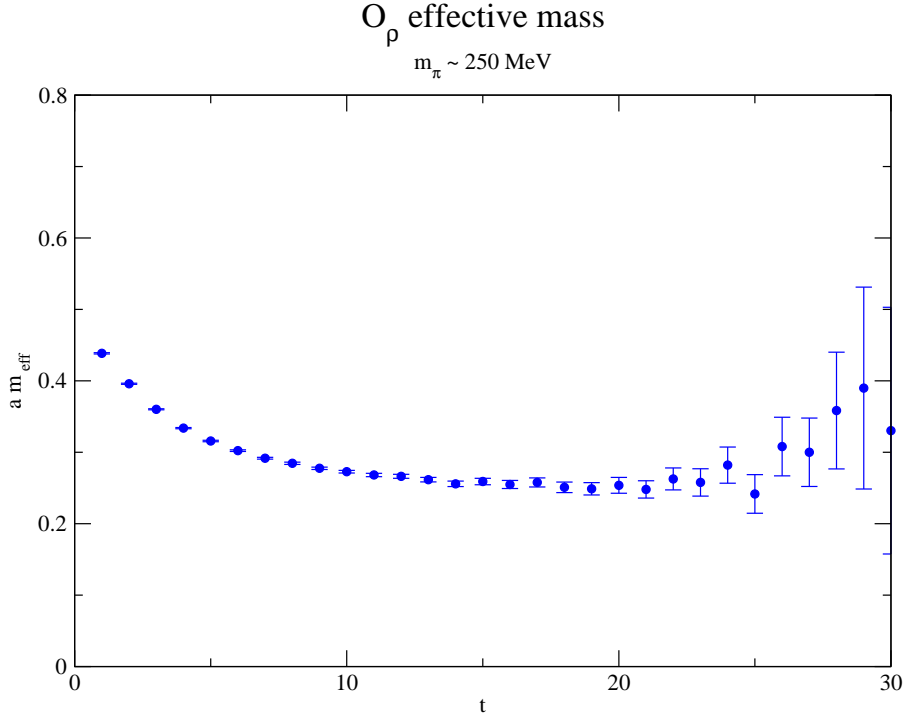


Figure 3.15.: Effective mass obtained with the 2-quark local O_ρ interpolator for the ensemble $\beta = 3.7$, $am_{ud}^{\text{bare}} = -0.0254$, $am_s^{\text{bare}} = -0.005$, $\Lambda = 48^3 \times 64$.

- Functional forms for M_ρ extra/interpolation to the physical point
 $\rightarrow d_\pi = 2$ or 3 , $d_K = 2$, $d_a = 1$ (to prevent overfitting), i.e. 2 variations
- Functional forms for g
 $\rightarrow d_g = 0$ or 1 , i.e. $g = g_0$ or $g_0 \frac{1+(m_\pi^{\text{phy}}/\Lambda)^2}{1+(m_\pi/\Lambda)^2}$ (2 variations)

This gives a total of 768 different methods to evaluate M_ρ^{phy} and $g_{\rho\pi\pi}^{\text{phy}}$.

Following [73], each method s is given an Akaike Information Criterion weight

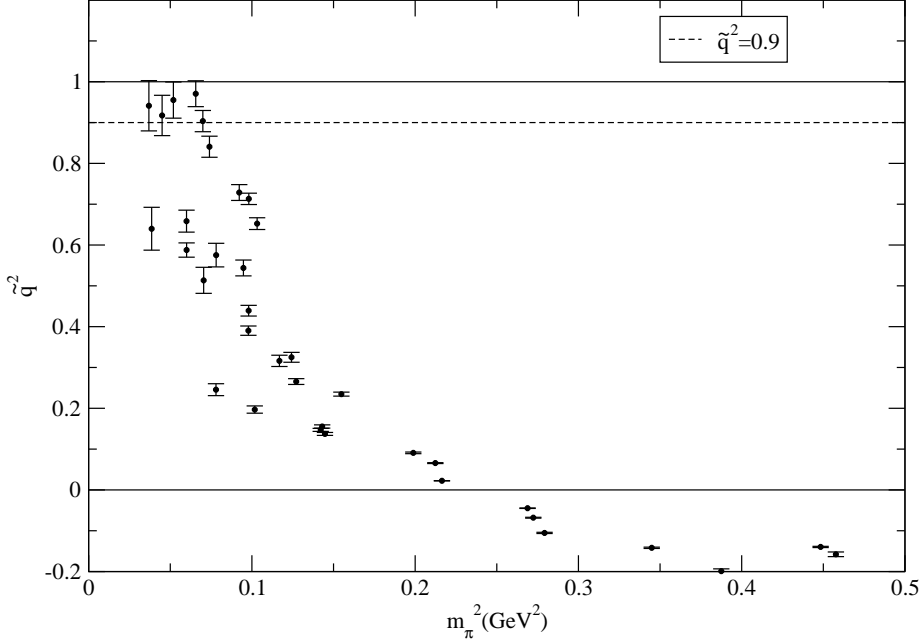
$$w_s = e^{-\frac{1}{2}(AIC_s - AIC_{\min})} \quad (3.48)$$

where

$$AIC_s = \chi_{s, \text{scale setting}}^2 \text{dof} + \chi_{s, M_\rho/g \text{ fit}}^2 \text{dof} + 2(\# \text{ parameters of method } s)$$

$\chi^2 \text{dof}$ denoting the χ^2 per degrees of freedom at the fitted minimum. We obtain the central value as the weighted average:

$$\bar{X} = \frac{1}{\sum_s w_s} \sum_s w_s X_s$$

Figure 3.16.: \tilde{q}^2 landscape computed with extracted plateaus

and the systematic error as the square root of the (unbiased) mean square weighted deviation:

$$S_X^2 = \frac{\sum_s w_s}{(\sum_s w_s)^2 - \sum_s w_s^2} \sum_s w_s (X_s - \bar{X})^2$$

We recall that the statistical errors are estimated through the bootstrap resampling method with 2000 bootstraps as before.

3.5.4. Resonance parameters

We show in Fig. 3.17 a global fit example of M_ρ extrapolated to the continuum and to the physical strange quark mass, as a function of m_π^2 . This fit was done with aggressive ranges, a \tilde{q}^2 cut at 0.9 and a scale setting cut at $m_\pi \leq 480$ MeV. The dependences are $M_\rho^2(m_\pi, m_K, a) = M^2 + A_2 m_\pi^2 + B_2 m_K^2 + C_1 a^2$ and $g(m_\pi, m_K, a) = g_0$. We were not able to detect any dependence of the coupling $g_{\rho\pi\pi}$ on the pion mass with our statistical precision, and when fitted, the parameter Λ in the Pade parametrization of $g(m_\pi)$ is mostly undetermined.

The full systematics analysis gives:

$$M_\rho^{\text{phy}} = 787 \text{ MeV} \pm 8.4 \text{ MeV (stat)} \pm 18 \text{ MeV (syst)} \quad (3.49)$$

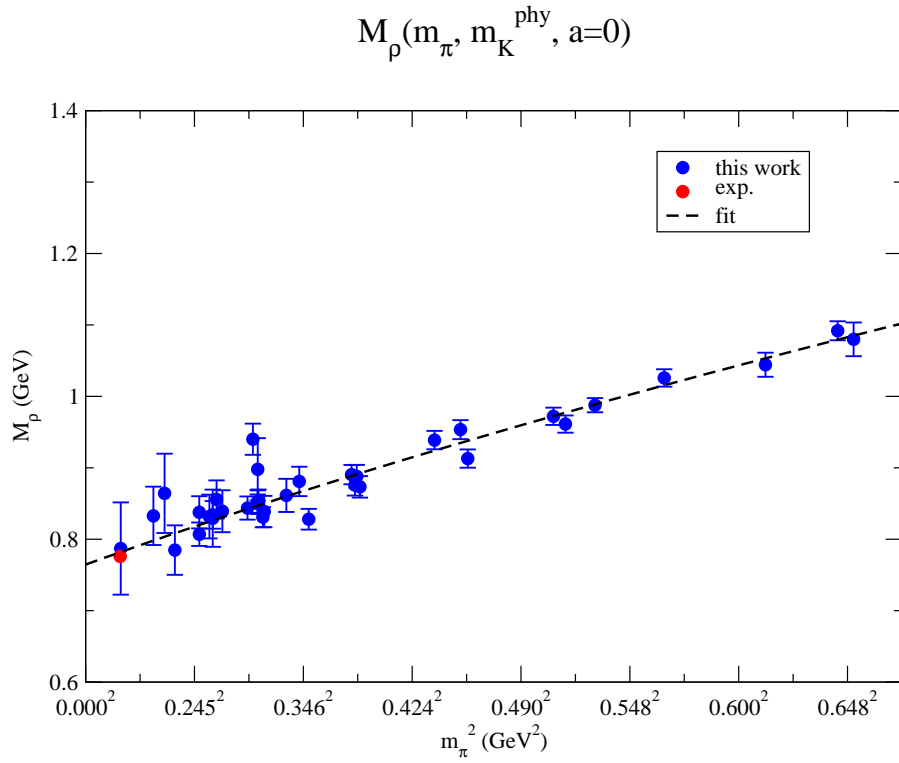


Figure 3.17.: Example of a global fit for M_ρ included in our systematic errors analysis. It corresponds to the method with aggressive ranges, \tilde{q}^2 cut at 0.9, $m_\pi \leq 480$ MeV in the scale setting Ω fit, $d_\pi = 2$ and $g = g_0$. The blue dots are the values of M_ρ after extrapolation to the continuum and to the physical kaon mass with the fit represented with the dashed line. The red dot is the experimental value as given by the PDG [74]. The resulting χ^2 ^{dof} is 1.3.

β	t_i aggressive	t_i conservative
3.31	9	10
3.5	10	11
3.61	12	14
3.7	13	15
3.8	14	16

Table 3.6.: Table of the initial times t_i used to fit plateaus. The final time is given by $t_f = \min(2 t_i, T/2)$. Note that if the plateau corresponds to an interpolator with strange content, the initial time is delayed to $t_i^{(s)} = 1.15^s t_i$ with s the strangeness absolute value.

Ensemble	t_0 aggressive	t_0 conservative	t_i
3.31, -.093, -.04, 32, 48	7	8	$t_0 + 1$
3.31, -.09756, -.04, 32, 48	7	8	$t_0 + 1$
3.31, -.09933, -.04, 48, 48	8	9	$t_0 + 3$
3.61, -.033, -.0045, 48, 48	10	11	$t_0 + 1$
3.61, -.0344, .0045, 48, 48	8	9	$t_0 + 2$

Table 3.7.: Table of the t_0 's used in the GEVP analysis, as well as the corresponding plateau initial fit times.

$$g_{\rho\pi\pi}^{\text{phy}} = 5.35 \pm 0.87 \text{ (stat)} \pm 0.36 \text{ (syst)} \quad (3.50)$$

The weighted histograms for these quantities are shown in Figs. 3.18–3.19.

The physical ρ width is then:

$$\Gamma_{\rho}^{\text{phy}} = 123 \text{ MeV} \pm 31 \text{ MeV (stat)} \pm 29 \text{ MeV (syst)} \quad (3.51)$$

Both the mass and width agree with experimental data as reported by the Particle Data Group [74], and the determination of the physical ρ mass is rather accurate, with a total uncertainty of only 2.5%. The physical point result for the width is less accurate (total uncertainty of 35%) which is due to the reduced precision on the coupling at low pion masses.

3.5.5. Conclusion

We conclude this first application of lattice QCD by a few comments and remarks. First we emphasize that this is the first calculation of the $\pi\pi$ phase shifts in the ρ channel with pion masses down to the physical value. The immediate consequence of this small pion mass is that the ρ actually decays even on the finite lattice. Up to now all calculations were done with such pion masses that the ρ was unstable in infinite volume but stable in the simulations. The crux of the matter when a particle is unstable on the finite lattice

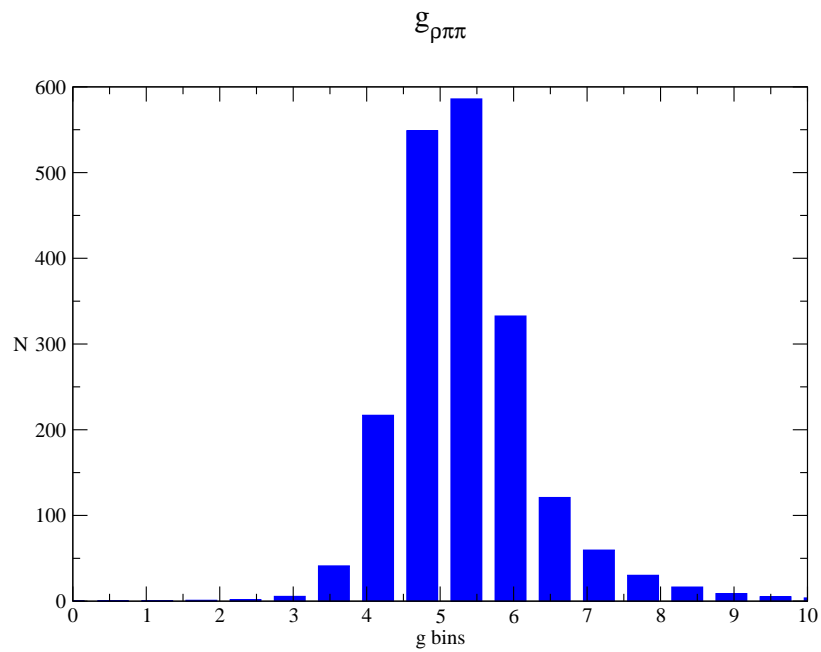


Figure 3.18.: Weighted histogram of the $\rho\pi\pi$ coupling obtained from the full systematics analysis.

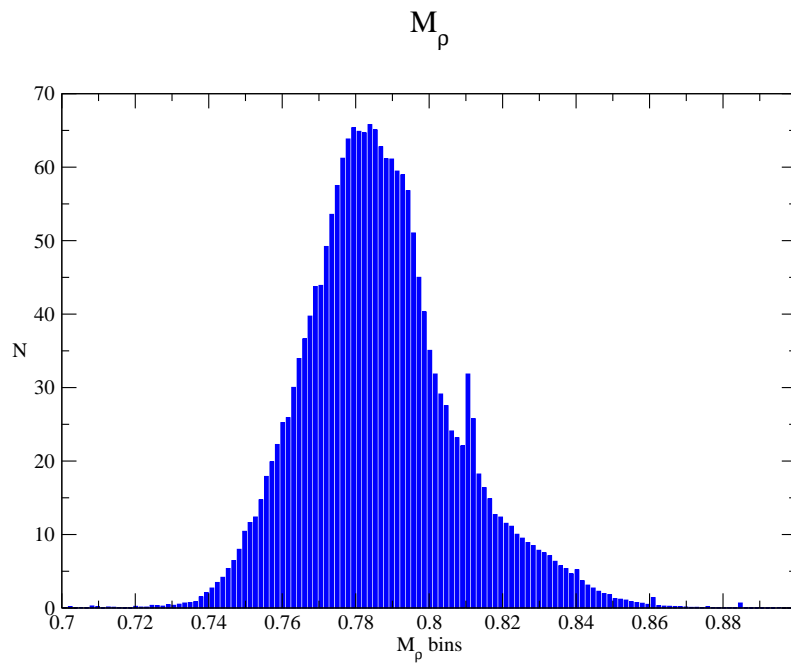


Figure 3.19.: Weighted histogram of the ρ mass obtained from the full systematics analysis.

is that it can only be an excited state with respect to its decay channel. Therefore its measurement necessarily involves some kind of deconvolution of the time dependence of the relevant correlators. Here we have deployed the Generalized EigenValue method which proved to be rather efficient but at the price of a heavy CPU cost. Our results are very satisfactory even though the precision is still modest due to CPU limitations. To improve the accuracy we have combined the GEV data with the ones at higher pion masses which are relatively cheap but nevertheless contain some information about the $\rho\pi\pi$ system. The combined fit based on general and well accepted hypotheses about the variation of the ρ mass versus the parameters (lattice spacing, kaon mass, pion mass) leads to a reliable determination of the effective $\rho\pi\pi$ coupling and of the ρ mass at the physical point. One limitation of our calculation is that the phase shift has been sampled at a few discrete energy values. The only way to improve this point, apart from generating new gauge configurations with larger volumes, would be to perform the calculation in moving frames, as in [58]. This is just a matter of work and CPU. Finally we note that the choice of the GEV basis is a delicate problem. As we have explained, if the state which is sensitive to the $\rho\pi\pi$ interaction, that is, which produces a good phase-shift, is at energy E then it is compulsory that the GEV basis includes all the 2 pions states below that energy. It is also necessary to include some 2 pion states above in order to protect the good state from the contamination by excited states. The trouble is that E is known only at the end of the calculation. This explains why some of our points miss the resonance region. To anticipate this problem we have used a model estimation of the ρ mass and compared it to the 2 pion levels. This lead us to the choice of GEV basis explained in Section 3.3.4. However a model is not QCD and moreover, a later recalibration of the lattice spacing has shown that the relative positions of the resonant state with respect to the 2 pion states was not always as expected. This is why in some cases our GEV basis includes more states than was actually necessary. Given the high CPU cost it is certainly desirable to optimize this point.

4. Nucleon form factors

4.1. Form factors

4.1.1. Electromagnetic form factors

Since the measurement of the proton's magnetic moment in 1933 [75], which showed a much larger value than expected from a spin half point-like Dirac particle, investigations of the electromagnetic structure of the nucleon have been led thoroughly from both the experimental and theoretical points of view. Form factors were introduced by Rosenbluth [76] and defined by Clementel and Villi [77] to account for the deviation of the electric and magnetic charge distributions of the proton from the point-like case.

In elastic scattering processes – like scattering of an electron on a proton – information about the electromagnetic structure of the nucleon lies in the matrix element of the electromagnetic hadronic current between nucleon states:

$$\langle N, \mathbf{p}', s' | V_\mu^{(f)}(0) | N, \mathbf{p}, s \rangle \quad (4.1)$$

where \mathbf{p}, \mathbf{p}' are the nucleon initial and final momenta, s, s' the initial and final spins, and $(f) = (u)$ or (d) is the flavour of the vector current. In QCD, the current is given by

$$V_\mu^{(f)} = \bar{q}_f \gamma_\mu q_f \quad (4.2)$$

where $q_f = q_u, q_d$ or q_s is the up, down or strange quark field and γ_μ is a Dirac matrix. When not necessary, the (f) superscript will be omitted.

Note that we can also define the proton and neutron electromagnetic currents, denoted $V_\mu^{(p)}$ and $V_\mu^{(n)}$ respectively:

$$V_\mu^{(p)} = \frac{2}{3} V_\mu^{(u)} - \frac{1}{3} V_\mu^{(d)} \quad (4.3)$$

$$V_\mu^{(n)} = \frac{2}{3} V_\mu^{(d)} - \frac{1}{3} V_\mu^{(u)} \quad (4.4)$$

as well as the isovector combination, denoted $V_\mu^{(p-n)}$:

$$V_\mu^{(p-n)} = V_\mu^{(u)} - V_\mu^{(d)} \quad (4.5)$$

V_μ is the Noether current associated with the invariance of the continuum QCD action under U(1) phase rotation of the fermion fields. As such, it is a conserved current, i.e. $\partial^\mu V_\mu = 0$, and the corresponding charge – the electric charge $Q = \int d^3\mathbf{x} V_0$ – is a constant of the motion.

Using Lorentz invariance, conservation of the current and the Dirac equation, one can show (see for example [78]) that the matrix element Eq. (4.1) has the general form:

$$\langle N, \mathbf{p}', s' | V_\mu(0) | N, \mathbf{p}, s \rangle = \bar{u}(\mathbf{p}', s') \left[\gamma_\mu F_1(k^2) + \frac{i\sigma_{\mu\nu}(p' - p)^\nu}{2M_N} F_2(k^2) \right] u(\mathbf{p}, s) \quad (4.6)$$

where u denotes the usual spin- $\frac{1}{2}$ Dirac spinor, M is the mass of the nucleon, $\sigma_{\mu\nu} = \frac{i}{2}[\gamma_\mu, \gamma_\nu]$, and we have defined $k \equiv p' - p$. The functions $F_1(k^2)$ and $F_2(k^2)$ are the so-called Dirac and Pauli electromagnetic form factors respectively.

In the Breit frame – the initial and final nucleons center-of-mass frame – the matrix elements can be written as

$$\langle N, -\mathbf{p}, s' | V_0(0) | N, \mathbf{p}, s \rangle = 2M_N \left[F_1(k^2) + \frac{k^2}{4M_N^2} F_2(k^2) \right] \delta_{s's} \quad (4.7)$$

$$\langle N, -\mathbf{p}, s' | \mathbf{V}(0) | N, \mathbf{p}, s \rangle = i [F_1(k^2) + F_2(k^2)] \chi_{s'}^\dagger (\boldsymbol{\sigma} \times \mathbf{k}) \chi_s \quad (4.8)$$

where $\boldsymbol{\sigma}$ are the Pauli matrices, and χ_s are the usual 2-component Pauli spinors $\chi_{\frac{1}{2}} = (1 \ 0)^T$, $\chi_{-\frac{1}{2}} = (0 \ 1)^T$.

It is therefore natural to introduce the Sachs form factors

$$G_E(k^2) \equiv F_1(k^2) + \frac{k^2}{4M_N^2} F_2(k^2) \quad (4.9)$$

$$G_M(k^2) \equiv F_1(k^2) + F_2(k^2) \quad (4.10)$$

The hermiticity of $V_\mu^{(q)}$ implies that the form factors are *real*.

Note that we are interested in the space-like form-factors, accessible through electron-proton scattering experiments. It is then conventional to define $Q^2 \equiv -k^2$, as $Q^2 \geq 0$ in the space-like region.

In the static limit ($|\mathbf{k}| \ll M$), they can be regarded as the Fourier transforms of respectively the charge and magnetization densities of the nucleon in the Breit frame. The slope at $Q^2 = 0$ then gives the mean-square nucleon charge or magnetic radius

$$\langle r_{E,M}^2 \rangle = -6 \frac{1}{G_{E,M}(0)} \left. \frac{dG_{E,M}(Q^2)}{dQ^2} \right|_{Q^2=0} \quad (4.11)$$

Note that, using the Dirac equation, Eq. (4.6) can also be rewritten as

$$\langle N, \mathbf{p}', s' | V_\mu(0) | N, \mathbf{p}, s \rangle = \bar{u}(\mathbf{p}', s') \left[\gamma_\mu G_M(k^2) - \frac{(p' + p)_\mu}{2M_N} F_2(k^2) \right] u(\mathbf{p}, s) \quad (4.12)$$

which gives a really convenient parametrization.

With the relativistic normalization of states

$$\langle N, \mathbf{p}', s' | N, \mathbf{p}, s \rangle = 2E_{\mathbf{p}} (2\pi)^3 \delta^3(\mathbf{p}' - \mathbf{p}) \delta_{s's}$$

one can show (see for example [79]) that at zero momentum transfer, the Sachs form factors hold the static values of the charge and magnetic moments of the considered nucleon, i.e.

$$G_E^{(p)}(0) = 1 \text{ and } G_M^{(p)}(0) = \mu_p \approx 2.793 \quad (4.13)$$

for the proton and

$$G_E^{(n)}(0) = 0 \text{ and } G_M^{(n)}(0) = \mu_n \approx -1.913 \quad (4.14)$$

for the neutron, where the charge is in units of $|e|$ and the magnetic moment in units of the nucleon Bohr magneton $\mu_N = \frac{e}{2M_N}$.

The first experimental measurements of the nucleon form factors were made with the Rosenbluth separation method, which uses the dependence of the elastic electron-proton cross-section on the electron scattering angle. They date back to the 1950s at the High Energy Physics Laboratory (Stanford), and led to a proton charge radius of 0.77 fm [80]. Since these early works [81], analyses based on the Rosenbluth separation method were refined, and new techniques emerged with the recent construction of highly polarized electron beam accelerators, like the recoil polarization method, which allows precise extraction of the ratio $\frac{G_E}{G_M}$ [82]. A comprehensive review of the electromagnetic structure of the nucleon from the electron-proton scattering point of view can be found in [83].

Independently, the proton radius has been obtained from accurate measurements of the Lamb shift transition frequencies of muonic hydrogen [84]. It gives the value 0.84087(39) fm, with an order of magnitude more precision than the value obtained from electron scattering and hydrogen and deuteron spectroscopy experiments – the CODATA value [85], 0.8775(51) fm. The discrepancy between the two values led to the so-called proton radius puzzle and motivated the computation of the electromagnetic form factors and hence of the proton radius from lattice QCD.

As shown in [83], for $Q^2 \lesssim 1 \text{ GeV}^2$, the proton electric and magnetic form factors are well described by a dipole $G_E = \frac{G_M}{\mu} = G_D$ with

$$G_D(Q^2) = \frac{1}{\left(1 + \frac{Q^2}{\Lambda^2}\right)^2} \quad (4.15)$$

with $\Lambda^2 = 0.71 \text{ GeV}^2$. This form is compatible with the vector meson dominance model, which assumes that the photon-nucleon coupling is dominated by the virtual conversion of the photon into a vector meson such as the $\rho(770)$, the $\omega(782)$ or the $\phi(1020)$, which then interacts with the nucleon.

For $Q^2 > 1 \text{ GeV}^2$, experimental data show a significant deviation from the dipolar form, as shown in Figs. 4.1 and 4.2.

We use as experimental reference the results of [86]. For the proton, form factors are parametrized with a functional form proposed by Kelly [87]:

$$G_E^{(p)}(Q^2), \frac{G_M^{(p)}(Q^2)}{\mu_p} = \frac{1 + a_{p,1}^{E,M} \tau}{1 + b_{p,1}^{E,M} \tau + b_{p,2}^{E,M} \tau^2 + b_{p,3}^{E,M} \tau^3} \quad (4.16)$$

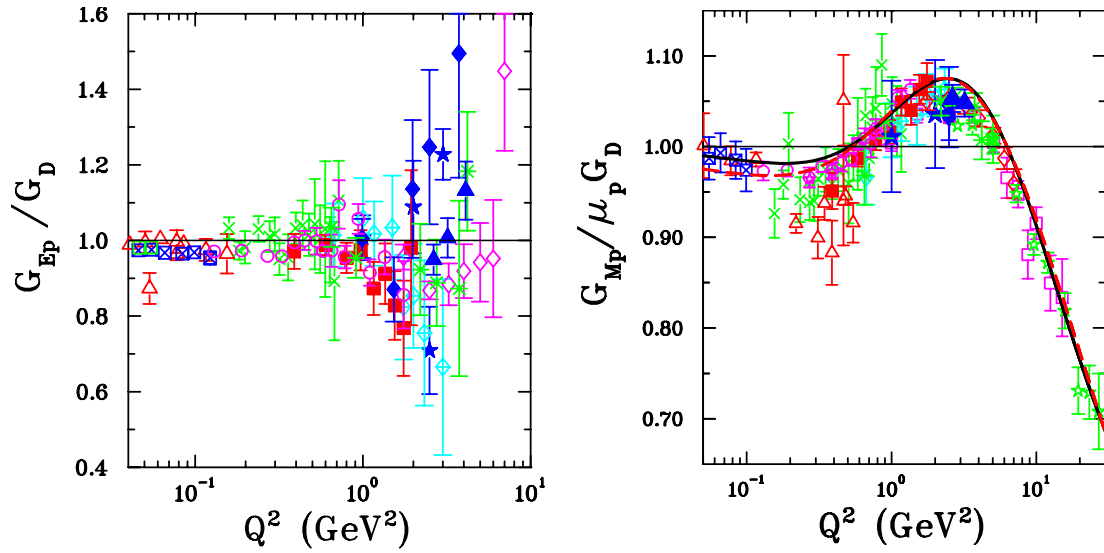


Figure 4.1.: Proton form factors experimental data from [83] and references therein.

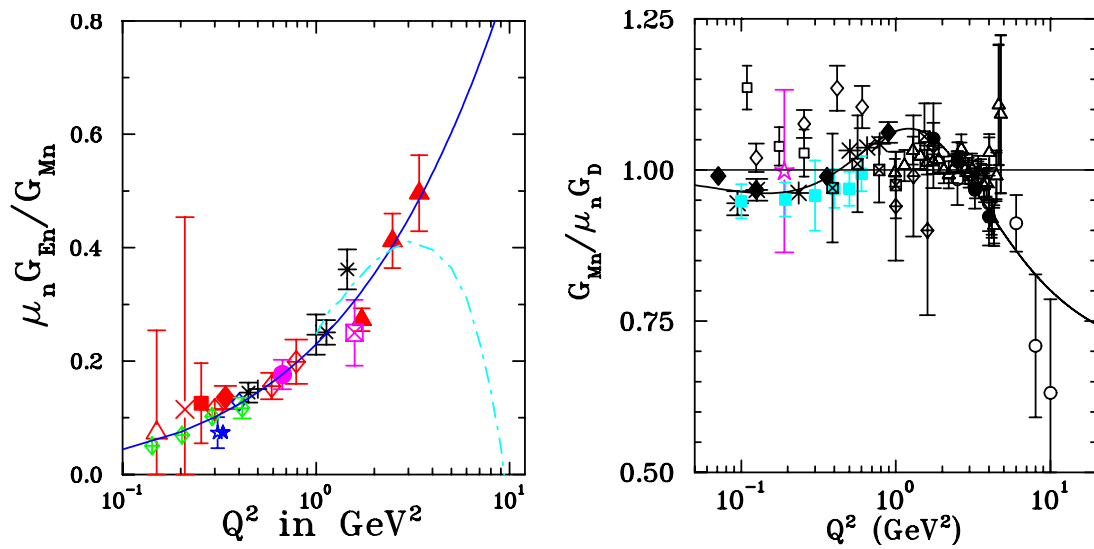


Figure 4.2.: Neutron form factors experimental data from [83] and references therein.

where $\tau \equiv \frac{Q^2}{4M_p^2}$, fitted on Rosenbluth cross-sections and recoil polarization data. The fitted parameters are

$$\begin{aligned} a_{p,1}^E &= -0.19 \pm 0.06, & b_{p,1}^E &= 11.12 \pm 0.15, & b_{p,2}^E &= 15.16 \pm 1.03, & b_{p,3}^E &= 21.25 \pm 3.27 \\ a_{p,1}^M &= 1.09 \pm 0.01, & b_{p,1}^M &= 12.31 \pm 0.07, & b_{p,2}^M &= 25.57 \pm 0.22, & b_{p,3}^M &= 30.61 \pm 0.27 \end{aligned} \quad (4.17)$$

For the neutron, $G_E^{(n)}(Q^2)$ is parametrized with a BLAST-like [88] functional form

$$G_E^{(n)}(Q^2) = \frac{a_n^E}{\left(1 + b_{n,1}^E Q^2\right)^2} - \frac{a_n^E}{\left(1 + b_{n,2}^E Q^2\right)^2} \quad (4.18)$$

with

$$a_n^E = -0.10 \pm 0.02, \quad b_{n,1}^E = 2.83 \pm 0.37, \quad b_{n,2}^E = 0.43 \pm 0.11 \quad (4.19)$$

and $G_M^{(n)}(Q^2)$ with Kelly's parametrization

$$\frac{G_M^{(n)}(Q^2)}{\mu_n} = \frac{1 + a_{n,1}^M \tau}{1 + b_{n,1}^M \tau + b_{n,2}^M \tau^2 + b_{n,3}^M \tau^3} \quad (4.20)$$

with

$$a_{n,1}^M = 8.28 \pm 3.89, \quad b_{n,1}^M = 21.30 \pm 4.56, \quad b_{n,2}^M = 77 \pm 31, \quad b_{n,3}^M = 238 \pm 105 \quad (4.21)$$

Note that the precision of Lattice QCD results does not allow the use of such refined functional parametrizations. We shall therefore restrain our analysis to the low Q^2 sector (the typical accessible Q^2 range on the lattice lies between 0 and 1.6 GeV^2), and use simple dipole functional forms to parametrize the Q^2 dependence of the form factors.

4.1.2. Axial form factors

Similarly to Eq. (4.1), the axial structure of the nucleon is described by matrix elements of the QCD axial current

$$\langle N, \mathbf{p}', s' | A_\mu^a(0) | N, \mathbf{p}, s \rangle \quad (4.22)$$

with

$$A_\mu^a = \bar{q} \gamma_\mu \gamma_5 T^a q \quad (4.23)$$

where q denotes the vector of flavour quark fields, and T^a are generators of $\text{SU}(N_f)$, which depend on the number of quark flavours considered.¹

¹For $\text{SU}(2)$ (2 flavours), $q = \begin{pmatrix} q_u \\ q_d \end{pmatrix}$, and $T^a = \frac{\tau^a}{2}$ are the conventional Pauli isospin matrices. For $\text{SU}(3)$

(3 flavours), $q = \begin{pmatrix} q_u \\ q_d \\ q_s \end{pmatrix}$, and $T^a = \frac{\lambda^a}{2}$ are the Gell-Mann matrices.

In the massless quarks limit, A_μ^a is also a Noether current of the continuum QCD action, associated with the chiral rotations of fermion fields

$$q \rightarrow e^{i\alpha\gamma_5 T^a} q, \quad \bar{q} \rightarrow \bar{q} e^{i\alpha\gamma_5 T^a} \quad (4.24)$$

However, the quark mass term in the QCD action breaks the chiral symmetry, leading to the Partially Conserved Axial Current (PCAC) equation:

$$\partial^\mu A_\mu^a = i\bar{q}\gamma_5 \{T^a, \mathcal{M}\} q \quad (4.25)$$

where \mathcal{M} is the mass matrix.

As before, Lorentz invariance, together with the charge conjugation, parity and time-reversal symmetries, and the absence of second-class current [89] allows us to write Eq. (4.22) in terms of two real form factors

$$\langle N, \mathbf{p}', s' | A_\mu^a(0) | N, \mathbf{p}, s \rangle = \bar{u}(\mathbf{p}', s') \left[\gamma_\mu G_A(Q^2) + \frac{(p' - p)_\mu}{2M_N} G_P(Q^2) \right] \gamma_5 \frac{\tau^a}{2} u(\mathbf{p}, s) \quad (4.26)$$

where G_A is the axial form factor, G_P the induced pseudoscalar form factor, and we have again defined $Q^2 \equiv -(p' - p)^2$.

More specifically, we consider the SU(2) isovector axial current, and write

$$A_\mu^{(p-n)} \equiv A_\mu^{(u)} - A_\mu^{(d)} \quad (4.27)$$

where we have defined $A_\mu^{(f)} \equiv \bar{q}_f \gamma_\mu \gamma_5 q_f$. In the isospin limit, it has the decomposition

$$\langle N, \mathbf{p}', s' | A_\mu^{(p-n)}(0) | N, \mathbf{p}, s \rangle = \bar{u}(\mathbf{p}', s') \left[\gamma_\mu G_A(Q^2) + \frac{(p' - p)_\mu}{2M_N} G_P(Q^2) \right] \gamma_5 u(\mathbf{p}, s) \quad (4.28)$$

We can also define the nucleon axial charge radius

$$\langle r_A^2 \rangle = -6 \frac{1}{G_A(0)} \left. \frac{dG_A(Q^2)}{dQ^2} \right|_{Q^2=0} \quad (4.29)$$

The axial coupling constant $G_A(0)$ is measured in neutron beta decay rather accurately [74]:

$$G_A(0) = 1.2701 \pm 0.0025 \quad (4.30)$$

and the axial form factor is determined experimentally through neutrino scattering off protons and through charged pion electroproduction.

Experimental measurements suggest that for $Q^2 \lesssim 1 \text{ GeV}^2$, the axial form factor can be described with a dipole functional form

$$G_A(Q^2) = \frac{G_A(0)}{\left(1 + \frac{Q^2}{M_A^2}\right)^2} \quad (4.31)$$

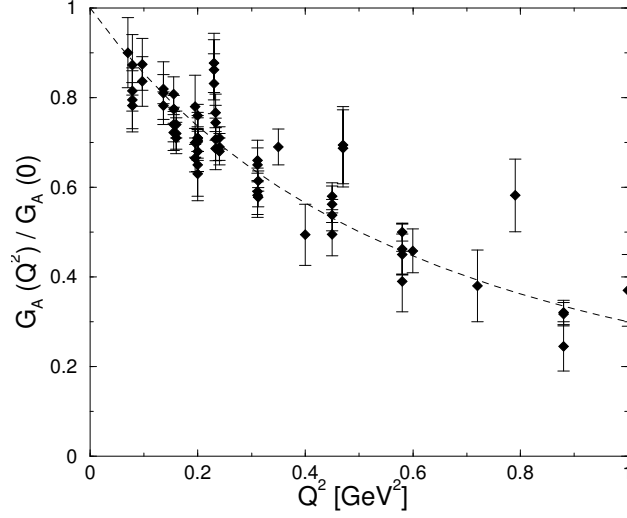


Figure 4.3.: Experimental data for $\frac{G_A(Q^2)}{G_A(0)}$ as obtained from pion electroproduction measurements. The dashed line shows a dipole with axial mass $M_A = 1.1$ GeV. Reprinted from [90].

where M_A is the so-called axial mass. [90] gives $M_A = (1.026 \pm 0.021)$ GeV for neutrino-proton scattering data and $M_A = (1.069 \pm 0.016)$ GeV for pion electroproduction data. We show a compilation of $G_A(Q^2)$ data in Fig. 4.3. More details can be found in [90] and [91].

The induced pseudoscalar form factor $G_P(Q^2)$ is experimentally not accurately measured. The data come from muon capture on the proton or from low momentum transfer pion electroproduction. $G_P(Q^2)$ can be theoretically related to $G_A(Q^2)$ using the PCAC relation Eq. (4.25) and the pion pole dominance hypothesis, giving the approximate relation

$$G_P(Q^2) \simeq \frac{4M^2}{Q^2 + m_\pi^2} G_A(Q^2) \quad (4.32)$$

The “world data” are shown in Fig. 4.4, together with theoretical – pion-pole and chiral perturbation theory – predictions.

4.2. Methodology

4.2.1. Lattice currents, renormalization and Ward identities

To evaluate the matrix elements of the vector and axial current between nucleon states with lattice QCD, we need to choose discrete versions of the continuum currents to use in our calculations. The simplest realizations are the local currents, analogue to their continuum counterparts:

$$\tilde{V}_\mu^{(f)\text{loc}}(n) = \bar{q}_f(n) \gamma_\mu q_f(n) \quad (4.33)$$

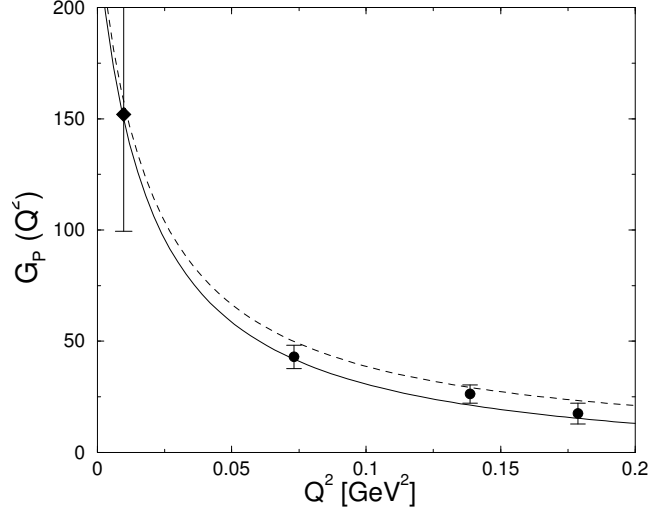


Figure 4.4.: Experimental data for $G_P(Q^2)$. The filled circle are pion electroproduction measurements while the diamond is the muon capture point. The dashed line shows the pion-pole prediction and the solid line the next-to-leading order chiral perturbation theory. Reprinted from [90]. See references therein.

$$\tilde{A}_\mu^{(f)\text{loc}}(n) = \bar{q}_f(n) \gamma_\mu \gamma_5 q_f(n) \quad (4.34)$$

where n denotes a lattice site, and the $\tilde{}$ indicates that these are lattice operators.

Computations on the lattice are inherently done with a finite lattice spacing a , which imposes a momentum cut-off of $\frac{1}{a}$. To relate the correlation functions computed on the lattice to their correct continuum values, the former need to be renormalized. This amounts to a multiplicative renormalization of the operator O involved with a renormalization constant Z_O which depends on the lattice spacing a , and on the continuum renormalization scale μ :

$$O(\mu) = Z_O(\mu, a) O(a) \quad (4.35)$$

In our case, the current operators are finite operators, i.e. they have finite values as the regularization parameter $a \rightarrow 0$. Therefore, their renormalization constants do not depend on any renormalization scale and Eq. (4.35) becomes:

$$V_\mu^{(f)} = Z_V(a) \tilde{V}_\mu^{(f)} \quad (4.36)$$

$$A_\mu^{(f)} = Z_A(a) \tilde{A}_\mu^{(f)} \quad (4.37)$$

where $Z_V(a)$ and $Z_A(a)$ are the vector and axial current renormalization constants respectively.

These constants can be determined non-perturbatively with lattice calculations in the so-called Regularization Independent – or RI/MOM – scheme [92], which consists in

imposing as a renormalization condition for operator O that the correlation functions of O between external off-shell quark states in a fixed gauge coincide with their tree level value.

Conserved vector current

The need for renormalization of the vector current V_μ can be lifted if one uses the current conserved by the lattice action (2.40). Indeed, the U(1) Noether current of the Wilson action can also be used as a realization of $V_\mu^{(f)}$ on the lattice.

We consider a infinitesimal U(1) local rotation of the fermion fields

$$q(n) \rightarrow [1 + i\alpha(n)] q(n), \quad \bar{q}(n) \rightarrow \bar{q}(n) [1 - i\alpha(n)] \quad (4.38)$$

The variation of the fermionic action Eq. (2.40) at first order in α can be written after some straightforward algebra

$$\delta S_F = -i \sum_{n,\mu} \alpha(n) \Delta_\mu \tilde{V}_\mu^{(f)\text{ cons}}(n) \quad (4.39)$$

with

$$\Delta_\mu \tilde{V}_\mu^{(f)\text{ cons}}(n) \equiv \frac{1}{a} \left[\tilde{V}_\mu^{(f)\text{ cons}}(n) - \tilde{V}_\mu^{(f)\text{ cons}}(n - \mu) \right]$$

and

$$\tilde{V}_\mu^{(f)\text{ cons}}(n) = \frac{1}{2} \left[\bar{q}(n + \mu) (1 + \gamma_\mu) U_\mu^\dagger(n) q(n) - \bar{q}(n) (1 - \gamma_\mu) U_\mu(n) q(n + \mu) \right] \quad (4.40)$$

where $U_\mu(n)$ are the lattice gauge links and γ_μ are the Dirac matrices appearing in the lattice action – i.e. the Euclidean Dirac matrices, defined in Sec. 2.2.1.

Since the lattice action is invariant under such local U(1) rotations, $\tilde{V}_\mu^{(f)\text{ cons}}$ is a lattice *conserved* current, i.e. $\sum_\mu \Delta_\mu \tilde{V}_\mu^{(f)\text{ cons}} = 0$, and hence need not be renormalized – $Z_{V\text{ cons}} = 1$, since the values of its associated charge are algebraically known.

Then, if we consider the lattice expectation value

$$\left\langle N_{\alpha_f}(n_f) \sum_\mu \Delta_\mu \tilde{V}_\mu^{(f)\text{ cons}}(n) \bar{N}_{\alpha_i}(n_i) \right\rangle_U$$

for a given gauge configuration (i.e. with integration on the quark fields only in the functional integral), it satisfies the Ward-Takahashi identity

$$\begin{aligned} \left\langle N_{\alpha_f}(n_f) \sum_\mu \Delta_\mu \tilde{V}_\mu^{(f)\text{ cons}}(n) \bar{N}_{\alpha_i}(n_i) \right\rangle_U = \\ Q^{(f)} \langle N_{\alpha_f}(n_f) \bar{N}_{\alpha_i}(n_i) \rangle_U [\delta^4(n, n_i) - \delta^4(n_f, n)] \end{aligned} \quad (4.41)$$

where $Q^{(f)}$ is the “charge” of the N operator ², i.e.

$$\left[\tilde{V}_0^{(f)\text{cons}}(\mathbf{n}, t), N_\alpha(\mathbf{n}', t) \right] = -Q^{(f)} N_\alpha(\mathbf{n}', t) \delta^3(\mathbf{n} - \mathbf{n}') \quad (4.42)$$

For the usual proton interpolator $N_\alpha(n) = \epsilon_{abc} q_{u\alpha}(n)_a (q_u(n)_b^T C \gamma_5 q_d(n)_c)$, $Q^{(u)} = 2$ and $Q^{(d)} = 1$.

In the case of zero momentum transfer on a nucleon at rest $\mathbf{p}_f = \mathbf{p}_i = \mathbf{0}$, Eq. (4.41) gives

$$\begin{aligned} \sum_{\mathbf{n}_f} \sum_{\mathbf{n}} \left\langle N_{\alpha_f}(n_f) \Delta_0 \tilde{V}_0^{(f)\text{cons}}(\mathbf{n}, t) \bar{N}_{\alpha_i}(n_i) \right\rangle_U = \\ Q^{(f)} \sum_{\mathbf{n}_f} \left\langle N_{\alpha_f}(n_f) \bar{N}_{\alpha_i}(n_i) \right\rangle_U [\delta(t, t_i) - \delta(t_f, t)] \end{aligned} \quad (4.43)$$

which highlights the conservation of the charge operator $\sum_{\mathbf{n}} \tilde{V}_0^{(f)\text{cons}}(\mathbf{n}, t)$.

Stated differently, it gives in momentum space the 3-pt function relations

$$\left\langle N_{\alpha_f}(\mathbf{0}, t_f) \tilde{V}_0^{(f)\text{cons}}(\mathbf{0}, t) \bar{N}_{\alpha_i}(n_i) \right\rangle_U = \left\langle N_{\alpha_f}(\mathbf{0}, t_f) \tilde{V}_0^{(f)\text{cons}}(\mathbf{0}, t') \bar{N}_{\alpha_i}(n_i) \right\rangle_U \quad (4.44)$$

for $t, t' \in]t_i, t_f[$, and

$$\begin{aligned} \left\langle N_{\alpha_f}(\mathbf{0}, t_f) \tilde{V}_0^{(f)\text{cons}}(\mathbf{0}, t) \bar{N}_{\alpha_i}(n_i) \right\rangle_U - \left\langle N_{\alpha_f}(\mathbf{0}, t_f) \tilde{V}_0^{(f)\text{cons}}(\mathbf{0}, t') \bar{N}_{\alpha_i}(n_i) \right\rangle_U \\ = Q^{(f)} \left\langle N_{\alpha_f}(\mathbf{0}, t_f) \bar{N}_{\alpha_i}(n_i) \right\rangle_U \end{aligned} \quad (4.45)$$

for $t \in]t_i, t_f[$ and $t' \in]t_f, T[$.

We insist on the fact that these relations are valid configuration per configuration, and are numerically exact at the precision of the Dirac operator inversions used to compute the contractions (i.e. usually about 10^{-7} or smaller). As such, they provide an invaluable tool to test our computations. Note that similar relations for non-zero momentum transfer can be derived.

We also note that after averaging on gauge configurations, the 3-pt functions give time-ordered vacuum expectation values of the corresponding operators, so that, in the limit

$$t \gg \frac{1}{\Delta}, \quad t_f - t \gg \frac{1}{\Delta}, \quad 2(T - t') \gg \frac{1}{\Delta}$$

with Δ the mass splitting between the nucleon and its first allowed excited-state, the second term of the left-hand side of Eq. (4.45) goes statistically to 0, and

$$\frac{\left\langle N_{\alpha_f}(\mathbf{0}, t_f) \tilde{V}_0^{(f)\text{cons}}(\mathbf{0}, t) \bar{N}_{\alpha_i}(n_i) \right\rangle_U}{\left\langle N_{\alpha_f}(\mathbf{0}, t_f) \bar{N}_{\alpha_i}(n_i) \right\rangle_U} \rightarrow Q^{(f)} = \begin{cases} 2 & \text{for } f = u \\ 1 & \text{for } f = d \end{cases} \quad (4.46)$$

²note that $Q^{(f)}$ is a number, the eigenvalue of the charge operator

Axial current

The chiral rotation symmetry does not hold for the lattice QCD Wilson action even with massless quarks, as the Wilson term in Eq. (2.33)

$$\frac{a^5}{2} \sum_{n,\mu} \bar{q}(n) \partial_\mu^* \partial_\mu q(n)$$

strongly violates chiral symmetry (it is of order $\frac{1}{a}$). It is therefore not possible to define a partially conserved axial current on the lattice with Wilson action.

We choose to use the local axial current $\tilde{A}_\mu^{(f)\text{loc}}(n) = \bar{q}_f(n) \gamma_\mu \gamma_5 q_f(n)$, with the renormalization constants $Z_A(a)$ determined as in [49].

Illustrative results for Z_A for the different values of β are given in Table 4.1. The provided errors are only statistical, and obtained through the bootstrap resampling method. The provided values are averages over the different procedures used to compute Z_A . Note that our values for Z_A are rather close to 1, which is related to the presence of improvement and smearing in our lattice action [33].

The systematic uncertainty that they carry can therefore be combined in a fully self-consistent approach with the observable of interest (in our case $G_A(0)$) by repeating the calculation for the value of Z_A given by each procedure.

β	Z_A
3.31	0.9206(15)
3.5	0.9468(5)
3.61	0.9632(4)
3.7	0.9707(3)
3.8	0.9756(1)

Table 4.1.: Results for the axial renormalization constant Z_A determined on the lattice in the RI/MOM scheme for each of our values of β .

4.2.2. Spectral decomposition

To extract physical quantities from the correlation functions computed on the lattice, we assume that the latter approximate continuum and infinite volume vacuum expectation values of the form

$$C \equiv \langle \Omega | \mathcal{T} \{ N_{\alpha_f}(\mathbf{p}_f, t_f) O(t) \bar{N}_{\alpha_i}(\mathbf{x}_i, t_i) \} | \Omega \rangle$$

where \mathcal{T} is the time-ordering operator, O is a lattice operator, and the momentum-projected operators are defined as

$$N(\mathbf{p}, t) = \int d\mathbf{x} e^{-i\mathbf{p}\cdot\mathbf{x}} N(\mathbf{x}, t) \quad (4.47)$$

As in Sec. 2.4.2, we use the closure relation to obtain the spectral representation of C . Recalling the normalization of momentum states

$$\langle \mathbf{p}', s' | \mathbf{p}, s \rangle = \mathcal{N}(\mathbf{p}) \delta^3(\mathbf{p}' - \mathbf{p}) \delta(s', s)$$

where $\mathcal{N}(\mathbf{p}) = 2 E_{\mathbf{p}} (2\pi)^3$, the closure is

$$\sum_{s=\pm\frac{1}{2}} \int \frac{d\mathbf{p}}{\mathcal{N}(\mathbf{p})} |\mathbf{p}, s\rangle \langle \mathbf{p}, s| = \mathbf{1} \quad (4.48)$$

For $t_f > t > t_i$, $C = \langle \Omega | N_{\alpha_f}(\mathbf{p}_f, t_f) O(t) \bar{N}_{\alpha_i}(\mathbf{n}_i, t_i) | \Omega \rangle$, so that assuming that both $(t_f - t)$ and $(t - t_i)$ are so large that the intermediate states are dominated by the nucleon (ground) state, we can write

$$C = \sum_{s, s'} \int \frac{d\mathbf{p}'}{\mathcal{N}(\mathbf{p}')} \frac{d\mathbf{p}}{\mathcal{N}(\mathbf{p})} T(t_f, t, t_i) \quad (4.49)$$

$$\langle \Omega | N_{\alpha_f}(\mathbf{p}_f, 0) | \mathbf{N}, \mathbf{p}', s' \rangle \langle \mathbf{N}, \mathbf{p}', s' | O | \mathbf{N}, \mathbf{p}, s \rangle \langle \mathbf{N}, \mathbf{p}, s | \bar{N}_{\alpha_i}(\mathbf{x}_i, 0) | \Omega \rangle$$

where the time factor is

$$T(t_f, t, t_i) = \exp[-E_{\mathbf{p}'}(t_f - t) - E_{\mathbf{p}}(t - t_i)] \quad (4.50)$$

The overlap matrix elements can be written

$$\langle \mathbf{N}, \mathbf{p}, s | \bar{N}_{\alpha_i}(\mathbf{x}_i, 0) | \Omega \rangle = z(p) e^{-i\mathbf{p}\cdot\mathbf{x}_i} \bar{u}(\mathbf{p}, s) \quad (4.51)$$

$$\langle \Omega | N_{\alpha_f}(\mathbf{x}_f, 0) | \mathbf{N}, \mathbf{p}', s' \rangle = z(p')^* e^{i\mathbf{p}'\cdot\mathbf{x}_f} u(\mathbf{p}', s')$$

where u is a nucleon Dirac spinor.

We insist on the fact that u is solution of the free Dirac equation *consistent* with the action. Here, we use the Euclidean QCD action, so that the Dirac equation writes

$$\left[-\gamma_0^E \sqrt{\mathbf{p}^2 + M_N^2} + i\gamma^E \cdot \mathbf{p} + M_N \right] u(\mathbf{p}, s) = 0 \quad (4.52)$$

$$\bar{u}(\mathbf{p}, s) \left[-\gamma_0^E \sqrt{\mathbf{p}^2 + M_N^2} + i\gamma^E \cdot \mathbf{p} + M_N \right] = 0$$

where the Dirac matrices $\gamma_\mu^E = \gamma^{E\mu} = \gamma^{E\mu\dagger}$ are the Euclidian Dirac matrices used in the action and which satisfy $\{\gamma_\mu^E, \gamma_\nu^E\} = 2\delta_{\mu\nu}\mathbf{1}$.

For convenience we define the phase factor

$$\eta^\mu = \begin{cases} 0 & \mu = 0 \\ 1 & \mu = 1, 2, 3 \end{cases}, \quad \eta_\mu = \begin{cases} 0 & \mu = 0 \\ -1 & \mu = 1, 2, 3 \end{cases} \quad (4.53)$$

which allows us to define Euclidean 4-vectors according to³

$$a_E^\mu = (-i)^{\eta^\mu} a^\mu, \quad a_{\mu E} = (-i)^{\eta_\mu} a_\mu \quad (4.54)$$

³Beware that the phase factor is on the Minkowski side of the equation because it is on that side that the distinction between covariant and contravariant components makes sense.

and analogously for a tensor of higher rank. Obviously $a_E^\mu = a_{E\mu}$ and the metric is $g_E^{\mu\nu} = \delta_{\mu\nu}$. Note that $a^E \cdot b^E \equiv a \cdot b$. The Dirac equation (4.52) becomes

$$\begin{aligned} [\gamma^E \cdot p^E - M_N] u(\mathbf{p}, s) &= 0 \\ \bar{u}(\mathbf{p}, s) [\gamma^E \cdot p^E - M_N] &= 0 \end{aligned} \quad (4.55)$$

with $p^E = \{E_{\mathbf{p}} = \sqrt{\mathbf{p}^2 + M_N^2}, -i\mathbf{p}\}$. We choose the normalization $\bar{u}(\mathbf{p}, s)u(\mathbf{p}, s') = 2M_N \delta_{ss'}$ so that we have the sum rule

$$\sum_s u(\mathbf{p}, s) \bar{u}(\mathbf{p}, s) = \gamma^E \cdot p^E + M_N. \quad (4.56)$$

The matrix element of the operator O can be parametrized as

$$\langle N, \mathbf{p}', s' | O | N, \mathbf{p}, s \rangle = \bar{u}(\mathbf{p}', s') W(p', p) u(\mathbf{p}, s) \quad (4.57)$$

where the matrix $W(p', p)$ depends on the way the operator is actually implemented in the lattice simulation. Finally the correlator (4.49) writes

$$\begin{aligned} C = \int \frac{d\mathbf{p}'}{\mathcal{N}(\mathbf{p}')} \frac{d\mathbf{p}}{\mathcal{N}(\mathbf{p})} T(t_f, t, t_i) z(p)^* z(p') (2\pi)^3 \delta^3(\mathbf{p}' - \mathbf{p}_f) \\ (\gamma^E \cdot p'^E + M_N) W(p', p) (\gamma^E \cdot p^E + M_N) e^{-i\mathbf{p} \cdot \mathbf{x}_i} \end{aligned} \quad (4.58)$$

This is the master formula that will be used in the following.

2-pt function

If we choose $O(t) = \mathbf{1}$, we get the 2-point correlator as a special case. We have

$$\langle N, \mathbf{p}', s' | \mathbf{1} | N, \mathbf{p}, s \rangle = \mathcal{N}(\mathbf{p}) \delta^3(\mathbf{p}' - \mathbf{p}) \delta(s', s) = \frac{\bar{u}(\mathbf{p}, s') u(\mathbf{p}, s)}{2M_N} \mathcal{N}(\mathbf{p}) \delta^3(\mathbf{p}' - \mathbf{p}) \quad (4.59)$$

so

$$W(p', p) = \frac{\mathcal{N}(\mathbf{p}) \delta^3(\mathbf{p}' - \mathbf{p})}{2M_N} \quad (4.60)$$

and we get

$$\begin{aligned} C_2(\mathbf{p}_f, t_f; \mathbf{x}_i, t_i) &= \langle \Omega | \mathcal{T} \{ N_{\alpha_f}(\mathbf{p}_f, t_f) \bar{N}_{\alpha_i}(\mathbf{x}_i, t_i) \} | \Omega \rangle \\ &= \frac{(2\pi)^3}{\mathcal{N}(\mathbf{p}_f)} |z(p_f)|^2 (\gamma^E \cdot p_f^E + M_N) e^{-i\mathbf{p}_f \cdot \mathbf{x}_i} e^{-E_{\mathbf{p}_f}(t_f - t_i)} \end{aligned} \quad (4.61)$$

In the following we shall set $\mathbf{x}_i = 0$ and define the traced quantity

$$\begin{aligned} \bar{C}_2(\mathbf{p}_f, t_f; \mathbf{0}, t_i) &= \frac{1}{4} \text{Tr} \left[\frac{(\gamma^E \cdot p_f^E + M_N)}{2M_N} C_2(\mathbf{p}_f, t_f; \mathbf{0}, t_i) \right] \\ &= \frac{M_N (2\pi)^3 |z(p_f)|^2}{\mathcal{N}(\mathbf{p}_f)} e^{-E_{\mathbf{p}_f}(t_f - t_i)} \\ &= \frac{M_N}{2E_{\mathbf{p}_f}} |z(p_f)|^2 e^{-E_{\mathbf{p}_f}(t_f - t_i)} \end{aligned} \quad (4.62)$$

3-pt function

The operator which we insert in the 3-point correlator is

$$O(t) = \int d\mathbf{x} e^{-i\mathbf{k}\cdot\mathbf{x}} J(\mathbf{x}, t) \quad (4.63)$$

where J is the vector or axial current, denoted for simplicity J^μ and J_5^μ respectively in the following.

Recalling the parametrizations of the current matrix elements in term of the corresponding form factors (Eqs. 4.12 and 4.28), we have

$$\langle N, \mathbf{p}', s' | J^\mu(0) | N, \mathbf{p}, s \rangle = \bar{u}(\mathbf{p}', s') \left[\gamma^{E\mu} G_M(k^2) - \frac{(p'^E + p^E)^\mu}{2M_N} F_2(k^2) \right] u(\mathbf{p}, s)$$

$$\langle N, \mathbf{p}', s' | J_5^\mu(0) | N, \mathbf{p}, s \rangle = \bar{u}(\mathbf{p}', s') \left[\gamma^{E\mu} G_A(k^2) + \frac{(p'^E - p^E)^\mu}{2M_N} G_P(k^2) \right] \gamma_5^E u(\mathbf{p}, s)$$

with $J^\mu = V^\mu$ and $J_5^\mu = A^\mu$ (p^{-n}) and where the u spinors are now Euclidean Dirac spinors. The W matrices are then:

$$\begin{aligned} W^\mu(p', p) &= (2\pi)^3 \delta^3(\mathbf{p}' - \mathbf{p} - \mathbf{k}) \Gamma^\mu(p', p), \\ \text{with } \Gamma^\mu(p', p) &= \gamma^{E\mu} G_M(k^2) - \frac{(p'^E + p^E)^\mu}{2M_N} F_2(k^2) \end{aligned} \quad (4.64)$$

for the vector current and

$$\begin{aligned} W_5^\mu(p', p) &= (2\pi)^3 \delta^3(\mathbf{p}' - \mathbf{p} - \mathbf{k}) \Gamma^{\mu 5}(p', p), \\ \text{with } \Gamma_5^\mu(p', p) &= \left[\gamma^{E\mu} G_A(k^2) + \frac{(p'^E - p^E)^\mu}{2M_N} G_P(k^2) \right] \gamma_5^E \end{aligned} \quad (4.65)$$

for the axial current.

Inserted into Eq. (4.58), they give the spectral decompositions of the 3-pt correlators

$$C_3^\mu(\mathbf{p}_f, t_f; t; \mathbf{p}_i = \mathbf{p}_f - \mathbf{k}, t_i) = \frac{z(\mathbf{p}_f)^* z(\mathbf{p}_i)}{4E_i E_f} T(t_f, t, t_i) \quad (4.66)$$

$$\begin{aligned} & (\gamma^E \cdot p_f^E + M_N) \Gamma^\mu(p_f, p_i) (\gamma^E \cdot p_i^E + M_N) \\ C_{3,5}^\mu(\mathbf{p}_f, t_f; t; \mathbf{p}_i = \mathbf{p}_f - \mathbf{k}, t_i) &= \frac{z(\mathbf{p}_f)^* z(\mathbf{p}_i)}{4E_i E_f} T(t_f, t, t_i) \quad (4.67) \\ & (\gamma^E \cdot p_f^E + M_N) \Gamma^{\mu,5}(p_f, p_i) (\gamma^E \cdot p_i^E + M_N) \end{aligned}$$

where $E_{i,f} \equiv E_{\mathbf{p}_{i,f}}$ and

$$T(t_f, t, t_i) = \exp[-E_f(t_f - t) - E_i(t - t_i)].$$

4.2.3. Form factor extraction

To remove the time dependence and the overlap z factors of the 3-pt function, we consider

$$R(\mathbf{p}, t) \equiv \frac{\bar{C}_2(\mathbf{p}, t_f - t + t_i; \mathbf{0}, t_i)}{\bar{C}_2(\mathbf{p}, t + t_i; \mathbf{0}, t_i)\bar{C}_2(\mathbf{p}, t_f + t_i; \mathbf{0}, t_i)} = \frac{2E_{\mathbf{p}}}{M_N |z(p)|^2} e^{2E_{\mathbf{p}}t}$$

and

$$\frac{C_{3,(5)}^\mu(\mathbf{p}_f, t_f + t_i; t + t_i; \mathbf{p}_i, t_i)}{\bar{C}_2(\mathbf{p}_f, t_f + t_i; \mathbf{0}, t_i)} = \frac{z(p_i)}{2z(p_f)M_N E_i} e^{-(E_i - E_f)t} (\gamma^E \cdot p_f^E + M_N) \Gamma_{(5)}^\mu(p_f, p_i) (\gamma^E \cdot p_i^E + M_N)$$

so that if we define the ratio

$$G_{(5)}^\mu(\mathbf{p}_f, \mathbf{p}_i) \equiv \frac{\mathcal{P}(p_f) C_{3,(5)}^\mu(\mathbf{p}_f, t_f + t_i; t + t_i; \mathbf{p}_i, t_i) \mathcal{P}(p_i)}{\bar{C}_2(\mathbf{p}_f, t_f + t_i; \mathbf{0}, t_i)} \sqrt{\frac{R(\mathbf{p}_i, t)}{R(\mathbf{p}_f, t)}} \quad (4.68)$$

where $\mathcal{P}(p)$ is the projector

$$\mathcal{P}(p) = \frac{(\gamma^E \cdot p^E + M_N)}{2M_N} \quad (4.69)$$

we have

$$G_{(5)}^\mu(\mathbf{p}_f, \mathbf{p}_i) = \frac{|z(p_f)| z(p_i)}{|z(p_i)| z(p_f)} \frac{1}{2M_N \sqrt{E_i E_f}} (\gamma^E \cdot p_f^E + M_N) \Gamma_{(5)}^\mu(p_f, p_i) (\gamma^E \cdot p_i^E + M_N).$$

The phases of $z(p_i), z(p_f)$ are equal so that our working expression is

$$G_{(5)}^\mu(\mathbf{p}_f, \mathbf{p}_i) = \frac{1}{2M_N \sqrt{E_i E_f}} (\gamma^E \cdot p_f^E + M_N) \Gamma_{(5)}^\mu(p_f, p_i) (\gamma^E \cdot p_i^E + M_N). \quad (4.70)$$

Note that explicit projection onto the nucleon positive energy states with $\mathcal{P}(p)$ in Eqs. 4.62 and 4.68 is used to reduce the contamination by negative parity excited states.

$G_{(5)}^\mu$ is time-independent when only the nucleon ground state contributes. In practice, contaminations from excited states are exponentially suppressed as the lattice time increases, so that when plotted as a function of t , $G_{(5)}^\mu$ exhibits a plateau for ts with $(T - t_f)$, $(t_f - t)$ and $(t - t_i)$ large enough.

To extract the required form factors, we then take appropriate covariant traces and get the equations:

$$\frac{1}{4} \text{Tr} [G^\mu(\mathbf{p}_f, \mathbf{p}_i)] P^{E\mu} = \frac{P^2}{2\sqrt{E_i E_f}} G_E \quad (4.71)$$

$$\frac{1}{4} \text{Tr} [\gamma_5^E \gamma^{E\nu} G^\mu(\mathbf{p}_f, \mathbf{p}_i)] \varepsilon^{\nu\mu\rho\sigma} p_f^{E\rho} p_i^{E\sigma} = i \frac{k^2 P^2}{4M_N \sqrt{E_i E_f}} G_M \quad (4.72)$$

for the electromagnetic form factors, and

$$\frac{1}{4}\text{Tr} [\gamma^{E\nu} G_5^\mu(\mathbf{p}_f, \mathbf{p}_i)] \varepsilon^{\nu\mu\rho\sigma} p_f^{E\rho} p_i^{E\sigma} = i \frac{k^2 P^2}{4M_N \sqrt{E_i E_f}} G_A \quad (4.73)$$

$$\frac{1}{4}\text{Tr} [\gamma_5^E \gamma^{E\mu} G_5^\mu(\mathbf{p}_f, \mathbf{p}_i)] = \frac{3M_N}{\sqrt{E_i E_f}} \left(G_A + \frac{k^2}{12M_N^2} (G_P - 2G_A) \right) \quad (4.74)$$

for the axial ones, where summation over the repeated Greek indices is implied and $P = p_f + p_i$ and $k = p_f - p_i$ ($k^2 < 0$). We stress the fact that the Levi-Civita tensor is the Euclidean one, defined with Eq. (4.54).

Note that working with fully covariant traced equations requires the computation of the whole Dirac $G_{(5)}^\mu$ matrix (i.e. we need the 16 α_f, α_i combinations), and is therefore more expensive than the usual “component-per-component” equations. However, in addition to the improved statistics, this is expected to restore Lorentz invariance more efficiently.

4.2.4. Excited states

As mentioned above, the information extracted from $G_{(5)}^\mu$ is dominated by the nucleon to nucleon matrix element term as long as $(T - t_f)$, $(t_f - t)$ and $(t - t_i)$ are sufficiently large. However, the need to annihilate the nucleon a time t_f where the signal still dominates the noise imposes restriction on the time extents that we can use. Because of the relatively limited time extents involved in practice, the signal can be contaminated by excited states contributions which may lead to a systematic bias in the extraction of form factors from the “plateau” fit of $G_{(5)}^\mu$.

To account for these excited states contributions, several methods such as the *summed operator insertion method* [93] or *Generalized Eigenvalue Problem*-based (GEVP) methods [94–96] have for example been introduced.

We choose to assess excited states contaminations in our analysis by directly taking into account the first excited state contribution in the fit of the time-dependence of $G_{(5)}^\mu$.

As we can see in Fig.4.5, which shows the corresponding effective mass for the lowest Q^2 of our physical pion mass ensemble, the \bar{C}_2 ratio

$$\sqrt{\frac{R(\mathbf{p}_i, t)}{R(\mathbf{p}_f, t)}}$$

does not seem strongly contaminated by excited states, and its spectral decomposition appears dominated by the $e^{(E_{\mathbf{p}_i} - E_{\mathbf{p}_f})t}$ term. We can therefore safely neglect the excited states contributions coming from this term and only consider the ones introduced by $C_{3,(5)}^\mu$. This is not surprising, as for $\mathbf{p}_i = \mathbf{p}_f$, the ratio gives exactly 1, so that excited states can only enter as corrective recoil effects, of order p^2/M_N^2 .

Excited state contributions therefore arise from terms beyond the nucleon ground state one in the spectral decomposition of $C_{3,(5)}^\mu$. We recall that $G_{(5)}^\mu$ is constructed with

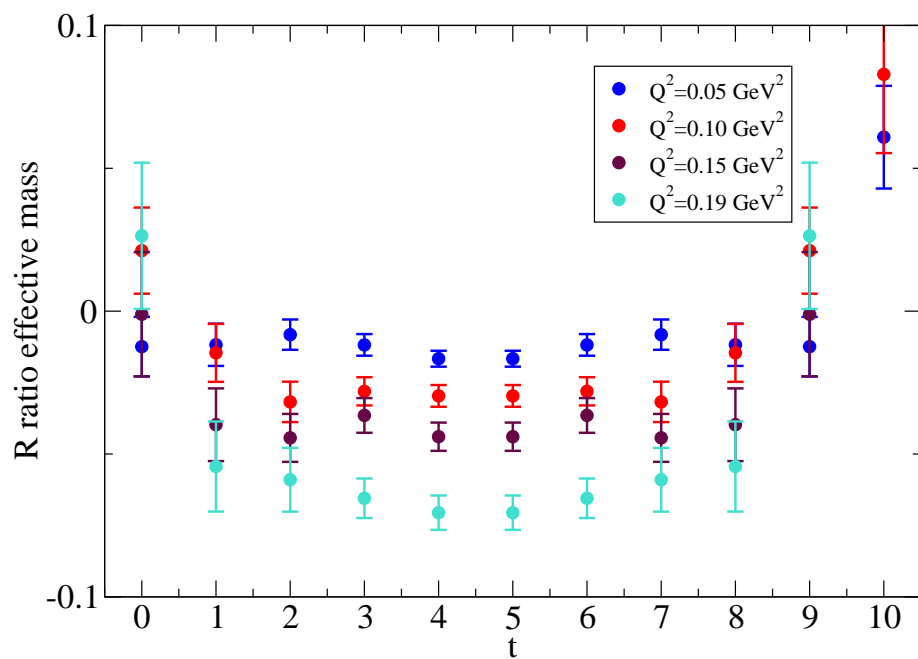


Figure 4.5.: Effective mass for the ratio $\sqrt{\frac{R(\mathbf{p}_i,t)}{R(\mathbf{p}_f,t)}}$ plotted against the lattice time for the lowest Q^2 of our physical pion mass ensemble.

$C_{3,(5)}^\mu$ projected at the source and sink onto the positive energy states with $\mathcal{P}(\mathbf{p}_i)$ and $\mathcal{P}(\mathbf{p}_f)$ respectively.

At zero momentum, this projector also selects the positive parity states, and removes the negative parity ones. We have also checked that in practice, it also eliminates negative parity states for non-zero momenta, which is theoretically expected as long as the momenta are small compared to the masses of the ground and negative parity state masses.

Therefore, we include in the 3-pt function spectral decomposition contributions coming from the first positive parity state, and write, taking $t_i = 0$,

$$G_{(5)}^\mu(\mathbf{p}_f, \mathbf{p}_i; t) = A(\mathbf{p}_f, \mathbf{p}_i) + B(\mathbf{p}_f, \mathbf{p}_i) e^{-\Delta(\mathbf{p}_i)t} + C(\mathbf{p}_f, \mathbf{p}_i) e^{-\Delta(\mathbf{p}_f)(t_f-t)} + D(\mathbf{p}_f, \mathbf{p}_i) e^{-\Delta(\mathbf{p}_f)(t_f-t) - \Delta(\mathbf{p}_i)t} \quad (4.75)$$

where A , B , C , and D are time-independent, and

$$\Delta(\mathbf{p}) \equiv E_{\mathbf{p}}^* - E_{\mathbf{p}}$$

with $E_{\mathbf{p}}^*$ the energy of the lowest positive parity excited state of the nucleon with momentum \mathbf{p} .

Up to effects of order p^2/M^2 with $\mathbf{p} = \mathbf{p}_i, \mathbf{p}_f$ and $M = M_N, M_N^*$, the last “ D ” term in Eq. (4.75) is also a constant, exponentially suppressed with $e^{-\Delta(\mathbf{p}_f)t_f}$, so that it can be safely neglected and we are left with the three first terms.

The time-dependence of $G_{(5)}^\mu$ directly propagates to the *effective* form factors as defined in Eqs.4.71, 4.72, 4.73 and 4.74, which we can therefore fit with a function of the form:

$$A(\mathbf{p}_f, \mathbf{p}_i) + B(\mathbf{p}_f, \mathbf{p}_i) e^{-\Delta(\mathbf{p}_i)t} + C(\mathbf{p}_f, \mathbf{p}_i) e^{-\Delta(\mathbf{p}_f)(t_f-t)} \quad (4.76)$$

and then extract the relevant nucleon ground state form factor from the constant part $A(\mathbf{p}_f, \mathbf{p}_i)$.

In practice, fitting the time-dependence with $\Delta(\mathbf{p})$ as a free parameter is difficult because of the small available lattice time extents and the sometimes important statistical errors which make non-linear fits challenging. Consequently, we determine the energy splitting $\Delta(\mathbf{p})$ from the time-dependence of the 2-pt correlation function \bar{C}_2 , using the variable projection algorithm [97, 98] presented in Appendix E, which allows us to extract the first (positive parity) nucleon excited state mass in addition to the ground one from the time-dependence of the \bar{C}_2 correlator.

Using this input for the splitting $\Delta(\mathbf{p})$, we can then proceed to the linear fit of the effective form factors with 4.76 in the whole available lattice time range, just taking care to avoid contact terms at $t = 0(, 1)$ and $t = t_f(, t_f - 1)$ where the additional times in brackets pertain to the non-local current case.

4.3. Lattice calculation details

4.3.1. Ensembles, kinematics and parameters

We perform our calculation using gauge configuration ensembles introduced in Sec. 2.4.1. The pion masses range from about 500 MeV down to 138 MeV, with lattice spacings going

from about 0.12 fm down to 0.05 fm.

Computation of the nucleon 3-pt functions is done in the rest frame $-\mathbf{p}_f = 0$ – to save CPU (as the momentum of the “generalized propagator” defined in Sec. 4.3.2 is fixed to 0) and to allow for reasonably small squared momentum transfers.

The use of the Breit frame $-\mathbf{p}_f = -\mathbf{p}_i$ was considered, since the kinematics in this frame greatly simplifies the extraction of the form factors from the 3-pt function. However, in addition to the high CPU cost needed to compute the correlators for each \mathbf{p}_f , this has the drawback that the discretization of momenta allowed on the lattice imposes momentum transfers twice as big as the for the rest frame case, which is strongly disabling if one wants to extract the electric or axial radii.

The nucleon sink time t_f has to be chosen as large as possible to ensure appearance of a clear plateau in the 3-pt correlation function, with small contamination from excited states. However, to obtain satisfactory errors on the results, we need to make compromises between the removal of these unwanted excited state contaminations and the quickly exploding noise which shows up in baryon correlation functions as the lattice time increases. Thus, we choose a sink time of about 1.15 fm in physical units.

4.3.2. Contractions and smearing

Contractions

To build the ratio $G_{(5)}^\mu$, we need to compute the 2-pt and 3-pt correlation functions

$$\tilde{C}_2(\mathbf{p}_f, t_f; \mathbf{x}_i, t_i) \equiv \langle N_{\alpha_f}(\mathbf{p}_f, t_f) \bar{N}_{\alpha_i}(\mathbf{n}_i, t_i) \rangle \quad (4.77)$$

$$\tilde{C}_3^{(f)}(\mathbf{p}_f, t_f; t; \mathbf{p}_i, t_i) \equiv \langle N_{\alpha_f}(\mathbf{p}_f, t_f) J^{(f)}(m, n) \bar{N}_{\alpha_i}(\mathbf{n}_i, t_i) \rangle \quad (4.78)$$

on the lattice, where $N_\alpha(\mathbf{p}, t)$ now denotes the lattice proton interpolator

$$N_\alpha(\mathbf{p}, t) = \sum_{\mathbf{n}} e^{-i\mathbf{p}\cdot\mathbf{n}} N_\alpha(\mathbf{n}, t), \quad \mathbf{p} \in \frac{2\pi}{L}\mathbb{Z}^3$$

with $N_\alpha(\mathbf{n}, t) \equiv \epsilon_{abc} q_{u\alpha}^a(n) \left(q_u^b T(n) C \gamma_5 q_d^c(n) \right)$

with $C = i\gamma_2\gamma_0$ the charge conjugation matrix, and where $J^{(f)}(m, n)$ is a possibly non-local lattice current of the form

$$J^{(f)}(m, n) = \bar{q}_f(m) \Gamma(m, n) q_f(n)$$

where Γ is a general “spinor matrix”, i.e. $\Gamma_{\alpha\alpha'}$.

We evaluate these correlators on the lattice as sums of products of quark propagators, using Wick’s theorem [38].

The Wick contraction formula gives for the 2-pt function

$$\begin{aligned} \tilde{C}_2(\mathbf{p}_f, t_f; \mathbf{x}_i, t_i) = \sum_{\mathbf{n}_f} e^{-i\mathbf{p}_f \cdot \mathbf{n}_f} \epsilon_{abc} \epsilon_{a'b'c'} (C\gamma_5)_{\alpha\beta} (C\gamma_5)_{\alpha'\beta'} D_d^{-1}(n_f, n_i)_{\beta\beta'} \\ \left\{ D_u^{-1}(n_f, n_i)_{\alpha\alpha'} D_u^{-1}(n_f, n_i)_{\alpha_f\alpha_i} + D_u^{-1}(n_f, n_i)_{\alpha_f\alpha'} D_u^{-1}(n_f, n_i)_{\alpha\alpha_i} \right\} \end{aligned} \quad (4.79)$$

where $D_{(f)}^{-1}$ is the lattice flavour f quark propagator, the Greek letters are spinor indices, the Latin letters are color indices and summation over repeated indices is implied.

The Wick contractions for the 3-pt function depend on the flavour of the inserted current. Moreover, they contain quark-disconnected contributions, of the form

$$\left\langle N_{\alpha_f}(\mathbf{n}_f, t_f) J^{(f)}(m, n) \bar{N}_{\alpha_i}(\mathbf{n}_i, t_i) \right\rangle_{\text{disc}} = \text{Tr}[D_{(f)}^{-1}(n, m) \Gamma(m, n)] \left\langle N_{\alpha_f}(\mathbf{n}_f, t_f) \bar{N}_{\alpha_i}(\mathbf{n}_i, t_i) \right\rangle \quad (4.80)$$

We only compute the connected parts, and therefore drop contributions like the one above. This introduces a systematic bias in our calculation, except if we consider the isovector combinations $J = V_\mu^{(p-n)}$ or $A_\mu^{(p-n)}$, for which the disconnected contractions cancel out, since we work in the isospin limit $m_u = m_d$.

The connected contributions are written

$$\begin{aligned} \tilde{C}_3^{(u)}(\mathbf{p}_f, t_f; t; \mathbf{p}_i, t_i) = \sum_{\mathbf{n}_f} e^{-i\mathbf{p}_f \cdot \mathbf{n}_f} \epsilon_{abc} \epsilon_{a'b'c'} D_u^{-1}(n_f, m)_{cd}^{\alpha\gamma} [\Gamma(m, n) D_u^{-1}(n, n_i)]_{d'c'}^{\gamma\rho} \\ \left\{ \delta_{\alpha_f\alpha} \text{Tr} [D_u^{-1}(n_f, n_i)_{aa'} \Delta_d^T(n_f, n_i)_{bb'}] \delta_{\rho\alpha_i} \right. \\ + \delta_{\alpha_f\alpha} [\Delta_d^T(n_f, n_i)_{bb'} D_u^{-1}(n_f, n_i)_{aa'}]_{\rho\alpha_i} \\ + [D_u^{-1}(n_f, n_i)_{aa'} \Delta_d^T(n_f, n_i)_{bb'}]_{\alpha_f\alpha} \delta_{\rho\alpha_i} \\ \left. + D_u^{-1}(n_f, n_i)_{\alpha_f\alpha_i} \Delta_d^T(n_f, n_i)_{\rho\alpha} \right\} \end{aligned} \quad (4.81)$$

for $J^{(f)} = J^{(u)}$, and

$$\begin{aligned} \tilde{C}_3^{(d)}(\mathbf{p}_f, t_f; t; \mathbf{p}_i, t_i) = \sum_{\mathbf{n}_f} e^{-i\mathbf{p}_f \cdot \mathbf{n}_f} \epsilon_{abc} \epsilon_{a'b'c'} D_d^{-1}(n_f, m)_{cd}^{\alpha\gamma} [\Gamma(m, n) D_d^{-1}(n, n_i)]_{d'c'}^{\gamma\rho} \\ \left\{ [D_u^{-1}(n_f, n_i)_{aa'} (C\gamma_5)]_{\alpha_f\rho} [(C\gamma_5)^T D_u^{-1}(n_f, n_i)_{bb'}]_{\alpha\alpha_i} \right. \\ \left. + D_u^{-1}(n_f, n_i)_{\alpha_f\alpha_i} \Delta_u^T(n_f, n_i)_{\rho\alpha} \right\} \end{aligned} \quad (4.82)$$

for $J^{(f)} = J^{(d)}$, where we have defined $\Delta_{(f)}(n_f, n_i)_{\alpha\beta} \equiv [(C\gamma_5) D_{(f)}^{-1}(n_f, n_i)_{ab} (C\gamma_5)^T]_{\alpha\beta}$, and where traces, products $[\cdot]$ and transpositions run on spinor indices.

We see, as expected, that the contractions for the 3-pt functions involve propagation of a quark from every m to n_f , which naively requires all-to-all propagators. However, to circumvent the prohibitive cost of computation full all-to-all propagators, we use the technique of so-called “generalized propagators” introduced in [99]. Indeed, in our application, we do not request the 3-pt function for all \mathbf{p}_f, t_f . Fixing \mathbf{p}_f and t_f , the idea is to compute directly the propagation of a diquark from n_i and a quark from m , both going to \mathbf{p}_f .

Formally, we define the generalized propagators $P_{G(f)}(\mathbf{p}_f, t_f, \alpha_f; m; n_i, \alpha_i)_{c'd}^{\rho\gamma}$ for $(f) = u, d$ as

$$\begin{aligned}
P_{Gu}(\mathbf{p}_f, t_f, \alpha_f; m; n_i, \alpha_i)_{c'd}^{\rho\gamma} &\equiv \sum_{\mathbf{n}_f} e^{-i\mathbf{p}_f \cdot \mathbf{n}_f} \epsilon_{abc} \epsilon_{a'b'c'} D_u^{-1}(n_f, m)_{cd}^{\alpha\gamma} \\
&\quad \left\{ \delta_{\alpha_f \alpha} \text{Tr} [D_u^{-1}(n_f, n_i)_{aa'} \Delta_d^T(n_f, n_i)_{bb'}] \delta_{\rho\alpha_i} \right. \\
&\quad + \delta_{\alpha_f \alpha} [\Delta_d^T(n_f, n_i)_{bb'} D_u^{-1}(n_f, n_i)_{aa'}]_{\rho\alpha_i} \\
&\quad + [D_u^{-1}(n_f, n_i)_{aa'} \Delta_d^T(n_f, n_i)_{bb'}]_{\alpha_f \alpha} \delta_{\rho\alpha_i} \\
&\quad \left. + D_u^{-1}(n_f, n_i)_{\alpha_f \alpha_i} \Delta_d^T(n_f, n_i)_{\rho\alpha} \right\}
\end{aligned} \tag{4.83}$$

$$\begin{aligned}
P_{Gd}(\mathbf{p}_f, t_f, \alpha_f; m; n_i, \alpha_i)_{c'd}^{\rho\gamma} &\equiv \sum_{\mathbf{n}_f} e^{-i\mathbf{p}_f \cdot \mathbf{n}_f} \epsilon_{abc} \epsilon_{a'b'c'} D_d^{-1}(n_f, m)_{cd}^{\alpha\gamma} \\
&\quad \left\{ [D_u^{-1}(n_f, n_i)_{aa'} (C\gamma_5)]_{\alpha_f \rho} [(C\gamma_5)^T D_u^{-1}(n_f, n_i)_{bb'}]_{\alpha\alpha_i} \right. \\
&\quad \left. + D_u^{-1}(n_f, n_i)_{\alpha_f \alpha_i} \Delta_d^T(n_f, n_i)_{\rho\alpha} \right\}
\end{aligned} \tag{4.84}$$

so that

$$\tilde{C}_3^{(f)}(\mathbf{p}_f, t_f; t; \mathbf{p}_i, t_i) = P_{G(f)}(\mathbf{p}_f, t_f, \alpha_f; m; n_i, \alpha_i)_{c'd}^{\rho\gamma} \left[\Gamma(m, n) D_{(f)}^{-1}(n, n_i) \right]_{\gamma\rho}^{\alpha\alpha_i} \tag{4.85}$$

We write

$$P_{G(f)}(\mathbf{p}_f, t_f, \alpha_f; m; n_i, \alpha_i)_{c'd}^{\rho\gamma} \equiv \sum_{\mathbf{n}_f} e^{-i\mathbf{p}_f \cdot \mathbf{n}_f} B_{(f)}(n_f, \alpha_f; n_i, \alpha_i)_{c'e}^{\rho\alpha} D_{(f)}^{-1}(n_f, m)_{cd}^{\alpha\gamma}$$

and using the Dirac operator γ_5 -hermiticity:

$$D_{(f)}^{-1}(n_f, m)_{cd}^{\alpha\gamma} = \gamma_5 \alpha_{\alpha'} D_{(f)}^{-1}(m, n_f)_{\gamma'\alpha'}^* \gamma_5 \gamma'\gamma_{dc}$$

we get

$$P_{G(f)}(\mathbf{p}_f, t_f, \alpha_f; m; n_i, \alpha_i)_{c'd}^{\rho\gamma} = C_{(f)}(\mathbf{p}_f, t_f, \alpha_f; m; n_i, \alpha_i)_{\gamma'\rho}^* \gamma_5 \gamma'\gamma_{dc} \tag{4.86}$$

with

$$C_{(f)}(\mathbf{p}_f, t_f, \alpha_f; m; n_i, \alpha_i)_{\gamma'\rho}^{dc'} = \sum_{\mathbf{n}_f} e^{i\mathbf{p}_f \cdot \mathbf{n}_f} D_{(f)}^{-1}(m, n_f)_{\gamma'\alpha'}^{dc} [B_{(f)}(n_f, \alpha_f; n_i, \alpha_i)_{c'b}^* \gamma_5]_{\rho\alpha'}$$

It is then straightforward to show that $C_{(f)}(n_f, \alpha_f; m; n_i, \alpha_i)_{\gamma'\rho}^{dc'}$ is solution of the Dirac equation

$$D_{(f)}(m', m)_{\beta\gamma'}^{bd} C_{(f)}(n_f, \alpha_f; m; n_i, \alpha_i)_{\gamma'\rho}^{dc'} = \sum_{\mathbf{n}_f} e^{i\mathbf{p}_f \cdot \mathbf{n}_f} \delta_{m' n_f} [B_{(f)}(n_f, \alpha_f; n_i, \alpha_i)_{c'b}^* \gamma_5]_{\rho\beta} \quad (4.87)$$

so that to compute the generalized propagators, we first compute the generalized sources

$$\sum_{\mathbf{n}_f} e^{i\mathbf{p}_f \cdot \mathbf{n}_f} \delta_{m' n_f} [B_{(f)}(n_f, \alpha_f; n_i, \alpha_i)_{c'b}^* \gamma_5]_{\rho\beta} \quad (4.88)$$

and then invert the Dirac operator with these source terms and build the propagators with the solutions according to Eq. (4.86).

These generalized propagators are then contracted with the usual quark propagators and the current matrices to get the 3-pt function (see Eq. (4.85)).

Smearing

As mentioned in Sec. 2.4.2, to improve the signal in our correlation functions, we can use spatially extended nucleon interpolators, as long as they keep the right quantum numbers. Smearing the nucleon operators then helps improving the overlap between them and the true nucleon states, therefore enhancing the ground state signal. The smearing of interpolators is usually taken as a factorizable function, such that the smearing procedure amounts to a replacement of the local fermion spinors in N_{α_f} and \bar{N}_{α_i} with smeared fermions

$$q_{(f)}^S(\mathbf{n}, t) \equiv \sum_{\mathbf{n}'} S(\mathbf{n}'; \mathbf{n}, t) q_{(f)}(\mathbf{n}', t) \quad (4.89)$$

Since we work in fixed Coulomb gauge, we can use a non-covariant smearing function. We choose a Gaussian spatial distribution at the source and sink,

$$S(\mathbf{n}'; \mathbf{n}, t) = e^{-\frac{(\mathbf{n}' - \mathbf{n})^2}{s^2}} \quad (4.90)$$

where s is the spatial extension of the Gaussian, chosen of order 0.3 fm.

The smearing of the interpolators is in practice obtained with a replacement of the usual local quark propagators by their smeared counterparts, computed by inverting the Dirac equation on an extended source, and then convoluting with the smearing function at the sink.

Note that the smearing of the generalized propagators used to compute the 3-pt function is done similarly by replacing the local propagators with the smeared ones, and by using smeared generalized sources (Eq. (4.88)) in the inversion of Eq. (4.87).

We insist on the fact that the source and sink smearings used within the 2-pt and 3-pt functions must be the same, so that the overlap factors cancel out in the ratio 4.68.

β	t_{\min}	t_{\max}
3.31	2	5
3.5	2	6
3.61	2	6
3.7	4	8

Table 4.2.: Lattice time ranges used to fit the effective form factors plateaus for each β .

4.4. Results

4.4.1. Form factors

In this section, we report our results for the nucleon isovector electromagnetic and axial form factors. The form factor values are extracted with the equations derived in Sec. 4.2.3. More precisely, for each Q^2 , we compute the considered form factor at each lattice time t , using the ratio $G_{(5)}^\mu(t)$.

This *effective* form factor should exhibit a plateau for $(t_f - t)$ and $(t - t_i)$ large enough. However, as mentioned in Sec. 4.2.4, excited-state contributions can still contaminate the signal for our time extents. We then perform a correlated fit of the effective form factor either with a constant within some range, which depends on the value of β for the studied ensemble, or with the functional form (4.76) in the whole range (without the sides). The time fit ranges for the effective form factors plateau are given in Table 4.2. The procedure for the excited state deconvolution fit is described in Sec. 4.2.4; we just recall here that the required energy splitting between the ground state and the first positive parity excited state is extracted from the 2-pt correlator.

The results for both fitting procedures are given in the figures.

The reported – statistical only – errors are obtained with a full bootstrap analysis.

When applicable (i.e. for $G_E^{(p-n)}(Q^2)$, $G_M^{(p-n)}(Q^2)$ and $G_A(Q^2)$), we plot along our lattice results the experimental parametrizations introduced in Sec. 4.1.1, and the fit of the data with a dipole functional form

$$\frac{A}{\left(1 + \frac{Q^2}{M^2}\right)^2} \quad (4.91)$$

in the range $0 \text{ GeV}^2 \leq Q^2 \leq 1 \text{ GeV}^2$.

Note that to improve our statistics, we have used several norm-degenerate momenta to obtain the Q^2 -dependence of the form factors. These degenerate momenta values are all taken into account in the fits, but are averaged over in the plots for the sake of readability.

We also insist on the fact that the presented form factors are raw lattice results, with finite volume and lattice spacing. The study of the finite volume effects and the continuum extrapolation shall only be performed for the nucleon electric radius and for the axial charge in a later section, as these are the two main quantities of interest of this thesis.

Electric form factor

We show the results for the isovector electric nucleon form factor $G_E^{(p-n)}(Q^2)$ for each ensemble in Figs. 4.7 and 4.8. Fig. 4.6 shows an example of plateaus exhibited by our data at the physical point for several Q^2 .

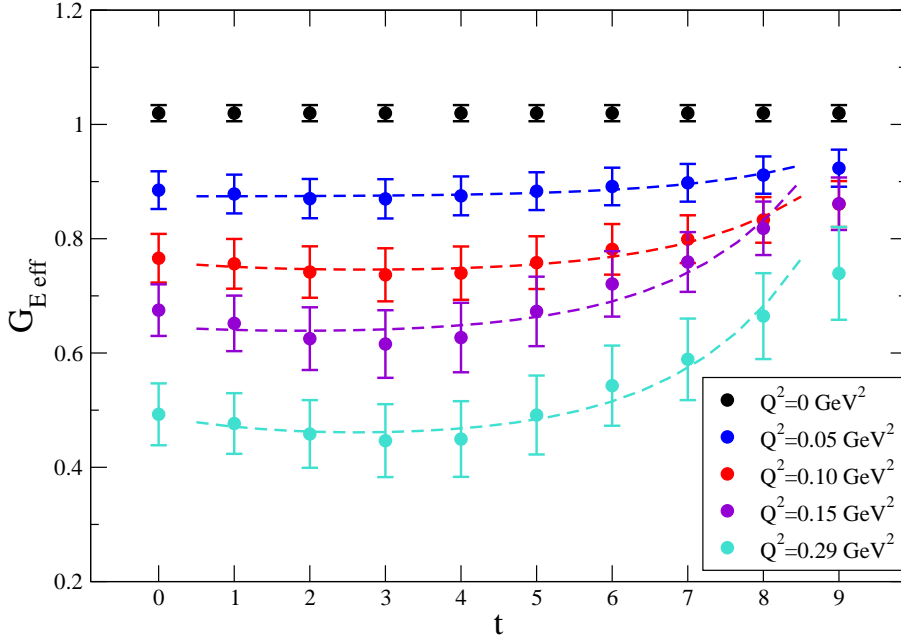


Figure 4.6.: Examples of plateaus for $G_E^{(p-n)}(Q^2)$ for the physical pion mass ensemble $\beta = 3.31$, $am_{ud}^{\text{bare}} = -0.09933$, $am_s^{\text{bare}} = -0.04$, $\Lambda = 48^3 \times 48$. The dotted lines show the fits of the plateaus with the functional form Eq. (4.76), which accounts for excited-state contributions.

We also show in Fig. 4.6 the fits of the corresponding plateaus with the functional form of Eq. (4.76), which takes excited-state contributions into account. This form fits the data very well, and is in good agreement with the constant fit of the plateaus.

The dipole fits are in really good agreement with the data, and are independent of the Q^2 fit range, as the higher momentum transfer values have larger error bars. As mentioned in Sec. 4.2.1, the Ward identities do indeed ensure that our lattice conserved current need not be renormalized, and the electric charge $G_E^{(p-n)}(0)$ is found equal to 1, as expected. To prevent introduction of any bias in our analysis, we have however kept the dipole fit parameter A free, just checking afterwards that it was fitted to 1, which is the case since the errors on the electric charge are orders of magnitude smaller than for

other Q^2 .

As the pion mass goes to its physical value, our results appear in rather good agreement with experimental data.

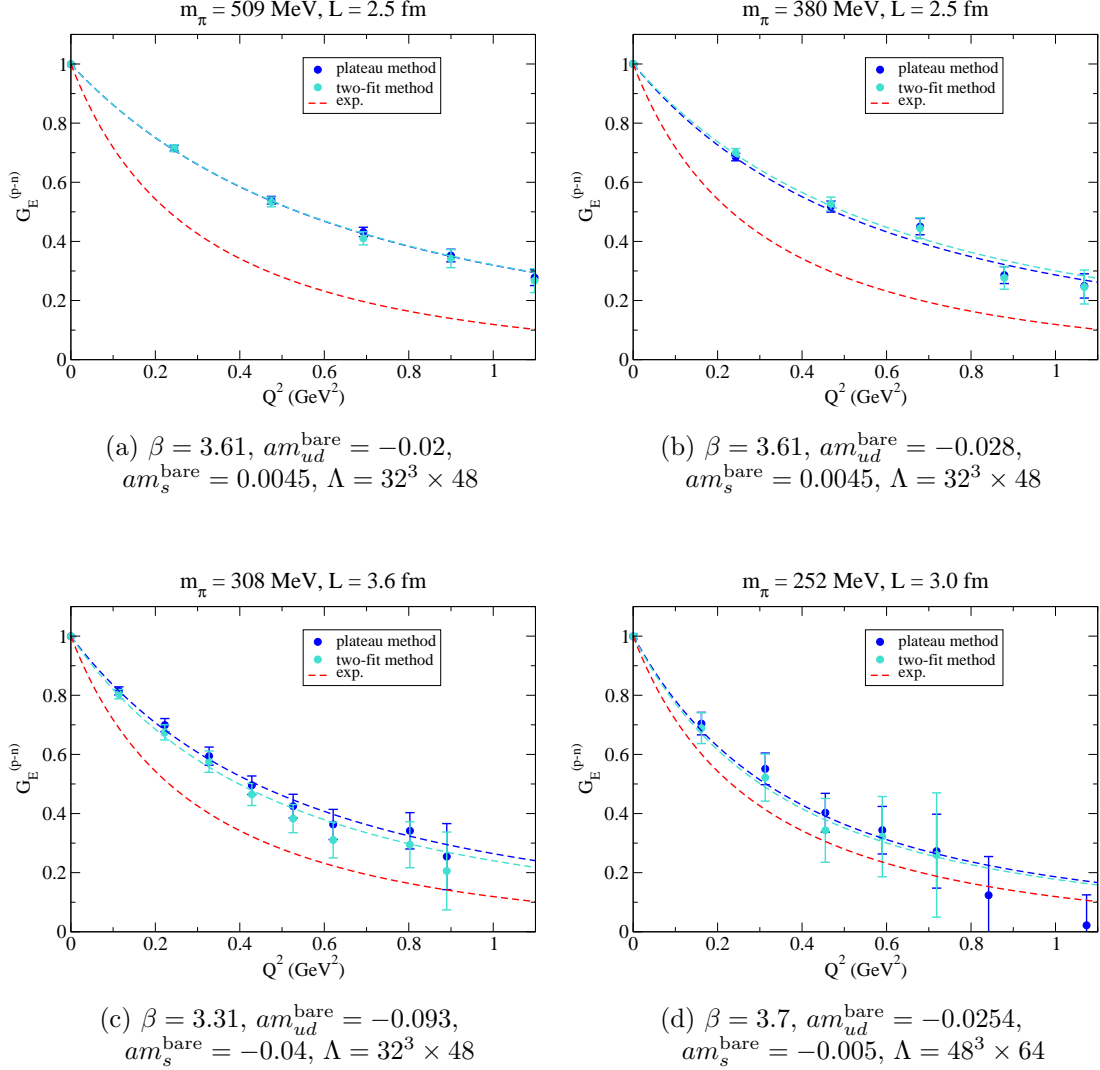


Figure 4.7.: Results for the nucleon isovector electric form factor $G_E^{(p-n)}(Q^2)$, plotted as a function of Q^2 . The red dotted lines show the experimental parametrization and the blue ones our dipole fits.

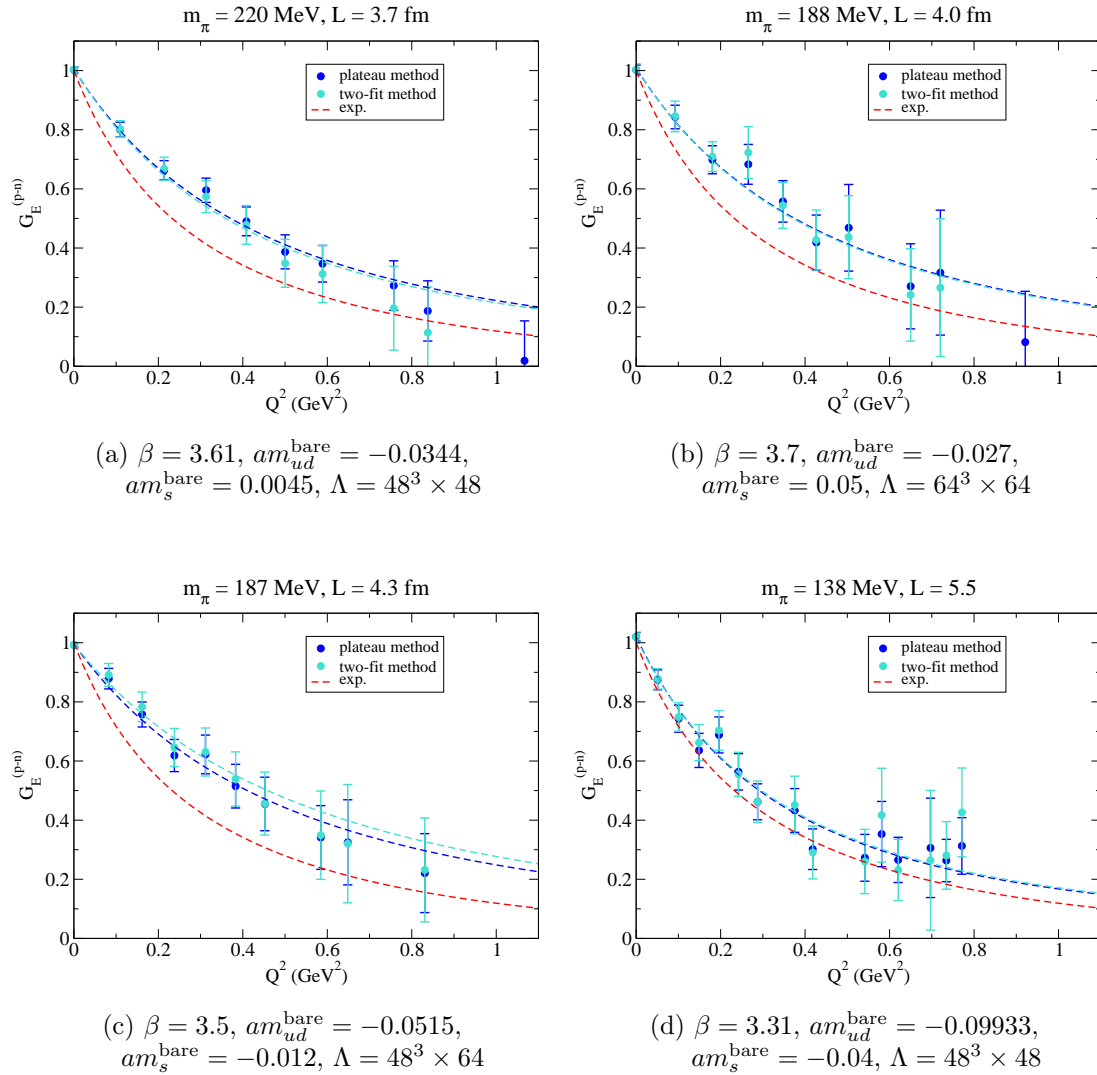


Figure 4.8.: Results for the nucleon isovector electric form factor $G_E^{(p-n)}(Q^2)$, plotted as a function of Q^2 . The red dotted lines show the experimental parametrization and the blue ones our dipole fits.

Magnetic form factor

The results for the nucleon isovector magnetic form factor $G_M^{(p-n)}(Q^2)$ are shown in Figs. 4.10 and 4.11, and examples of plateaus obtained at the physical pion mass are given in Fig. 4.9.

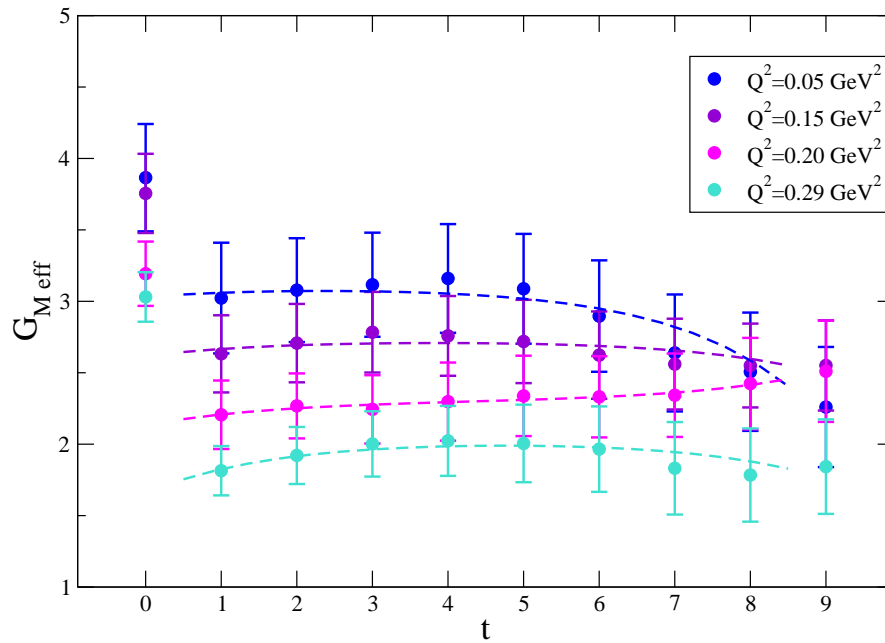


Figure 4.9.: Examples of plateaus for $G_M^{(p-n)}(Q^2)$ for the physical pion mass ensemble $\beta = 3.31$, $am_{ud}^{\text{bare}} = -0.09933$, $am_s^{\text{bare}} = -0.04$, $\Lambda = 48^3 \times 48$. The dotted lines show the fits of the plateaus with the functional form Eq. (4.76), which accounts for excited states contributions.

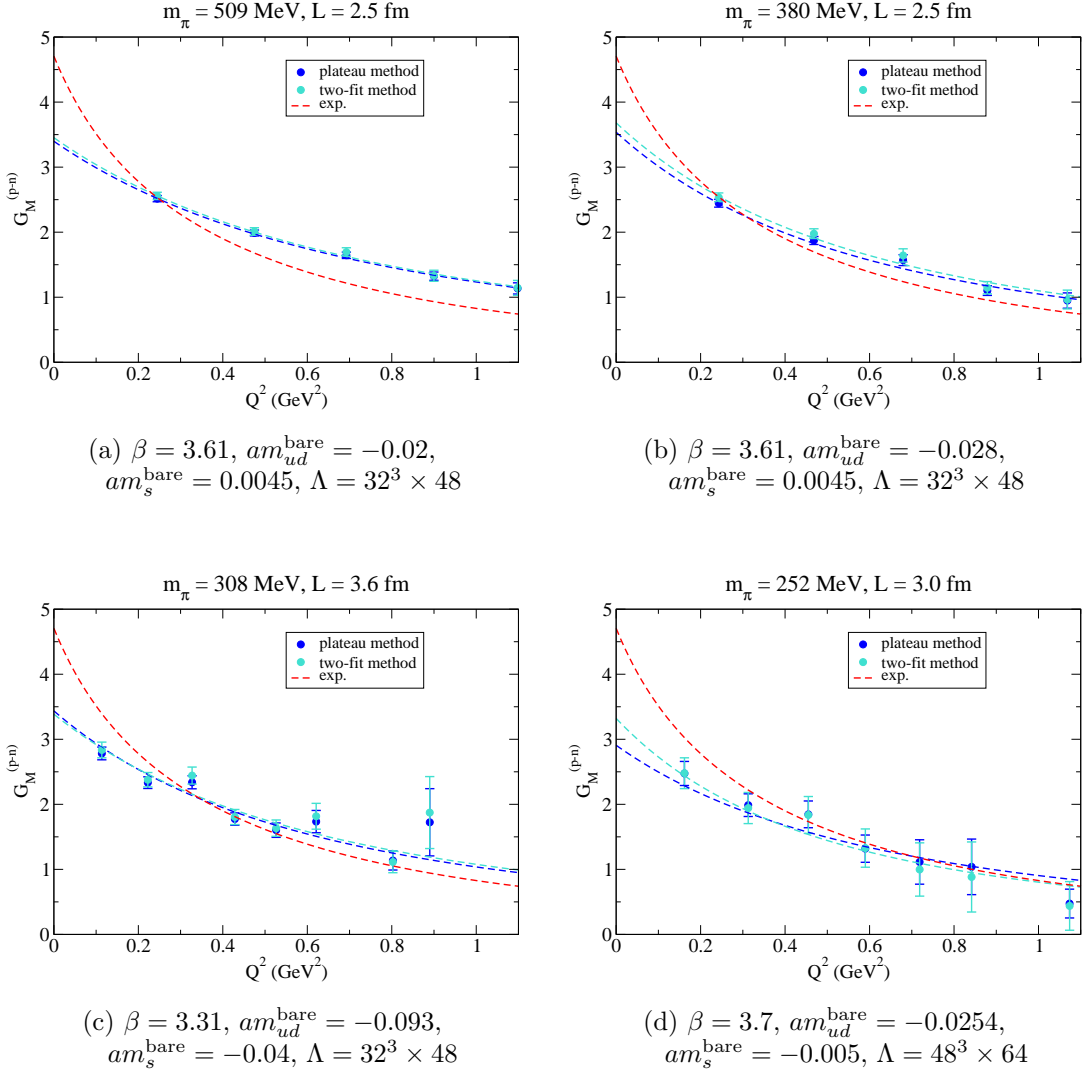


Figure 4.10.: Results for the nucleon isovector magnetic form factor $G_M^{(p-n)}(Q^2)$, plotted as a function of Q^2 . The red dotted lines show the experimental parametrization and the blue ones our dipole fits.

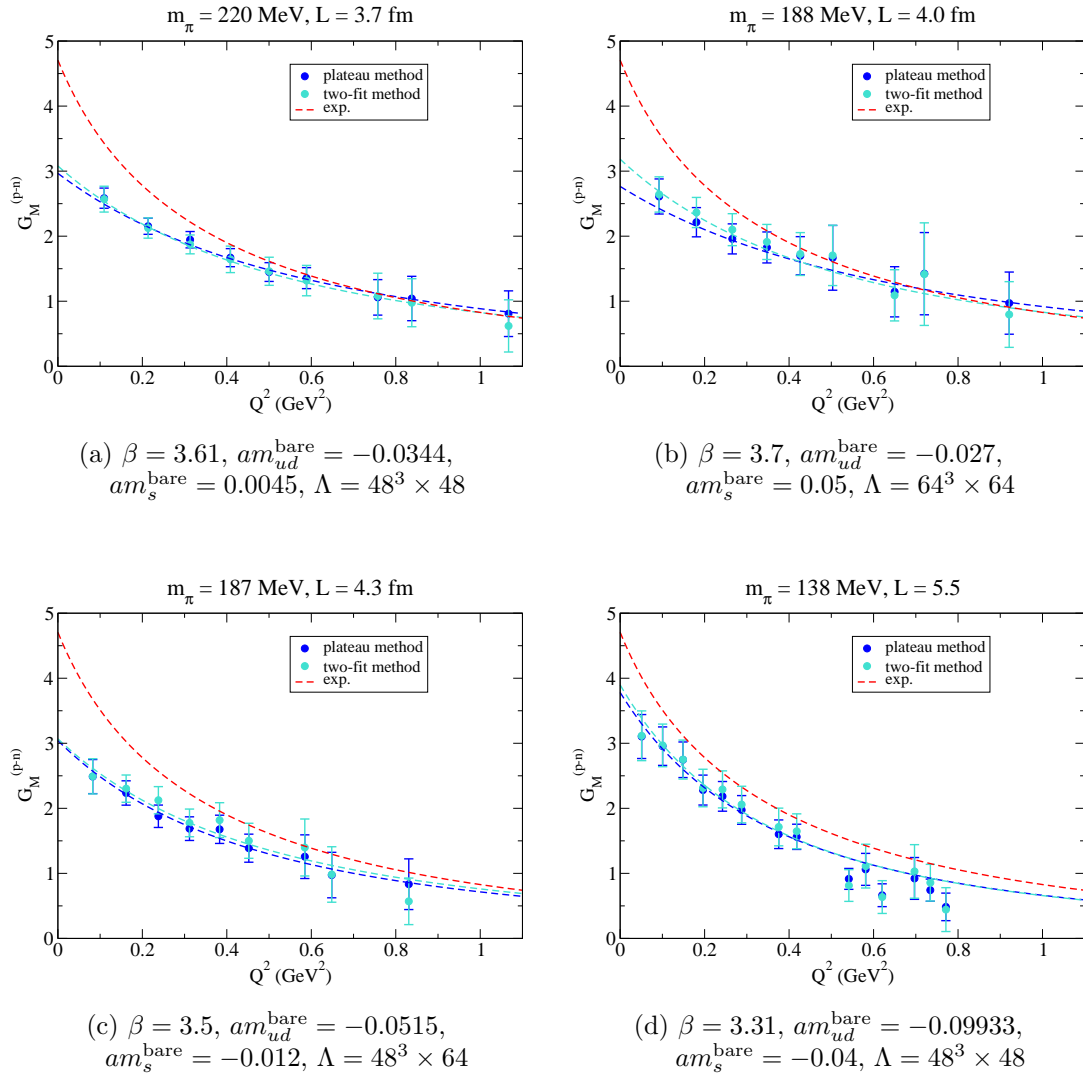


Figure 4.11.: Results for the nucleon isovector magnetic form factor $G_M^{(p-n)}(Q^2)$, plotted as a function of Q^2 . The red dotted lines show the experimental parametrization and the blue ones our dipole fits.

Axial form factor

The results for the nucleon isovector axial form factor $G_A(Q^2)$ are shown in Figs. 4.13 and 4.14, and examples of plateaus obtained at the physical pion mass are given in Fig. 4.12.

They are in agreement with the previous recent results from [100] and [101].

Note that the shown form factors do not include renormalization with Z_A .

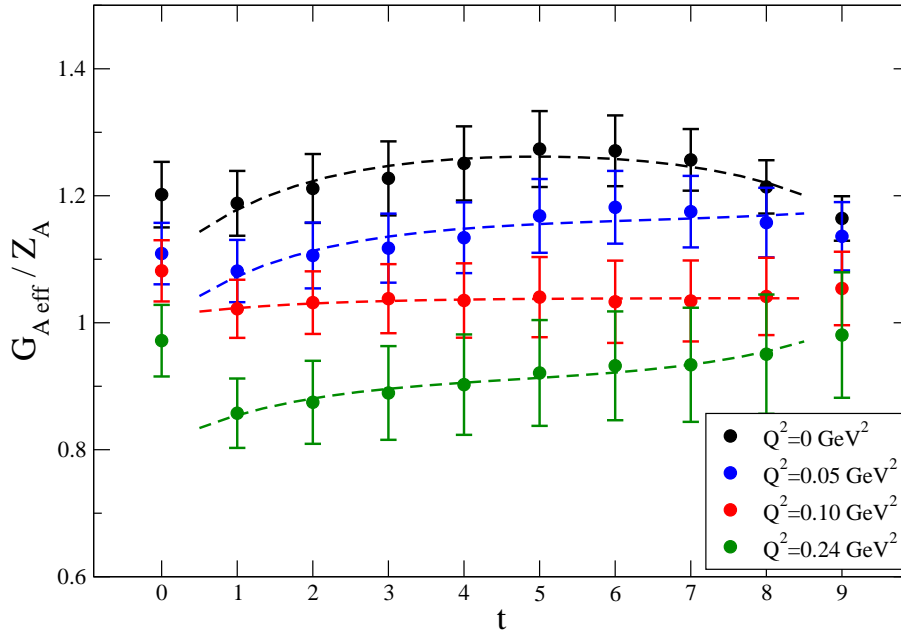


Figure 4.12.: Examples of plateaus for G_A for the physical pion mass ensemble $\beta = 3.31$, $am_{ud}^{\text{bare}} = -0.09933$, $am_s^{\text{bare}} = -0.04$, $\Lambda = 48^3 \times 48$. The dotted lines show the fits of the plateaus with the functional form Eq. (4.76), which accounts for excited-state contributions.

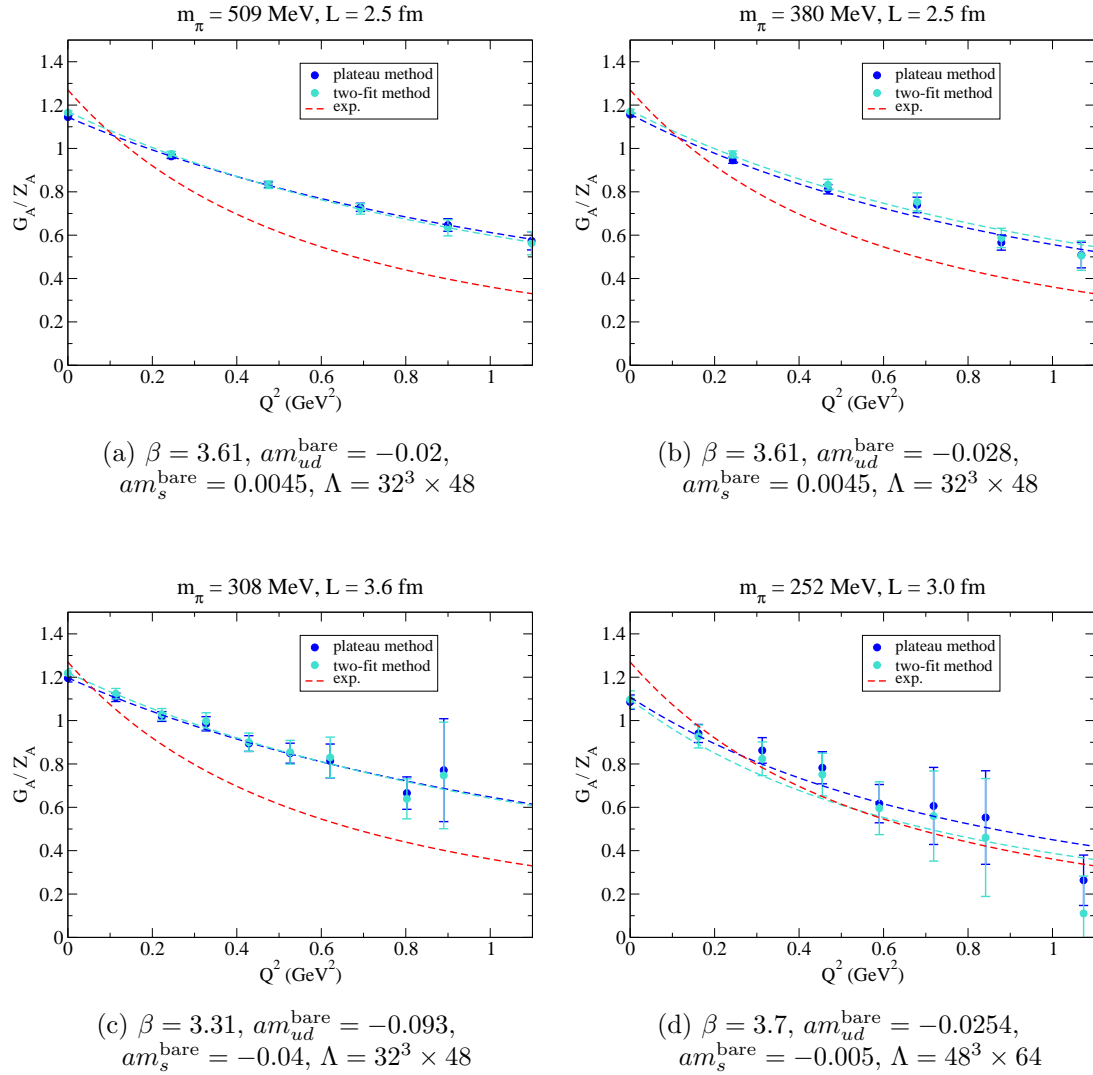


Figure 4.13.: Results for the nucleon isovector axial form factor $G_A(Q^2)$, plotted as a function of Q^2 . The red dotted lines show the experimental parametrization and the blue ones our dipole fits.

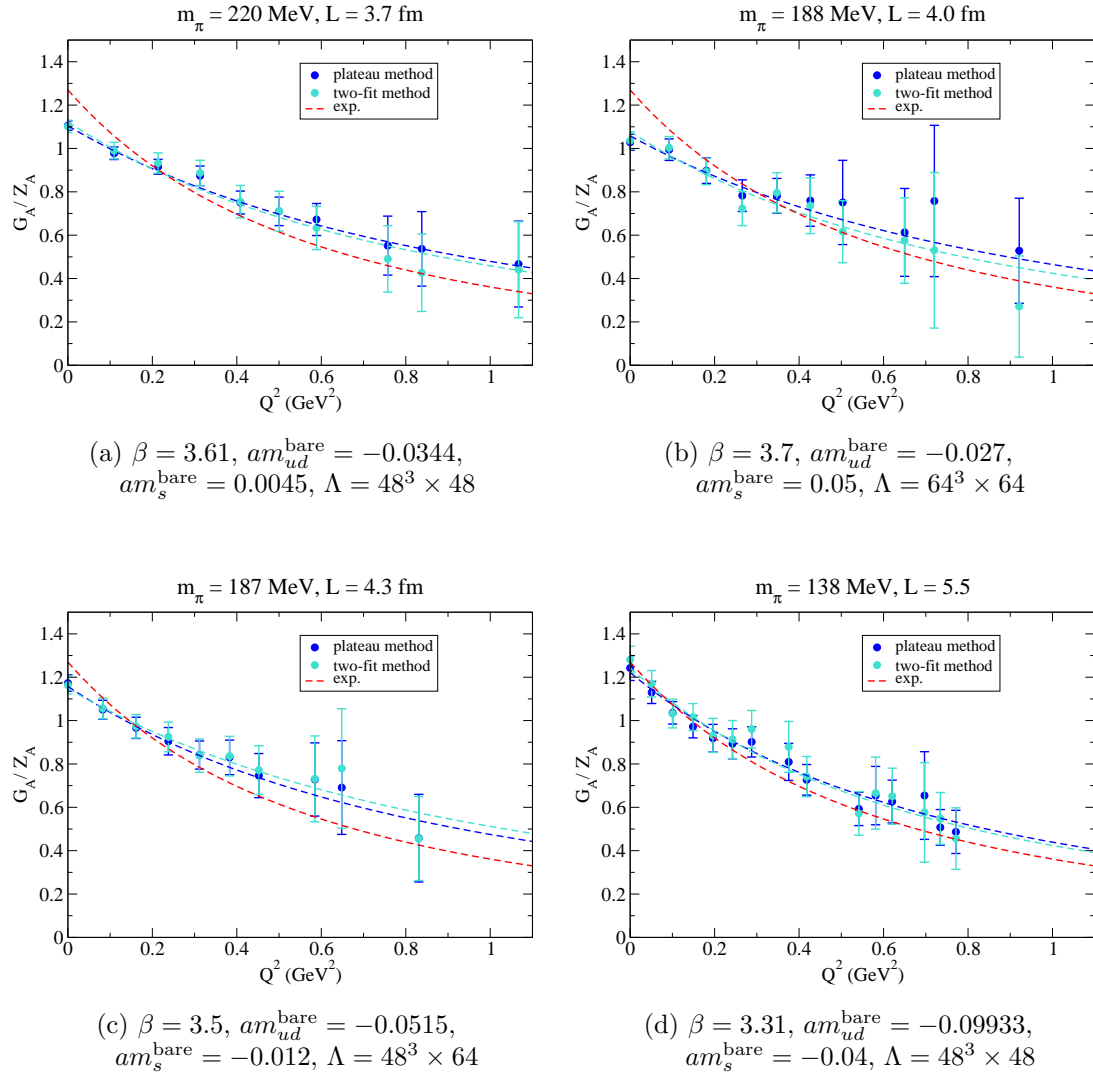


Figure 4.14.: Results for the nucleon isovector axial form factor $G_A(Q^2)$, plotted as a function of Q^2 . The red dotted lines show the experimental parametrization and the blue ones our dipole fits.

Pseudo-scalar form factor

For completeness, we show the results for the isovector pseudo-scalar nucleon form factor $G_P(Q^2)$ for each ensemble in Figs. 4.15 and 4.16.

We can observe the rapid increase of G_P at low Q^2 , which can be associated with pion pole. However, we do not attempt any further comparison with experiment, as experimental data are rather inaccurate and turn out not to overlap our Q^2 range.

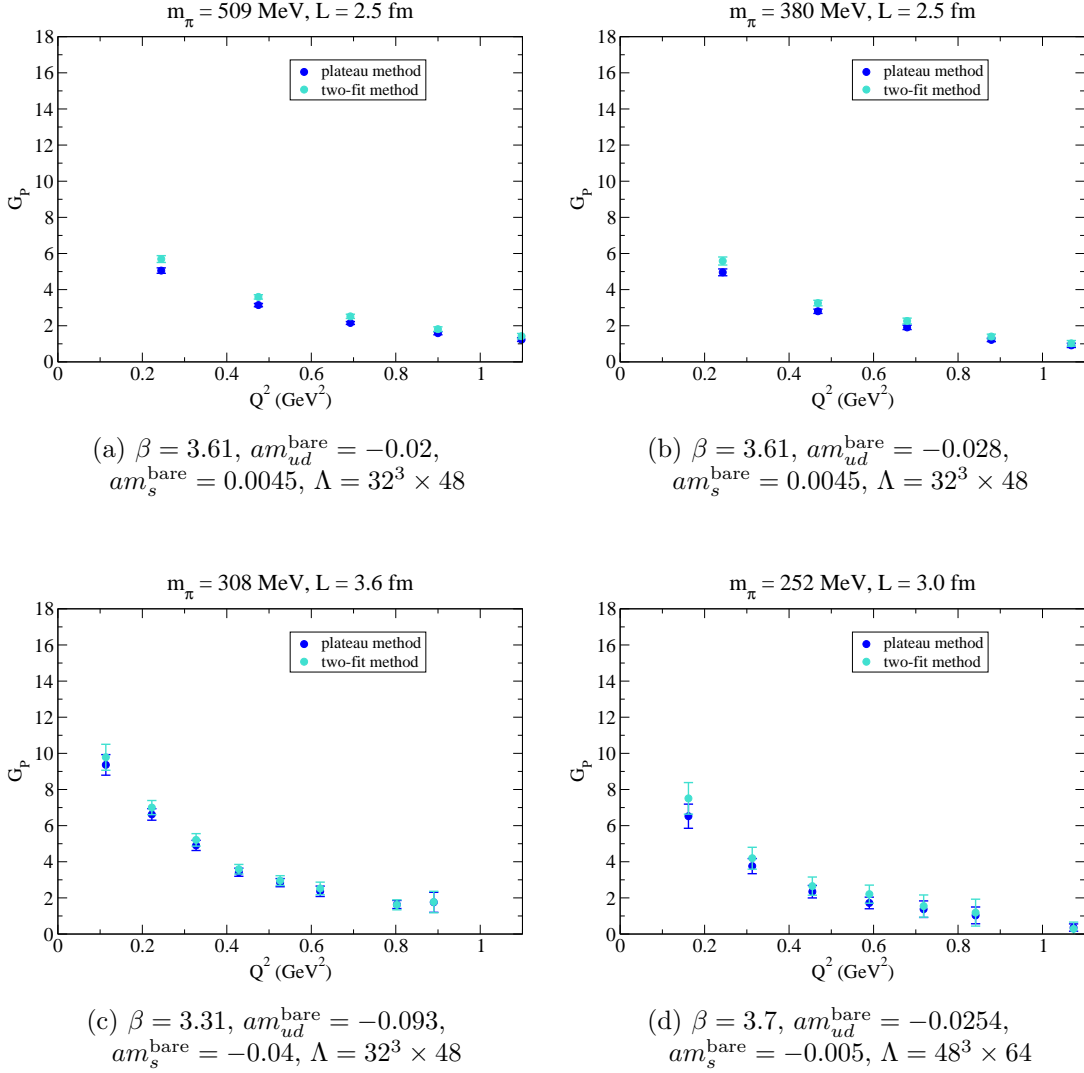


Figure 4.15.: Results for the nucleon pseudo-scalar form factor $G_P(Q^2)$, plotted as a function of Q^2 .

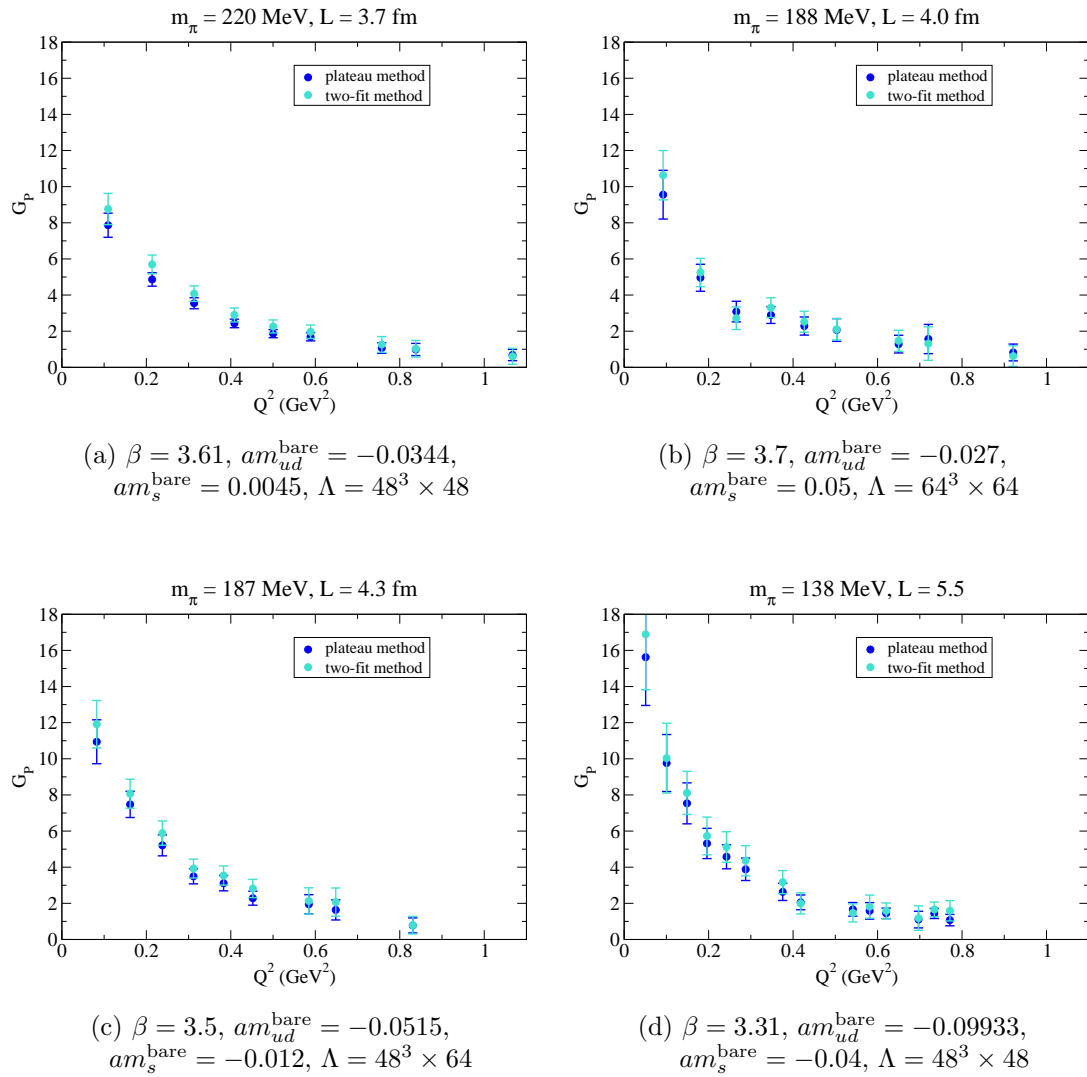


Figure 4.16.: Results for the nucleon pseudo-scalar form factor $G_P(Q^2)$, plotted as a function of Q^2 .

4.4.2. Electric charge radius

The isovector nucleon electric charge mean squared radius is obtained from the fits of the electric form factors with a dipole functional form 4.91 as :

$$\langle r_E^2 \rangle \equiv -6 \frac{1}{G_E^{(p-n)}(0)} \left. \frac{dG_E^{(p-n)}(Q^2)}{dQ^2} \right|_{Q^2=0} = \frac{12}{M_E^2} \quad (4.92)$$

The lattice “raw” results computed from the fitted electric dipole masses are shown in Fig. 4.18, plotted versus m_π^2 . Again, the reported errors are only statistical and estimated with the bootstrap method, each bootstrap sample being fitted independently.

Being a spatial density, the squared radius is directly sensitive to long-range behaviours, and can be therefore strongly affected by finite volume effects.

Finite volume effects

To estimate the finite-volume corrections, we assume that they are due to the pion contribution to the form factors, which allows us to use chiral perturbation theory. In this approach the form factors are given by a point like nucleon surrounded by a pion cloud. Since the point source form factor has no finite volume correction we only need to consider diagrams where the current is carried by the pion. This is shown on Fig.4.17 where the thin (resp. fat) lines represent the nucleon (resp. delta) and the dotted line is the pion.

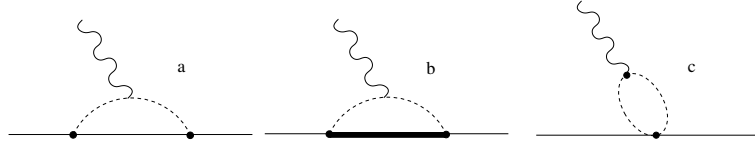


Figure 4.17.: Pion contribution to the current

According to [102] the pion contribution to the proton and neutron electric form factor is

$$G_{E,\pi}^{(p)}(Q^2) = -G_{E,\pi}^{(n)}(Q^2) = \frac{g_A^2}{16\pi^3 f_\pi^2} \left(I_N - \frac{16}{25} I_\Delta + \frac{1}{g_A^2} I_{tp} \right)$$

where the loop integrals are given by the following expressions:

$$\begin{aligned} I_N &= \int d\mathbf{k} \frac{u(\mathbf{k})u(\mathbf{k}-\mathbf{q}) \mathbf{k} \cdot (\mathbf{k}-\mathbf{q})}{\omega(\mathbf{k})\omega(\mathbf{k}-\mathbf{q}) [\omega(\mathbf{k}) + \omega(\mathbf{k}-\mathbf{q})]} \\ I_\Delta &= \int d\mathbf{k} \frac{u(\mathbf{k})u(\mathbf{k}-\mathbf{q}) \mathbf{k} \cdot (\mathbf{k}-\mathbf{q})}{[\omega(\mathbf{k}) + \Delta] [\omega(\mathbf{k}-\mathbf{q}) + \Delta] [\omega(\mathbf{k}) + \omega(\mathbf{k}-\mathbf{q})]} \\ I_{tp} &= \int d\mathbf{k} \frac{u(\mathbf{k})^2}{[\omega(\mathbf{k} + \mathbf{q}/2) + \omega(\mathbf{k} - \mathbf{q}/2)]} \end{aligned}$$

$m_\pi(\text{GeV})$	$L(\text{fm})$	$\delta \langle r_E^2 \rangle (\text{fm}^2)$
0.138	5.46	0.071
0.187	4.3	0.058
0.188	4.0	0.068
0.220	3.7	0.055
0.252	3.0	0.065
0.308	3.6	0.019
0.380	2.5	0.033
0.509	2.5	0.011

Table 4.3.: The volume corrections to the isovector electric mean squared radius.

with $\omega(\mathbf{k}) = \sqrt{k^2 + m_\pi^2}$ and $u(\mathbf{k})$ a form factor which regulates the integral in the ultra violet. We choose it to be a dipole

$$u(\mathbf{k}) = \frac{1}{(1 + k^2/\Lambda^2)^2}$$

but we stress that the exact shape of the regulator is irrelevant for the volume correction. We use the physical values of the constants that is $g_A = 1.27$, $f_\pi = 93 \text{ MeV}$.

For a quantity G^{FV} computed in the finite volume V we define the correction

$$\delta G = G^\infty - G^{FV}$$

and we estimate this difference by replacing the loops integral $I_{N,\Delta,tp}$ by discrete sums according to the replacement:

$$\frac{1}{(2\pi)^3} \int d\mathbf{k} \rightarrow \frac{1}{L^3} \sum_{k_x k_y k_z}, \quad k_{x,y,z} = \frac{2\pi}{L} n_{x,y,z}.$$

In Table 4.3 we give the finite volume corrections $\delta \langle r_E^2 \rangle$ to the isovector mean squared radius for the parameters used in our calculation. The cut-off parameter Λ has been set to $\Lambda = 2 \text{ GeV}$ and we have checked that the difference between the loop integrals and their discrete sum version was actually saturated with this value. This amounts to saying that the cut-off has been removed.

Chiral behaviour

As the pion mass approaches its physical value, we observe a rapid increase of $\langle r_E^2 \rangle$, as predicted by Chiral Perturbation Theory. This behaviour is a really interesting output of our calculation, as it appears to take place at low pion masses, and could not be unambiguously detected without data at the physical pion mass. Our values are in agreement with the experimental data, although less accurate.

The effects of excited-state contributions are rather small, unlike in Ref. [103] and [104], and we have not observed any strong deviation between the *excited states* plateau fit method and the usual *constant* plateau fit one.

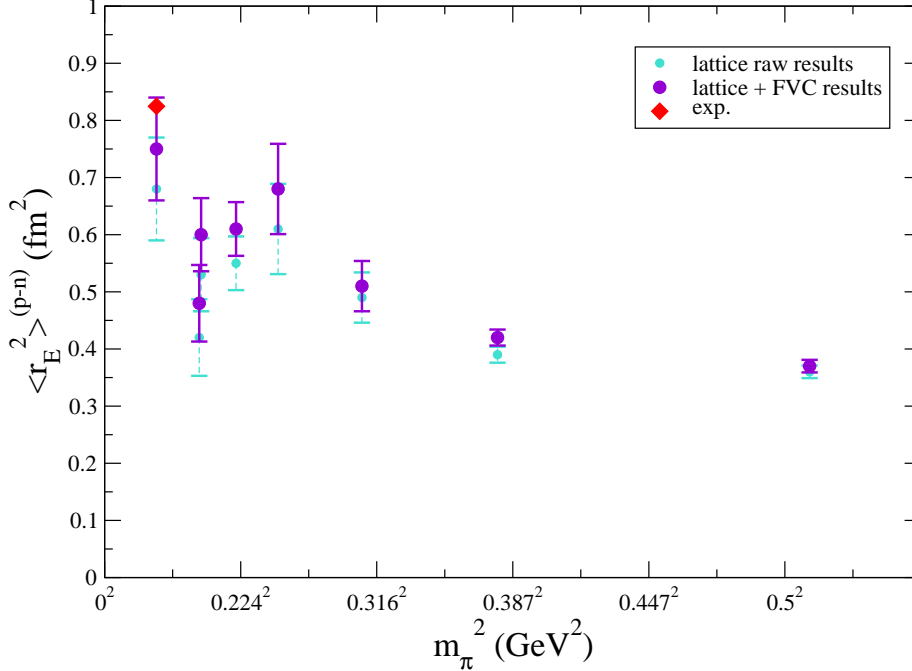


Figure 4.18.: Pion mass dependence of the isovector electric charge squared radius. The turquoise dots with dotted error riser lines are the raw lattice results obtained from the dipole fits of $G_E^{(p-n)}(Q^2)$, extracted with the two-fit method. The violet dots are the results after correction of the finite volume effects computed as in Sec. 4.4.2.

Although [104] also used a method similar to our *excited-state* plateau fit, they did not project the 3-pt correlator with $\mathcal{P}(\mathbf{p}_i)$ at the source, and used a mass splitting Δ equal to m_π or $2m_\pi$, which gives strong excited-state effects. However, the mass splitting we have fitted from \bar{C}_2 appears closer to the mass splitting between the nucleon and its first positive parity $P_{11}(1710)$ radial excitation.

As for the strong excited-state contributions reported in [103], a few tests conducted with our data suggest that they could be related to the absence of projection at the source, which allows for strong contamination by the relatively low lying negative parity excitation of the nucleon.

Following [102], we parametrize the dependence of the squared radius on the pion mass as

$$\langle r_E^2 \rangle = A + B m_\pi^2 - \frac{10 g_A^2 + 2}{16\pi^2 f_\pi^2} \log \frac{m_\pi}{\mu}$$

where A and B are free parameters, μ is a mass scale (which can be arbitrarily absorbed

in A , and is therefore chosen to be 1 GeV) and where we take the physical values of the chiral parameters $g_A = 1.267$ and $f_\pi = 92.4 \text{ MeV}$. As we can see in [105], the discretization effects can be safely accounted for with some $O(a^2)$ functional; and we choose to add an m_K^2 term to extrapolate to the physical strange quark mass.

So that our functional parametrization of the electric charge squared radius eventually writes:

$$\langle r_E^2 \rangle = A + B m_\pi^2 - \frac{10 g_A^2 + 2}{16\pi^2 f_\pi^2} \log \frac{m_\pi}{\mu} + C m_K^2 + D a^2 \quad (4.93)$$

where A , B , C and D are the fit parameters.

In Fig. 4.19, we show our results extrapolated to the continuum and at the physical strange quark mass together with the corresponding chiral fit.

The physical point value we obtain is:

$$\langle r_E^2 \rangle^{\text{phy}} = 0.79 \text{ fm}^2 \pm 0.05 \text{ fm}^2 \text{ (stat)} \quad (4.94)$$

which is in agreement with the experimental value.

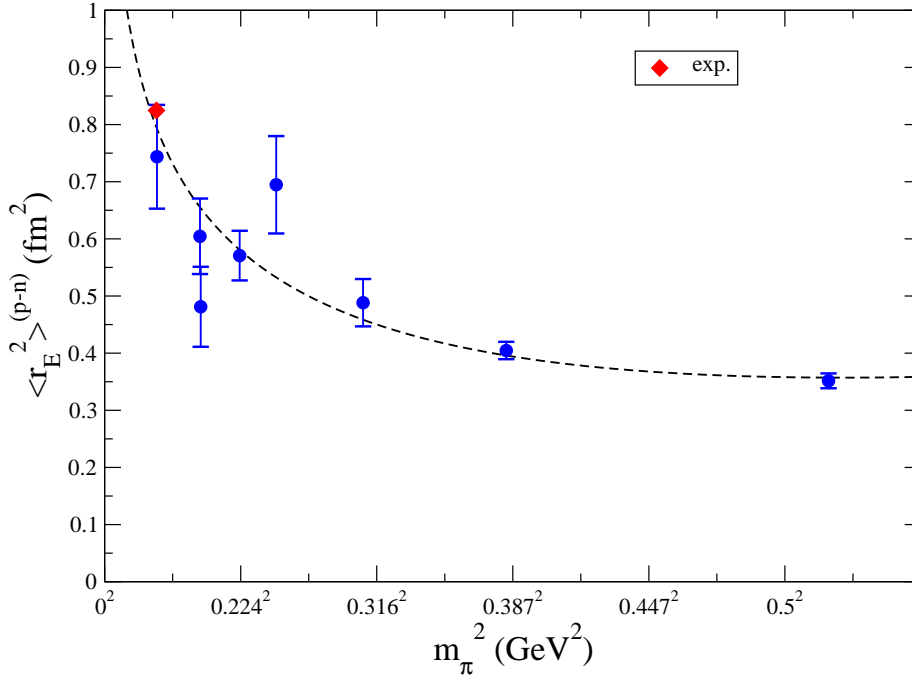


Figure 4.19.: Results for the electric charge squared radius extrapolated to the continuum, infinite-volume and physical strange quark mass. The dotted line shows the corresponding fit performed with the functional form (4.93).

4.4.3. Magnetic moment

For completeness, we present here the results for the isovector magnetic moment $G_M(0)$. These are shown in Fig. 4.20, plotted against m_π^2 .

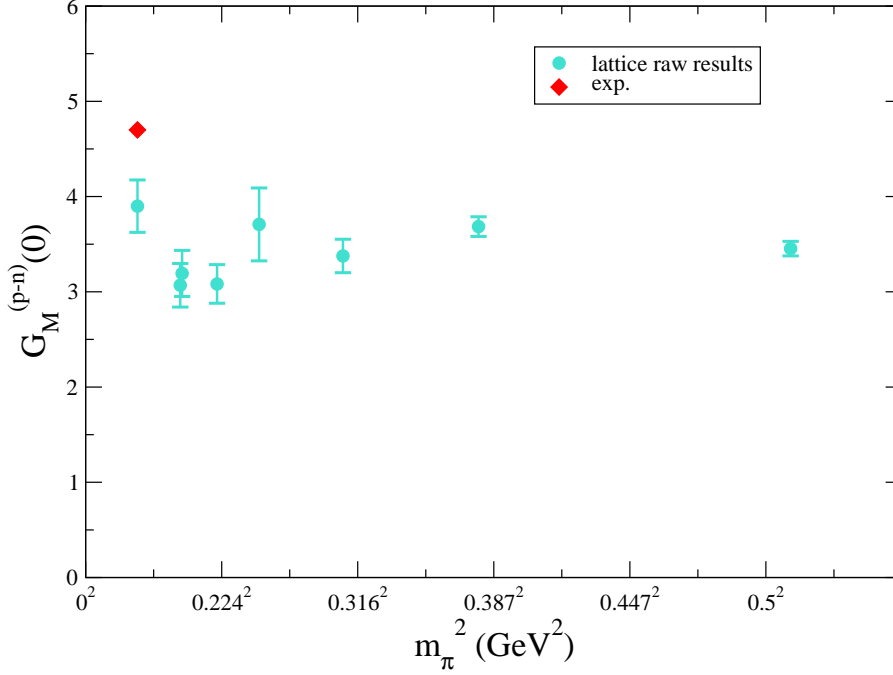


Figure 4.20.: Pion mass dependence of the isovector magnetic moment. The turquoise dots are the raw lattice results obtained from the dipole fits of $G_M^{(p-n)}(Q^2)$, extracted with the two-fit method.

At the physical pion mass, the fitted raw magnetic moment obtained is

$$G_M(0)_{m_\pi, \text{phys}} = 3.90 \quad (27) \quad (4.95)$$

Again, we stress that this value is only given by one ensemble, at finite volume and lattice spacing, with statistical errors only.

The magnetic form factor is not very accurate, as it is computed on the lattice as the difference between two large numbers, which is then divided by Q^2 , which is relatively small. Moreover, its value at $Q^2 = 0$ can only be extrapolated, as $G_M^{(p-n)}(Q^2)$ enters the nucleon current matrix element multiplied by Q^μ . This extrapolation brings another large source of uncertainty for the magnetic charge.

The values obtained from our lattice calculations seem to slightly underestimate the magnetic moment experimental value, as was already observed in [105]. However, a

more detailed study of finite-volume effects and an extension of the calculation with other ensembles presented in Sec. 2.4.1 along with a continuum and infinite-volume extrapolation need to be performed in order to get a more robust lattice value.

4.4.4. Axial charge

We present here our results for the axial charge $g_A = G_A(0)$. The reported values in this section take the renormalization with Z_A into account.

Our result at the physical pion mass is compatible with the experimental value within 2σ , and mainly agrees with the previous calculations of Refs. [106] and [107]. We also note the sharp increase of g_A which takes place in a small m_π range of about 100 MeV when approaching the physical mass.

Note that, like [108]), we do not observe the violent excited-state effect of [103], which seems to be associated with the *summation* method employed.

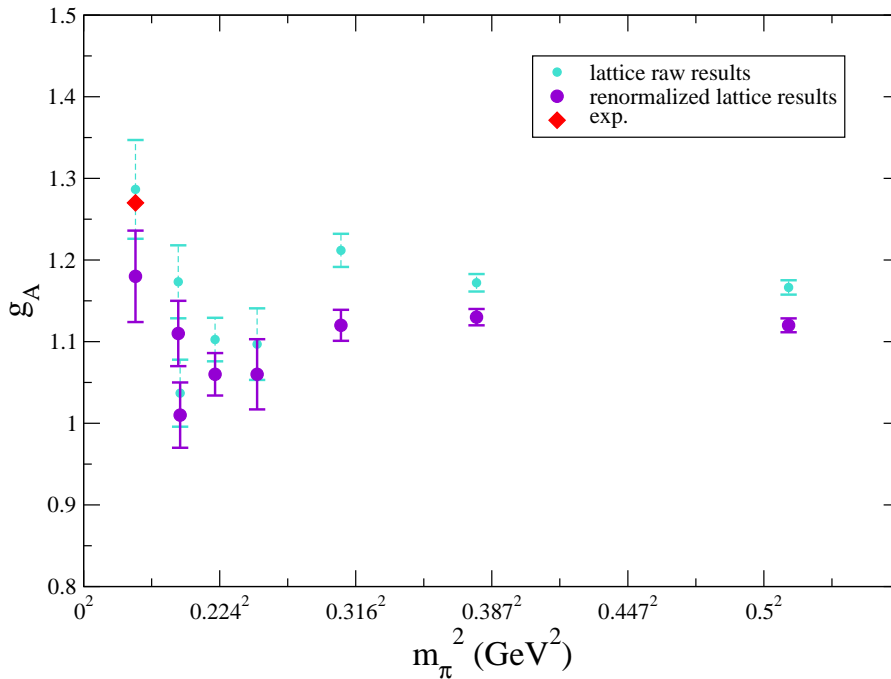


Figure 4.21.: Pion mass dependence of the nucleon axial charge. The turquoise dots with dotted error riser lines are the raw lattice results. The violet dots are the results after renormalization with Z_A .

Note that the volume corrections to g_A have been estimated in ref. [106]. For our combinations of pion masses and volumes, they are negligible.

4.5. Conclusion

To conclude this chapter about the lattice QCD computation of the nucleon form factors, we emphasize that the results obtained go down to the physical pion mass, and appear in rather good agreement with experimental data. Under the assumptions made regarding the functional form of the form factors and the size of finite-volume corrections, the lattice $\langle r_E^2 \rangle$ and g_A puzzles seem to be under control and well understood., though a thorough continuum and infinite-volume extrapolation has yet to be performed.

We remind the reader that only the isovector parts have been computed in this work, in order to avoid the computation of disconnected contractions.

To complete this study, the extrapolations mentioned above and a thorough analysis of systematic errors (including those associated with the choice of form factor functional form) within a global fit combining all our ensembles are ongoing and their presentation is postponed to a future paper.

5. Conclusion and outlooks

In this thesis, we have used the framework of Lattice QCD with gauge configurations from the BMW collaboration to perform a detailed study of two issues in hadronic physics.

With impressive results for hadron spectroscopy and the recent understanding of matter stability as the consequence of strong competing isospin breaking and electromagnetic effects [73], Lattice QCD provides an invaluable formalism to perform ab-initio non-perturbative calculations of strong interaction related processes. As such, this work meshes with recently growing attempts to study the structure of hadrons and hadronic interactions from first principles.

In a first study, we have analysed $\pi\pi$ scattering in the ρ channel, using Lüscher's formalism. Our results encompass the first calculation of the $\pi\pi$ scattering phase-shifts and the ρ resonance parameters at the physical pion mass, and as such provide an important step as the first direct evidence of a particle decaying on the lattice. After continuum extrapolation, the ρ mass and width are in excellent agreement with the experimental values.

The outcome of our calculation relied intensively on the use of the Generalized Eigenvalue Problem variational method, which proved to be a powerful tool to extract excited-state energies in addition to the ground state one. This however requires huge computing time, as well as the construction of several independent interpolating operators, which, in the case of particle scattering, correspond to multi-hadronic interpolators.

The second part of this work was dedicated to the study of the electroweak nucleon form factors, computed down to the physical pion mass. We restricted the calculation to the isovector case to avoid the computation of disconnected contractions.

The extraction of form factors from the three-point correlation functions computed on the lattice was performed using a novel fully covariant formalism, combined with a full projection onto the nucleon state at the source and sink. In addition to providing an extraction method which does not favour any particular polarisation, this also proved useful to strongly reduce excited-state contributions in our signal.

The study of excited-state contaminations was achieved using a *two-state* fitting procedure of the effective form factors in addition to the usual plateau method. The mass splitting needed in the two-state fit method was obtained through multi-exponential fits of the two-point correlation functions performed with the variable projection algorithm. The effect of excited-state contributions was found to be small, and within error bars.

At the physical pion mass, our results are in good agreement with experimental values. The investigations of the electric nucleon squared radius $\langle r_E^2 \rangle$ and of the axial charge g_A included their behaviour as functions of the pion mass. We have observed their sharp variation related to the non-analytic term going like $\log(m_\pi)$ near the physical pion mass,

predicted by chiral perturbation theory. The sudden increase induced by this term takes place for rather low pion masses and is therefore difficult to correctly assess without data at the physical mass.

The statistical precision of our lattice results still needs improvement in order to compete with experimental data, for example to solve the proton radius puzzle, which would require a total precision of about 3%. We insist on the fact that calculations at the physical pion mass is compulsory for the nucleon structure quantities, as chiral parametrizations can lead to untrustworthy results when not constrained at low pion masses.

... n'abolira le hasard.

S. Mallarmé

A. Statistics

As mentioned in Sec. 2.3, the computation of vacuum expectation values of observables in lattice QCD is done with a Monte-Carlo importance sampling of the space of gauge configurations. Typically, we use a few hundreds configurations to estimate the involved integral, which provides a rather good precision on the central value of the expectation value (considered here as a random variable). However, this number of configurations is usually too small to estimate accurately the variance of the computed quantity. Moreover, the expectation values are often used in some physical post-analysis, involving arithmetical and statistical manipulations, such as fits. It may then become difficult to propagate errors reliably throughout the procedure. To overcome both limitations, we use a resampling method introduced in [47], called the *bootstrap* method.

Bootstrap resampling method

The idea of *bootstrap* resampling is, starting from a set of N realizations $\{x_1, \dots, x_N\}$ of some random variable X , to consider new *bootstrap sample* sets $\{x_1^*, \dots, x_N^*\}$ of realizations, where the samples x_i^* are randomly drawn (*with replacement*) from the original set $\{x_i, i = 1 \dots N\}$.

If we now consider the result of this drawing procedure as the realizations of a new bootstrap random variable X^* , then the sampling distribution of any observable $O(X)$ depending on X can be shown to be well approximated by the *bootstrap distribution* of $O^* \equiv O(X^*)$.

In practice, we therefore need to build several (say M) bootstrap samples $\{x_i^*\}_m$, $m = 1, \dots, M$, and perform our analysis on each bootstrap sample, to obtain M bootstrap realizations O_m^* of the observable. Typically, in our case, $M = 2000$.

At the end of our analysis process, we can then get the central value and error of the considered quantity using standard (unbiased) statistical estimators for the mean and standard deviation:

$$\bar{O} = \frac{1}{M} \sum_{m=1}^M O_m^* \quad (\text{A.1})$$

$$\sigma_O^2 = \frac{1}{M-1} \sum_m (O_m^* - \bar{O})^2 \quad (\text{A.2})$$

However, more robust estimators can also naturally be used, for example to limit the impact of outliers which can appear in the course of some analysis including non-linear manipulations.

Robust statistics

In the analysis process of our lattice data within the bootstrap resampling framework, it can happen that some highly non-linear procedure favours the occurrence of outlying bootstrap realizations. Then, as thoroughly studied in [109], a way to avoid the strong contamination of the mean and standard deviation estimators by the few outliers is to use robust estimators for the expectation value and the variance square root. The two robust estimators we shall use to this end are the median, and the normalized median absolute deviation MAD, defined as

$$\text{MAD}\{O\} = \frac{\text{med}\{|O_m^* - \text{med}\{O_m^*\}|\}}{\Phi^{-1}\left(\frac{3}{4}\right)} \quad (\text{A.3})$$

where normalization by the inverse gaussian cumulative distribution function evaluated at $\frac{3}{4}$

$$\Phi^{-1}\left(\frac{3}{4}\right) \approx 0.6745$$

is to ensure that for a normal distribution $\text{MAD}\{O\} = \sigma_O$.

B. Two-point functions

Generalities

Hadron masses can be extracted from the Euclidean-time dependence of two-point correlation functions

$$C(t) = \langle \Omega | \mathcal{T} \{ O_2(t) O_1(0) \} | \Omega \rangle \quad (\text{B.1})$$

where $|\Omega\rangle$ is the vacuum state, and O_1 and O_2 are *timeslice* hadron operators $O_i(t) = \sum_{\mathbf{x}} e^{-i\mathbf{x}\cdot\mathbf{p}} O_i(\mathbf{x}, t)$ with definite spatial momentum \mathbf{p} ¹ and the same quantum numbers as the hadron we are interested in, called *interpolators*. Time-ordering in Eq. (B.1) implies

$$C(t) = \begin{cases} \langle \Omega | O_2(t) O_1(0) | \Omega \rangle & : t \geq 0 \\ \pm \langle \Omega | O_1(0) O_2(t) | \Omega \rangle & : t < 0 \end{cases} \quad (\text{B.2})$$

where the "±" sign accounts for the bosonic or fermionic nature of the operators.

The correlation functions then have the Hamiltonian representation

$$C(t) = \lim_{T \rightarrow \infty} \text{Tr} \left[e^{-T\hat{H}} \right]^{-1} \begin{cases} \text{Tr} \left[e^{-(T-t)\hat{H}} O_2(0) e^{-t\hat{H}} O_1(0) \right] & : t \geq 0 \\ \pm \text{Tr} \left[e^{-T\hat{H}} O_1(0) e^{t\hat{H}} O_2(0) e^{-t\hat{H}} \right] & : t < 0 \end{cases} \quad (\text{B.3})$$

where \hat{H} is the Hamiltonian of QCD.

Expanding the trace, and inserting a complete set of eigenstates in Eq. (B.3), we obtain²

$$C(t) = \lim_{T \rightarrow \infty} \text{Tr} \left[e^{-T\hat{H}} \right]^{-1} \begin{cases} \sum_{m,n} e^{-(T-t)E_m} \langle m | O_2 | n \rangle e^{-tE_n} \langle n | O_1 | m \rangle & : t \geq 0 \\ \pm \sum_{m,n} e^{-(T+t)E_m} \langle m | O_1 | n \rangle e^{tE_n} \langle n | O_2 | m \rangle & : t < 0 \end{cases}$$

$$= \begin{cases} \sum_n \langle \Omega | O_2 | n \rangle \langle n | O_1 | \Omega \rangle e^{-tE_n} \\ \pm \sum_n \langle \Omega | O_1 | n \rangle \langle n | O_2 | \Omega \rangle e^{tE_n} \end{cases} \quad (\text{B.4})$$

In the special case $O_2 = O_1^\dagger = O$, $\langle \Omega | O | n \rangle = \langle n | O | \Omega \rangle^\dagger$ and Eq. (B.4) becomes

$$C(t) = \begin{cases} |\langle \Omega | O | N \rangle|^2 e^{-tE_N} & : t \geq 0 \\ \pm |\langle \bar{N} | O | \Omega \rangle|^2 e^{tE_{\bar{N}}} & : t < 0 \end{cases} \quad (\text{B.5})$$

¹In practice, only O_2 is momentum-projected, and momentum conservation selects the right fourier component in O_1 .

²We choose $E_\Omega = 0$

where $|\langle \Omega | O | N \rangle|^2$ also includes any spin sum that might appear with $|N\rangle$ and $\langle N|$ if these are fermion states. We have kept only the lowest contributing state, as the other ones decay faster as t increases. Note the appearance for $t < 0$ of a ground state \bar{N} , which can in general be different from N . It is however often related to N through invariance of the action under some discrete symmetries.

On the lattice, one works with large but finite T , along with time-direction boundary conditions. In the case of *(anti)periodic* boundary conditions, the computed two-point function on the lattice is (anti)periodic by construction and given by:

$$C_{lat}(t) = \sum_{m=-\infty}^{+\infty} (\pm)^m C(t + mT) \quad (\text{B.6})$$

where now $0 < t < T$, and the $+(-)$ sign stands for periodic (antiperiodic) boundary conditions. Splitting the sum and using Eq. (B.5), we get

$$\begin{aligned} C(t) &= \sum_{m \geq 0} (\pm)^m C(t + mT) + \sum_{m < 0} (\pm)^m C(t + mT) \\ &= |\langle \Omega | O | N \rangle|^2 \sum_{m \geq 0} (\pm)^m e^{-(t+mT)E_N} \pm |\langle \bar{N} | O | \Omega \rangle|^2 \sum_{m < 0} (\pm)^m e^{(t+mT)E_{\bar{N}}} \\ &= \frac{|\langle \Omega | O | N \rangle|^2}{1 - (\pm)_{b.c.} e^{-TE_N}} e^{-tE_N} \pm \frac{|\langle \bar{N} | O | \Omega \rangle|^2}{1 - (\pm)_{b.c.} e^{-TE_{\bar{N}}}} e^{-(T-t)E_{\bar{N}}} \end{aligned} \quad (\text{B.7})$$

where in the last line we have summed the geometric series. For T large enough, the denominators go to 1 and we find the usual lattice spectral decomposition

$$C(t) = |\langle \Omega | O | N \rangle|^2 e^{-tE_N} \pm |\langle \bar{N} | O | \Omega \rangle|^2 e^{-(T-t)E_{\bar{N}}} \quad (\text{B.8})$$

with $+$ (resp. $-$) for a bosonic (resp. fermionic) operator O .

We now turn to a more detailed study of usual meson and baryon correlators.

Meson correlators

Mesons are bosons made out of a valence quark-antiquark pair. Hence the simplest interpolator one can use has the form

$$O_M = \bar{\psi}^{(1)} \Gamma \psi^{(2)} \quad (\text{B.9})$$

where Γ is a monomial of Dirac gamma matrices. Note that in the continuum – with full $SO(3)$ symmetry – O_M has definite spin, parity and baryonic charge.

Using charge conjugation invariance of the action, we get

$$\langle \Omega | O_M | N \rangle = \langle \Omega | O_M^c | N^c \rangle = \pm \langle \Omega | O_M^\dagger | N^c \rangle \quad (\text{B.10})$$

so that if N is the lowest state contributing to Eq. (B.8) for $t \geq 0$, then the lowest contributing state for $t < 0$ is N^c ; the energies and prefactors are therefore the same

and Eq. (B.8) becomes

$$\begin{aligned} C_M(t) &= |\langle \Omega | O | N \rangle|^2 (e^{-t E_N} + e^{-(T-t) E_N}) \\ &= 2 |\langle \Omega | O | N \rangle|^2 e^{-\frac{T}{2} E_N} \cosh \left[E_N \left(t - \frac{T}{2} \right) \right] \end{aligned} \quad (\text{B.11})$$

To extract the mass of the meson ground state, we then just need to set $\mathbf{p} = 0$ in the momentum projection of the interpolator, and consider the *effective mass* m_{eff} defined by the implicit equation

$$\frac{C_M(t)}{C_M(t+1)} = \frac{\cosh \left[m_{\text{eff}} \left(t - \frac{T}{2} \right) \right]}{\cosh \left[m_{\text{eff}} \left(t + 1 - \frac{T}{2} \right) \right]} \quad (\text{B.12})$$

which we solve for each t . For t large enough, m_{eff} is constant and shows a *plateau* which provides the ground state mass.

Baryon correlators

Baryons are fermions made out of three valence quarks with well-defined spin, isospin and parity. We consider the simplest general three-quark interpolator with definite spin and isospin

$$O_B = \epsilon_{abc} \Gamma^A \psi_a^{(1)} \left(\psi_b^{(2)T} \Gamma^B \psi_c^{(3)} \right) \quad (\text{B.13})$$

where Γ^A and Γ^B are monomials of Dirac gamma matrices chosen so that O_B has the wanted spin and isospin.

However, O_B has no definite parity, and hence couples to states with positive or negative parity, denoted $|N^+\rangle$ and $|N^-\rangle$ respectively. Note that these states are fermions, so that $|\langle \Omega | O | N^\pm \rangle|^2$ involves a spin sum $\pi^\pm(\mathbf{p}) = \sum_\sigma |N^\pm(\mathbf{p}; \sigma)\rangle \langle N^\pm(\mathbf{p}; \sigma)|$ where the helicity dependence has been made explicit.

By definition, the fermion free state $|N^\pm\rangle$ has half-integer spin $j = n + \frac{1}{2}$ where n is an integer. We choose $|N^\pm\rangle$ to transform in the $\left[\left(\frac{n}{2}, \frac{n}{2} \right) \right] \otimes \left[\left(\frac{1}{2}, 0 \right) \oplus \left(0, \frac{1}{2} \right) \right]$ representation³ of the Lorentz group. We can then write

$$\langle \Omega | O | N^\pm(\mathbf{p}; \sigma) \rangle^{\mu_1, \dots, \mu_n} = t_{\sigma - \frac{1}{2}}^{\mu_1, \dots, \mu_n}(\mathbf{p}) u_{\frac{1}{2}}^\pm(\mathbf{p}) + t_{\sigma + \frac{1}{2}}^{\mu_1, \dots, \mu_n}(\mathbf{p}) u_{-\frac{1}{2}}^\pm(\mathbf{p}) \quad (\text{B.14})$$

where $u_{\pm \frac{1}{2}}^+(\mathbf{p})$, $u_{\pm \frac{1}{2}}^-(\mathbf{p})$ are Dirac spinors transforming in $(\frac{1}{2}, 0)$, $(0, \frac{1}{2})$ respectively, and $t_{\sigma \pm \frac{1}{2}}^{\mu_1, \dots, \mu_n}(\mathbf{p})$ are traceless symmetric rank- n tensors normalized according to

$$t_\sigma^{\mu_1, \dots, \mu_n}(\mathbf{p}) t_{\sigma'; \mu_1, \dots, \mu_n}^*(\mathbf{p}) = \delta_{\sigma\sigma'} \quad (\text{B.15})$$

³where $\left[\left(\frac{n}{2}, \frac{n}{2} \right) \right]$ denotes the traceless symmetric rank- n tensor representation

Then

$$\begin{aligned} \pi^\pm(\mathbf{p})_{\nu_1, \dots, \nu_n}^{\mu_1, \dots, \mu_n} = & \sum_{\sigma=-(n+1/2)}^{n+1/2} \left[t_{\sigma-\frac{1}{2}}^{\mu_1, \dots, \mu_n}(\mathbf{p}) u_{\frac{1}{2}}^\pm(\mathbf{p}) \bar{u}_{\frac{1}{2}}^\pm(\mathbf{p}) t_{\sigma-\frac{1}{2}}^*_{\nu_1, \dots, \nu_n} \right. \\ & + t_{\sigma-\frac{1}{2}}^{\mu_1, \dots, \mu_n}(\mathbf{p}) u_{\frac{1}{2}}^\pm(\mathbf{p}) \bar{u}_{-\frac{1}{2}}^\pm(\mathbf{p}) t_{\sigma+\frac{1}{2}}^*_{\nu_1, \dots, \nu_n} \\ & + t_{\sigma+\frac{1}{2}}^{\mu_1, \dots, \mu_n}(\mathbf{p}) u_{-\frac{1}{2}}^\pm(\mathbf{p}) \bar{u}_{\frac{1}{2}}^\pm(\mathbf{p}) t_{\sigma-\frac{1}{2}}^*_{\nu_1, \dots, \nu_n} \\ & \left. + t_{\sigma+\frac{1}{2}}^{\mu_1, \dots, \mu_n}(\mathbf{p}) u_{-\frac{1}{2}}^\pm(\mathbf{p}) \bar{u}_{-\frac{1}{2}}^\pm(\mathbf{p}) t_{\sigma+\frac{1}{2}}^*_{\nu_1, \dots, \nu_n} \right] \end{aligned} \quad (\text{B.16})$$

$\pi^\pm(\mathbf{p})^{\mu_1, \dots, \mu_n, \nu_1, \dots, \nu_n}$ is a rank- $2n$ tensor, and can therefore be written as

$$\pi^\pm(\mathbf{p})^{\mu_1, \dots, \mu_n, \nu_1, \dots, \nu_n} = S^\pm(\mathbf{p}) P^{\mu_1, \dots, \mu_n, \nu_1, \dots, \nu_n}(\mathbf{p})$$

with $S(\mathbf{p})$ a Lorentz scalar. Using the normalization Eq. (B.15) in Eq. (B.16), we obtain

$$S^\pm(\mathbf{p}) \propto \sum_{\lambda} u_{\lambda}^\pm(\mathbf{p}) \bar{u}_{\lambda}^\pm(\mathbf{p}) = \gamma \cdot p \pm m$$

so that absorbing constants, we have

$$\pi^\pm(\mathbf{p})^{\mu_1, \dots, \mu_n, \nu_1, \dots, \nu_n} = (\gamma \cdot p \pm m) P^{\mu_1, \dots, \mu_n, \nu_1, \dots, \nu_n}(\mathbf{p}) \quad (\text{B.17})$$

Recalling that O_B couples to both $|N^+\rangle$ and $|N^-\rangle$, and using Eq. (B.17), Eq. (B.5) now states

$$C(t) = \begin{cases} c_+ (\gamma \cdot p + m_{N^+}) e^{-tE_{N^+}} + c_- (\gamma \cdot p - m_{N^-}) e^{-tE_{N^-}} & : t \geq 0 \\ \bar{c}_+ (\gamma \cdot p + m_{\bar{N}^+}) e^{tE_{\bar{N}^+}} + \bar{c}_- (\gamma \cdot p - m_{\bar{N}^-}) e^{tE_{\bar{N}^-}} & : t < 0 \end{cases} \quad (\text{B.18})$$

Note that when $\mathbf{p} = 0$, $\gamma \cdot p \pm m = \pm m(1 \pm \gamma^4)$.

Keeping in mind that charge conjugation changes the parity of fermions – because $C\gamma^\mu C^{-1} = -\gamma^{\mu T}$ where C is the usual charge conjugation matrix acting on spinors, we can now proceed through the same steps as with meson correlators to prove $c_+ = \bar{c}_-$, $c_- = \bar{c}_+$, $\bar{N}^- = (N^+)^c$, $\bar{N}^+ = (N^-)^c$ and we eventually get for the lattice-computed correlator with $\mathbf{p} = 0$:

$$\begin{aligned} C_B(t) = & (1 + \gamma^4) \left(c_{N^+} e^{-tm_{N^+}} + c_{N^-} e^{-(T-t)m_{N^-}} \right) \\ & + (1 - \gamma^4) \left(c_{N^-} e^{-tm_{N^-}} + c_{N^+} e^{-(T-t)m_{N^+}} \right) \end{aligned} \quad (\text{B.19})$$

C. Lüscher equation

In this appendix, we discuss Lüscher’s equation for two-particle states, and present a proof of the generalized Lüscher’s equation for particles in non-rest frames – also called the Rummukainen-Gottlieb equation – valid in quantum field theories and based on [65].

We consider two hadrons of equal mass m with total momentum \mathbf{P} in a cubic box of size L with periodic boundary conditions, and we assume the center-of-mass (COM) energy E^* to sit below the 4π inelastic threshold. We note $2q^*$ the magnitude of the relative momentum so that $E^{*2} = (2q^*)^2 + (2m)^2$. In the case of non-degenerate hadrons, the results are easily generalized with standard modifications to the kinematic relations. In general in this appendix, starred quantities correspond to their COM versions.

C.1. Some useful results

In this section, we present and derive some key ingredients for the following quantization condition.

Summation Formula

In finite volume with given boundary condition – which we take as periodic for the remainder of the section –, available momenta are discrete, so that usual QFT integrals turn to sums. The summation formula we present here relates the generic sums one encounters in finite-volume QFT computations to their infinite volume integral counterparts.

The building block is the Poisson summation formula, which states in our case:

Theorem C.1. *Let $g : \mathbb{R}^3 \rightarrow \mathbb{C}$ be a Schwartz (i.e. a rapidly decreasing) function, and \hat{g} its Fourier transform. Then*

$$\sum_{\mathbf{n} \in \mathbb{Z}^3} g(\mathbf{k}) = \sum_{\mathbf{l} \in \mathbb{Z}^3} \hat{g}(\mathbf{l})$$

.

Proof. We consider

$$G(\mathbf{x}) \equiv \sum_{\mathbf{n} \in \mathbb{Z}^3} g(\mathbf{x} + \mathbf{n})$$

G is 1-periodic, so that it can be expanded in a Fourier series

$$G(\mathbf{x}) = \sum_{\mathbf{l} \in \mathbb{Z}^3} \hat{G}_1 e^{2i\pi \mathbf{l} \cdot \mathbf{x}}$$

with Fourier coefficient

$$\begin{aligned}
\hat{G}_1 &= \int_0^1 d^3\mathbf{x} G(\mathbf{x}) e^{-2i\pi \mathbf{l}\cdot\mathbf{x}} \\
&= \int_0^1 d^3\mathbf{x} \sum_{\mathbf{n}\in\mathbb{Z}^3} g(\mathbf{x} + \mathbf{n}) e^{-2i\pi \mathbf{l}\cdot\mathbf{x}} \\
&= \sum_{\mathbf{n}\in\mathbb{Z}^3} \int_0^1 d^3\mathbf{x} g(\mathbf{x} + \mathbf{n}) e^{-2i\pi \mathbf{l}\cdot\mathbf{x}} \text{ (uniform convergence)} \\
&= \sum_{\mathbf{n}\in\mathbb{Z}^3} \int_n^{n+1} d^3\mathbf{x} g(\mathbf{x}) e^{-2i\pi \mathbf{l}\cdot\mathbf{x}} \\
&= \int_{\mathbb{R}^3} d^3\mathbf{x} g(\mathbf{x}) e^{-2i\pi \mathbf{l}\cdot\mathbf{x}} \\
&= \hat{g}(\mathbf{l})
\end{aligned}$$

Then $G(\mathbf{x}) = \sum_{\mathbf{l}\in\mathbb{Z}^3} \hat{g}(\mathbf{l}) e^{2i\pi \mathbf{l}\cdot\mathbf{x}}$ and evaluating at $\mathbf{x} = 0$ gives the result. \square

Now, we consider functions f such that $\hat{f}(\mathbf{r}) = o_{|\mathbf{r}|\rightarrow\infty}(e^{-|\mathbf{r}|})$. Then

Corollary C.2.

$$\frac{1}{L^3} \sum_{\mathbf{k}\in\frac{2\pi}{L}\mathbb{Z}^3} f(\mathbf{k}) = \int \frac{d^3\mathbf{k}}{(2\pi)^3} f(\mathbf{k}) + o_{L\rightarrow\infty}(e^{-L})$$

Proof. The proof immediately follows from the Fourier scaling property

$$\mathcal{F}[f(ax)](k) = \frac{1}{|a|} \hat{f}\left(\frac{k}{a}\right)$$

and the Poisson summation formula, considering terms $\mathbf{l} = 0$ and $\mathbf{l} \neq 0$ in the sum separately. \square

As we shall see below, the evaluation of finite-volume effects in two-hadron correlators with an energy below the inelastic threshold require formulae for sums of the form

$$S(q^*) \equiv \frac{1}{L^3} \sum_{\mathbf{k}} \frac{\omega_k^*}{\omega_k} \frac{f(\mathbf{k}^*)}{q^{*2} - k^{*2}} \quad (\text{C.1})$$

where the summation is over the moving frame momenta $\mathbf{k} = (2\pi/L)\mathbf{n}$, $\mathbf{n} \in \mathbb{Z}^3$, $\omega_k = \sqrt{k^2 + m^2}$, $\omega_k^* = \sqrt{k^{*2} + m^2}$ and $*$ labels the center-of-mass quantities. The series is well defined for $q \notin (2\pi/L)\mathbb{Z}^3$ since $f(\mathbf{k}) = o_{k\rightarrow\infty}(e^{-k})$. Note that since $\frac{d^3\mathbf{k}}{\omega_k}$ is a Lorentz invariant, we have $\frac{d^3\mathbf{k}}{\omega_k} = \frac{d^3\mathbf{k}^*}{\omega_k^*}$ i.e. $d^3\mathbf{k} \frac{\omega_k^*}{\omega_k} = d^3\mathbf{k}^*$.

The singularities at $k^2 = q^2$ forbid a direct use of the corollary (C.2). Therefore, we define the spherical coordinates $\mathbf{k}^* = (k^*, \theta^*, \phi^*)$ and expand $f(\mathbf{k}^*)$ in spherical harmonics:

$$f(\mathbf{k}^*) = \sum_{l=0}^{\infty} \sum_{m=-l}^l f_{lm}(k^*) k^{*l} \sqrt{4\pi} Y_{lm}(\theta^*, \phi^*) \quad (\text{C.2})$$

We insert in (C.1):

$$S(q^*) = \sum_{l,m} S_{lm}(q^*) \quad (\text{C.3})$$

$$S_{lm}(q^*) = \frac{1}{L^3} \sum_{\mathbf{k}} \frac{\omega_k^*}{\omega_k} \frac{f_{lm}(k^*)}{q^{*2} - k^{*2}} k^{*l} \sqrt{4\pi} Y_{lm}(\theta^*, \phi^*) \quad (\text{C.4})$$

and write

$$\begin{aligned} S_{lm}(q^*) &= \frac{1}{L^3} \sum_{\mathbf{k}} \frac{\omega_k^*}{\omega_k} \frac{f_{lm}(k^*) - f_{lm}(q^*) e^{\alpha(q^{*2} - k^{*2})}}{q^{*2} - k^{*2}} k^{*l} \sqrt{4\pi} Y_{lm}(\theta^*, \phi^*) \\ &\quad + \frac{1}{L^3} \sum_{\mathbf{k}} \frac{\omega_k^*}{\omega_k} \frac{f_{lm}(q^*) e^{\alpha(q^{*2} - k^{*2})}}{q^{*2} - k^{*2}} k^{*l} \sqrt{4\pi} Y_{lm}(\theta^*, \phi^*) \end{aligned} \quad (\text{C.5})$$

for $\alpha > 0$, to cancel the poles at $k^2 = q^2$ and ensure convergence of the series. Note that the $e^{\alpha(q^{*2} - k^{*2})}$ term was introduced to prevent ultraviolet divergence in the subtracted part, but the result is independent of α .

The use of corollary (C.2) on the first part of the right-hand side of equation (C.5) gives (neglecting the exponentially suppressed corrections)

$$\frac{1}{L^3} \sum_{\mathbf{k}} \frac{\omega_k^*}{\omega_k} \frac{f_{lm}(k^*) - f_{lm}(q^*) e^{\alpha(q^{*2} - k^{*2})}}{q^{*2} - k^{*2}} k^{*l} \sqrt{4\pi} Y_{lm}(\theta^*, \phi^*) \quad (\text{C.6})$$

$$= \int \frac{d^3\mathbf{k}}{(2\pi)^3} \frac{\omega_k^*}{\omega_k} \frac{f_{lm}(k^*) - f_{lm}(q^*) e^{\alpha(q^{*2} - k^{*2})}}{q^{*2} - k^{*2}} k^{*l} \sqrt{4\pi} Y_{lm}(\theta^*, \phi^*) \quad (\text{C.7})$$

$$= \int \frac{d^3\mathbf{k}^*}{(2\pi)^3} \frac{f_{lm}(k^*) - f_{lm}(q^*) e^{\alpha(q^{*2} - k^{*2})}}{q^{*2} - k^{*2}} k^{*l} \sqrt{4\pi} Y_{lm}(\theta^*, \phi^*) \quad (\text{C.8})$$

$$= \delta_{l0} \int \frac{d^3\mathbf{k}^*}{(2\pi)^3} \frac{f_{00}(k^*) - f_{00}(q^*) e^{\alpha(q^{*2} - k^{*2})}}{q^{*2} - k^{*2}} \quad (\text{C.9})$$

where in the last step, we use the rotation invariance of the integrand¹. Since there is no pole in (C.6), we can regulate the integral (C.9) with the principal value prescription, denoted \mathcal{P} . Hence, one gets

$$\begin{aligned} S_{lm}(q^*) &= \delta_{l0} \mathcal{P} \int \frac{d^3\mathbf{k}^*}{(2\pi)^3} \frac{f_{00}(k^*)}{q^{*2} - k^{*2}} - \delta_{l0} f_{00}(q^*) \mathcal{P} \int \frac{d^3\mathbf{k}^*}{(2\pi)^3} \frac{e^{\alpha(q^{*2} - k^{*2})}}{q^{*2} - k^{*2}} \\ &\quad + f_{lm}(q^*) \frac{1}{L^3} \sum_{\mathbf{k}} \frac{\omega_k^*}{\omega_k} \frac{e^{\alpha(q^{*2} - k^{*2})}}{q^{*2} - k^{*2}} k^{*l} \sqrt{4\pi} Y_{lm}(\theta^*, \phi^*) \end{aligned} \quad (\text{C.10})$$

¹A rotation-invariant quantity is proportional to $Y_{00} = \sqrt{4\pi}$, and the spherical harmonics are orthogonal with each other.

Rotation-invariance of the first integral and re-summation over l, m lead finally to the result

$$\frac{1}{L^3} \sum_{\mathbf{k}} \frac{\omega_k^*}{\omega_k} \frac{f(\mathbf{k}^*)}{q^{*2} - k^{*2}} = \mathcal{P} \int \frac{d^3 \mathbf{k}^*}{(2\pi)^3} \frac{f(\mathbf{k}^*)}{q^{*2} - k^{*2}} + \sum_{l=0}^{\infty} \sum_{m=-l}^l f_{lm}(q^*) c_{lm}^{MV}(q^{*2}) \quad (\text{C.11})$$

with

$$\begin{aligned} c_{lm}^{MV}(q^{*2}) &= \frac{1}{L^3} \sum_{\mathbf{k}} \frac{\omega_k^*}{\omega_k} \frac{e^{\alpha(q^{*2} - k^{*2})}}{q^{*2} - k^{*2}} k^{*l} \sqrt{4\pi} Y_{lm}(\theta^*, \phi^*) \\ &\quad - \delta_{l0} \mathcal{P} \int \frac{d^3 \mathbf{k}^*}{(2\pi)^3} \frac{e^{\alpha(q^{*2} - k^{*2})}}{q^{*2} - k^{*2}} \end{aligned} \quad (\text{C.12})$$

The last step is to relate the $c_{lm}^{MV}(q^{*2})$ to the zeta functions

$$\mathcal{Z}_{lm}^{MV}(s; a^2) = \sum_{\mathbf{n} \in \mathbb{Z}^3} \frac{1}{(r_{\mathbf{n}}^2 - a^2)^s} r_{\mathbf{n}}^l Y_{lm}(\hat{\mathbf{r}}_{\mathbf{n}}) \quad (\text{C.13})$$

$$\mathbf{r}_{\mathbf{n}} = \frac{1}{\gamma} \left(\mathbf{n}_{\parallel} - \left(\frac{L}{2\pi} \right) \frac{\mathbf{P}}{2} \right) + \mathbf{n}_{\perp} \quad (\text{C.14})$$

$$\mathbf{n}_{\parallel} = \frac{(\mathbf{n} \cdot \mathbf{P}) \mathbf{P}}{P^2} \text{ and } \mathbf{n}_{\perp} = \mathbf{n} - \mathbf{n}_{\parallel} \quad (\text{C.15})$$

analytically continued to the whole (s -)complex plane. However, since we chose to use an "exponential" regularization of the sums involved – instead of the analytic "zeta-function regularization" –, one can only expect the relation between $c_{lm}^{MV}(q^{*2})$ and \mathcal{Z}_{lm}^{MV} to be up to terms exponentially suppressed with L , as highlighted in [65].

The key idea is to re-express the factor $\frac{\omega_k^*}{\omega_k} \frac{1}{q^{*2} - k^{*2}}$ in terms of r , using relations given by the Lorentz transforms recalling the definitions

$$E^* = \frac{E}{\gamma} \quad (\text{C.16})$$

$$\beta = \frac{P}{E} \quad (\text{C.17})$$

$$\omega_k^* = \sqrt{k_{\parallel}^{*2} + m^2} \quad (\text{C.18})$$

$$\omega_k = \gamma(\omega_k^* + \beta k_{\parallel}^*) \quad (\text{C.19})$$

$$k_{\parallel} = \gamma(k_{\parallel}^* + \beta \omega_k^*) \quad (\text{C.20})$$

$$\mathbf{k}_{\perp} = \mathbf{k}_{\perp}^* \quad (\text{C.21})$$

Then we have

$$k^{*2} - r_{\mathbf{k}}^2 = k_{\parallel}^{*2} + k_{\perp}^{*2} - r_{\mathbf{k}_{\parallel}}^2 - r_{\mathbf{k}_{\perp}}^2 \quad (\text{C.22})$$

$$= k_{\parallel}^{*2} - r_{\mathbf{k}_{\parallel}}^2 \quad (\text{C.23})$$

$$= k_{\parallel}^{*2} - \frac{1}{\gamma^2} \left(k_{\parallel}^2 - k_{\parallel} P + \frac{P^2}{4} \right) \quad (\text{C.24})$$

$$= 2\beta k_{\parallel}^* \left(\frac{E^*}{2} - \omega_k^* \right) - \beta^2 \left(\frac{E^*}{2} - \omega_k^* \right)^2 \quad (\text{C.25})$$

after some basic manipulations, and

$$\frac{E^*}{2} - \omega_k^* = \frac{(E^*/2)^2 - \omega_k^{*2}}{2\omega_k^*} + O \left(\frac{E^*}{2} - \omega_k^* \right)^2 \quad (\text{C.26})$$

$$= \frac{q^{*2} - k^{*2}}{2\omega_k^*} + O \left(\frac{E^*}{2} - \omega_k^* \right)^2 \quad (\text{C.27})$$

together with (C.19) leads to

$$q^{*2} - r_{\mathbf{k}}^2 = \frac{\omega_k}{\gamma\omega_k^*} (q^{*2} - k^{*2}) + O \left(q^{*2} - k^{*2} \right)^2 \quad (\text{C.28})$$

When inserted in the expression (C.12) for c_{lm}^{MV} , the $O \left(q^{*2} - k^{*2} \right)^2$ terms give rise to *non-singular* functions of \mathbf{k} which only contribute through exponentially suppressed terms when applying the Poisson formula (C.2). After some manipulations², we can therefore show that up to terms exponentially suppressed with L ,

$$c_{lm}^{MV}(q^{*2}) = -\frac{\sqrt{4\pi}}{\gamma L^3} \left(\frac{2\pi}{L} \right)^{l-2} \mathcal{Z}_{lm}^{MV}(1; \tilde{q}^{*2}) \quad (\text{C.29})$$

where we have introduced the lattice-unit momentum

$$\tilde{q}^* = \frac{L}{2\pi} q^* \quad (\text{C.30})$$

Equation (C.11) now reads

$$\begin{aligned} \frac{1}{L^3} \sum_{\mathbf{k}} \frac{\omega_k^*}{\omega_k} \frac{f(\mathbf{k}^*)}{q^{*2} - k^{*2}} &= \mathcal{P} \int \frac{d^3\mathbf{k}^*}{(2\pi)^3} \frac{f(\mathbf{k}^*)}{q^{*2} - k^{*2}} \\ &- \frac{\sqrt{4\pi}}{\gamma L^3} \sum_{l=0}^{\infty} \sum_{m=-l}^l f_{lm}(q^*) \left(\frac{2\pi}{L} \right)^{l-2} \mathcal{Z}_{lm}^{MV}(1; \tilde{q}^{*2}) \end{aligned} \quad (\text{C.31})$$

²Which can be found in details in [65]

Bethe-Salpeter kernels

The spectrum of two-particle states in finite-volume can be extracted from the exponential dependence of correlation functions of composite – interpolating – operators σ of the form

$$\langle \tilde{\sigma}_{\mathbf{P}}(t) \sigma^\dagger(\mathbf{0}, \mathbf{0}) \rangle \quad (\text{C.32})$$

with implicit time-ordering of the operators. Then, the energy eigenvalues correspond to poles of the correlation function in energy space³

$$\tilde{C}_{\mathbf{P}}(E) \equiv \int dt e^{-iEt} \langle \tilde{\sigma}_{\mathbf{P}}(t) \sigma^\dagger(\mathbf{0}, \mathbf{0}) \rangle \quad (\text{C.33})$$

In order to study the finite-volume effects on such correlators, we follow [63] and consider the expansion of $\tilde{C}_{\mathbf{P}}(E)$ in terms of Bethe-Salpeter kernels, which we define below.

Let $G^{(4)}(p_1, p_2, p_3, p_4)$ be the full connected 4-point function for some theory. We define the Bethe-Salpeter kernel K as the 2-particle irreducible amputated 4-point function, related to G with the Schwinger-Dyson integral equation

$$G = K + \frac{1}{2} K G^{(2)} G \quad (\text{C.34})$$

which we can formally write

$$G^{(4)} = K + \frac{1}{2} K G_2 G^{(4)}$$

with $G_2 \equiv G^{(2)} \left(\frac{P}{2} + k \right) G^{(2)} \left(\frac{P}{2} - k \right)$, $G^{(2)}$ being the "dressed" correlator – or two-point function, P the total momentum flowing through K , and k the "loop" momentum. We can iterate this equation to obtain a series expression for G , which reads

$$G^{(4)} = K + \frac{1}{2} K G_2 K + \frac{1}{2^2} K G_2 K G_2 K + \dots \quad (\text{C.35})$$

These expressions can be straightforwardly transposed in finite-volume with a 4-point function G_L expanded in terms of the finite-volume Bethe-Salpeter kernel K_L and G_{2L} , all integrals over space components of the loop momenta being replaced by sums over the lattice momenta.

The interest of the expressions of G and G_L in terms of K or K_L comes from the analytic properties of the kernel when the total energy $E = P_0$ is below the 4-particle threshold and the relative energies of both the two incoming and outgoing particles are

³Since $\int dt e^{-iEt} e^{-E_n t} \theta(t) = \frac{-i}{E - iE_n}$ where $\theta(t)$ is the Heaviside function.

below the 1-particle threshold, as discussed in [63]: in this case, K is an analytic non-singular function of the momenta flowing through it, and one can prove that $K_L - K$ decays exponentially as $L \rightarrow \infty$. The same is also true for the single particles dressed propagators, so that these expansions allow us to identify the power-law volume effects as coming only from the two-particle loops.


If we consider the correlation function

$$\tilde{C}_{\mathbf{P}}(E) = \int dt e^{-iEt} \langle \tilde{\sigma}_{\mathbf{P}}(t) \sigma^\dagger(\mathbf{0}, \mathbf{0}) \rangle$$

in the case where σ is a two-particle interpolating operator – for example a pion-pion interpolating field as we shall discuss in greater details later –, we know that in perturbation theory, $\tilde{C}_{\mathbf{P}}(E)$ can be expressed as the integral equation

$$\tilde{C}_{\mathbf{P}}(E) = \frac{G_2}{(2\pi)} + \frac{1}{2} \frac{1}{(2\pi)^2} G_2 G^{(4)} G_2 \quad (\text{C.36})$$

where the symmetry factors are not explicitly written and the $\frac{1}{(2\pi)}$ factors account for the loops over p_0 's. Inserting (C.35), we have the expansion of $\tilde{C}_{\mathbf{P}}(E)$ in terms of the kernel K as



$$(\text{C.37})$$

Note that this expansion can be directly used for the finite-volume correlator, with all quantities replaced by their finite-volume counterparts.

We are now ready to use the tools presented above to evaluate the finite-volume effects, expressed under the form of the aforementioned quantization condition.

C.2. Quantization Condition

In finite volume, the usual infinite-volume branch cut of the S matrix in the s -plane⁴ which corresponds to two-particle – ”on shell” – states turns into a series of poles, associated with the quantized energy values. In this section, we study the influence of the size of the ”box” on the position of these poles quantitatively and relate this influence to the infinite-volume phase shifts.

As mentioned above, we start from the correlation function $\tilde{C}_{\mathbf{P}}(E)$ and focus on the finite-volume corrections, defining

$$\tilde{C}_{\mathbf{P}}^{FV}(E) \equiv \tilde{C}_{\mathbf{P}}(E) - \tilde{C}_{\mathbf{P}}^{\infty}(E) \quad (\text{C.38})$$

⁴ $s = E^2 - P^2$ is the Mandelstam variable.

which only contains the poles we are looking for.

We use the expansion (C.37) for both $\tilde{C}_{\mathbf{P}}(E)$ and $\tilde{C}_{\mathbf{P}}^{\infty}(E)$ and diagrammatically evaluate the difference. Note that this procedure is therefore valid in perturbation field theory to all orders, and seems to be also valid non-perturbatively as discussed in [62].

The expansion (C.37) is particularly useful here since as mentioned above, the finite-volume meson self-energy and the Bethe-Salpeter kernel differ from their infinite volume counterparts only through exponentially L -dependent terms in the energy region we consider, so that up to exponentially suppressed terms, $G_{2L} = G_2$ and $K = K_L$. The only finite-volume correction comes from the two-particle loops, which we write symbolically L .

Then, we can formally write – leaving the symmetry factors out –

$$\begin{aligned}
\tilde{C}_{\mathbf{P}}^{FV}(E) &= (L^{FV} + L^{\infty}) + (L^{FV} + L^{\infty})K(L^{FV} + L^{\infty}) + \dots \\
&\quad - L^{\infty} - L^{\infty}KL^{\infty} - \dots \\
&= L^{FV} + L^{FV}KL^{FV} + L^{FV}KL^{\infty} + L^{\infty}KL^{FV} + \dots \\
&= \underbrace{(1 + L^{\infty}K + L^{\infty}KL^{\infty}K + \dots)}_{A'} L^{FV} \\
&\quad \underbrace{(1 + KL^{\infty} + KL^{\infty}KL^{\infty} + \dots)}_A \\
&\quad + A' L^{FV} \underbrace{(K + KL^{\infty}K + KL^{\infty}KL^{\infty}K + \dots)}_{iM/2} L^{FV} A \\
&\quad + A' L^{FV} \left(\frac{iM}{2}\right) L^{FV} \left(\frac{iM}{2}\right) L^{FV} A + \dots \\
&= A' L^{FV} \frac{1}{1 - i\frac{ML^{FV}}{2}} A
\end{aligned} \tag{C.39}$$

where we haven't written the $\frac{1}{2\pi}$ factors for clarity. For the moment, we just note that A and A' are matrix elements which couple the external operators to the on-shell two-particle states and turn to an evaluation of the quantities involved in this expression, before considering the main result of the section.

Generic Loop Summation

In this subsection, we evaluate the needed L^{FV} contribution appearing in the expansion (C.39) for $\tilde{C}_{\mathbf{P}}^{FV}(E)$. Following the notation of [65], we call I the generic loop integration appearing in (C.37) and define

$$I^{FV} = I - I^{\infty} \tag{C.40}$$

Then I is of the form

$$I \equiv \frac{1}{L^3} \sum_{\mathbf{k}} \int \frac{dk_0}{2\pi} \frac{i^2 f(k_0, \mathbf{k})}{(k^2 - m^2 + i\epsilon)((P - k)^2 - m^2 + i\epsilon)} \tag{C.41}$$

where f is a smooth function which accounts for the energy-momentum dependence related to the dressing of the propagators and the kernels – or the σ matrix element – on the "sides" of the loop. Since we focus on the sector $0 < E^2 - P^2 < (4m)^2$, f has no singularity for real \mathbf{k} , and its Fourier transform $\hat{f}(\mathbf{r})$ has a finite range.

The integrand is singular, with poles shifted with Feynman's prescription, and closing the contour, we perform the k_0 integration and use the theorem of residues to obtain

$$I = i \frac{1}{L^3} \sum_{\mathbf{k}} \left\{ \frac{f(\omega_k, \mathbf{k})}{2\omega_k((E - \omega_k)^2 - \omega_{P-k}^2)} + \frac{f(\omega_{P-k}, \mathbf{k})}{2\omega_{P-k}((E + \omega_{P-k})^2 - \omega_k^2)} \right\} \quad (\text{C.42})$$

with

$$\omega_k = \sqrt{\mathbf{k}^2 + m^2} \text{ and } \omega_{P-k} = \sqrt{(\mathbf{P} - \mathbf{k})^2 + m^2} \quad (\text{C.43})$$

Note that the limit $\epsilon = 0$ has been taken. This is possible as long as the poles in the summand do not coincide with allowed values of \mathbf{k} in the sum, which is generally the case since the energies are shifted from the "free" values by the interaction.

In the energy range we consider ($0 < E^2 - P^2 < (4m)^2$), the only singularity in the summand is a pole at $E = \omega_k + \omega_{P-k}$ in the first term inside the sum in (C.42). We can then directly apply the Poisson Summation Formula corollary (C.2) to the other term and write

$$I = I_1 + I_2 \quad (\text{C.44})$$

with

$$I_1 = i \frac{1}{L^3} \sum_{\mathbf{k}} \frac{f(\omega_k, \mathbf{k})}{2\omega_k((E - \omega_k)^2 - \omega_{P-k}^2)} \quad (\text{C.45})$$

$$I_2 = i \int \frac{d^3k}{(2\pi)^3} \frac{f(\omega_{P-k}, \mathbf{k})}{2\omega_{P-k}((E + \omega_{P-k})^2 - \omega_k^2)} \quad (\text{C.46})$$

i.e. $I_2^{FV} = 0$ – up to exponentially suppressed terms. We now focus on I_1 to determine I^{FV} . We first express it in the center-of-mass frame using equations (C.16)-(C.21) and rearrange to get

$$I_1 = i \frac{1}{L^3} \frac{1}{2E^*} \sum_{\mathbf{k}} \frac{\omega_k^*}{\omega_k} \frac{f^*(\mathbf{k}^*)}{(q^{*2} - k^{*2})} \frac{E^* + 2\omega_k^*}{4\omega_k^*} \quad (\text{C.47})$$

where the poles $q^{*2} = k^{*2}$ have been exhibited. In this form, we can directly use Eq. (C.31) to write

$$I_1 = i \frac{1}{2E^*} \mathcal{P} \int \frac{d^3k}{(2\pi)^3} \frac{f^*(\mathbf{k}^*)}{(q^{*2} - k^{*2})} \frac{E^* + 2\omega_k^*}{4\omega_k^*} - \frac{i}{2E^*} \frac{\sqrt{4\pi}}{\gamma L^3} \sum_{l=0}^{\infty} \sum_{m=-l}^l f_{lm}(q^*) \left(\frac{2\pi}{L} \right)^{l-2} \mathcal{Z}_{lm}^{MV}(1; \tilde{n}^{*2}) \quad (\text{C.48})$$

Finally, to pick out the infinite-volume contribution, we replace the principal value integral by the corresponding Feynman $i\epsilon$ prescription integral, which introduces an

extra – residual – term proportional to $f_{00}(q^*)$ (because of rotation-invariance) and I_1 now reads

$$\begin{aligned}
I_1 = & i \frac{1}{2E^*} \mathcal{P} \int \frac{d^3k}{(2\pi)^3} \frac{f^*(\mathbf{k}^*)}{(q^{*2} - k^{*2} + i\epsilon)} \frac{E^* + 2\omega_k^*}{4\omega_k^*} \\
& - \frac{q^* f_{00}(q^*)}{8\pi E^*} \\
& - \frac{i}{2E^*} \frac{\sqrt{4\pi}}{\gamma L^3} \sum_{l=0}^{\infty} \sum_{m=-l}^l f_{lm}(q^*) \left(\frac{2\pi}{L}\right)^{l-2} \mathcal{Z}_{lm}^{MV}(1; \tilde{n}^{*2})
\end{aligned} \tag{C.49}$$

We then arrive at the result

$$I^{FV} = -\frac{q^* f_{00}(q^*)}{8\pi E^*} - \frac{i}{2E^*} \frac{\sqrt{4\pi}}{\gamma L^3} \sum_{l=0}^{\infty} \sum_{m=-l}^l f_{lm}(q^*) \left(\frac{2\pi}{L}\right)^{l-2} \mathcal{Z}_{lm}^{MV}(1; \tilde{n}^{*2}) \tag{C.50}$$

Recalling the definition of f_{lm} and using the spherical harmonics orthogonality and completeness, we can isolate the loop part and project it in the partial wave basis to obtain

$$L_{l_1, m_1; l_2, m_2}^{FV} = -\frac{q^*}{8\pi E^*} (\delta_{l_1, l_2} \delta_{m_1, m_2} + i \mathfrak{L}_{l_1, m_1; l_2, m_2}^{FV}) \tag{C.51}$$

$$\mathfrak{L}_{l_1, m_1; l_2, m_2}^{FV} = \frac{(4\pi)^2}{q^* \gamma L^3} \sum_{l, m} \frac{1}{q^{*l}} \left(\frac{2\pi}{L}\right)^{l-2} \mathcal{Z}_{lm}^{MV}(1; \tilde{n}^{*2}) \int d\Omega^* Y_{l_1, m_1}^* Y_{l, m}^* Y_{l_2, m_2} \tag{C.52}$$

where the integral can be expressed in terms of Wigner 3j-symbols⁵ as

$$\begin{aligned}
\int d\Omega^* Y_{l_1, m_1}^* Y_{l, m}^* Y_{l_2, m_2} = & (-1)^{m_1+m} \sqrt{\frac{(2l_1+1)(2l+1)(2l_2+1)}{4\pi}} \\
& \begin{pmatrix} l_1 & l & l_2 \\ 0 & 0 & 0 \end{pmatrix} \begin{pmatrix} l_1 & l & l_2 \\ -m_1 & -m & m_2 \end{pmatrix}
\end{aligned} \tag{C.53}$$

The "M" matrix

In this section, we look closely at the M matrix defined in (C.39) with

$$\frac{iM}{2} = \frac{1}{(2\pi)} \left(K + \frac{1}{2} KL^\infty K + \frac{1}{2^2} KL^\infty KL^\infty K + \dots \right) \tag{C.54}$$

recalling the $\frac{1}{2\pi}$ factor which was skipped for clarity purposes.

We recognize in (C.54) the expression for the renormalized amputated four-point function $G_{amp}^{(4)}$, i.e., reintroducing the symmetry factors,

$$\frac{iM}{2} = \frac{1}{(2\pi)} G_{amp}^{r(4)} \tag{C.55}$$

⁵The spherical harmonics form a basis for different irreducible representations of the rotation group, see [110].

Working in the center-of-mass, we can use the reduction formula to relate S -matrix elements to Green functions, to write $\frac{iM}{2}$ in terms of the *on-shell* transition matrix defined above. The LSZ reduction formula, with states normalized as $\langle \mathbf{p} | \mathbf{p}' \rangle = \delta(\mathbf{p} - \mathbf{p}')$ reads⁶

$$G_{amp}^{r(4)}(\mathbf{p1}, \mathbf{p2}, \mathbf{k1}, \mathbf{k2}) = -(2\pi)^6 E^{*2} \langle \mathbf{p1}, \mathbf{p2} | S | \mathbf{k1}, \mathbf{k2} \rangle \quad (\text{C.56})$$

If we drop the trivial part of the S matrix, and project onto the energy shell, we obtain – in the center-of-mass frame –

$$\begin{aligned} G_{amp}^{r(4)}(\mathbf{p1}, \mathbf{p2}, \mathbf{k1}, \mathbf{k2}) &= -(2\pi)^6 E^{*2} \frac{dE^*/dq^*}{(2\pi)^4 q^{*2}} \langle \mathbf{p1}, \mathbf{p2} | S - 1 | \mathbf{k1}, \mathbf{k2} \rangle_{on-shell} \\ &= -(2\pi)^2 \frac{2E^*}{q^*} \langle \mathbf{p1}, \mathbf{p2} | S - 1 | \mathbf{k1}, \mathbf{k2} \rangle_{on-shell} \end{aligned} \quad (\text{C.57})$$

where we have used $E^* = 2\sqrt{q^{*2} + m^2}$ and

$$\frac{dE^*}{dq^*} = \frac{d(2\sqrt{q^{*2} + m^2})}{dq^*} = \frac{2q^*}{E^*}$$

In the partial wave basis, the on-shell S matrix is diagonal, with eigenvalues $S_l = e^{2i\delta_l}$, which implies

$$M_{l_1, m_1; l_2, m_2} = \delta_{l_1, l_2} \delta_{m_1, m_2} \frac{16\pi E^*}{q^*} \frac{e^{2i\delta_{l_1}} - 1}{2i} \quad (\text{C.58})$$

The condition

In this section, we finally put all the results together to write the quantization condition imposed by the finite volume of the "box".

We recall

$$\tilde{C}_{\mathbf{P}}^{FV}(E) = A' L^{FV} \frac{1}{1 - i \frac{ML^{FV}}{2}} A$$

Written in the partial wave basis, A and A' simply turn to unknown vectors A_{lm} and A'_{lm} , irrelevant for our discussion. In fact, as already mentioned, we want to find the poles since these correspond to the finite-volume energy eigenvalues. These poles in $\tilde{C}_{\mathbf{P}}^{FV}(E)$ are determined by the singularities of

$$L^{FV} \frac{1}{1 - i \frac{ML^{FV}}{2}}$$

In absence of interaction (i.e. $M = 0$), they are given by the poles of L^{FV} , which come from \mathcal{Z}_{lm}^{MV} . But when the interaction is turned on, these poles are shifted⁷ to the

⁶Usually, this formula is written in terms of states with the relativistic normalization $\langle \mathbf{p} | \mathbf{p}' \rangle = (2\pi)^3 (2E_p) \delta(\mathbf{p} - \mathbf{p}')$. This difference in the normalization of states introduces the factor $(2\pi)^6 (2E_p)^2 = (2\pi)^6 E^{*2}$.

⁷In fact, if a is a pole of L^{FV} (projected in the partial wave basis for example), then $L^{FV}(z) = \frac{H(z)}{(z-a)^n}$ with H some holomorphic matrix and n a positive integer. So that defining $m \equiv iM(z)/2$, we have $L^{FV} \frac{1}{1 - i \frac{ML^{FV}}{2}} = \frac{H(z)}{(z-a)^n} \frac{1}{1 - m \frac{H(z)}{(z-a)^n}} = \frac{H(z)}{(z-a)^{n-mH(z)}}$ and we see that the pole is indeed shifted to the solution of $1 - i \frac{ML^{FV}}{2} = 0$.

solutions of

$$\left(1 - i \frac{ML^{FV}}{2}\right) v = 0$$

which implies the formal quantization condition

$$\det \left(1 - i \frac{ML^{FV}}{2}\right) = 0 \quad (\text{C.59})$$

with

$$M_{l_1, m_1; l_2, m_2} = \delta_{l_1, l_2} \delta_{m_1, m_2} \frac{16\pi E^*}{q^*} \frac{e^{2i\delta_{l_1}} - 1}{2i} \quad (\text{C.60})$$

$$L_{l_1, m_1; l_2, m_2}^{FV} = -\frac{q^*}{8\pi E^*} (\delta_{l_1, l_2} \delta_{m_1, m_2} + i \mathfrak{L}_{l_1, m_1; l_2, m_2}^{FV}) \quad (\text{C.61})$$

$$\mathfrak{L}_{l_1, m_1; l_2, m_2}^{FV} = \frac{(4\pi)^2}{q^* \gamma L^3} \sum_{l, m} \frac{1}{q^{*l}} \left(\frac{2\pi}{L}\right)^{l-2} \mathcal{Z}_{lm}^{MV}(1; \tilde{n}^{*2}) \int d\Omega^* Y_{l_1, m_1}^* Y_{l, m}^* Y_{l_2, m_2} \quad (\text{C.62})$$

This equation is the main result of the section. It provides the relation between the infinite-volume phase-shifts – hold in $M_{l_1, m_1; l_2, m_2}$ – and kinematical finite-volume effects – the matrix $L_{l_1, m_1; l_2, m_2}^{FV}$ in the form of an infinite secular equation. However, to be of practical use, this formula needs to be truncated with some angular momentum cut-off and projected out to some symmetry sector. We shall discuss the latter in Appendix D and focus on the former in the next section.

C.3. Angular momentum cut-off

When working at sufficiently low energy, only the lowest partial wave phase-shifts contribute to the cross-section, and therefore to the scattering amplitude M . Indeed, the restriction to a finite number of contributing partial waves is necessary to make the condition (C.59) a practical tool for computations. Here we discuss the truncation of the determinant through the application of an angular momentum cut-off l_{max} , and consequently assume that $\delta_l = 0$ for $l > l_{max}$, which implies

$$M_{l_1, m_1; l_2, m_2} = 0, \forall l_1, l_2 > l_{max}$$

and we prove that in this case, the quantization condition is equivalent to its restriction to the block $l_1, l_2 \leq l_{max}$, i.e.

$$\det \left(1 - i \frac{ML^{FV}}{2}\right) \Big|_{l_1, l_2 \leq l_{max}} = 0 \quad (\text{C.63})$$

This result is not a straightforward restriction of (C.59) since L^{FV} connects for example sectors with $l_1 \leq l_{max}$ to sectors with $l_2 > l_{max}$. To obtain it, we need to return

to the expansion (C.39) and apply the cut-off. If we denote Π the projection operator onto the subspace $l \leq l_{max}$, then we have by assumption $M = M_{\Pi} \equiv \Pi M \Pi$, so that

$$\begin{aligned}
\tilde{C}_{\mathbf{P}}^{FV}(E) &= A' L^{FV} A + A' L^{FV} \left(\frac{iM}{2} \right) L^{FV} A \\
&\quad + A' L^{FV} \left(\frac{iM}{2} \right) L^{FV} \left(\frac{iM}{2} \right) L^{FV} A + \dots \\
&= A' L^{FV} A + A' L^{FV} \Pi \left(\frac{iM}{2} \right) \Pi L^{FV} A \\
&\quad + A' L^{FV} \Pi \left(\frac{iM}{2} \right) \Pi L^{FV} \Pi \left(\frac{iM}{2} \right) \Pi L^{FV} A + \dots \\
&= A' L^{FV} A + A' L^{FV} \Pi \left(\frac{iM}{2} \right) \left(1 + L_{\Pi}^{FV} \left(\frac{iM}{2} \right) + \dots \right) \Pi L^{FV} A \\
&= A' \left(L^{FV} + L^{FV} \Pi \left(\frac{iM}{2} \right) \frac{1}{1 - L_{\Pi}^{FV} \left(\frac{iM}{2} \right)} \Pi L^{FV} \right) A \\
&= A' L^{FV} \Pi \left(\frac{iM}{2} \right) \left[\frac{1}{1 - L_{\Pi}^{FV} \left(\frac{iM}{2} \right)} \right] A
\end{aligned} \tag{C.64}$$

where the matrix inverse denotes a matrix with the inverse of the block in the "Π" subspace and zeros everywhere else. Then we see that the pole of L^{FV} is again shifted by the interaction, and the new poles are to be found solving $\det(1 - L_{\Pi}^{FV} m) = 0$, i.e. multiplying right and left by the determinant of m and m^{-1} in the subspace

$$\det \left(1 - i \frac{ML^{FV}}{2} \right) \Big|_{l_1, l_2 \leq l_{max}} = 0 \tag{C.65}$$

which gives the result.

D. Lüscher equation and symmetries

D.1. Introduction

We now want to use the quantization condition discussed in Appendix C to extract the physical resonance parameters of the ρ , the unstable neutral meson identified in $\pi^+\pi^-$ scattering processes in the isospin $I = 1$ channel. On the lattice, one way to deal with such a dynamical effect is to use the formalism we set up before to compute $\pi^+\pi^-$ scattering phase-shifts. Recalling the expression of the scattering cross-section in terms of partial-wave phase-shifts

$$\sigma = \frac{4\pi}{p^2} \sum_{l=0}^{\infty} (2l+1) \sin^2 \delta_l$$

we see that the mass and width of the ρ can be identified as the position where the leading P-wave contributing phase shift passes $\frac{\pi}{2}$ and $\frac{\pi}{4}$ respectively.

We shall therefore in this section briefly present the different physical frames and the corresponding interpolating operators to be used for Lattice QCD calculations and analyse the symmetries of the system to derive “practical use” formulas expressing the quantization condition.

D.2. Kinematics

We consider a system of two π mesons in a cubic box of volume L^3 . For the moment, we assume that the pions are not interacting, and we study the energy levels of the system as functions of L the size of the box.

In the laboratory frame – i.e. the box rest frame –, the total energy is given by

$$E_L = \sqrt{\mathbf{p}_1^2 + m_\pi^2} + \sqrt{\mathbf{p}_2^2 + m_\pi^2} \quad (\text{D.1})$$

where \mathbf{p}_1 and \mathbf{p}_2 are the 3-momenta of the pions.

If we now impose periodic boundary conditions on our box, the momenta are quantized to values

$$\mathbf{p}_i = \frac{2\pi}{L} \mathbf{n}_i, \quad \mathbf{n} \in \mathbb{Z}^3 \quad (\text{D.2})$$

and the total momentum $\mathbf{P} = \mathbf{p}_1 + \mathbf{p}_2$ is similarly quantized.

If $\mathbf{P} = 0$, then the laboratory frame corresponds to the center-of-mass (COM) frame, and $\mathbf{p}_1 = -\mathbf{p}_2$ which implies

$$E_{COM}^{P=0} = 2 \sqrt{\left(\frac{2\pi}{L} \mathbf{n}\right)^2 + m_\pi^2} \quad (\text{D.3})$$

and if $\mathbf{P} = \frac{2\pi}{L} \mathbf{e}_3$ for example – one of the lowest non-zero values for P –, we have $\mathbf{p}_1 = \frac{2\pi}{L}(\mathbf{n} + \mathbf{e}_3)$ and $\mathbf{p}_2 = -\frac{2\pi}{L}\mathbf{n}$, so that using the relativistic relation $E_{COM}^2 = E_L^2 - \mathbf{P}^2$ we obtain

$$E_{COM}^P = \sqrt{\left(\sqrt{\mathbf{p}_1^2 + m_\pi^2} + \sqrt{\mathbf{p}_2^2 + m_\pi^2}\right)^2 - \left(\frac{2\pi}{L}\right)^2} \quad (\text{D.4})$$

Fig. D.1 gives a schematic plot of the energy levels of non-interacting particles in the box for several values of \mathbf{n} .

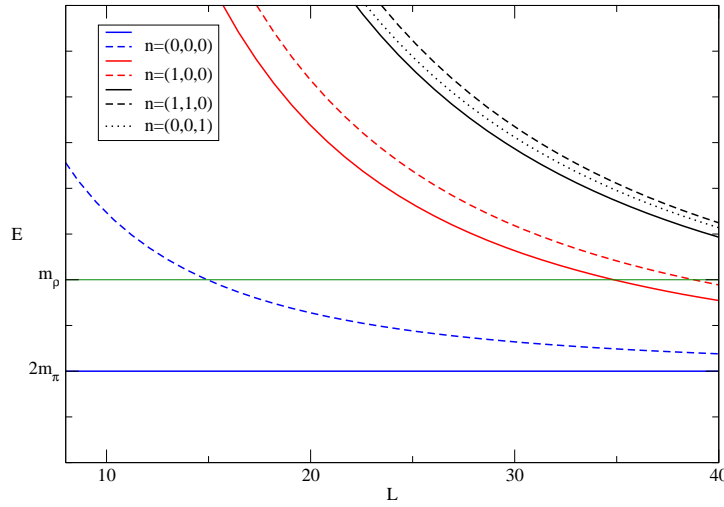


Figure D.1.: Center-of-mass energy levels of the two-“free”-pion state in the box as functions of the size L of the box. E and L are in lattice units (i.e. $E = Ea$ and $L = L/a$). The solid lines correspond to $P = 0$ and the dashed ones to $P = \frac{2\pi}{L}$.

If we now introduce the pion-pion interaction into the game – through a small 3-point $\pi\pi\rho$ term for example –, the energy eigenstates become mixtures of ρ and $\pi\pi$ states and *avoided level crossing* phenomena occur at the intersections of the ρ and $\pi\pi$ levels. Now, if we consider a simple treatment of the interaction in perturbation theory in quantum mechanics, we know that at second order, the shift in energies (for a non-degenerate level) is given by

$$\Delta E_i = \langle E_i | V | E_i \rangle + \sum_{E_j \neq E_i} \frac{|\langle E_i | V | E_j \rangle|^2}{E_i - E_j}$$

So that we expect the ρ resonance to be dominant near the avoided crossings and therefore need to choose the size of the box to probe regions near the intersections of the

levels.

Hence, using $P \neq 0$ frames can prove really useful: in fact, looking at Fig. D.1, one can see that the first avoided crossing for the sector $P = 0$ occurs around $L = 35a$ whereas for $P = \frac{2\pi}{L}$, it occurs near $L = 15a$. So that the avoided level crossings can be numerically probed in much smaller boxes.

We shall therefore consider three different frames, as suggested in [70] and [111], identified by their total momenta:

$$\text{COM: } \mathbf{P} = 0$$

$$\text{MF1: } \mathbf{P} = \frac{2\pi}{L} \mathbf{e}_3$$

$$\text{MF2: } \mathbf{P} = \frac{2\pi}{L} (\mathbf{e}_1 + \mathbf{e}_2)$$

and derive a “quantization” formula for each of these three cases.

D.3. Symmetry considerations

D.3.1. Symmetries and group theory

In the continuum, we know that the symmetry group related to angular momentum conservation is the 3 dimensional rotation group $O(3)$, which is a subgroup of the total Lorentz group $O(3,1)$. However, in Lattice QCD, the finite volume of the box breaks Lorentz symmetry into the so-called *hypercubic symmetry* and the rotation symmetry is replaced by the *cubic group symmetry* O_h ¹.

O_h contains 48 elements and is the direct product of the cubic pure-rotation group O and the inversion group \mathcal{C}_i which contains the identity E and the inversion I . Therefore, it consists of 10 conjugate classes – twice the number of classes of O – and using C_n to denote the n-fold rotation class, $S_n = C_n \sigma_h$ the n-fold rotation-reflection – where σ_h is the “perpendicular” reflection –, and σ_v, σ_d the “vertical” and “diagonal” reflections, we can compute the character table for O_h using standard group representation procedures – which can be found in [110] for example. Table D.1 gives this character table.

Moreover, the presence of a total momentum in the moving frames induces further breakdown of the cubic symmetry into smaller subgroups. In fact, if $\mathbf{P} \neq 0$ the pure-rotation cubic group O is no longer a symmetry of the system, and is replaced by the subgroup leaving \mathbf{P} invariant.

For MF1, $\mathbf{P} = \frac{2\pi}{L} \mathbf{e}_3$ so that the 4-fold rotation around \mathbf{e}_3 is not broken, but the other C_2 and C_3 rotations are broken, and only a system of two classes of 2-fold rotations subsists. Hence, the symmetry group is now the dihedral group D_{4h} , which contains 16 elements in 10 classes.

¹Here and for the remainder of the section, we use the Schoenflies notation for point groups, and the Mulliken symbols for the irreducible representations. Note that the subscripts g and u stand for “gerade” and “ungerade” respectively and describe the behaviour of the basis functions belonging to some irreducible representation upon inversion.

O_h	E	$C_3(8)$	$C_4^2(3)$	$C_2(6)$	$C_4(6)$	I	$S_4(6)$	$S_6(8)$	$\sigma_h(3)$	$\sigma_d(6)$
A_{1g}	1	1	1	1	1	1	1	1	1	1
A_{2g}	1	1	1	-1	-1	1	-1	1	1	-1
E_g	2	-1	2	0	0	2	0	-1	2	0
T_{1g}	3	0	-1	-1	1	3	1	0	-1	-1
T_{2g}	3	0	-1	1	-1	3	-1	0	-1	1
A_{1u}	1	1	1	1	1	-1	-1	-1	-1	-1
A_{2u}	1	1	1	-1	-1	-1	1	-1	-1	1
E_u	2	-1	2	0	0	-2	0	1	-2	0
T_{1u}	3	0	-1	-1	1	-3	-1	0	1	1
T_{2u}	3	0	-1	1	-1	-3	1	0	1	-1

Table D.1.: Character table for the cubic group O_h

D_{4h}	E	$C_4(2)$	$C_4^2(1)$	$C_2(2)$	$C_2'(2)$	I	$S_4(2)$	$\sigma_h(1)$	$\sigma_v(2)$	$\sigma_d(2)$
A_{1g}	1	1	1	1	1	1	1	1	1	1
A_{2g}	1	1	1	-1	-1	1	1	1	-1	-1
B_{1g}	1	-1	1	1	-1	1	-1	1	1	-1
B_{2g}	1	-1	1	-1	1	1	-1	1	-1	1
E_g	2	0	-2	0	0	2	0	-2	0	0
A_{1u}	1	1	1	1	1	-1	-1	-1	-1	-1
A_{2u}	1	1	1	-1	-1	-1	-1	-1	1	1
B_{1u}	1	-1	1	1	-1	-1	1	-1	-1	1
B_{2u}	1	-1	1	-1	1	-1	1	-1	1	-1
E_u	2	0	-2	0	0	-2	0	2	0	0

Table D.2.: Character table for the cubic group D_{4h}

For MF2, $\mathbf{P} = \frac{2\pi}{L}(\mathbf{e}_1 + \mathbf{e}_2)$ and only three orthogonal C_2 rotations subsists. The symmetry group then becomes D_{2h} , which has 8 elements in 8 classes.

The character tables for D_{4h} and D_{2h} are given in Table D.2 and Table D.3 respectively.

These different 3-dimensional symmetry groups need to be taken into account in the construction of the $\pi\pi$ interpolating operator, in order to exhibit the best possible coupling to the ρ . We can also use the remaining symmetries to simplify the quantization condition (3.1) and bring it into a practical form for our computations.

We know from experiments that the ρ meson has spin 1. Hence, it transforms in the $l = 1$ irreducible representation of the rotation group $O(3)$, which we denote $D^{(1)}$. To study $\pi\pi$ scattering in the ρ channel, we then have to build a $\pi\pi$ interpolating operator belonging to the same representation. However, since the lattice operators actually belong to representations of O_h (for the COM) or its subgroups (for MF1 and MF2), we need to consider the expansion of $D^{(1)}$ in terms of irreducible representations of O_h , D_{4h} and D_{2h} .

\mathbf{D}_{2h}	E	$C_2(1,z)$	$C_2(1,y)$	$C_2(1,x)$	I	$\sigma(1,xy)$	$\sigma(1,xz)$	$\sigma(1,yz)$
A_g	1	1	1	1	1	1	1	1
B_{1g}	1	1	-1	-1	1	1	-1	-1
B_{2g}	1	-1	1	-1	1	-1	1	-1
B_{3g}	1	-1	-1	1	1	-1	-1	1
A_u	1	1	1	1	-1	-1	-1	-1
B_{1u}	1	1	-1	-1	-1	-1	1	1
B_{2u}	1	-1	1	-1	-1	1	-1	1
B_{3u}	1	-1	-1	1	-1	1	1	-1

Table D.3.: Character table for the cubic group D_{2h}

\mathbf{O}_h	E	$C_3(8)$	$C_4^2(3)$	$C_2(6)$	$C_4(6)$	I	$S_4(6)$	$S_6(8)$	$\sigma_h(3)$	$\sigma_d(6)$
$D^{(1)}$	3	0	-1	-1	1	-3	-1	0	1	1

\mathbf{D}_{4h}	E	$C_4(2)$	$C_4^2(1)$	$C_2(2)$	$C_2'(2)$	I	$S_4(2)$	$\sigma_h(1)$	$\sigma_v(2)$	$\sigma_d(2)$
$D^{(1)}$	3	1	-1	-1	-1	-3	-1	1	1	1

\mathbf{D}_{2h}	E	$C_2(z)$	$C_1(y)$	$C_2(x)$	I	$\sigma(xy)$	$\sigma(xz)$	$\sigma(yz)$
$D^{(1)}$	3	-1	-1	-1	-3	1	1	1

Table D.4.: Characters of the classes of O_h , D_{4h} and D_{2h} in the $D^{(1)}$ irreducible representation of $O(3)$.

To proceed, we first compute the characters of the conjugate classes of O_h , D_{4h} and D_{2h} in the $D^{(1)}$ representation of $O(3)$ using the fact that $D^{(1)}$ is isomorphic to the fundamental representation, in which a rotation of angle Φ around any axis can be expressed in some basis as the matrix

$$\begin{pmatrix} \cos \Phi & -\sin \Phi & 0 \\ \sin \Phi & \cos \Phi & 0 \\ 0 & 0 & 1 \end{pmatrix}$$

so that the character $\chi^{(1)}$ of a rotation of angle $\frac{2\pi}{n}$ in $D^{(1)}$ is

$$\chi^{(1)}\left(\frac{2\pi}{n}\right) = 1 + 2 \cos\left(\frac{2\pi}{n}\right) \quad (\text{D.5})$$

The results are given in Table D.4.

Then we use the relation between the expansion coefficients and the characters, i.e. if $D^{(1)} = \sum_{\mu} a_{\mu} D^{(\mu)}$, then (c.f. for example [110])

$$a_{\mu} = \frac{1}{g} \sum_i g_i \chi_i^{(\mu)} \chi_i \quad (\text{D.6})$$

where g is the order of the group considered (i.e. 48, 16 and 8 respectively), i labels the classes of the group, g_i is the number of elements in class i and $\chi_i^{(\mu)}$, χ_i are the characters of class i in the μ^{th} irreducible representation and in $D^{(1)}$ respectively. Using the character tables provided, we can then compute the different coefficients a_μ and finally obtain the decompositions:

$$\begin{aligned} D^{(1)} &= T_{1u} && \text{for COM} \\ D^{(1)} &= A_{2u} + E_u && \text{for MF1} \\ D^{(1)} &= B_{1u} + B_{2u} + B_{3u} && \text{for MF2} \end{aligned} \tag{D.7}$$

These decompositions are of great importance, since they will allow us to project the $\pi\pi$ interpolating operators on sectors belonging to the spin 1 infinite-volume representation, as is necessary in order to recover the right partial wave sector when extrapolating our finite-volume to infinite volume.

Note however that the mixing of partial waves cannot be avoided. The point groups irreducible representations are indeed contained in several different $D^{(l)}$ representations (for example, in the COM, T_{1u} is also contained in $D^{(3)}$, $D^{(5)}$, ...), and we shall assume that the interaction only involves low energy processes, so that the phase shifts δ_l can be neglected for $l \geq 3$.

D.3.2. Symmetries and interpolating operators

Given the group theory results obtained above, we now turn to the discussion of the interpolating operators to be used in our $\pi\pi$ scattering Lattice QCD calculation. For the case that we consider – $\pi\pi$ scattering in the ρ channel, two symmetries are to be taken into account, in relation to two conserved quantum numbers: the isospin I and the angular momentum l . From experiment, we know that the ρ meson is an isospin triplet, and therefore belong to the $I = 1$ representation. Moreover, as aforementioned, it belongs to the $l = 1$ representation of the rotation group – in infinite volume. Then, to “observe” the ρ resonance on the lattice in $\pi\pi$ scattering – actually, it is more accurate to speak in terms of coupling between the fields representing 2π and ρ states; so the word “observe” means to have a good coupling between the operator fields – we need to construct a $\pi\pi$ interpolating operator transforming in the $I = 1$ and $l = 1$ representations.

On the lattice, the isospin symmetry is not broken so that the operator can be directly built so as to belong to the $I = 1$ representation. To do so, we recall that the π meson form an isospin triplet ($I = 1$). Labelling the isospin representation with $|I, I_3\rangle$, we have the π states

$$\begin{aligned} |1, +1\rangle &= |\pi^+\rangle \\ |1, 0\rangle &= |\pi^0\rangle \\ |1, -1\rangle &= |\pi^-\rangle \end{aligned} \tag{D.8}$$

Then, using the well-known results for the product of irreducible representations of the rotation group, we have

$$|\pi\rangle \otimes |\pi\rangle = |I = 0\rangle \oplus |I = 1\rangle \oplus |I = 2\rangle \tag{D.9}$$

and computing the Clebsch-Gordan coefficients, we obtain for the $I = 1$ sector the three decompositions:

	$I = 1$
$I_3 = +1$	$\frac{1}{\sqrt{2}} (\pi^+(\mathbf{p}_1, t)\pi^0(\mathbf{p}_2, t) - \pi^0(\mathbf{p}_1, t)\pi^+(\mathbf{p}_2, t))$
$I_3 = 0$	$\frac{1}{\sqrt{2}} (\pi^+(\mathbf{p}_1, t)\pi^-(\mathbf{p}_2, t) - \pi^-(\mathbf{p}_1, t)\pi^+(\mathbf{p}_2, t))$
$I_3 = -1$	$\frac{1}{\sqrt{2}} (\pi^0(\mathbf{p}_1, t)\pi^-(\mathbf{p}_2, t) - \pi^-(\mathbf{p}_1, t)\pi^0(\mathbf{p}_2, t))$

Then, to obtain the right $l = 1$ operator, we use the finite group projection operator (see again [110] for a derivation of this projection operator)

$$P^{(\mu)} \equiv \frac{n_\mu}{g} \sum_{R \in G} \chi^{(\mu)*}(R) O_R \quad (\text{D.10})$$

where μ labels the different irreducible representations, n_μ is the dimension of the corresponding representation, g is the order of the group, χ denotes the characters and the sum runs over the elements of the group. O_R is the linear operator acting on functions $\psi(x)$ associated with the transformation R of x , i.e.

$$O_R \psi(x) = \psi(R^{-1}x)$$

Following [70] and [56], we choose to study the ρ^0 ($I_3 = 0$) resonance properties and choose according to the decompositions (D.7) the irreducible representation T_{1u} for the COM, A_{2u} for MF1 and B_{3u} for MF2. And the projection operator acting on an operator $(\pi\pi)(\mathbf{p}_1, \mathbf{p}_2; t)$ chosen such that $\mathbf{p}_1 + \mathbf{p}_2 = \mathbf{P}$ gives for these representations (see tables D.1, D.2 and D.3):

$$\begin{aligned} \text{COM: } (\pi\pi)_{T_{1u}}(t) &= \frac{1}{2} \left[(\pi\pi) \left(\frac{2\pi}{L} \mathbf{e}_3, -\frac{2\pi}{L} \mathbf{e}_3; t \right) - (\pi\pi) \left(-\frac{2\pi}{L} \mathbf{e}_3, \frac{2\pi}{L} \mathbf{e}_3; t \right) \right] \\ \text{MF1: } (\pi\pi)_{A_{2u}}(t) &= \frac{1}{2} \left[(\pi\pi) \left(\frac{2\pi}{L} \mathbf{e}_3, \mathbf{0}; t \right) - (\pi\pi) \left(-\frac{2\pi}{L} \mathbf{e}_3, \mathbf{0}; t \right) \right] \\ \text{MF2: } (\pi\pi)_{B_{3u}}(t) &= \frac{1}{2} \left[(\pi\pi) \left(\frac{2\pi}{L} (\mathbf{e}_1 + \mathbf{e}_2), \mathbf{0}; t \right) - (\pi\pi) \left(-\frac{2\pi}{L} (\mathbf{e}_1 + \mathbf{e}_2), \mathbf{0}; t \right) \right] \end{aligned}$$

If we substitute the $I = 1$, $I_3 = 0$ operator in these expressions, we finally obtain the interpolating operators we will use in our Lattice QCD computations:

COM:

$$(\pi\pi)_{T_{1u}}(t) = \frac{1}{\sqrt{2}} \left[\pi^+ \left(\frac{2\pi}{L} \mathbf{e}_3, t \right) \pi^- \left(-\frac{2\pi}{L} \mathbf{e}_3, t \right) - \pi^- \left(\frac{2\pi}{L} \mathbf{e}_3, t \right) \pi^+ \left(-\frac{2\pi}{L} \mathbf{e}_3, t \right) \right] \quad (\text{D.11})$$

MF1:

$$(\pi\pi)_{A_{2u}}(t) = \frac{1}{\sqrt{2}} \left[\pi^+ \left(\frac{2\pi}{L} \mathbf{e}_3, t \right) \pi^- (\mathbf{0}, t) - \pi^- \left(\frac{2\pi}{L} \mathbf{e}_3, t \right) \pi^+ (\mathbf{0}, t) \right] \quad (\text{D.12})$$

MF2:

$$(\pi\pi)_{B_{3u}}(t) = \frac{1}{\sqrt{2}} \left[\pi^+ \left(\frac{2\pi}{L} (\mathbf{e}_1 + \mathbf{e}_2), t \right) \pi^- (\mathbf{0}, t) - \pi^- \left(\frac{2\pi}{L} (\mathbf{e}_1 + \mathbf{e}_2), t \right) \pi^+ (\mathbf{0}, t) \right] \quad (\text{D.13})$$

D.4. Finite-size formulae

As mentioned in Sec. C.3, the “infinite determinant” quantization condition (3.1) can be truncated through an angular momentum cut-off, which is compulsory in order to use it in real computations. But the determinant can be further simplified thanks to the symmetries of the systems considered for our Lattice QCD evaluation of the ρ resonance parameters. In this section, we shall therefore analyse the generic truncated condition (C.65) for the three aforementioned setups COM, MF1 and MF2 and derive finite-size formulae relating the ρ phase-shift to the finite-volume spectrum in each case.

We are interested in extracting $\pi\pi$ scattering physical quantities in the $l = 1$ channel. Hence we need to evaluate the phase-shift δ_1 , and consequently choose a momentum cut-off $l_{max} = 2$. As proved in Sec. C.3, we only need to consider the restriction of the quantization condition in the $l_1, l_2 \leq 2$ subspace:

$$\det \left(1 - \frac{i}{2} M_{l_1, m_1; l', m'} L_{l', m'; l_2, m_2}^{FV} \right) \Big|_{l_1, l', l_2 \leq 2} = 0 \quad (\text{D.14})$$

Recalling the definition of L^{FV} (C.51), we see that the computation of the determinant can be reduced thanks to the symmetries of \mathcal{Z}_{lm}^{MV} and of the Wigner 3j-symbols. The symmetries of the zeta function \mathcal{Z}_{lm}^{MV} are direct consequences of its definition in terms of spherical harmonics (see C.13). In fact, the spherical harmonics for a given l form the basis of the irreducible representation $D^{(l)}$ of the rotation group $O(3)$, so that under the action of rotations, they transform as

$$Y_{lm}(R\hat{\mathbf{r}}) = \sum_{m'=-l}^l D_{mm'}^{(l)}(R) Y_{lm'}$$

and since

$$\mathcal{Z}_{lm}^{MV} = \sum_{\mathbf{r} \in \mathbb{L}^{\mathbf{P}}} \frac{1}{(r^2 - a^2)^s} r^l Y_{lm}(\hat{\mathbf{r}})$$

with

$$\mathbb{L}^{\mathbf{P}} = \left\{ \mathbf{r} \in \mathbb{R}^3 \mid \exists \mathbf{n} \in \mathbb{Z}^3, \mathbf{r} = \frac{1}{\gamma} \left(\mathbf{n}_{\parallel} - \left(\frac{L}{2\pi} \right) \frac{\mathbf{P}}{2} \right) + \mathbf{n}_{\perp} \right\}$$

we have

$$\mathcal{Z}_{lm}^{MV} = \sum_{\mathbf{r} \in \mathbb{L}^{\mathbf{P}}} \frac{1}{(r^2 - a^2)^s} r^l Y_{lm}(R\hat{\mathbf{r}}) \quad \forall R \text{ in the subgroup of symmetry of } \mathbb{L}^{\mathbf{P}} \quad (\text{D.15})$$

which provides constraints on the values of \mathcal{Z}_{lm}^{MV} .

In particular, choosing R to be the inversion I (which belongs to all the considered subgroups: O_h , D_{4h} and D_{2h}) this relation imply for \mathcal{Z}_{lm}^{MV} (see [112] for the values of $D_{mm'}^{(l)}(R)$):

$$\mathcal{Z}_{lm}^{MV}(s; a^2) = 0 \quad \text{if } l \text{ is odd} \quad (\text{D.16})$$

The symmetry properties of the 3j-symbols can be found in [113], and with D.16 imply

$$L_{l,m;l',m'}^{FV} = 0 \quad \text{if } l \not\equiv l' \pmod{2} \quad \text{for COM, MF1 and MF2} \quad (\text{D.17})$$

The even and odd l sectors therefore decouple in all the considered frames – the matrix inside the determinant in D.14 is block diagonal in the basis ($l = 0, l = 1, l = 2$). So that we can restrict our analysis to the $l = 1$ sector, which provides the finite-size formula for δ_1 . Table D.5 gives the different values we computed for $\mathfrak{L}_{1,m;1,m'}^{FV}$.

	-1	0	1
-1	$\frac{1}{\gamma \bar{n}^* \pi^{3/2}} \left(\mathcal{Z}_{00}^{MV} - \frac{1}{\bar{n}^* 2 \sqrt{5}} \mathcal{Z}_{20}^{MV} \right)$	$-\frac{1}{\gamma \bar{n}^* 3 \pi^{3/2}} \sqrt{\frac{3}{5}} \mathcal{Z}_{21}^{MV}$	$-\frac{1}{\gamma \bar{n}^* 3 \pi^{3/2}} \sqrt{\frac{6}{5}} \mathcal{Z}_{22}^{MV}$
0	$\frac{1}{\gamma \bar{n}^* 3 \pi^{3/2}} \sqrt{\frac{3}{5}} \mathcal{Z}_{2-1}^{MV}$	$\frac{1}{\gamma \bar{n}^* \pi^{3/2}} \left(\mathcal{Z}_{00}^{MV} + \frac{2}{\bar{n}^* 2 \sqrt{5}} \mathcal{Z}_{20}^{MV} \right)$	$\frac{1}{\gamma \bar{n}^* 3 \pi^{3/2}} \sqrt{\frac{3}{5}} \mathcal{Z}_{21}^{MV}$
1	$-\frac{1}{\gamma \bar{n}^* 3 \pi^{3/2}} \sqrt{\frac{6}{5}} \mathcal{Z}_{2-2}^{MV}$	$-\frac{1}{\gamma \bar{n}^* 3 \pi^{3/2}} \sqrt{\frac{3}{5}} \mathcal{Z}_{2-1}^{MV}$	$\frac{1}{\gamma \bar{n}^* \pi^{3/2}} \left(\mathcal{Z}_{00}^{MV} - \frac{1}{\bar{n}^* 2 \sqrt{5}} \mathcal{Z}_{20}^{MV} \right)$

Table D.5.: Computed values for $\mathfrak{L}_{1,m;1,m'}^{FV}$. Note $\bar{n}^* = \frac{L}{2\pi} q^*$.

Moreover, as we have seen before, since the $O(3)$ symmetry is broken in our box, the $l = 1$ ($D^{(1)}$) representation is not irreducible and breaks into irreducible representations depending on the studied frame as given by D.7. In order to obtain the finite-size formulae corresponding to the considered representations (T_{1u} for the COM, A_{2u} for MF1 and B_{3u} for MF2), we therefore also need to write the matrix in the determinant in the basis of these irreducible representations.

We shall now study the three cases separately.

COM

We consider the 3-dimensional irreducible representation T_{1u} of the O_h cubic group. This group contains in particular $C_4(\mathbf{e}_3)$, a rotation of angle $\frac{\pi}{2}$ around the 3-axis, and

C_3 rotations around “long-diagonal” axis (i.e. of the form $\mathbf{e}_1 + \mathbf{e}_2 + \mathbf{e}_3$). These two types of rotations inserted in D.15 give after some algebra

$$\begin{aligned} \mathcal{Z}_{lm}^{COM}(s; a^2) &= 0 \quad \text{if } m \not\equiv 0 \pmod{4} \\ \mathcal{Z}_{20}^{COM} &= 0 \end{aligned} \quad (\text{D.18})$$

and hence, using also table D.5,

$$L_{1,m;1,m'}^{FV} = 0 \quad \text{if } m \neq m' \quad (\text{D.19})$$

$$L_{1,-1;1,-1}^{FV} = L_{1,0;1,0}^{FV} = L_{1,1;1,1}^{FV} = 1 + i \mathfrak{L}_{1,0;1,0}^{FV} \quad (\text{D.20})$$

The determinant equation is therefore “diagonal” and reduces to a single formula in this sector. If we insert the expression of $M_{l_1, m_1; l', m'}$ in terms of the phase-shifts Eq. (C.58) into Eq. (D.14), we get

$$\begin{aligned} \det \left(1 - \frac{4\pi E^*}{q^*} (e^{2i\delta_1} - 1) L_{1, m_1; 1, m_2}^{FV} \right) \Big|_{l_1, l_2 \leq 2} \\ = \left(1 + \frac{e^{2i\delta_1} - 1}{2} (1 + i \mathfrak{L}_{1,0;1,0}^{FV}) \right)^3 \\ = 0 \end{aligned} \quad (\text{D.21})$$

and after some algebra, we get the finite-size formula

$$\cot(\delta_1) = \frac{1}{\bar{n}^* \pi^{3/2}} \mathcal{Z}_{00}^{COM}(1; \bar{n}^{*2}) \quad (\text{D.22})$$

MF1

Here the symmetry group is the D_{4h} subgroup, and we consider the 1-dimensional irreducible representation A_{2u} . This group still contains the $C_4(\mathbf{e}_3)$ rotation, but not the C_3 rotations. Hence the determinant is still diagonal, but

$$L_{1,-1;1,-1}^{FV} = L_{1,1;1,1}^{FV} \neq L_{1,0;1,0}^{FV} \quad (\text{D.23})$$

and since we work in A_{2u} , the finite-size formula is now

$$\cot(\delta_1) = \frac{1}{\gamma \bar{n}^* \pi^{3/2}} \left(\mathcal{Z}_{00}^{MF1} + \frac{2}{\bar{n}^{*2} \sqrt{5}} \mathcal{Z}_{20}^{MF1} \right) \quad (\text{D.24})$$

MF2

Eventually, the cubic group is broken to D_{2h} , and we consider the B_{3u} irreducible representation. To get the right finite-size formula, we need to build the symmetry adapted vector basis. Note however that since $\mathbf{P} = \frac{\mathbf{e}_1 + \mathbf{e}_2}{2}$ in this frame, the 3 C_2 axes are “aligned” with $\mathbf{e}_1 + \mathbf{e}_2$ (i.e. one axis is given by $\mathbf{e}_1 + \mathbf{e}_2$ and the others are at right angles to it). So that when expressing the symmetry adapted vector basis in terms of

the $\{|m\rangle\}$ basis for $D^{(1)}$, we need to rotate the $\{|m\rangle\}$ vectors by $-\frac{\pi}{4}$ around the 3-axis in order to express them in terms of the lattice $\{|m\rangle\}$ basis. This only involves multiplication by the phase $e^{-im(\pi/4)}$ for each $|m\rangle$. Using the table from [114], we then obtain

$$\begin{aligned} |B_{1u}\rangle &= |m=0\rangle \\ |B_{2u}\rangle &= -\frac{1+i}{2} |m=1\rangle + \frac{1-i}{2} |m=-1\rangle \\ |B_{3u}\rangle &= -\frac{1-i}{2} |m=1\rangle + \frac{1+i}{2} |m=-1\rangle \end{aligned}$$

and the action of the $C_2(\mathbf{e}_1 + \mathbf{e}_2)$ in D.15 gives

$$\mathfrak{L}_{1,-1;1,1}^{FV} + \mathfrak{L}_{1,1;1,-1}^{FV} = 0$$

so that D.14 can be rewritten in the $\{|B_{1u}\rangle, |B_{2u}\rangle, |B_{3u}\rangle\}$ basis as

$$\begin{vmatrix} \cot(\delta_1) - \mathfrak{L}_{1,0;1,0}^{FV} & 0 & 0 \\ 0 & \cot(\delta_1) - \mathfrak{L}_{1,1;1,1}^{FV} - \frac{i}{2} (\mathfrak{L}_{1,1;1,-1}^{FV} - \mathfrak{L}_{1,-1;1,1}^{FV}) & 0 \\ 0 & 0 & \cot(\delta_1) - \mathfrak{L}_{1,1;1,1}^{FV} + \frac{i}{2} (\mathfrak{L}_{1,1;1,-1}^{FV} - \mathfrak{L}_{1,-1;1,1}^{FV}) \end{vmatrix} = 0 \quad (\text{D.25})$$

so that the finite-size formula for B_{3u} reads

$$\cot(\delta_1) = \frac{1}{\gamma \bar{n}^* \pi^{3/2}} \left(\mathcal{Z}_{00}^{MF2} - \frac{1}{\bar{n}^* 2 \sqrt{5}} \mathcal{Z}_{20}^{MF2} - i \frac{\sqrt{3}}{\bar{n}^* 2 \sqrt{10}} (\mathcal{Z}_{22}^{MF2} - \mathcal{Z}_{2-2}^{MF2}) \right) \quad (\text{D.26})$$

E. Variable projection method

In this appendix, we briefly describe the variable projection method, and its use to fit the time dependence of 2-pt correlation functions. More detailed accounts can be found in [97, 98] and [115].

As shown in Sec. 2.4.2, the time dependence of hadronic 2-pt correlation functions is given by the spectral decomposition (in the region $0 < t < T/2$, where the contribution of backward propagating states is negligible)

$$C_{2h}(t) \equiv \langle \tilde{O}_h(t) \bar{O}_h(0) \rangle = \sum_{k=0}^N \langle \Omega | \tilde{O}_h(0) | k \rangle \langle k | O_h^\dagger(0) | \Omega \rangle e^{-tE_k} \quad (\text{E.1})$$

where t is the discrete time in lattice units and N is the number of states considered. We define

$$\alpha_k \equiv \langle \Omega | \tilde{O}_h(0) | k \rangle \langle k | O_h^\dagger(0) | \Omega \rangle$$

and

$$y_i \equiv C_{2h}(i)$$

for $i = 1, \dots, n_t$, $n_t < T/2$.

Our goal is then to determine the parameters $\{\alpha_k\}$ and $\{aE_k\}$, $k = 1, \dots, N$ from a set of n_t values $\{y_i\}$, which corresponds to solving a system of non-linear equations of the form

$$y_i = \sum_{k=0}^N \alpha_k [\exp(-aE_k)]^i = \sum_{k=0}^N \Phi_{ik} \alpha_k = (\Phi \alpha)_i \quad (\text{E.2})$$

where we have defined $\Phi_{ik} = [\exp(-aE_k)]^i$.

The solution is found by minimizing the Least-Square functional

$$\chi^2 = \|\mathbf{y} - (\Phi \alpha)\|_2^2 = \sum_i |y_i - (\Phi \alpha)_i|^2 \quad (\text{E.3})$$

with respect to both the non-linear parameters aE_k (entering χ^2 through Φ) and the linear ones α_k .

Now, the variable projection method idea is to notice that if we introduce Φ^+ , the Moore-Penrose generalized inverse of Φ , then if we knew the values of the aE_k , we would have directly

$$\alpha = \Phi^+ \mathbf{y} \quad (\text{E.4})$$

Inserting this expression into the χ^2 functional, we see that the quantity to minimize becomes

$$\chi^2 = \|\mathbf{y} - (\Phi \Phi^+ \mathbf{y})\|_2^2 \quad (\text{E.5})$$

The minimization now only involves the $\{aE_k\}$ parameters, and the amplitudes $\{\alpha_k\}$ can be found afterwards using Eq. (E.4). This two-step process can be proved to be equivalent to minimizing with respect to both $\{\alpha_k\}$ and $\{aE_k\}$ directly, and is much more stable, as the minimization only involves half the parameters.

Note that the matrix $I - \Phi\Phi^+$ appearing in the variable projection Least-Square functional is the projection onto the kernel of Φ , which justifies the name of the method, and motivates its efficiency.

Bibliography

- [1] M. Gell-Mann, “A Schematic Model of Baryons and Mesons,” *Phys.Lett.*, vol. 8, pp. 214–215, 1964.
- [2] G. Zweig, “An $su(3)$ model for strong interaction symmetry and its breaking,” *CERN Report*, no. 8182/TH.401, 1964.
- [3] M. Gell-Mann and Y. Neemam, “The Eightfold way: a review with a collection of reprints,” 1964.
- [4] P. N. Burrows, “Precise tests of QCD in $e^+ e^-$ annihilation,” in *The Strong interaction, from hadrons to partons: Proceedings, 24th SLAC Summer Institute on Particle Physics (SSI 96), Stanford, Calif., 19-30 Aug 1996*, 1997.
- [5] S. Weinberg, “Phenomenological Lagrangians,” *Physica*, vol. A96, p. 327, 1979.
- [6] J. Gasser and H. Leutwyler, “Quark Masses,” *Phys.Rept.*, vol. 87, pp. 77–169, 1982.
- [7] P. Guichon, “QCD et le confinement.” Sept. 1998.
- [8] K. G. Wilson, “Renormalization group and critical phenomena. 1. Renormalization group and the Kadanoff scaling picture,” *Phys.Rev.*, vol. B4, pp. 3174–3183, 1971.
- [9] J. Callan, Curtis G., “Broken scale invariance in scalar field theory,” *Phys.Rev.*, vol. D2, pp. 1541–1547, 1970.
- [10] K. Symanzik, “Small distance behavior in field theory and power counting,” *Commun.Math.Phys.*, vol. 18, pp. 227–246, 1970.
- [11] D. J. Gross and F. Wilczek, “Ultraviolet Behavior of Nonabelian Gauge Theories,” *Phys.Rev.Lett.*, vol. 30, pp. 1343–1346, 1973.
- [12] H. D. Politzer, “Reliable Perturbative Results for Strong Interactions?,” *Phys.Rev.Lett.*, vol. 30, pp. 1346–1349, 1973.
- [13] M. Creutz and K. Moriarty, “Numerical Studies of Wilson Loops in $SU(3)$ Gauge Theory in Four-dimensions,” *Phys.Rev.*, vol. D26, p. 2166, 1982.
- [14] S. Weinberg, “Dynamical approach to current algebra,” *Phys.Rev.Lett.*, vol. 18, pp. 188–191, 1967.

-
- [15] S. Weinberg, “Nonlinear realizations of chiral symmetry,” *Phys.Rev.*, vol. 166, pp. 1568–1577, 1968.
- [16] S. Weinberg, “The quantum theory of fields. Vol. 2: Modern applications,” 1996.
- [17] S. Scherer and M. R. Schindler, “A Primer for Chiral Perturbation Theory,” *Lect.Notes Phys.*, vol. 830, pp. pp.1–338, 2012.
- [18] V. Bernard and U.-G. Meissner, “Chiral perturbation theory,” *Ann.Rev.Nucl.Part.Sci.*, vol. 57, pp. 33–60, 2007.
- [19] V. Bernard, “Chiral Perturbation Theory and Baryon Properties,” *Prog.Part.Nucl.Phys.*, vol. 60, pp. 82–160, 2008.
- [20] K. G. Wilson, “Quarks and Strings on a Lattice,” in *Boston Conf. 1975:99, Erice Subnucl.Phys.1975:0069*, p. 99, 1975. [0069(1975)].
- [21] M. Bochicchio, L. Maiani, G. Martinelli, G. C. Rossi, and M. Testa, “Chiral Symmetry on the Lattice with Wilson Fermions,” *Nucl.Phys.*, vol. B262, p. 331, 1985.
- [22] H. B. Nielsen and M. Ninomiya, “No Go Theorem for Regularizing Chiral Fermions,” *Phys.Lett.*, vol. B105, p. 219, 1981.
- [23] H. B. Nielsen and M. Ninomiya, “Absence of Neutrinos on a Lattice. 1. Proof by Homotopy Theory,” *Nucl.Phys.*, vol. B185, p. 20, 1981.
- [24] H. B. Nielsen and M. Ninomiya, “Absence of Neutrinos on a Lattice. 2. Intuitive Topological Proof,” *Nucl.Phys.*, vol. B193, p. 173, 1981.
- [25] D. B. Kaplan, “Chiral Symmetry and Lattice Fermions,” pp. 223–272, 2009.
- [26] K. G. Wilson, “Confinement of Quarks,” *Phys.Rev.*, vol. D10, pp. 2445–2459, 1974.
- [27] K. Osterwalder and E. Seiler, “Gauge Field Theories on the Lattice,” *Annals Phys.*, vol. 110, p. 440, 1978.
- [28] K. Symanzik, “Continuum Limit and Improved Action in Lattice Theories. 1. Principles and ϕ^4 Theory,” *Nucl.Phys.*, vol. B226, p. 187, 1983.
- [29] K. Symanzik, “Continuum Limit and Improved Action in Lattice Theories. 2. $O(N)$ Nonlinear Sigma Model in Perturbation Theory,” *Nucl.Phys.*, vol. B226, p. 205, 1983.
- [30] B. Sheikholeslami and R. Wohlert, “Improved Continuum Limit Lattice Action for QCD with Wilson Fermions,” *Nucl.Phys.*, vol. B259, p. 572, 1985.
- [31] M. Luscher, S. Sint, R. Sommer, P. Weisz, and U. Wolff, “Nonperturbative $O(a)$ improvement of lattice QCD,” *Nucl.Phys.*, vol. B491, pp. 323–343, 1997.

-
- [32] M. Luscher and P. Weisz, “On-Shell Improved Lattice Gauge Theories,” *Commun.Math.Phys.*, vol. 97, p. 59, 1985.
- [33] S. Capitani, S. Durr, and C. Hoelbling, “Rationale for UV-filtered clover fermions,” *JHEP*, vol. 0611, p. 028, 2006.
- [34] C. Morningstar and M. J. Peardon, “Analytic smearing of SU(3) link variables in lattice QCD,” *Phys.Rev.*, vol. D69, p. 054501, 2004.
- [35] A. Hasenfratz and F. Knechtli, “Flavor symmetry and the static potential with hypercubic blocking,” *Phys.Rev.*, vol. D64, p. 034504, 2001.
- [36] S. Durr, Z. Fodor, C. Hoelbling, S. Katz, S. Krieg, *et al.*, “Lattice QCD at the physical point: simulation and analysis details,” *JHEP*, vol. 1108, p. 148, 2011.
- [37] A. Haar, “Der massbegriff in der theorie der kontinuierlichen gruppen,” *Annals of Mathematics*, vol. 34, no. 1, pp. pp. 147–169, 1933.
- [38] G. Wick, “The Evaluation of the Collision Matrix,” *Phys.Rev.*, vol. 80, pp. 268–272, 1950.
- [39] M. Luscher, “Computational Strategies in Lattice QCD,” pp. 331–399, 2010.
- [40] S. Duane, A. Kennedy, B. Pendleton, and D. Roweth, “Hybrid Monte Carlo,” *Phys.Lett.*, vol. B195, pp. 216–222, 1987.
- [41] D. Weingarten and D. Petcher, “Monte Carlo Integration for Lattice Gauge Theories with Fermions,” *Phys.Lett.*, vol. B99, p. 333, 1981.
- [42] C. Gattringer and C. B. Lang, “Quantum chromodynamics on the lattice,” *Lect.Notes Phys.*, vol. 788, pp. 1–343, 2010.
- [43] I. P. Omelyan, I. M. Mryglod, and R. Folk, “Symplectic analytically integrable decomposition algorithms: classification, derivation, and application to molecular dynamics, quantum and celestial mechanics simulations,” vol. 151, pp. 272–314, Apr. 2003.
- [44] S. Schaefer, “Simulations with the hybrid Monte Carlo algorithm: Implementation and data analysis,” pp. 401–422, 2009.
- [45] Y. Saad, *Iterative Methods for Sparse Linear Systems*. Philadelphia, PA, USA: Society for Industrial and Applied Mathematics, 2nd ed., 2003.
- [46] L. Giusti, M. Paciello, C. Parrinello, S. Petrarca, and B. Taglienti, “Problems on lattice gauge fixing,” *Int.J.Mod.Phys.*, vol. A16, pp. 3487–3534, 2001.
- [47] B. Efron, “Bootstrap methods: Another look at the jackknife,” *Ann. Statist.*, vol. 7, pp. 1–26, 01 1979.

- [48] S. Durr, Z. Fodor, J. Frison, C. Hoelbling, R. Hoffmann, *et al.*, “Ab initio determination of light hadron masses,” *Science*, vol. 322, pp. 1224–1227, 2008.
- [49] S. Dürer *et al.*, “Lattice QCD at the physical point meets SU(2) chiral perturbation theory,” *Phys.Rev.*, vol. D90, no. 11, p. 114504, 2014.
- [50] S. A. Gottlieb, P. B. Mackenzie, H. Thacker, and D. Weingarten, “The rho- pi pi Coupling Constant in Lattice Gauge Theory,” *Phys.Lett.*, vol. B134, p. 346, 1984.
- [51] R. D. Loft and T. A. DeGrand, “Vector Meson Decay Into Pseudoscalars From Quenched Lattice QCD,” *Phys.Rev.*, vol. D39, p. 2692, 1989.
- [52] C. McNeile and C. Michael, “Hadronic decay of a vector meson from the lattice,” *Phys.Lett.*, vol. B556, pp. 177–184, 2003.
- [53] S. Aoki *et al.*, “Lattice QCD Calculation of the rho Meson Decay Width,” *Phys.Rev.*, vol. D76, p. 094506, 2007.
- [54] M. Gockeler *et al.*, “Extracting the rho resonance from lattice QCD simulations at small quark masses,” *PoS*, vol. LATTICE2008, p. 136, 2008.
- [55] S. Aoki *et al.*, “ ρ Meson Decay in 2+1 Flavor Lattice QCD,” *Phys.Rev.*, vol. D84, p. 094505, 2011.
- [56] C. Lang, D. Mohler, S. Prelovsek, and M. Vidmar, “Coupled channel analysis of the rho meson decay in lattice QCD,” *Phys.Rev.*, vol. D84, no. 5, p. 054503, 2011.
- [57] J. Frison *et al.*, “Rho decay width from the lattice,” *PoS*, vol. LATTICE2010, p. 139, 2010.
- [58] X. Feng, K. Jansen, and D. B. Renner, “Resonance Parameters of the rho-Meson from Lattice QCD,” *Phys.Rev.*, vol. D83, p. 094505, 2011.
- [59] J. J. Dudek, R. G. Edwards, and C. E. Thomas, “Energy dependence of the ρ resonance in $\pi\pi$ elastic scattering from lattice QCD,” *Phys.Rev.*, vol. D87, no. 3, p. 034505, 2013.
- [60] M. Luscher, “Two particle states on a torus and their relation to the scattering matrix,” *Nucl. Phys.*, vol. B354, pp. 531–578, 1991.
- [61] M. Luscher, “Signatures of unstable particles in finite volume,” *Nucl.Phys.*, vol. B364, pp. 237–254, 1991.
- [62] M. Luscher, “Volume Dependence of the Energy Spectrum in Massive Quantum Field Theories. 1. Stable Particle States,” *Commun.Math.Phys.*, vol. 104, p. 177, 1986.
- [63] M. Luscher, “Volume Dependence of the Energy Spectrum in Massive Quantum Field Theories. 2. Scattering States,” *Commun.Math.Phys.*, vol. 105, pp. 153–188, 1986.

- [64] K. Rummukainen and S. A. Gottlieb, “Resonance scattering phase shifts on a nonrest frame lattice,” *Nucl.Phys.*, vol. B450, pp. 397–436, 1995.
- [65] C. Kim, C. Sachrajda, and S. R. Sharpe, “Finite-volume effects for two-hadron states in moving frames,” *Nucl.Phys.*, vol. B727, pp. 218–243, 2005.
- [66] L. Lellouch, “Flavor physics and lattice quantum chromodynamics,” *Les Houches 2009, Session XCIII*, pp. 629–698, 2011.
- [67] L. S. Brown and R. L. Goble, “Pion-Pion Scattering, Current Algebra, Unitarity, and the Width of the Rho Meson,” *Phys.Rev.Lett.*, vol. 20, pp. 346–349, 1968.
- [68] M. Luscher and U. Wolff, “How to Calculate the Elastic Scattering Matrix in Two-dimensional Quantum Field Theories by Numerical Simulation,” *Nucl.Phys.*, vol. B339, pp. 222–252, 1990.
- [69] B. Blossier, M. Della Morte, G. von Hippel, T. Mendes, and R. Sommer, “On the generalized eigenvalue method for energies and matrix elements in lattice field theory,” *JHEP*, vol. 0904, p. 094, 2009.
- [70] X. Feng, *Investigating scattering phenomena form Lattice QCD using twisted mass fermions*. PhD thesis, Westfälischen Wilhelms-Universität Münster, 2010.
- [71] W. Armour, C. Allton, D. B. Leinweber, A. W. Thomas, and R. D. Young, “Unified chiral analysis of the vector meson spectrum from lattice QCD,” *J.Phys.*, vol. G32, pp. 971–992, 2006.
- [72] J. Frison, *Ab-initio determination of Light Hadronic Resonance Properties*. PhD thesis, 2012. 2012AIXM4082.
- [73] S. Borsanyi, S. Durr, Z. Fodor, C. Hoelbling, S. Katz, *et al.*, “Ab initio calculation of the neutron-proton mass difference,” *Science*, vol. 347, pp. 1452–1455, 2015.
- [74] K. Olive *et al.*, “Review of Particle Physics,” *Chin.Phys.*, vol. C38, p. 090001, 2014.
- [75] I. Estermann, R. Frisch, and O. Stern, “Magnetic moment of the proton,” *Nature*, vol. 132, pp. 169–170, July 1933.
- [76] M. Rosenbluth, “High Energy Elastic Scattering of Electrons on Protons,” *Phys.Rev.*, vol. 79, pp. 615–619, 1950.
- [77] E. Clementel, C. Villi, and L. Jess, “Phase shift analysis of proton-proton scattering experiments,” *Il Nuovo Cimento*, vol. 5, no. 4, pp. 907–920, 1957.
- [78] S. Weinberg, “The Quantum theory of fields. Vol. 1: Foundations,” 1995.
- [79] M. Peskin and D. Schroeder, *An Introduction to Quantum Field Theory*. Advanced book classics, Addison-Wesley Publishing Company, 1995.

- [80] E. Chambers and R. Hofstadter, "Structure of the Proton," *Phys.Rev.*, vol. 103, pp. 1454–1463, 1956.
- [81] R. Hofstadter, "Electron scattering and nuclear structure," *Rev.Mod.Phys.*, vol. 28, pp. 214–254, 1956.
- [82] A. Puckett, E. Brash, O. Gayou, M. Jones, L. Pentchev, *et al.*, "Final Analysis of Proton Form Factor Ratio Data at $Q^2 = 4.0, 4.8$ and 5.6 GeV^2 ," *Phys.Rev.*, vol. C85, p. 045203, 2012.
- [83] V. Punjabi, C. Perdrisat, M. Jones, E. Brash, and C. Carlson, "The Structure of the Nucleon: Elastic Electromagnetic Form Factors," 2015.
- [84] A. Antognini, F. Nez, K. Schuhmann, F. D. Amaro, F. Biraben, *et al.*, "Proton Structure from the Measurement of $2S - 2P$ Transition Frequencies of Muonic Hydrogen," *Science*, vol. 339, pp. 417–420, 2013.
- [85] P. J. Mohr, B. N. Taylor, and D. B. Newell, "CODATA Recommended Values of the Fundamental Physical Constants: 2010," *Rev.Mod.Phys.*, vol. 84, pp. 1527–1605, 2012.
- [86] W. Alberico, S. Bilenky, C. Giunti, and K. Graczyk, "Electromagnetic form factors of the nucleon: New Fit and analysis of uncertainties," *Phys.Rev.*, vol. C79, p. 065204, 2009.
- [87] J. Kelly, "Simple parametrization of nucleon form factors," *Phys.Rev.*, vol. C70, p. 068202, 2004.
- [88] E. Geis *et al.*, "The Charge Form Factor of the Neutron at Low Momentum Transfer from the H-2-polarized (e-polarized, e-prime n) p Reaction," *Phys.Rev.Lett.*, vol. 101, p. 042501, 2008.
- [89] S. Weinberg, "Charge symmetry of weak interactions," *Phys.Rev.*, vol. 112, pp. 1375–1379, 1958.
- [90] V. Bernard, L. Elouadrhiri, and U. Meissner, "Axial structure of the nucleon: Topical Review," *J.Phys.*, vol. G28, pp. R1–R35, 2002.
- [91] M. Schindler and S. Scherer, "Nucleon Form Factors of the Isovector Axial-Vector Current: Situation of Experiments and Theory," *Eur.Phys.J.*, vol. A32, pp. 429–433, 2007.
- [92] G. Martinelli, C. Pittori, C. T. Sachrajda, M. Testa, and A. Vladikas, "A General method for nonperturbative renormalization of lattice operators," *Nucl.Phys.*, vol. B445, pp. 81–108, 1995.
- [93] L. Maiani, G. Martinelli, M. L. Paciello, and B. Taglienti, "Scalar Densities and Baryon Mass Differences in Lattice QCD With Wilson Fermions," *Nucl. Phys.*, vol. B293, p. 420, 1987.

-
- [94] J. Bulava, M. Donnellan, and R. Sommer, “On the computation of hadron-to-hadron transition matrix elements in lattice QCD,” *JHEP*, vol. 01, p. 140, 2012.
- [95] Y. Hua and T. K. Sarkar, “Matrix pencil method for estimating parameters of exponentially damped/undamped sinusoids in noise,” *Acoustics, Speech and Signal Processing, IEEE Transactions on*, vol. 38, no. 5, pp. 814–824, 1990.
- [96] T. K. Sarkar and O. Pereira, “Using the matrix pencil method to estimate the parameters of a sum of complex exponentials,” *Antennas and Propagation Magazine, IEEE*, vol. 37, no. 1, pp. 48–55, 1995.
- [97] G. H. Golub and V. Pereyra, “The differentiation of pseudo-inverses and nonlinear least squares problems whose variables separate,” *SIAM Journal on numerical analysis*, vol. 10, no. 2, pp. 413–432, 1973.
- [98] G. Golub and V. Pereyra, “Separable nonlinear least squares: the variable projection method and its applications,” *Inverse problems*, vol. 19, no. 2, p. R1, 2003.
- [99] L. Maiani and G. Martinelli, “Current Algebra and Quark Masses from a Monte Carlo Simulation with Wilson Fermions,” *Phys.Lett.*, vol. B178, p. 265, 1986.
- [100] C. Alexandrou, M. Brinet, J. Carbonell, M. Constantinou, P. A. Harraud, P. Guichon, K. Jansen, T. Korzec, and M. Papinutto, “Axial Nucleon form factors from lattice QCD,” *Phys. Rev.*, vol. D83, p. 045010, 2011.
- [101] P. M. Junnarkar, S. Capitani, D. Djukanovic, G. von Hippel, J. Hua, B. Jäger, H. B. Meyer, T. D. Rae, and H. Wittig, “Nucleon axial form factors from two-flavour Lattice QCD,” *PoS*, vol. LATTICE2014, p. 150, 2015.
- [102] J. Hall, D. Leinweber, and R. Young, “Chiral extrapolations for nucleon electric charge radii,” *Phys.Rev.*, vol. D88, no. 1, p. 014504, 2013.
- [103] J. R. Green, M. Engelhardt, S. Krieg, J. W. Negele, A. V. Pochinsky, and S. N. Syritsyn, “Nucleon Structure from Lattice QCD Using a Nearly Physical Pion Mass,” *Phys. Lett.*, vol. B734, pp. 290–295, 2014.
- [104] S. Capitani, M. Della Morte, D. Djukanovic, G. von Hippel, J. Hua, B. Jäger, B. Knippschild, H. B. Meyer, T. D. Rae, and H. Wittig, “Nucleon electromagnetic form factors in two-flavour QCD,” 2015.
- [105] C. Alexandrou, M. Brinet, J. Carbonell, M. Constantinou, P. A. Harraud, P. Guichon, K. Jansen, T. Korzec, and M. Papinutto, “Nucleon electromagnetic form factors in twisted mass lattice QCD,” *Phys. Rev.*, vol. D83, p. 094502, 2011.
- [106] R. Horsley, Y. Nakamura, A. Nobile, P. Rakow, G. Schierholz, *et al.*, “Nucleon axial charge and pion decay constant from two-flavor lattice QCD,” 2013.
- [107] A. Abdel-Rehim *et al.*, “Nucleon and pion structure with lattice QCD simulations at physical value of the pion mass,” 2015.

-
- [108] A. Abdel-Rehim, C. Alexandrou, M. Constantinou, K. Hadjiyiannakou, K. Jansen, and G. Koutsou, “Nucleon electromagnetic form factors from twisted mass lattice QCD,” *PoS*, vol. LATTICE2014, p. 148, 2015.
- [109] P. Huber, *Robust Statistics*. Wiley Series in Probability and Statistics - Applied Probability and Statistics Section Series, Wiley, 2004.
- [110] M. Hamermesh, *Group Theory and its Application to Physical Problems*. Addison-Wesley Publishing Company, Inc., 1962.
- [111] T. Yamazaki *et al.*, “ $I = 2$ $\pi\pi$ scattering phase shift with two flavors of $O(a)$ improved dynamical quarks,” *Phys.Rev.*, vol. D70, p. 074513, 2004.
- [112] A.R. Edmonds, *Angular Momentum in Quantum Mechanics*. Princeton University Press, 1957.
- [113] M. Rotenberg, R. Bivins, N. Metropolis and J.K. Wooten, Jr., *The 3-j and 6-j symbols*. MIT Press, 1959.
- [114] G. Grenet, P. Guichon and M. Kibler, “Tables of Clebsch-Gordan coefficients adapted to the cubical, tetragonal and digonal double groups.” LYCEN/7834.
- [115] G. T. Fleming, “What can lattice QCD theorists learn from NMR spectroscopists?,” in *QCD and numerical analysis III. Proceedings, 3rd International Workshop, Edinburgh, UK, June 30-July 4, 2003*, pp. 143–152, 2004.